Università degli Studi di Milano

Dipartimento di Chimica

Ph.D. in Chemistry – XXIX Cycle

OPTOELECTRONICALLY ACTIVE DINUCLEAR RHENIUM(I) AND MANGANESE(I) COMPLEXES: FROM DESIGN TO APPLICATIONS

(CHIM/02, CHIM/03)

LORENZO VERONESE

R10448

Supervisor: Dr. Monica Panigati

Coordinator: Prof. Emanuela Licandro

A.A. 2016-2017

TABLE OF CONTENTS

CHAPTER 1

Transition metal complexes as triplet emitters

Abstract

Interaction phenomena between UV-Vis light and molecules, in terms of absorption and emission of photons, are here briefly outlined. d^6 transition metal complexes, especially Re(I), will be discussed in particular, focusing on electronic structure and transitions involved.

1.1 Photophysics: general considerations

Electromagnetic radiation and matter can interact with each other in different ways, mostly depending on the energy of the involved photons. In a molecule, the energy of a photon is exploited to promote the electronic transitions, with the subsequent transfer of an electron from a bonding or non-bonding orbital to an antibonding orbital lying at higher energy. In this way, the electronic state of the molecule switches from the non-excited ground state to an excited, more energetic state. This electronic transition occurs only if the energy, $h\nu$, of the incident photon corresponds to the difference between the ground and the excited state (equation 1.1):

$$A + h\nu \rightarrow A^{*} \qquad \text{(eq. 1.1)}$$

It is important to note that the absorption of a photon is an ultrafast process (10^{-15} s) compared to any other process, nuclear motion included (*Franck-Condon principle*). Hence, the nuclei are considered to be in their ground state position after the generation of the excited state.

An excited molecule, due to the higher energy and different electronic configuration compared to the ground state, shows different chemical and physical properties, such as different reactivity, geometry or dipole moment. Therefore, an excited molecule should be regarded as an unstable, different species from a non-excited counterpart.

Many relaxation pathways to the ground state can be followed in competitive ways: 1) conversion, via heat production (non-radiative decay); 2) conversion, with emission of a photon (radiative decay), this

process being referred to as photoluminescence (PL); 3) transformation into other chemical species (photochemical reaction).[1] A simple method to portray the light-molecule interaction relies on a state energy diagram (figure 1.1) called "Jabłonski diagram", that schematically describes all the possible photophysical processes, photon absorption, internal conversion (IC), fluorescence, intersystem crossing (ISC), phosphorescence and vibrational relaxation being the most common.

Each state is usually labeled by its *spin multiplicity* and a number according to its relative energy. For example, S_0, S_1, S_2... S_n represent singlet states of increasing energy and a total spin quantum number equal to zero. T_1, T_2, T_3... T_n represent instead triplet states having total spin equal to one. Furthermore, vibrational levels are associated with each electronic state, thus actually considering transitions that lead to different *vibronic* states.

Transitions within vibronic states can be due to radiative (straight lines) processes, leading to an emission of electromagnetic radiation or non-radiative (wavy lines) processes, leading to thermal alterations. Both theory and experimental evidence have proven that most of the photophysical phenomena originate from the lowest vibrational state of the first excited state of a species (*Kasha's rule*) therefore, after an absorption process, a fast internal conversion followed by vibrational relaxation brings the species back to S_1.

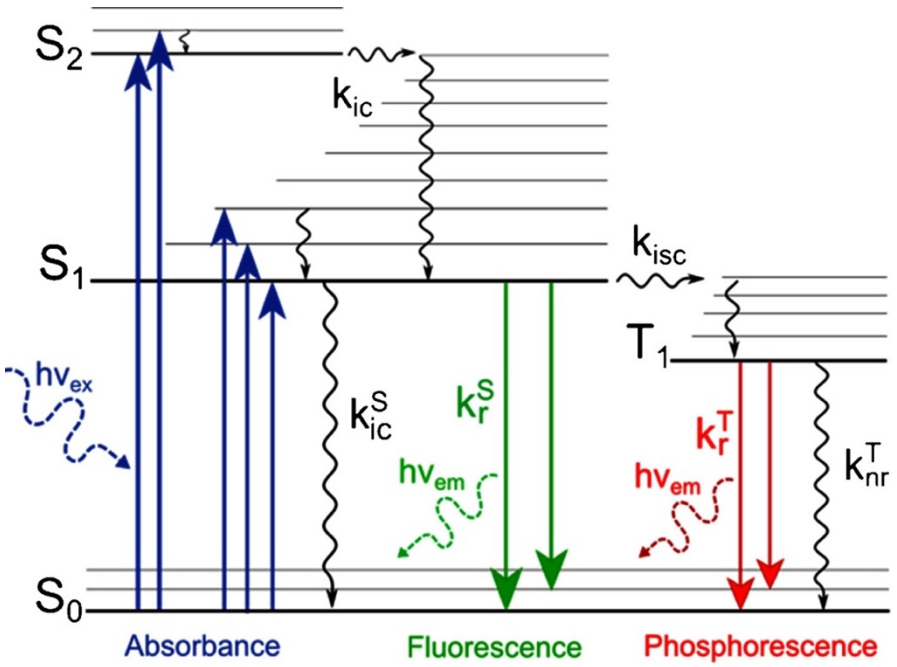

Figure 1.1 Jabłonski diagram. The main electronic transitions and corresponding rates are depicted.

A set of *selection rules* (electronic, vibrational and spin) governs the probability of a transition. Those between identical spin multiplicity are allowed, therefore singlet-singlet and triplet-triplet processes are the most favored and give rise to intense bands in the absorption and emission spectra. The emission of a photon involving two singlet states, namely $S_1 \rightarrow S_0$ transition (equation 1.2), is called *fluorescence*.

$$^1A^* \rightarrow {}^1A + h\nu' \qquad \text{(eq. 1.2)}$$

On the other hand, the emission involving the triplet excited state ($T_1 \rightarrow S_0$, equation 1.3) is called *phosphorescence* and is generally spin-forbidden and, thus, triplet states decay non-radiatively to the ground state.

$$^3A^* \rightarrow {}^1A + h\nu'' \qquad \text{(eq. 1.3)}$$

However, an interaction occurs between wavefunctions with different multiplicity via spin-orbit (SO) coupling (i.e. coupling between the orbital magnetic moment and the spin magnetic moment). The intensity of this coupling varies directly as the 4th power of the atomic number Z and the radiative rate constant k_r for emitters from triplet states can be expressed as follows (equation 1.4):[2]

$$k_r \approx ({}^3E_1)^3 \sum_i \frac{\left\langle {}^1\phi_i \middle| H_{SO} \middle| {}^3\phi_1 \right\rangle}{{}^1E_i - {}^3E_1} \frac{{}^1F_1}{{}^1E_i} \qquad \text{(eq. 1.4)}$$

in which $^1\phi_i$ and $^3\phi_1$, and ^1E_i and $^3E_1$ are the wavefunctions and the energies, respectively, of the singlet manifold of excited states S_i and of the lowest triplet excited state T_1, ^1F_i is the oscillator strength of the singlet–singlet excitations, and H_{SO} is the spin–orbit coupling operator. It follows that the magnitude of the radiative decay rate is governed by many factors: the singlet–triplet spin-orbit mixing, the transition moments of the mixed singlet transitions, the energy of the excited states, and the separation between triplet and singlet.

In some cases, the spin-orbit coupling can be large enough to lead to efficient ISC from the lowest singlet excited state (S_1) to the lowest triplet manifold state (T_1). Furthermore, the same effect induces a mixing between singlet and triplet excited states, removing the spin-forbidden nature of the $T_1 \rightarrow S_0$ transition and resulting in phosphorescence emission. This effect is particularly evident for metals belonging to the 2nd and 3rd row of the transition metals block, especially for the d^6 metal complexes such as Ru(II), Re(I) and Ir(III).

Another consequence of *Kasha's rule* is that the aforementioned processes involving S_1 and T_1 are always competitive. The nature of the excited species, as well as the environmental and experimental conditions (temperature, media, concentration) determine whether fluorescence, phosphorescence or non-radiative decay dominate the deactivation pathway. The most important parameters to describe emitting excited states are the lifetime (τ) and the emission quantum yield (ϕ_{em}). Since emission is kinetically a first-order process, the lifetime of an excited state can be considered as the time needed to reduce the concentration of an excited state by 1/*e*, or as the reciprocal of the summation of all the deactivation rate constants (equation 1.5):

$$\tau = \frac{1}{\sum_i k_i} = \frac{1}{k_{em}+k_{ic}+k_{isc}+k_{nr}} \qquad \text{(eq. 1.5)}$$

where k_{em} is the sum of the rate constants of emission, k_{ic} of internal conversion, k_{isc} of intersystem crossing and k_{nr} of non-radiative decays. In general, the lifetime of a singlet excited state ranges from tens of picoseconds (10^{-12} s) to several nanoseconds (10^{-9} s), while lifetimes for triplets are usually much longer (microseconds to seconds) due to their forbidden nature. The emission quantum yield is the ratio between the number of emitted photons and the number of absorbed photons, and can also be expressed in terms of kinetic rate constants, as in equation 1.6:

$$\phi_{em} = \frac{emitted\ photons}{absorbed\ photons} = \frac{k_r}{k_r+k_{nr}} \Longrightarrow 0 < \phi_{em} \leq 1 \qquad \text{(eq. 1.6)}$$

1.2 Luminescent transition metal complexes

The photophysical properties of transition metal complexes exhibit interesting features due to the presence of a heavy metal atom, which induces a considerable degree of spin-orbit coupling to such an extent that spin-forbidden $T_1 \rightarrow S_0$ electronic transitions are usually allowed. In contrast with organic molecules, the efficiency of the ISC in these complexes can be close to unity, providing emission only as phosphorescence in nature, even at room temperature (RT).

A simplified method to describe the electronic structure of metal complexes is illustrated by the crystal field theory.[3] In this approach, ligands are treated as negative point charges generating an electrostatic field. In an octahedral complex, it results in a splitting of the five metal d orbitals (normally degenerate) into two sets because of their different spatial orientation which makes them not equivalent. One set consists of three equivalent orbitals labeled t_{2g}, while the second one of two equivalent orbitals labeled e_g (see figure 1.2). The e_g orbitals point directly towards the ligands and lie higher in energy than the t_{2g} orbitals, which point to the space between the ligands. The magnitude of the splitting between these two sets, generally denoted as Δ, and depends on the central metal ion and the strength of the involved ligands. Moreover, it increases with the principal quantum number along a row in the periodic table. It is also dependent on the field strength of the ligands, that can be ordered along the so called "spectrochemical series".[4] Although the electronic structure of a complex must be treated as a single entity, it is convenient to divide the electrons into two separate sets, one mainly localized on the metal center and another mainly localized on the ligands.

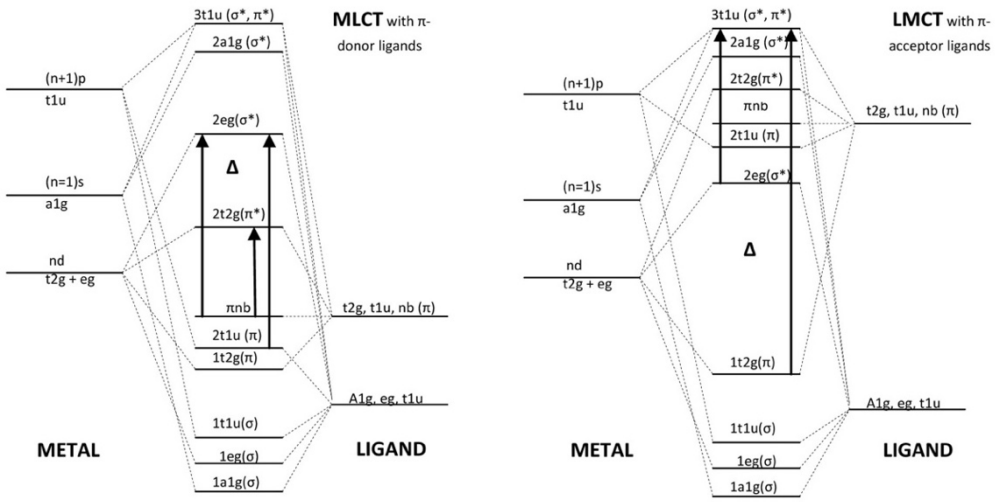

Figure 1.2 General Molecular Orbital diagram for a metal complex with octahedral geometry. The main electronic transitions involved in the absorption processes are depicted.

By using the Molecular Orbital (MO) theory, four types of electronic transitions are typically observed in an absorption process for octahedral metal complexes: 1) *metal centered* (MC) transitions between molecular orbitals localized on the metal; 2) *ligand centered* (LC) transitions, which involve electrons of the π orbitals located on the ligands; 3) *ligand-to-metal charge transfer* (LMCT) transitions, where the absorbed photon causes a movement of an electron from a ligand-centered orbital to an empty metal-centered orbital; 4) *metal-to-ligand charge transfer* (MLCT) transitions, in which the electron moves from a metal centered molecular orbital to a π* orbital of the ligand. Singlet and triplet states labeled as MC, LC, LMCT and MLCT can be theoretically observed, but actually the nature of the metal and the ligands influences the relative energy of these states and only some of them actively participate to the photophysical deactivation processes stimulated by a photon.

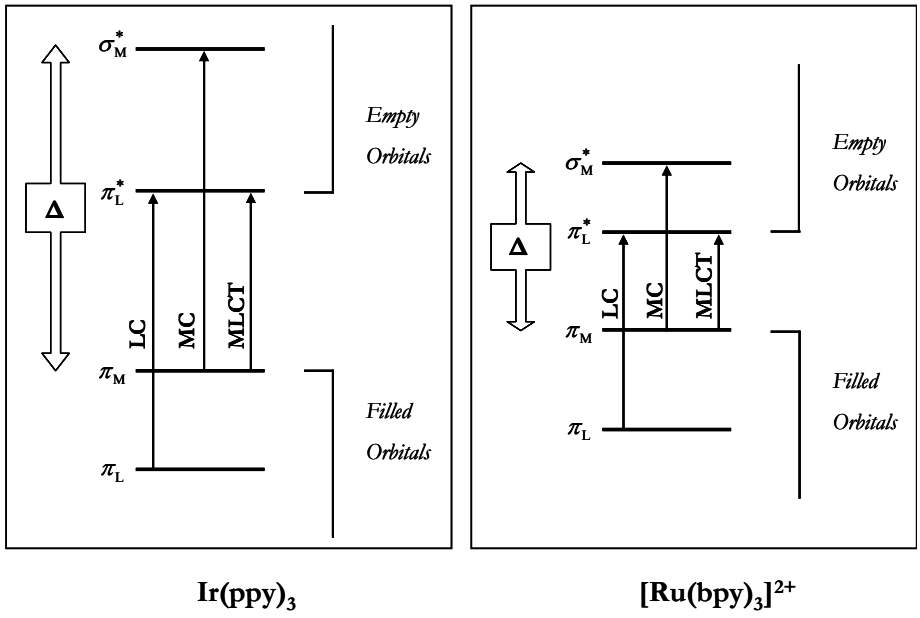

Figure 1.3 Simplified Molecular Orbital diagram for two of the most important octahedral luminescent complexes, $[Ir(ppy)_3]$ and $[Ru(bpy)_3]^{2+}$, showing the three main types of electronic transitions occurring at low energies. Ligand field splitting energy Δ is shown on the left side. LMCT transition not shown for clarity.

Among coordination complexes, d^6 metals show important differences in the electronic energy of the MC states, in particular for the lowest lying one. This state is not emissive, being strongly coupled to the ground state via non-radiative decay and/or ligand dissociation reactions. For metal ions belonging to the first row of the periodic table, such as Fe^{2+} (3*d* orbitals), the ligand field splitting Δ is so small that the lowest excited state for Fe^{2+}-polyimine complexes, like $[Fe(bpy)_3]^{2+}$ (bpy = 2,2'-bipyridine), exhibits MC character.[5-6] For d^6 metal complexes with central atoms having small ionization potentials and strong field ligands with easily accessible empty π* orbitals, like $[Ru(bpy)_3]^{2+}$ or $[Ir(ppy)_3]$, the lowest excited state is normally assigned to a ^{3}MLCT transition which, in the case of Ru^{2+} is only partially deactivated at RT by the ^{3}MC state, giving rise to poorly emissive

complexes.[7] On the contrary, Mn^{+}, Re^{+} and even more Ir^{3+} (5*d* orbitals) exhibit a very large Δ value and the ^{3}MC level are pushed so high in energy compared to the emissive ^{3}MLCT and ^{3}LC levels, that usually do not affect the emission properties (figure 1.3).

A careful choice of the employed ligands is crucial to increase the Δ splitting and to avoid parasitic radiationless deactivation channels involving the ^{3}MC level. The extent of Δ splitting is also reflected in the emission quantum yields, usually higher for iridium than ruthenium complexes for the aforementioned reasons. This behavior is in agreement with the so-called *energy gap law*, which states that the rate constant of non-radiative transitions k_{nr} increases with decreasing of the *energy gap* (ΔE) between the emissive state and the ground state (equation 1.7):

$$k_{nr} = \alpha \, exp^{-\beta \Delta E} \qquad \text{(eq. 1.7)}$$

where α and β are constant. In other words, due to the increase of the non-radiative rate constant, the lower the energy of the emitted photon, the poorer the emission quantum yield of the complex. In the MO approximation, oxidation and reduction processes can be regarded as metal or ligand centered. For metal complexes endowed with strong field ligands, the highest-occupied molecular orbital (HOMO) is usually metal centered (in some cases with some contribution from the ligands), while the lowest-unoccupied molecular orbital (LUMO) is ligand centered. Therefore, from the spectroscopic point of view, the MLCT transition can be *formally* regarded as an oxidation of the metal ion and a reduction of the ligands in the excited state and the electrochemical properties are strictly related to the nature of the lowest excited state.

1.3 Dinuclear rhenium(I) complexes

Tricarbonyl rhenium(I) complexes containing chelating diimine ligands, with general formula *fac*-$[Re(CO)_3(N\text{-}N)X]^{n+}$, (N–N = 1,10-phenanthroline, phen, or 2,2'-bipyridine, bpy; X = anionic or neutral monodentate ligand, with n = 0 or 1, respectively) have been studied for a long time for their characteristic luminescence.[8]

Thirty years have passed since the pioneer investigations in the field,[9] but there is still a vast interest towards the photochemical and photophysical properties of these complexes, justified by the many possible applications, such as photoredox chemistry,[10] chemi- or electrochemiluminescence,[11] chemical and biological sensing,[12] bioconjugation,[13] and use as phosphorescent dopants for organic light emitting devices (OLEDs).[14-15] The presence of a single electron-acceptor diimine ligand excludes the normally occurring problem of the localization of the excited electron for polypyridine Ru(II) complexes,[16] and makes these complexes very interesting for fundamental photophysical studies too.[17]

Like other d^6 metal complexes, tricarbonyl rhenium diimine complexes exhibit metal-to-ligand $d(\pi)(Re)\rightarrow\pi^*(N\text{–}N)$ charge transfer absorptions (MLCT), with relatively high molar absorptivity (ca. 10^4 cm^{-1} M^{-1}). Most of these species display intense and unstructured emission in solution, centered at about 600 nm, that originates from MLCT excited states mainly of triplet character. Very high photoluminescence quantum yields (PLQY) have been reported for cationic species (up to 0.8),[18] but those of neutral species usually do not exceed 0.05.[8-9] This issue seriously limited the applications of Re(I) complexes in optoelectronics to date.

To obtain high quantum yield values the efficiency of the emissive processes (related to the radiative constant k_r) must be maximized, while any other non-radiative deactivation process (related to k_{nr}) must be limited. Assuming a one-center description of the SO coupling operator, the coupling matrix elements increase with increasing d orbital participation in the MOs involved in the emission-responsible transition.[19] It follows that, limiting our attention to the SO coupling elements, equation 1.4 suggests that a feasible way to improve the emissive performances can be simply to link two heavy metal atoms to a single heterocyclic ligand, to further enhance the metal orbital character of the orbitals involved in the emissive process.

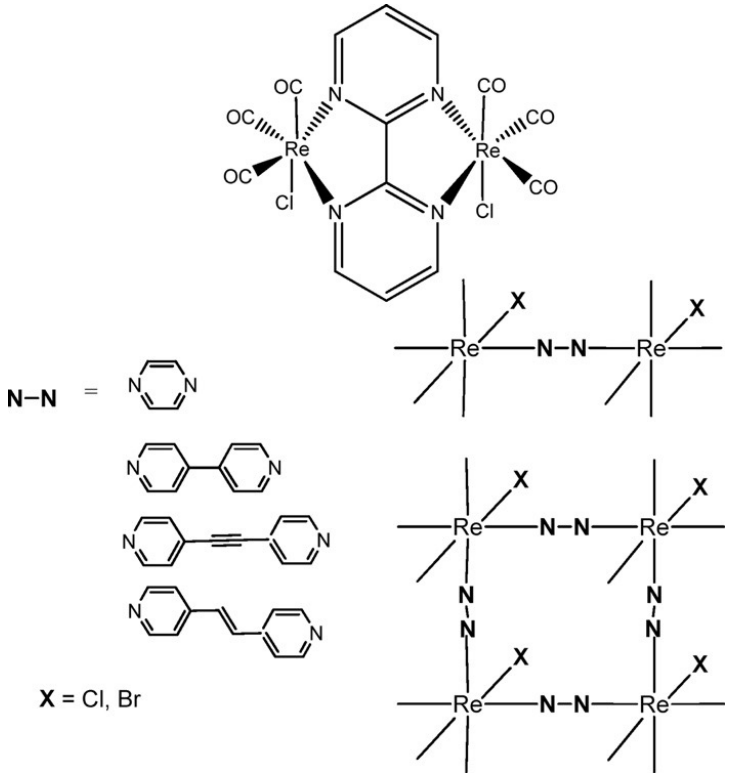

Chart 1.1 Structures of the complexes reported in references [20, 21], in which two $Re(CO)_3$ units are bound to the same chromophore and the ancillary ligands are terminally coordinated.

Using *fac*-$Re(CO)_3$ units, only two different structures can be designed to realize this purpose. The anionic ancillary ligands can be coordinated end-on, resulting in the metal centers being connected through a bis-chelating ligand (such as a 2,2′-bipyrimidine)[20] or through one or two chromophoric bidentate ligands, like a 4,4′-bipyridine,[21] giving rise to di- or tetranuclear (molecular rectangles) derivatives, as in chart 1.1. All of these species, however, have been proven to be rather poor emitters. In the other possible structure, the chromophore is bound to dinuclear "$(CO)_3Re(\mu\text{-}X)_2Re(CO)_3$" fragments, containing anionic ancillary bridging ligands (chart 1.2).

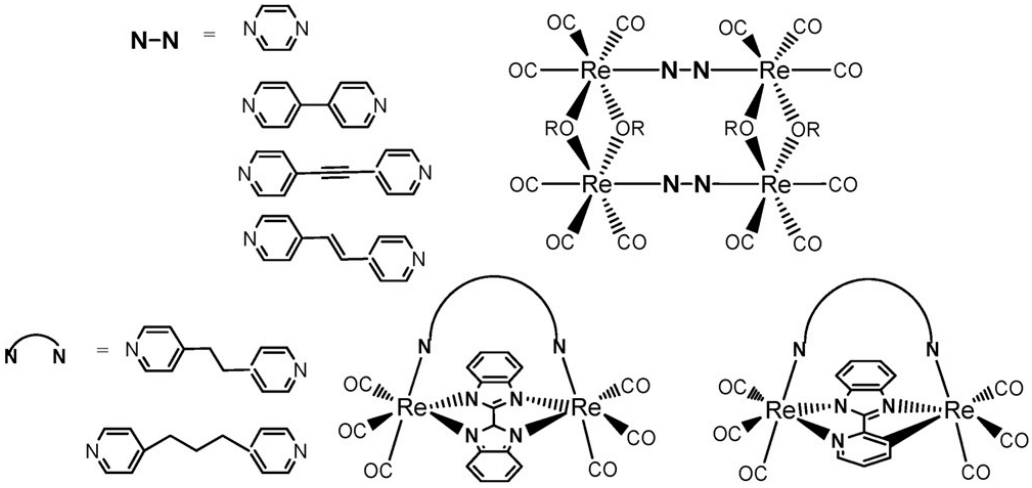

Chart 1.2 Structures of the complexes reported in references [22, 23] in which two $Re(CO)_3$ units are bound to the same chromophore and the ancillary ligands are in bridging coordination.

The use as chromophores of linear bridging nitrogen heterocycles (e.g. 1,4-diazine, 4,4′-bipyridine or more conjugated systems) affords weakly emitting molecular rectangles,[22] while more flexible N–N exobidentate ligands, such as dipyridylpropane or dipyridylethane, form highly emitting dinuclear complexes with PLQY up to 0.48, using pyridyl-benzoimidazolate as ancillary ligand.[23]

Other, although not flexible at all, N–N bidentate ligand is provided by 1,2-diazines. The orientation of the nitrogen lone pairs in 1,2-diazine does not allow chelation on a single metal center, but it is perfectly compatible with bridging coordination between two metal centers. Moreover, the presence of two nitrogen atoms on the same aromatic ring makes diazines more electron poor than bipyridines.

Therefore, our research group has, in the last years, prepared a vast series of tricarbonyl rhenium(I) complexes of general formula $[Re_2(\mu\text{-}X)_2(CO)_6(\mu\text{-diaz})]$ (diaz=1,2-diazine), in which a 1,2-diazine acts as a bridging ligand towards a dinuclear "$Re_2(\mu\text{-}X)_2(CO)_6$" core (chart 1.3), and X is either a halide (Cl, Br, and I),[24-26] a hydride,[27] or an ER^- group (E = S, R = C_6H_5; E = O, R = H, CH_3, C_6H_5, C_6F_5).[28] Upon optical excitation in the range 340–450 nm, most of these complexes show featureless emission in the range 550–710 nm in solution, arising from excited states that can be described as ^{3}MLCT states.[29]

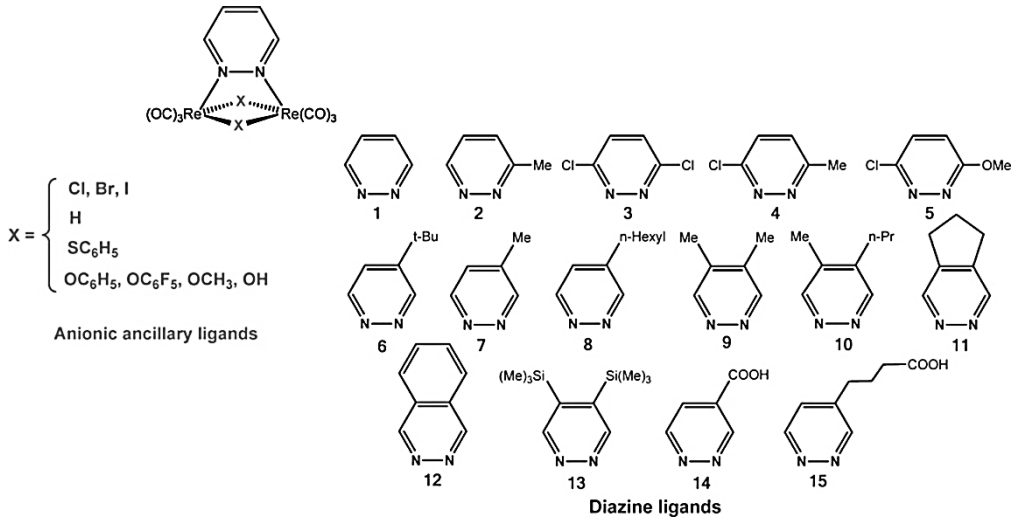

Chart 1.3 A library of 1,2-diazine ligands and anions used, respectively, as chromophoric and ancillary ligands, in some of the $[Re_2(\mu\text{-}X)_2(CO)_6(\mu\text{-diaz})]$ (diaz=1,2-diazine) complexes synthesized in our laboratories.

The energy, the intensity and the lifetime of the emission dramatically depends on the nature and the position of the diazine substituents, as well as on the nature of the ancillary ligands. For a series of dichloro derivatives, it was found[24] that the presence of substituents in the α position is detrimental for the emission properties, due to steric crowding with the CO ligands, while the effect of the substituents in the β positions is mainly related to their electron donor or acceptor character. In particular, it was observed that the introduction in the β positions of any alkyl group roughly doubled the PLQY and caused a blue shift of circa 25 nm, suggesting an additive effect of the substitution, both on the energy and on the intensity of the emission.[25] PLQY up to 0.53 have been measured in solution for the dichloro complexes containing diazines with two alkyl electron-donor groups and trimethylsilyl substituents in the two β positions.[25,26] This is the highest value ever reported in literature for neutral rhenium complexes.

These photophysical properties, pretty outstanding if compared to those of neutral mononuclear tricarbonyl Re(I) emitters, can be ascribed to a strong reduction of the non-radiative deactivation rate constant (k_{nr}), which arises from a rigid "Re(μ-X)$_2$Re" skeleton, further strengthened by the presence of the bridging ligand. An increase of the radiative constant (k_r) occurs at the same time in these dinuclear complexes, since the linkage of two metal atoms to the same chromophore increases the contribution of the *d* orbitals in the frontier molecular orbitals, therefore enhancing the spin–orbit coupling between the emissive triplet state and the singlet manifold. However, the latter effect appears too small to account for the improved photophysical properties observed for the dinuclear species.[29]

1.4 Density functional theory

A complete understanding of the structure and of the dynamics of electronic excited states is a fundamental goal of current spectroscopic, photo-physical/chemical and theoretical research. Pairing up experimental excited-state evidence with quantomechanical calculations provides a deeper insight into excited-state character, dynamics and relaxation pathways, more than experimental observations could do alone. Specifically, it is fundamental to deeply understand the redistribution of the electron density upon optical excitation and the subsequent structural changes of both the excited molecule and its surroundings. This aim might be a challenge for transition metal complexes for simultaneous different electronic states exist in a narrow energy range. Plus, intense spin-orbit coupling effect, long-range charge separation, strong interactions with the medium and very fast intersystem crossing complicate matters.

Theoretical calculations may use the electronic wavefunction or the electron density as the basic variable, leading to *ab initio* or *density functional* (DFT) or *time dependent* (TD-DFT) techniques, respectively.[30 - 31] Thus, vertical transitions are calculated, well reproducing absorption spectra. In addition to transition energies, oscillator strengths and symmetries, that are directly provided by TD-DFT calculations, a physical insight into the characters of electronic transitions and excited states is also needed. Their quantitative nature is described by the changes in the electron density distribution relative to the ground-state. This leads to usual categories like Ligand Field (LF), Metal-to-Ligand Charge-Transfer (MLCT), Ligand-to-Ligand Charge-Transfer (LLCT) and so on.

This fundamental part of the work has been developed in collaboration with Dr. Pierluigi Mercandelli of this University. However, during the last year of this thesis he has been seriously ill, hampering the complete theoretical characterization of the complexes. For this reason, in some chapters, the reported data are preliminary and the discussion is quite brief.

References

[1] L. Moggi, A. Juris, M. T. Gandolfi, *Manuale del Fotochimico*, Bononia University Press, **2006**

[2] S. Obara, M. Itabashi, F. Okuda, S. Tamaki, Y. Tanabe, Y. Ishii, K. Nozaki, M. Haga, *Inorg. Chem.* **2006**, 45, 8907

[3] M. Montalti, A. Credi, L. Prodi, M. T. Gandolfi, *Handbook of Photochemistry, 3rd Edition*, Taylor & Francis, **2006**

[4] D. M. Roundhill, *Photochemistry and Photophysics of Metal Complexes*, Plenum Press, New York **1994**

[5] C. Hamann, A. von Zelewsky, A. Neels, H. Stoeckli-Evans, *Dalton Trans.* **2004**, 402

[6] P. S. Braterman, J. I. Song, R. D. Peacock, *Inorg. Chem.* **1992**, 31, 555

[7] A. Juris, V. Balzani, F. Barigelletti, S. Campagna, P. Belser, A. Von Zelewsky, *Coord. Chem. Rev.* **1988**, 84, 85

[8] (a) D. J. Stukfens, A. Vlček Jr., *Coord. Chem. Rev.* **1998**, 177, 127; (b) A.G. Crosby, *Coord. Chem. Rev.* **2001**, 211, 163; (c) A.J. Lees, *Coord. Chem. Rev.* **1998**, 177, 3

[9] (a) M. Wrighton, D.L. Morse, J. Am. Chem. Soc., **1974**, 96, 998; (b) P.J. Giordano, S.M. Fredericks, M. Wrighton, D.L. Morse, *J. Am. Chem. Soc.* **1978**, 177, 2257; (c) J.C. Luong, L. Nadjo, M. Wrighton, *J. Am. Chem. Soc.* **1978**, 100, 5790 (d) S.M. Fredericks, J.C. Luong, M. Wrighton, *J. Am. Chem. Soc.* **1979**, 101, 7415; (e) P.J. Giordano, M. Wrighton, *J. Am. Chem. Soc.* **1979**, 101, 2888; (f) W.K. Smothers, M. Wrighton, *J. Am. Chem. Soc.* **1983**, 105, 1067; (g) J.V. Caspar, T.J. Meyer, *J. Phys. Chem.* **1983**, 87, 952 ; (h) J.V. Caspar, T.D. Westmoreland, G.H. Allen, P.G. Bradley, T.J. Meyer, W.H. Woodruff, *J. Am. Chem. Soc.* **1984**, 106, 3492 ; (i) J.V. Caspar, C.B. Sullivan, T.J. Meyer, *Inorg. Chem.* **1984**, 23, 2104

[10] (a) K. Kalyanasundaram, *J. Chem. Soc., Faraday Trans. 2* **1986**, 82, 2401 (b) H. Tsubaki, A. Sekine, Y. Ohashi, K. Koike, H. Takeda, O. Ishitani, *J. Am. Chem. Soc.* **2005**, 127, 15544

[11] M.M. Richter, *Chem. Rev.* **2004**, 101, 3003

[12] (a) M. P. Coogan, V. Fernandez-Moreira, *Chem. Commun.* **2014**, *50*, 384; (b) R. G. Balasingham, F. L. Thorp-Greenwood, C. F. Williams, M. P. Coogan, *Inorg. Chem.* **2012**, *51*, 1419; (c) F. L. Thorp-Greenwood, M. P. Coogan, L. Mishra, N. Kumari, G. Raic S. Saripella, *New J. Chem.* **2012**, *36*, 64; (d) V. Fernandez-Moreira, M. L. Ortego, C. F. Williams, M. P. Coogan, M. D. Villacampa, M. C. Gimeno, *Organomet.* **2012**, *31*, 5950; (e) V.Fernandez-Moreira, F.L. Thorp-Greenwood, M.P. Coogan, *Chem. Commun.* **2010**, 46, 186 (f) K.K.-W. Lo, Top. *Organomet. Chem.* **2010**, 29, 115; (g) K.K.-W. Lo, W.K. Hui, C.K. Chung, K.H.-K. Tsang, D.C.-M. Ng, K.-K. Cheung, *Coord. Chem. Rev.* **2005**, 249, 1434; (h) D. Beck, J. Brewer, J. Lee, D. McGraw, J.N. Demas, *Coord. Chem. Rev.* **2007**, 251, 546

[13] (a) S.James, K.P.Maresca, J.W.Babich, J.F.Valliant, L. Doering, J. Zubieta, *Bioconjugate Chem.* **2006**, 17, 590; (b) K.K.-W. Lo, K.H.-K. Tsang, N. Zhu, *Organometallics* **2006**, 25, 3220; (c) S.J. Reece, M.R. Seyedsayamdost, J. Stubbe, D.G. Nocera, *J. Am. Chem. Soc.* **2006**, 128, 13654; (d) K.K.-W. Lo, W.-K. Hui, C.-K. Chung, K.H.-K. Tsang, T.K.-M. Lee, C.-K. Li, J.S.-Y. Lau, D.C.-M. Ng, *Coord. Chem. Rev.* **2006**, 250, 1724; (e) K.K.-W. Lo, K.H.-K. Tsang, N. Zhu, *Inorg. Chem.* **2005**, 44, 6100; (f) L. Wei, J. Babich, W.C. Eckelman, J. Zubieta, *Inorg. Chem.* **2005**, 44, 2198; (g) A.J. Di Bilio, B.R. Crane, W.A. Wehbi, C.N. Kiser, M.M. Abu-Omar, R.M. Carlos, J.H. Richards, J.R. Winkler, H.B. Gray, *J. Am. Chem. Soc.*, **2001**, 123, 3181; (h) E.A. Hillard, G. Jaouen, *Organometallics* **2011**, 30, 20

[14] (a) X.Li, D.Zhang, H.Chi, G.Xiao, Y.Dong,S. Wu, Z. Su, Z. Zhang, P. Lei, Z. Hu, W. Li, *Appl. Phys. Chem.* 97, **2010**, 97, 263303; (b) S. Ranjan, S.-Y. Lin, K.-C. Hwang, Y. Chi, W.-L. Ching, C.-S. Liu, Y.-T. Tao, C.-H. Chien, S.-M. Peng, G.-H. Lee, *Inorg. Chem.* **2003**, 43, 1248; (c) Y. Li, Y. Liu, J. Guo, F. Wu, W. Tian, B. Li, Y. Wang, *Synth. Met.* **2001**, 118, 175; (d) X. Li, D. Zhang, W. Li, B. Chu, L. Han, J. Zhu, Z. Su, D. Bi, D. Wang, D. Yang, Y. Chen, *Appl. Phys. Lett.* **2008**, 92, 83302; (e) J. Li, Z. Si, C. Liu, C. Li, F. Zhao, Y. Duan, P. Chen, S. Liu, B. Li, *Semicond. Sci. Technol.* **2007**, 22, 553

[15] (a) L. Qian, D. Bera, P.H. Holloway, *Appl. Phys. Lett.* **2007**, 90, 103511; (b) Y.-Y. Lü, C.-C. Jü, D. Guo, Z.-B. Deng, K.-Z. Wang, *J. Phys. Chem. C* **2007**, 111, 5211; (c) G. David, P.J. Walsh, K.C. Gordon, *Chem. Phys. Lett.* **2004**, 383, 292; (d) Y.P. Wang, W.F. Xie, B. Li, W.L. Li, Chin. *Chem. Lett.* **2007**, 18, 1501; (e) B. Li, M. Li, Z. Hong, W. Li, T. Yu, H. Wei, *Appl. Phys. Lett.* **2004**, 85, 4786

[16] (a) S. Wallin, J. Davidsson, J. Modin, L. Hammarström, *J. Phys. Chem. A*, **2005**, 109, 4697; (b) J.K. McCusker, *Acc. Chem. Res.* **2003**, 36, 876

[17] (a) S. Záliš, C. Consani, A. El Nahhas, A. Cannizzo, M. Chergui, F. Hartl, A. Vlcek Jr., *Inorg. Chim. Acta* **2011**, 374, 578; (b) A. El Nahhas, A. Cannizzo, F. van Mourik, A.M. Blanco-Rodriguez, S. Záliš, A. Vlcek Jr., M. Chergui, *J. Phys. Chem. A* **2010**, 114, 6361; (c) A. Vlcek Jr., S. Záliš, *Coord. Chem. Rev.* **2007**, 251, 258

[18] (a) L. Sacksteder, M. Lee, J.N. Demas, B.A. DeGraff, *J. Am. Chem. Soc.* **1993**, 115, 8230; (b) L. Wallace, D.P. Rillema, *Inorg. Chem.* **1993**, 32, 3836; (c) J.M. Villegas, S.R. Stoyanov, W. Huang, D.P. Rillema, *Inorg. Chem.* **2005**, 44, 2297

[19] R. Baková, M. Chergui, C. Daniel, A. Vlcek Jr., S. Záliš, *Coord. Chem. Rev.* **2011**, 255, 975

[20] A. Juris, S. Campagna, S. Bidd, J.-M. Lehn, R. Ziessel, *Inorg. Chem.* **1988**, 27, 4007

[21] (a) T. Rajendran, B. Manimaran, F.-Y. Lee, G.-H. Lee, S.-M. Peng, C.M. Wang, K.-L. Lu, *Inorg. Chem.* **2000**, 39, 2016; (b) A. Kumar, S.-S. Sun, A.J. Lees, Top. *Organomet. Chem.* **2010**, 29, 1; (c) T. Rajendran, B. Manimaran, R.-T. Liao, R.-J. Lin, P. Thanasekaran, G.-H. Lee, S.-M. Peng, Y.-H. Liu, I.-J. Chang, S. Rajagopal, K.-L. Lu, *Inorg. Chem.* **2003**, 42, 6388

[22] (a) S.M. Woessner, J.B. Helms, Y. Shen, B.P. Sullivan, *Inorg. Chem.* **1998**, 37, 5406; (b) K.D. Benkstein, J.T. Hupp, C.L. Stern, *Inorg. Chem.* **1998**, 37, 5404; (c) R.V. Slone, K.D. Benkstein, S. Bélanger, J.T. Hupp, I.A. Guzei, A.L. Rheingold, *Coord. Chem. Rev.* **1998**, 171, 221; (d) B. Manimaran, P. Thanasekaran, T. Rajendran, R.-J. Lin, I.-J. Chang, G.-H. Lee, S.-M. Peng, S. Rajagopal, K.-L. Lu, *Inorg. Chem.* **2002**, 41, 5323

[23] Y.-H. Tseng, D. Bhattacharya, S.-M. Lin, P. Thanasekaran, J.-Y. Wu, L.-W. Lee, M. Sathiyendiran, M.-L. Ho, M.-W. Chung, K.-C. Hsu, P.-T. Chou, K.-L. Lu, *Inorg. Chem.* **2010**, 49, 6805

[24] D. Donghi, G. D'Alfonso, M. Mauro, M. Panigati, P. Mercandelli, A. Sironi, P. Mussini, L. D'Alfonso, *Inorg. Chem.* **2008**, 47, 4243

[25] (a) M. Mauro, E. Quartapelle Procopio, Y. Sun, C.-H. Chien, D. Donghi, M. Panigati, P. Mercandelli, P. Mussini, G. D'Alfonso, L. De Cola, *Adv. Funct. Mater.*, **2009**, 19, 2607; (b) M. Mauro, C.-H. Yang, C.-Y. Shin, M. Panigati, C.-H. Chang, G. D'Alfonso, L. De Cola, *Adv. Mater.* **2012**, *24*, 2054

[26] E. Quartapelle Procopio, M. Mauro, M. Panigati, D. Donghi, P. Mercandelli, A. Sironi, G. D'Alfonso, L. De Cola, *J. Am. Chem. Soc.* **2010**, 132, 14397

[27] M. Panigati, D. Donghi, G. D'Alfonso, P. Mercandelli, A. Sironi, L. D'Alfonso, *Inorg. Chem.* **2006**, 45, 10909

[28] A. Raimondi, M. Panigati, D. Maggioni, L. D'Alfonso, P. Mercandelli, P. Mussini, G. D'Alfonso, *Inorg. Chem.* **2012**, 51, 2966

[29] M. Panigati, M. Mauro, D. Donghi, P. Mercandelli, P. Mussini, L. De Cola and G. D'Alfonso, *Coord. Chem. Rev.* **2012**, *256*, 1621

[30] C. H. Martin, M. C. Zerner, in E. I. Solomon, A. B. P. Lecer (Eds.), *Inorganic Electronic Structure and Spectroscopy*, vol. 1: Methodology, John Wiley & Sons Inc., New York, **1999**, 555

[31] R. A. Friesner, *Proc. Natl. Acad. Sci.* USA **2005**, 102, 6648; P. Atkins, R. Friedman, *Molecular Quantum Mechanics*, Oxford University Press, Oxford, **2005**

CHAPTER 2

Energy solutions for a better future: photovoltaics

Abstract

The current situation of the photovoltaic energy market is briefly reported. Crystalline silicon photovoltaics lead the way to the development on the TW scale around the world, but thin film inorganic semiconductors (CIGS, CZTS, CdTe, GaAs) and some emerging PV (DSSC-SSD, OPV) are rapidly growing. A brief insight on the role of the transition metal complexes in the latter is also given.

2.1 Of photons and men

Energy is definitely the most important resource for mankind, and sunlight is without any doubt the ultimate energy source.[1] It is abundant (174 PW received at the Earth's upper atmosphere), inexhaustible on the human timescale (the sun, as main-sequence G2V star, will eventually collapse into red giant and white dwarf not before 4 billion years) and well distributed over the planet.[2] The rate of human energy consumption (17.2 TW in 2014) is about four orders of magnitude smaller than the solar energy irradiated on the surface of our planet (8.9×10^4 TW, time-and-space-averaged solar flux).

Solar energy is more useful for mankind when converted into the final usable forms: heat, electricity, and fuels. Conversion of solar energy into heat is straightforward, but conversion of solar energy into electricity or fuel poses several problems. [2] The conversion of sunlight into electricity and fuels can only be achieved by threshold-based processes, strongly limiting the conversion efficiency.

Since we cannot modify the solar spectrum, we need to find materials capable of exploiting sunlight through the threshold mechanism with the highest possible efficiency. Taking into account the average spectral distribution of solar energy, the most favorable threshold is about 885 nm (1.4 eV) which, in principle, allows 33 % of energy conversion efficiency.[3] The materials used for solar energy conversion should also be reasonably cheap and abundant on the earth's crust, with low environmental impact throughout their entire life cycle, and also stable for many years under irradiation. Another issue with solar energy is the intermittency (day/night cycles) and the intensity fluctuations of the radiation.

Therefore, in the case of solar energy conversion into electricity, storage components are often required as an integral part of the system. Any kind of storage option needs appropriate materials. The most common option for storing electricity is based on the reversible conversion into chemical energy by batteries or by electrochemical water splitting coupled with fuel cells. Finally, sunlight is dilute: the average solar power striking the earth's surface annually is about 170 W/m^2.[2] As mentioned above, only a fraction of this power can be converted into fuel or electricity. In practice, solar renewable energies have average annual power densities ranging between 5–20 W/m^2 (PV panels) and < 1 W/m^2 (biomass).[4]

Power densities of final energy uses in modern societies range between 10-70 W/m^2 for houses and low-energy intensity manufacturing buildings. Supermarkets or office buildings use 20–100 W/m^2, energy intensive industrial activities require 300–900 W/m^2 instead, and finally high-rise buildings may need up to a few thousands W/m^2.[4-5] These numbers clearly show that it is very easy to power a house with the sunlight intercepted by its roof, if covered with photovoltaic (PV) modules, but this will hardly be possible for a refinery or a skyscraper. Summing up, the amount of energy we can actually generate from the average solar power depends on our capacity of developing the conversion and storage devices we need with the materials we have on our planet. In the present epoch, Anthropocene,[6] mankind has apparently become more powerful than nature,[7] nevertheless we must recognize that our will to solve problems is hampered by practical limitations in the chemical composition of our planet. In the end, the limiting reactants in the exploitation of sunlight for social use are not photons, but atoms.[8]

2.2 Solar electricity

In the last five years, the photovoltaic systems worldwide have undergone substantial development in terms of manufacturing distribution (largely shifted from Europe to Asia), global deployment, and even new photoactive materials[9] which are very promising but, at present, remain at the laboratory research stage.

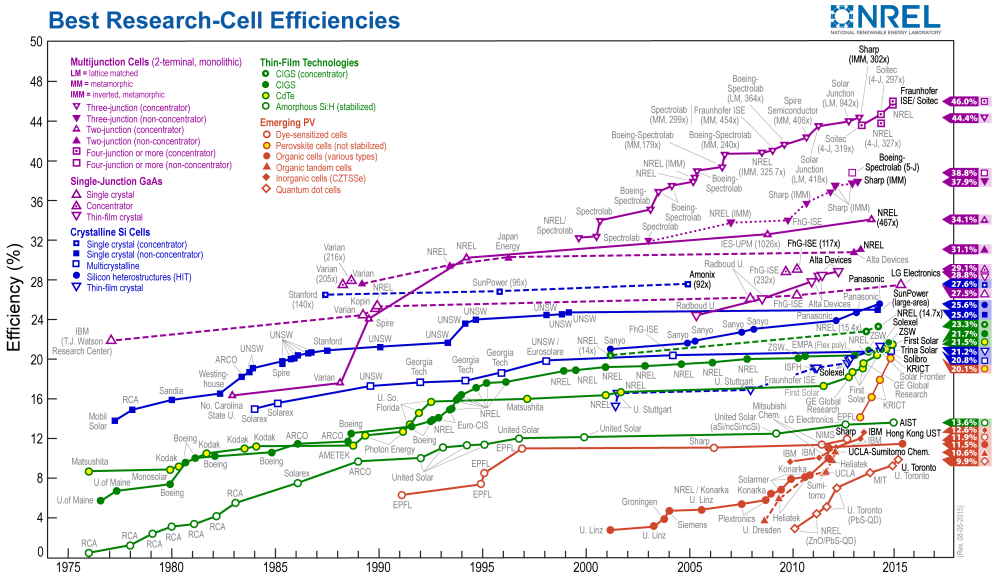

Figure 2.1 National Renewable Energy Laboratory (NREL) chart of the record efficiencies for all the types of solar cell (certified, research scale).

PV technology exhibits a series of remarkable features. It can be scaled quite easily up to the GW scale, both on-grid and off-grid, without affecting the efficiency and the economic performance (fossil fuels or nuclear plants have an optimal operational size; below or above that, they under-perform). It represents an up-front, one-time investment repaid by decades of electricity produced by a free primary source.

There are basically no moving parts in PV modules, this means negligible wear and very low maintenance cost. Also, installation is possible on already existing platforms, like roofs or walls, with no further land consumption. Last, but not least, PV technology allows to provide electricity to off-grid rural or isolated areas and communities, improving by far life quality in underdeveloped regions. Over 90% of today commercial solar cells are still based on the very same material and basic concepts developed in the 50's at the Bell Laboratories: light-induced charge separation at a p–n junction between two wafers of p- and n-doped silicon in either single-crystal or polycrystalline form (sc-Si and poly-Si, respectively), as shown in figure 2.2.

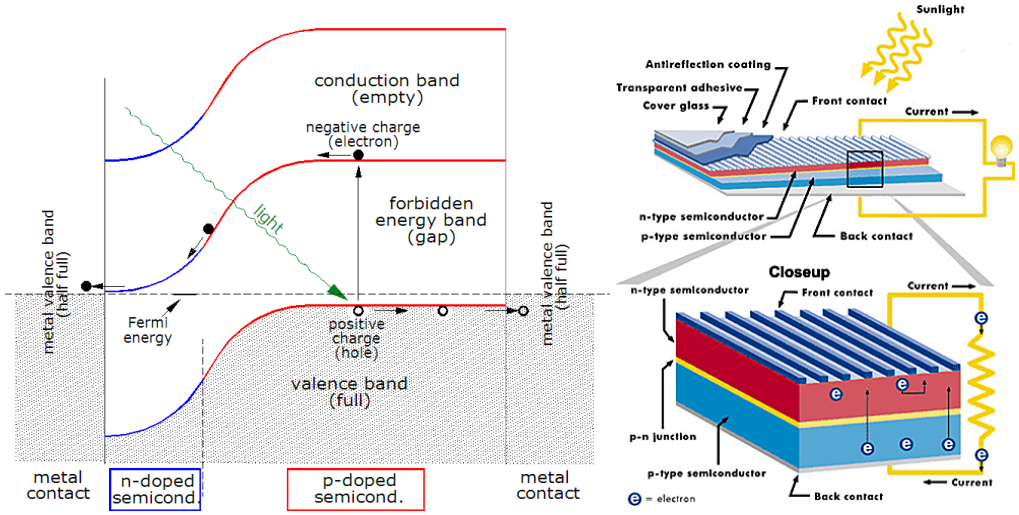

Figure 2.2 Left: band diagram for a generic p-n junction. Right: working diagram of a crystalline silicon solar cell.

The global share of Si PV has increased from 80% in 2009 to over 90% in 2014, because the main competitors, the so-called "2nd generation solar cells", thin film technologies like cadmium telluride (CdTe), copper-gallium-indium selenide (CIGS), and amorphous silicon (a-Si) have grown at a much lower rate.[9]

Since 2010, the world has added more PV capacity than in the previous 40 years. Such a massive expansion has been primarily driven by China, as a result of a strategic decision to make huge investments in production capacity rather than to lower labor cost (PV production is highly automated),[10-11] In fact, China accounts now for over 70% of the global Si PV output.[9]

The success of crystalline silicon technologies is based on a series of peculiar advantages that, even in the future, will be hardly rivaled by new PV concepts. The technology is over 60-years old and well-established: the lifetime of the modules is in the decade time scale, the efficiency of light-to-electricity conversion, in the range 15–22%, is comparable or greater than other successful devices that have conquered the world, like cars. Key materials (copper, silver, aluminum, plastics, silicon) are abundant and non-toxic; their recycling is easy and liable to further improvements within the first massive wave of re-placements (not expected anyway before another 20 years).[12]

Also, silicon PV production will reach the TW scale within ten years, a landmark goal for future dominance not only in the PV, but in the entire electricity market. These deployment targets are not unrealistic at all. Considering that the 2010 IEA PV roadmap had forecasted a cumulative capacity of 210 GW by 2020, a target that has actually been reached in 2015. In 2020 the global capacity is now estimated to exceed 450 GW.[9] The energy return on investment, EROI, (equations 2.1 and 2.2) of PV technology has been object of intense debate.[13-14]

The most recent global literature assessment concludes that the EROI of PV systems on the market (both modules and accessories) is quite positive: 8.7 (sc-Si), 11.6 (poly-Si), 14.5 (a-Si), 19.9 (CIGS), 34.2 (CdTe), under the assumption of a 30-year system lifetime.[15]

$$\boldsymbol{EROI} = \frac{\boldsymbol{E_{out}}}{\boldsymbol{E_{in}}} \qquad \text{(eq. 2.1)}$$

$$\boldsymbol{net\ energy} = \boldsymbol{E_{out}} - \boldsymbol{E_{in}} = \boldsymbol{E_{out}}\left(\mathbf{1} - \frac{\mathbf{1}}{\boldsymbol{EROI}}\right) \qquad \text{(eq. 2.2)}$$

The energy payback time (EPBT) is the period required for an energy production system to generate the same amount of energy that was used to make it. This parameter is related to EROI by equation 2.3:

$$\boldsymbol{EPBT} = \frac{\boldsymbol{lifetime}}{\boldsymbol{EROI}} \qquad \text{(eq. 2.3)}$$

In the same study mentioned above, EPBT turns out to be 4.1 (sc-Si), 3.1 (poly-Si), 2.3 (a-Si), 1.7 (CIGS) and 1.0 (CdTe) years,[15] remarkable values for devices that can operate easily for 30 years. Recently it has been assessed that the PV industry is a net energy producer since 2012 and, by 2020, it will completely pay back all the energy needed for its early growth.[16]

Furthermore, the cost of PV installations is fully affordable to medium-income people in wealthy countries.[2] Concerns that a vast deployment of PV panels may substantially downsize agricultural land or even affect the earth's albedo to such an extent to modify the global climate are completely unjustified.[17 -18] Instead, a very important issue is the availability of materials to enable PV deployment on the multi-TW scale.

In this regard, silicon photovoltaics turn out to be largely superior to inorganic semiconductor thin-film technologies. Silicon is the second most abundant and uniformly distributed element on the earth's crust and there is no risk of shortage in any foreseeable future. Even in the imaginary hypothesis that c-Si PV technologies provided 100% of the world's electricity supply by 2030, the required silicon production growth rate would fall within the historical range recorded over the last four decades.[19] Even silver, which is required for electrical contacts and is considered the most critical material in silicon PV panels,[20] does not need to exceed the historical production rate in a scenario of 80% PV electricity production share by 2030.[19]

By contrast, In, Ga, Se, Te, and Cd exhibit a way smaller crustal abundance and, accordingly, they are collected only as byproducts of minerals containing mostly other elements (Cu, Zn, and Al).[21] Even assuming that thin-film technologies covered 8% of the global electricity demand in 2030, In, Te, and Se would need to largely exceed the historical production trends; thus requiring a massive, and rather unlikely, extraction boost. For In and Te in particular, the material requirements for the 8% target would equalize, or even overcome, the estimated global reserves.[19] Therefore, only new formulations based on more abundant elements,[22] like copper-zinc-tin sulfide (CZTS) could make thin-film inorganic materials actual competitors to silicon-based technologies in a TW scale PV market.

2.2.1 Solar cell parameters

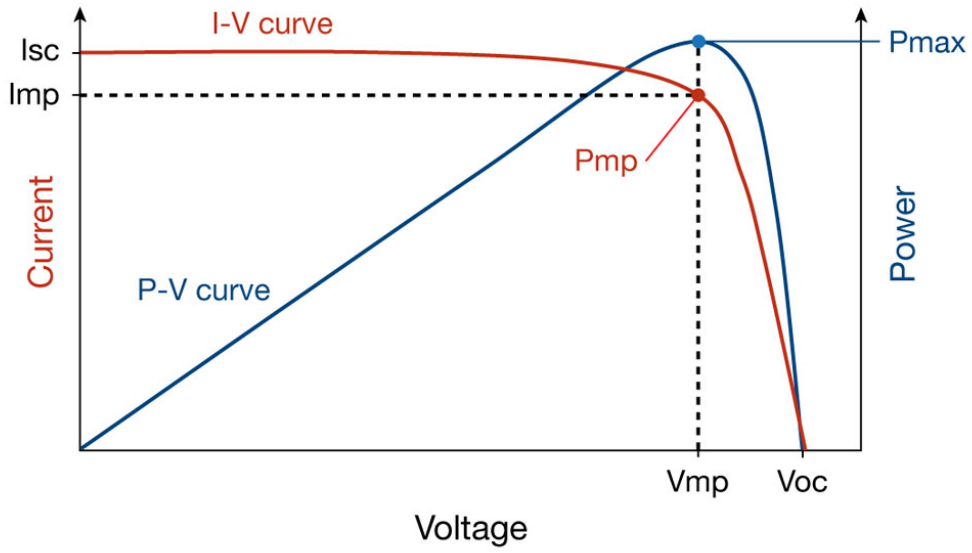

Figure 2.3 General I-V (red) and P-V (blue) curve for any photovoltaic cell, module or array.

The efficiency η, or power conversion efficiency PCE, of a solar cell is determined as the fraction of incident power which is converted to electricity and is defined as (equation 2.4):

$$\eta = \frac{V_{OC} J_{SC} FF}{P_{in}} \qquad \text{(eq. 2.4)}$$

where P_{in} is the power density of the incident light, usually fixed at 100 mW/cm^2 under an air mass (AM) of 1.5G. V_{OC} is the open-circuit photo-voltage:

$$V_{OC} = \frac{nkT}{q} \ln\left(\frac{I_L}{I_0} + 1\right) \qquad \text{(eq 2.5)}$$

the maximum voltage available from a solar cell, occurring at zero current.

The open-circuit voltage corresponds to the amount of forward bias on the solar cell due to the bias of the solar cell junction with the light-generated current. The above equation, where kT/q is the thermal voltage and n is the ideality factor, shows that V_{OC} depends on the dark saturation current I_O of the solar cell and the light-generated current I_L. The dark saturation current I_0 depends on recombination in the solar cell. Open-circuit voltage is then a measure of the amount of recombination events in the device.

I_{SC} is the short-circuit photocurrent:

$$\boldsymbol{I_{SC} = qG\,(L_n + L_p)} \qquad \text{(eq. 2.6)}$$

the current passing through the solar cell when the voltage is zero (short circuited). G is the generation rate, L_n and L_p are the electron and hole diffusion lengths, respectively. To remove the dependence of the solar cell area, it is more common to list the short-circuit current density J_{SC} (in mA/cm^2). The short-circuit current is due to the generation and collection of light-generated carriers. For an ideal solar cell at most moderate resistive loss mechanisms, the short-circuit current and the light-generated current are identical. Therefore, the short-circuit current is the largest current which may be drawn from the solar cell.

FF is the fill factor:

$$\boldsymbol{FF = \frac{V_{OC'} - ln(V_{OC}+0.72)}{V_{OC'}+1}} \qquad \text{(eq. 2.7)}$$

where $\boldsymbol{V'_{OC} = \frac{q}{nkT} V_{OC}}$

I_{SC} and V_{OC} are the maximum current and voltage from a solar cell. However, at both operating points, the power from the solar cell is zero. The fill factor FF, is a parameter which, in conjunction with V_{OC} and J_{SC}, determines the maximum power from a solar cell. The FF is defined as the ratio between the maximum power from the solar cell and the product of V_{OC} and J_{SC}. Graphically, the FF is a measure of the "squareness" of the solar cell and is also the area of the largest rectangle which will fit in the JV curve. A key limitation in the equations described above is that they represent a maximum possible FF, although in practice the FF will be lower due to the presence of parasitic resistive losses. Therefore, the FF is most commonly determined from measurement of the IV curve and is defined as the maximum power divided by the product of I_{SC} and V_{OC}.

$$\boldsymbol{FF = \frac{V_{MP}\, I_{MP}}{V_{OC}\, I_{SC}}} \qquad \text{(eq. 2.8)}$$

The ratio of the number of extracted charge carriers to the number of absorbed photons in the active layer is named external quantum efficiency (EQE) or incident photon to current efficiency (IPCE):

$$\boldsymbol{IPCE = \frac{J_{SC}}{P_{in}\lambda}\frac{hc}{e}} \qquad \text{(eq. 2.9)}$$

where *h*, *c*, and *e* are Planck's constant, the speed of light and the elementary charge, respectively. IPCE is the product of all the efficiencies in the energy transfer processes:

$$\boldsymbol{IPCE = \eta_{abs}\, \eta_{diff}\, \eta_{tc}\, \eta_{tr}\, \eta_{cc}} \qquad \text{(eq. 2.10)}$$

where η_{abs} is the photon absorption efficiency (number of excitons generated per number of incident photons), η_{diff} is the diffusion efficiency of the charge carrier (number of excitons diffusing per number of exactions generated), η_{tc} is the efficiency of the charge-carrier separation (number of dissociated excitons per number of excitons at the interface), η_{tr} is the charge transport efficiency and η_{cc} is the charge collection efficiency. The product of the last four parameters defines the internal quantum efficiency (IQE). Therefore:

$$\boldsymbol{EQE = \eta_{abs}\, IQE} \qquad \text{(eq. 2.11)}$$

IQE is a key factor that determines the quality of a PV cell. It provides a qualitative assessment of the ability of a solar cell to separate excitons into free charges and to collect them at the two electrodes.

2.3 Dye-sensitized solar cells (DSSC)

The third wave of PV technologies entering the market should be based on DSSC and organic photovoltaics (OPV). Expectations for their market debut have been high for years,[23-25] but so far they have materialized only to a very small extent. At present, the market share of these two technologies is still virtually zero, despite a few flagship demonstration projects, which support technical feasibility.[26-27]

Compared to the established technologies discussed in the previous section, DSSC and OPV can offer easier building integration, in windows and facades, good performances also under non-standard illumination and temperature conditions, lower requirements in terms of quantity and quality of raw materials. They can be manufactured at smaller economic and energetic costs, and their energy payback times are estimated to be shorter than conventional thin-film technologies.[28 - 29] Nonetheless, they are still not competitive on efficiency and lifetime, which constitutes a formidable barrier for widespread market diffusion.

The DSSC is an electrochemical device that relies on the sensitization of a wide band gap n-type semiconductor (usually TiO_2) by a light-harvesting molecule or particle to generate electricity from incident sunlight.[30] A key feature of the DSSC concept differing from conventional photovoltaics is that light absorption, and electron and hole transport are carried out by different components (dye, semi-conductor, electrodes, redox mediator), hence the degrees of freedom to optimize the device are, in principle, higher.

A conventional DSSC device consists of a ca. 10 μm thick mesoporous layer of sintered anatase TiO_2 nanoparticles (diameter ~20 nm) on a glass substrate with a transparent conductive oxide layer, usually FTO (Fluorine-doped Indium Tin Oxide). An additional light-scattering layer of TiO_2 nanoparticles with diameter of 400 nm is also applied in many cases.[31] The TiO_2 film is then covered with a monolayer of light-harvesting dye molecules. The high surface area of the mesoporous film is critical to device performance because it enables a high concentration of dye molecules for efficient light absorption. A thermoplastic spacer separating the TiO_2 anode from a counter-electrode (a thin layer of Pt or C on a conductive substrate) encapsulates an electrolyte solution that is introduced through holes in the counter-electrode itself.

The excitation and charge separation processes in high performance DSSCs, depicted in figure 2.4, rely on a series of kinetically controlled processes that are reminiscent of the electron-transfer events that occur within the photosynthetic apparatus. The first step in the scheme is the absorption of a photon by the dye molecule, resulting in the population of its own excited state. An appropriate geometry and thermodynamic position of this excited state will ideally favor the injection of this photo-excited electron into the nanocrystalline TiO_2 semiconductor over radiative and non-radiative decay processes back to the ground state. The rate of electron-transfer through the semiconducting layer to the collecting glass electrode occurs at a rate that is considered ultrafast compared to the reaction with the redox-active electrolyte species or photo-oxidized dyes. Electrons that are collected at the glass electrode pass through an external load to carry out useful electrical work.

The closure of the circuit is achieved when the electron is shuttled back to the photo-oxidized dye by an electrolyte species (usually I^-, but also Co^{2+}) that is generated at the platinized counter-electrode. A strategy to enhance V_{OC} involves the increase of the separation between the Fermi level E_F of the TiO_2 and the redox couple of the electrolyte species. These modifications can, however, lead to other drawbacks that compromise performance, particularly J_{SC}. For example, increasing the E_F may reduce the rate of electronic injection, whereas varying the electrolyte composition may adversely affect dye regeneration and electrolyte diffusion characteristics. A higher J_{SC} can be achieved by the chromophore absorbing the majority of incident photons at wavelengths shorter than ~900 nm while maintaining efficient rates of injection and regeneration.

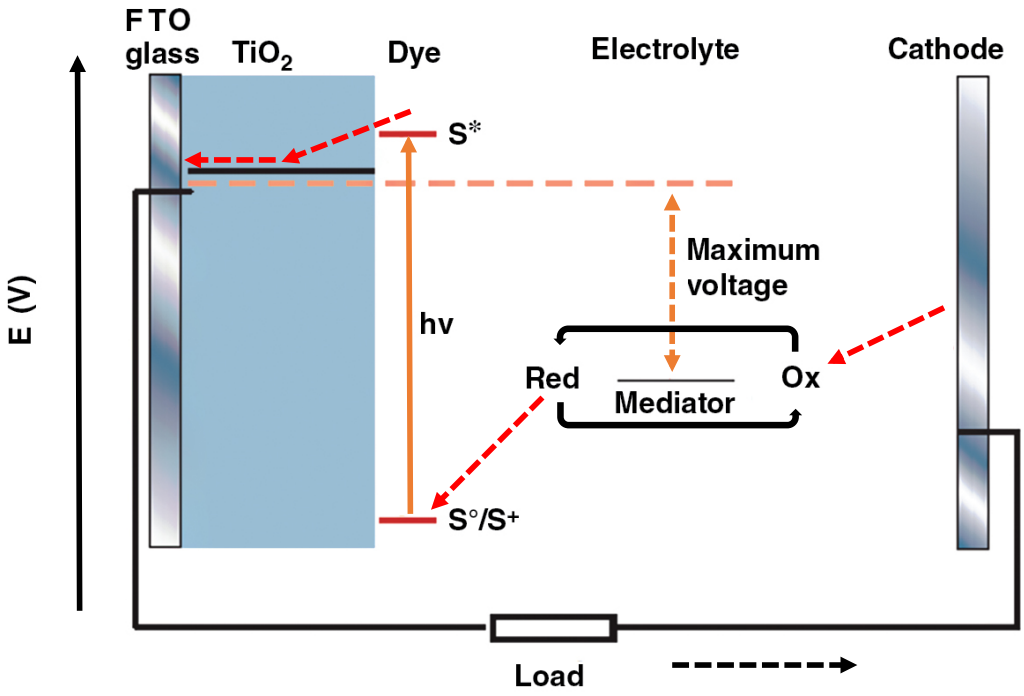

Figure 2.4 Working principle of a dye-sensitized solar cell.

Several types of organic and inorganic dyes are now available, as well as solid-state devices, including the redox mediator, as a result of a massive research effort throughout 25 years.[32-33] Despite the marked increase in the understanding of the DSSCs, numerous challenges remain related to cell/module performance and stability that need to be addressed before this technology can be deployed on a large scale. For example, the 10% benchmark for DSSC performance was first reached in 1993,[34] but the current DSSC exemplars display only nominally higher values (12%).[35] The latest certified record efficiency reported, under AM 1.5 irradiation at 25°C, is 11.9 ± 0.4% (1 cm^2 per cell).[36] The record sub-module efficiency is 8.8 ± 0.3%, with a surface of almost 400 cm^2 (26 serial cells).[36] The theoretical Shockley–Queisser limit for DSSCs is 20% (band gap 1.31 eV),[37] a target still far away in light of the slow efficiency progress of this technology.[38]

This incremental improvement in device performance is largely due to the fact that the state-of-the-art devices contain essentially the same main components as the seminal DSSC device: a mesoporous anatase TiO_2 layer covered by a molecular sensitizer that is regenerated by an electrolyte solution containing a redox couple (usually I_3^-/I^-, or Co^{2+}/Co^{3+}) and additives. Although a vast array of strategies have been explored to replace the mesoporous TiO_2 layer with other materials and geometries[39-41] and perhaps, more importantly from a commercialization prospect, the corrosive iodide-based electrolyte,[42-43] the lack of robust molecular sensitizers capable of sensitizing TiO_2 efficiently out towards 900 nm remains a major impediment to commercial viability[44-46]. In other words, DSSCs have not reached yet a level of maturity that enables actual competition with the established CdTe and CIGS technologies.

Low yields on large surfaces and stability problems are not only related to individual materials and components, but also to the way they interact in the cell structure.

2.4 Organic photovoltaics (OPV)

Organic photovoltaic (OPV) systems are based on photoactive p-conjugated polymers and small molecules; their working principle is schematically depicted in figure 2.6.[47-48] In 1992, Sariciftci et al.[49] demonstrated that photoexcitation of a mixture of a conjugated polymer and fullerene (C_{60}) resulted in an ultrafast, highly efficient photoinduced electron transfer. Later on, Yu et al. and Halls et al.[50] created the "bulk hetero-junction" (BHJ) concept, which is one of the best OPV device architectures so far.

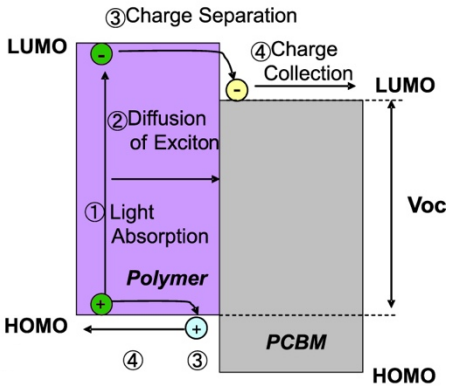

Figure 2.6 Working principle of an OPV system.

The bilayer hetero-junction and the BHJ OPV structures are shown in figure 2.7. In the two devices, the photoactive layers are sandwiched between an anode with high work function, typically a transparent indium tin oxide (ITO) layer, and a relatively low work function metal

cathode, such as Al. Compared to the bilayer hetero-junction, in which the donor material sticks to the anode and the acceptor material sticks to the cathode, the BHJ architecture significantly increases the D/A interfacial area, leading to enhanced efficiency of the OPV devices.[51] Actually, the BHJ is a blend of continuous and interpenetrating donor and acceptor components in a bulk volume. Such a nanoscale network exhibits a D/A phase separation in a 5–20 nm length scale, a lesser distance than the exciton diffusion length.

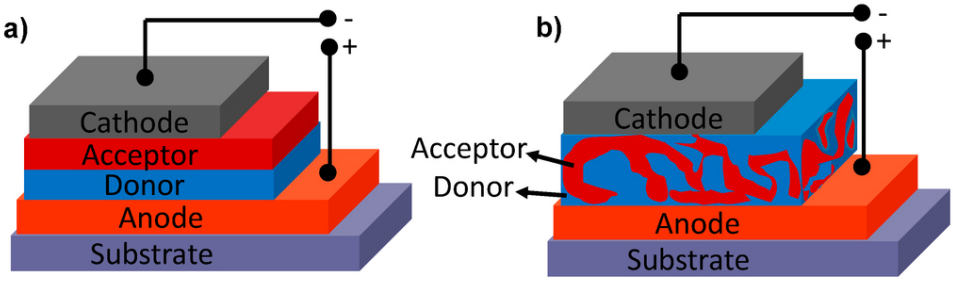

Figure 2.7 Schematic representation of an organic photovoltaic cell with a) bilayer and b) bulk heterojunction morphology.

Two or even more OPV cells can be stacked on top of each other to form a tandem OPV structure, which enables one to resolve two limiting factors existing intrinsically among organic semiconductor molecules, that is, poor charge carrier mobility and a narrow light absorption range. The photoactive materials, including polymeric and small molecular semiconductors, play a key role in influencing physical processes involved in energy conversion, which in turn determine the electrical characteristics of the solar cell. OPVs based on a p-type conjugated polymer as a donor and a fullerene derivative, [6,6]-phenyl-C_{61} (or C_{71})-butyric acid methyl ester ($PC_{61}BM$ or $PC_{71}BM$), as an acceptor have been rapidly developing, and showed the highest PCE so far.

On the other hand, small molecular semiconductors for OPVs have attracted considerable attention, owing to their advantages over their polymer counterparts, which include well-defined molecular structure, definite molecular weight, and high purity without batch-to-batch variations.[52] An increasing number of papers on OPVs based on small molecules has been published to date, and the PCEs of devices based on small molecule donors and fullerene acceptors fabricated by vacuum deposition or solution processing are both in excess of 6%.[53-56] As for small molecule acceptors, compared to the fullerene derivatives such as $PC_{61}BM$ and $PC_{71}BM$, the development of non-fullerene small molecular acceptors has been lagged with relatively low performance. The chemical nature of these materials and the simple device architecture may result in light weight, solution processable and flexible devices.

OPV systems are mostly based on abundant elements and low cost materials, can be produced at high manufacturing throughput, and allow easy recycling of precious embedded materials, if necessary.[57] In principle, these are valuable advantages in terms of application prospects and market diffusion. The latest certified record efficiency of OPV is 11.0 ± 0.3%. (1 cm^2 per cell), whereas a minimodule of 26 cm^2 affords 9.7 ± 0.3%.[36] Further efficiency progress is expected to come primarily from the optimization of the microstructure and morphology of the active layer to enhance charge mobility, so as to create rational and reproducible fabrication protocols.[58-59] However, a major issue of OPVs is stability,[60] for it is a colossal challenge to prevent chemical and photochemical degradation of organic molecules exposed to many years of intense light irradiation and very high temperatures, under increasing risk of oxygen and humidity contamination over time.

2.5 Aims and objectives of the present work

In this Ph.D. thesis attention was focused on dinuclear Re and Mn complexes able to operate as active materials in optoelectronic applications, such as dye-sensitized solar cells, organic photovoltaics devices (Re), and electrocatalytic reduction of CO_2 or hydrogen generation (Mn). Indeed, considering the state-of-the-art of the knowledge about the dinuclear rhenium complexes containing 1,2-diazine ligands developed in our research group, starting from the pioneering studies on the halide derivatives[61] and their application as dopants in OLED devices[62] and as dyes for bio-imaging[63],we have tried here to extend and tune the properties of these complexes, potentially widening their application in various sub-fields of optoelectronics. Therefore, starting from complexes with general formula $[M_2(\mu\text{-}X)(\mu\text{-}Y)(CO)_6(\mu\text{-}R\text{-diazine})]$ (M = Re, Mn), being X and Y two anionic bridging ligands, we have carried out tailored syntheses with joint experimental and theoretical studies to gain a deeper insight into the electronic processes involved in these classes of compounds. The spectroscopic and/or catalytic properties of the new complexes have been modulated by varying the substituents on the diazine ligand, as well as the ancillary ligands, thus modulating the LUMO and HOMO energy level, respectively.

This thesis is basically divided in four main sections:

1) New class of Re complexes with low energy-gap (chapter 7) and/or long-lived excited states as triplet photosensitizer for triplet-triplet annihilation (TTA) upconversion (chapter 4).
2) New class of hydrido-carboxylato Re complexes and applications in DSSC solar cells (chapter 5).
3) New low-band gap metallo-copolymers based on Re complexes as donors in bulk-heterojunction solar cells (chapter 6).

4) New polynuclear Mn complexes containing diazine ligands (chapter 8).

It is clear that this thesis is the result of a highly multidisciplinary and collaborative research work. We have collaborated with various research groups both in Italy and Europe:

The electrochemical characterization has been carried out in collaboration with Prof. Patrizia Mussini (Dipartimento di Chimica, Università degli Studi di Milano, Milano, Italy). The theoretical calculation and the molecules' design, together with the solid state analysis of the complexes, have been performed by Dr. Pierluigi Mercandelli of the same department.

The test concerning the TTA upconversion (chapter 4) has been performed in collaboration with Prof. Paola Ceroni (Dipartimento di Chimica, Alma Mater Studiorum - Università di Bologna, Bologna, Italy). A preliminary photophysical characterization was previously carried out by Dr. Matteo Mauro and Prof. Luisa De Cola (Institut de Science et d'Ingénierie Supramoléculaires (ISIS), Strasbourg, France).

Two different research groups have been involved in the fabrication of DSSC devices (chapter 5): preliminary tests were performed by Dr. Francesca De Rossi and Prof. Thomas M. Brown (Center for Hybrid and Organic Solar Energy - CHOSE, Rome, Italy), while the optimization of the cells and a second series of tests has been carried out in collaboration with Dr. Kazuteru Nonomura and Prof. Anders Hagfeldt (Laboratory of Photomolecular Science (LSPM), École Polytechnique Fédérale de Lausanne (EPFL), Lausanne, Switzerland).

Dr. Stefania Zappia and Dr. Silvia Destri have been involved in the synthesis and the characterization of the metallo-copolymers (chapter 6) (Istituto per lo Studio delle Macromolecole, Consiglio Nazionale delle Ricerche (ISMAC-CNR), Milan, Italy).

References

[1] N. Armaroli, V. Balzani, *Chem. Eur. J.* **2016**, 22, 32–57

[2] N. Armaroli, V. Balzani, Energy for a Sustainable World—From the Oil Age to a Sun Powered Future, Wiley-VCH, Weinheim (Germany), **2011**

[3] G. Porter, Criteria for Solar Energy Conversion, in Light, Chemical Change and Life. A Source Book in Photochemistry (Eds.: J. D. Coyle, R. R. Hill, D. R. Roberts), Open University Press, Milton Keynes (UK), **1982**, 338

[4] V. Smil, Power Densities. A Key to Understanding Energy Sources and Uses, MIT Press, Cambridge, MA (USA), **2015**

[5] V. Smil, Energy Transitions: History, Requirements, Prospects, Praeger/ ABC-CLIO, Santa Barbara, CA (USA), **2010**

[6] (a) V. Balzani, P. Ceroni, G. Bergamini, *Angew. Chem. Int. Ed.* **2015**, 54, 11320; (b) eidem, *Angew. Chem.* **2015**, 127, 11474

[7] V. Balzani, *Toxicol. Environ. Chem.* **2014**

[8] A. M. Bradshaw, T. Hamacher, *ChemSusChem* **2012**, 5, 550

[9] International Energy Agency, Technology Roadmap—Solar Photovoltaic Energy, **2014** https://www.iea.org

[10] J. A. Mathews, Greening of Capitalism. How Asia Is Driving the Next Great Transformation, Stanford University Press, Stanford, CA (USA), **2015**

[11] A. C. Goodrich, D. M. Powell, T. L. James, M. Woodhouse, T. Buonassisi, *Energy Environ. Sci.* **2013**, 6, 2811

[12] See for instance the Pan-European Producer Scheme for the treatment of photovoltaic waste: http://www.pvcycle.org

[13] D. J. Murphy, C. A. S. Hall, *Ann. N. Y. Acad. Sci.* **2010**, 1185, 102

[14] C. A. S. Hall, J. G. Lambert, S. B. Balogh, *Energy Policy* **2014**, 64, 141

[15] K. P. Bhandari, J. M. Collier, R. J. Ellingson, D. S. Apul, *Renewable Sustainable Energy Rev.* **2015**, 47, 133

[16] M. Dale, S. M. Benson, *Environ. Sci. Technol.* **2013**, 47, 3482

[17] G. F. Nemet, *Environ. Sci. Technol.* **2009**, 43, 2173

[18] M. Súri, T. A. Huld, E. D. Dunlop, H. A. Ossenbrink, *Sol. Energy* **2007**, 81, 1295

[19] G. Kavlak, J. McNerney, R. L. Jaffe, J. E. Trancik, *Energy Environ. Sci.* **2015**, 8, 1651

[20] A. Feltrin, A. Freundlich, *Renewable Energy* **2008**, 33, 180

[21] L. T. Peiró, G. Villalba Mendez, R. U. Ayres, *Environ. Sci. Technol.* **2013**, 47, 2939

[22] C. Wadia, A. P. Alivisatos, D. M. Kammen, *Environ. Sci. Technol.* **2009**, 43, 2072

[23] M. Jacoby, *Chem. Eng. News* **2010**, 88 (34), 12

[24] NanoMarkets Report, Dye-Sensitized Cell Markets 2012—Nano-531, **2012**, http://ntechresearch.com/market reports/dye sensitized cell markets **2012**

[25] International Energy Agency, Technology Roadmap-Solar Photovoltaic Energy **2010**, https://www.iea.org

[26] École Polytechnique Fédérale de Lausanne, EPFL's campus has the world's first solar window, can be found under https://actu.epfl.ch

[27] F. C. Krebs, N. Espinosa, M. Hosel, R. R. Sondergaard, M. Jorgensen, *Adv. Mater.* **2014**, 26, 29

[28] M. L. Parisi, S. Maranghi, R. Basosi, *Renewable Sustainable Energy Rev.* **2014**, 39, 124

[29] S. Lizin, S. Van Passel, E. De Schepper, W. Maes, L. Lutsen, J. Manca, D. Vanderzande, *Energy Environ. Sci.* **2013**, 6, 3136

[30] B. O'Regan, M. Grätzel, *Nature* **1991**, 353, 737

[31] B. C. O'Regan, J. R. Durrant, *Acc. Chem. Res.* **2009**, 42, 1799

[32] (a) S. F. Zhang, X. D. Yang, Y. H. Numata, L. Y. Han, *Energy Environ. Sci.* **2013**, 6, 1443; (b) P.G. Bomben et al. *Coord. Chem. Rev.* **2012**, 256, 1438

[33] S. Ardo, G.J. Meyer, *Chem. Soc. Rev.* **2009**, 38, 115

[34] (a) M. K. Nazeeruddin, A. Kay, I. Rodicio, R. Humphry-Baker, E. Mueller, P. Liska, N. Vlachopoulos, M. Grätzel, *J. Am. Chem. Soc.* **1993**, 115, 6382; (b) M. Nazeeruddin, F. De Angelis, S. Fantacci, A. Selloni, G. Viscardi, P. Liska, S. Ito, B. Takeru, M. Grätzel, *J. Am. Chem. Soc.* **2005** 127, 16835

[35] A. Yella, H.-W. Lee, H. N. Tsao, C. Yi , A. K. Chandiran, M. K. Nazeeruddin, E. W.-G. Diau, C.-Y. Yeh, S. M. Zakeeruddin, M. Grätzel, *Science* **2011**, 334, 629

[36] M. A. Green, K. Emery, Y. Hishikawa, W. Warta, E. D. Dunlop, *Prog. Photovoltaics* **2015**, 23, 805

[37] H. J. Snaith, *Adv. Funct. Mater.* **2010**, 20, 13

[38] L. M. Peter, *J. Phys. Chem. Lett.* **2011**, 2, 1861

[39] Q. Zhang, C.S. Dandeneau, X. Zhou, G. Cao, *Adv. Mater.* **2009**, 21, 4087

[40] T. W. Hamann, R. A. Jensen, A. B. F. Martinson, H. VanRyswyk, J. T. Hupp, *Energy Environ. Sci.* **2008**, 1, 66

[41] M. Pagliaro, G. Palmisano, R. Ciriminna, V. Loddo, *Energy Environ. Sci.* **2009**, 2, 838

[42] G. Boschloo, A. Hagfeldt, *Acc. Chem. Res.* **2009**, 42, 1819

[43] S. M. Feldt, E. A. Gibson, E. Gabrielsson, L. Sun, G. Boschloo, A. Hagfeldt, *J. Am. Chem. Soc.* **2011**, 132, 16714

[44] J. M. Kroon, N. J. Bakker, H. J. P. Smit, P. Liska, K. R. Thampi, P. Wang, S. M. Zakeeruddin, M. Grätzel, A. Hinsch, S. Hore, U. Würfel, R. Sastrawan, J. R. Durrant, E. Palomares, H. Pettersson, T. Gruszecki, J. Walter, K. Skupien, G. E. Tulloch, *Prog. Photovolt.: Res. App.* **2007**, 15, 1

[45] V. Likodimos, T. Stergiopoulos, P. Falaras, R. Harikisun, J. Desilvestro, G. Tulloch, *J. Phys. Chem.* C **2009**, 113, 9412

[46] M. I. Asghar, K. Miettunen, J. Halme, P. Vahermaa, M. Toivola, K. Aitola, P. Lund, *Energy Environ. Sci.* **2010**, 3, 418

[47] K. A. Mazzio, C. K. Luscombe, *Chem. Soc. Rev.* **2015**, 44, 78

[48] J. Roncali, P. Leriche, P. Blanchard, *Adv. Mater.* **2014**, 26, 3821

[49] N. S. Sariciftci, L. Smilowitz, A. J. Heeger and F. Wudl, *Science* **1992**, 258, 1474

[50] J. J. M. Halls, C. A. Walsh, N. C. Greenham, E. A. Marseglia and R. H. Friend, *Nature* **1995**, 376, 498

[51] C. J. Brabec, N. S. Sariciftci and J. C. Hummelen, *Adv. Funct. Mater.* **2001**, 11, 15

[52] X.-H. Zhu, J. Peng, Y. Cao and J. Roncali, *Chem. Soc. Rev.* **2011**, 40, 3509

[53] V. Steinmann, N. M. Kronenberg, M. R. Lenze, S. M. Graf, D. Hertel, K. Meerholz, H. Bürckstümmer, E.V. Tulyakovaand, F. Würthner, *Adv. Energy Mater.* **2011**, 1, 888

[54] S.-W. Chiu, L.-Y. Lin, H.-W. Lin, Y.-H. Liu, Z.-Y. Huang, Y.-T. Lin, F. Lin, Y.-H. Chen, K.-T. Wong, *Chem. Commun.* **2012**, 48, 1857

[55] Z. Li, G. He, X. Wan, Y. Liu, J. Zhou, G. Long, Y. Zuo, M. Zhang, Y. Chen, *Adv. Energy Mater.* **2012**, 2, 74

[56] Y. Sun, G. C. Welch, W. L. Leong, C. J. Takacs, G. C. Bazan, A. J. Heeger, *Nat. Mater.* **2012**, 11, 44

[57] R. R. Søndergaard, N. Espinosa, M. Jorgensen, F. C. Krebs, *Energy Environ. Sci.* **2014**, 7, 1006

[58] Y. Huang, E. J. Kramer, A. J. Heeger, G. C. Bazan, *Chem. Rev.* **2014**, 114, 7006

[59] N. E. Jackson, B. M. Savoie, T. J. Marks, L. X. Chen, M. A. Ratner, *J. Phys. Chem. Lett.* **2015**, 6, 77

[60] M. Jørgensen, K. Norrman, S. A. Gevorgyan, T. Tromholt, B. Andreasen, F. C. Krebs, *Adv. Mater.* **2012**, 24, 580

[61] D. Donghi, G. D'Alfonso, M. Mauro, M. Panigati, P. Mercandelli, A. Sironi, P. Mussini, L. D'Alfonso, *Inorg. Chem.* **2008**, 47, 4243

[62] (a) M. Mauro, E. Quartapelle Procopio, Y. Sun, C. H. Chien, D. Donghi, M. Panigati, P. Mercandelli, G. D'Alfonso, L. De Cola, *Adv. Funct. Mater.* **2009**, 19, 2607; (b) M. Mauro, C.-H. Yang, C.-Y. Shin, M. Panigati, C.-H. Chang, G. D'Alfonso, L. De Cola, *Adv. Mater.* **2012**, 24, 2054

[63] (a) E. Ferri, D. Donghi, M. Panigati, G. Prencipe, L. D'Alfonso, I. Zanoni, C. Baldoli, S. Maiorana, G. D'Alfonso, E. Licandro, *Chem. Commun.* **2010**, 46, 6255; (b) C. Mari, M. Panigati, L. D'Alfonso, I. Zanoni, D. Donghi, L. Sironi, M. Collini, S. Maiorana, C. Baldoli, G. D'Alfonso, E. Licandro, *Organometallics*, **2012**, 31 (16), 5918

CHAPTER 3

Experimental techniques

Abstract

The experimental methods used throughout this thesis work are described. These techniques involve steady-state and time-resolved absorption and emission spectroscopy, electrochemical analyses such as cyclic voltammetry and electrochemical impedance spectroscopy. Plus, a concise description of the fabrication and characterization of different types of solar cells (DSSC, SSD, OPV) is reported. The conditions for other common characterization techniques (NMR, IR, mass spectrometry, etc.) are given in the experimental sections of the corresponding chapters.

3.1 Steady-state absorption and emission spectroscopy

The absorbance A(λ) of a solution of a chromophore, in which no aggregation phenomena occur, is defined as the efficiency of light absorption at a fixed wavelength (λ). In sufficiently diluted solutions, and in absence of aggregation phenomena, the absorbance follows the Lambert-Beer law, expressed in equation 3.1:

$$A(\lambda) = \log_{10} \frac{I_0}{I} = \varepsilon c l \qquad \text{(eq. 3.1)}$$

I_0 is the intensity of the incident radiation passing through a reference cell, while I represents the intensity of the incident radiation passing through the sample cell; ε is the molar absorption coefficient (in L mol^{-1} cm^{-1}), *l* is the absorption path length (in cm) and *c* is the concentration of the absorbing species (in mol L^{-1}). In figure 3.1 a general scheme of a single-beam spectrophotometer is shown.[1] A compartment contains the cuvette, filled first with the reference (usually the solvent), and then with the sample to be analyzed.

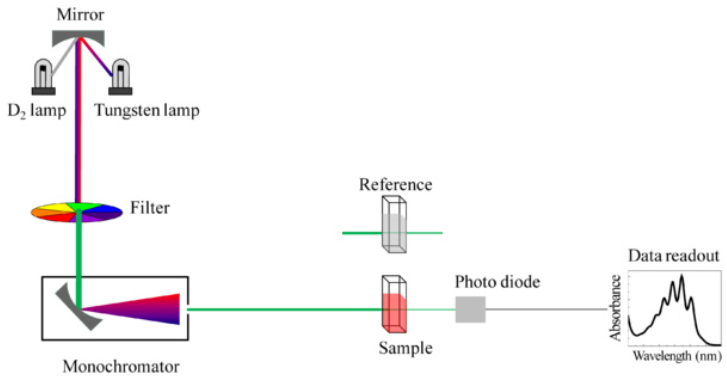

Figure 3.1 Scheme of a single-beam spectrophotometer.

The absorbance is automatically calculated subtracting the blank from the sample. In this thesis, all the absorption spectra were measured on an Agilent 8453 UV-Vis spectrophotometer. The samples were measured in fused quartz cuvettes (10 mm optical path, Hellma), adapted for freeze-pump-thaw technique in the case of oxygen-free measurements, as shown in figure 3.2.

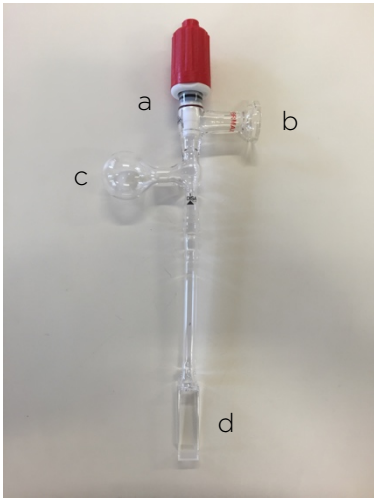

Figure 3.2 Home-made vacuum cuvette: a) PTFE stopper, b) high vacuum line joint c) round compartment for freeze-pump-thaw procedure d) quartz cuvette.

Emission spectra are normally recorded at a fixed excitation wavelength using a spectrofluorimeter. In this thesis, steady-state emission spectra were recorded on an Edinburgh FLS980 spectrofluorometer equipped with a 450 W ozone-free xenon arc lamp, double grating excitation and emission monochromators (2 x 300 mm focal length) and a Hamamatsu R928P photomultiplier tube.

Figure 3.3a describes a general setup for measuring emission spectra. The excitation light, generated by a xenon lamp, passes through two monochromators: part of the light is deviated by a beam splitter to a

reference channel, while the rest of the light passes through the sample. The luminescence, measured at a 90° angle relative to the excitation light, passes through other two monochromators before reaching the detector. Emission and excitation spectra were corrected for source intensity (lamp and grating) and emission spectral response (detector and grating) by standard correction curves.

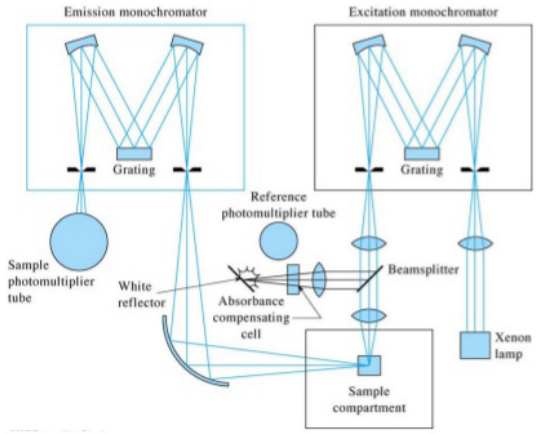

Figure 3.3a General scheme of a spectrofluorometer.

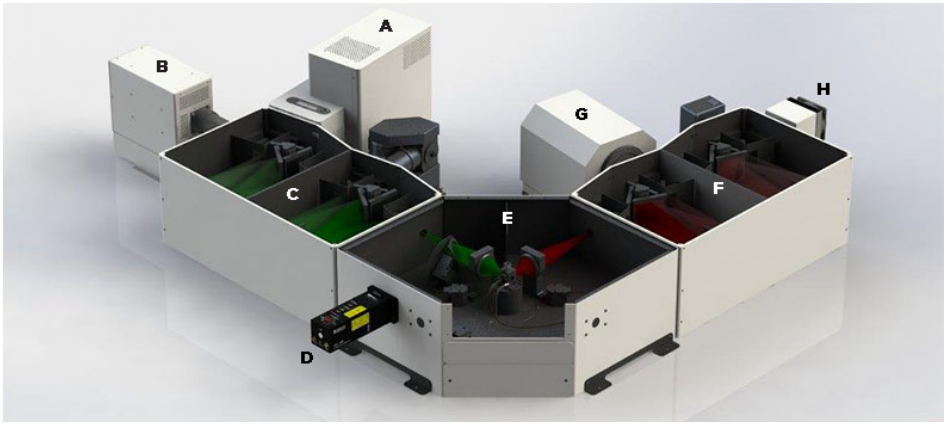

Figure 3.3b FLS980 spectrofluorometer architecture: a) steady state xenon lamp, b) microsecond flashlamp μF2, c) excitation monochromator, d) picosecond pulsed diode lasers/pulsed LEDs, e) sample chamber, f) emission monochromator, g) steady state PMT, h) time-correlated single photon counting PMT

3.2 Time-resolved emission spectroscopy

Single photon counting (SPC, figure 3.4) is a technique based on the ability to detect and count individual photons to measure properly the luminescence decay of a given chromophore. The profile of the decay over time is determined by measuring the time gap between the excitation of the sample and the subsequent photon emission detected by the photomultiplier.

During the measurement, an electrical pulse is created and directed to the "*start*" input of the time-to-amplitude (TAC) converter. The electrical response to the sample luminescence is used as the "*stop*" signal for the TAC. The *start* pulse initiates the charging of a capacitor while the *stop* pulse terminates it. The time between these two pulses, directly proportional to the generated voltage, is then calculated. Several repetitions of this measurements result in a histogram of events whose profile corresponds to the luminescence decay curve.

Time-resolved measurements were performed using the time-correlated single-photon counting (TCSPC) option on the FLS980. The excitation sources were mounted directly on the sample chamber and the emission is collected by a multichannel plate MCP-PMT Hamamatsu H10720-01 single-photon-counting detector. The photons collected at the detector were correlated by a time-to-amplitude converter (TAC) to the excitation pulse. The data analysis was performed using the commercially available F980 software (Edinburgh Instruments). The goodness of the data fitting was assessed by minimizing the reduced chi-squared function (χ^2).

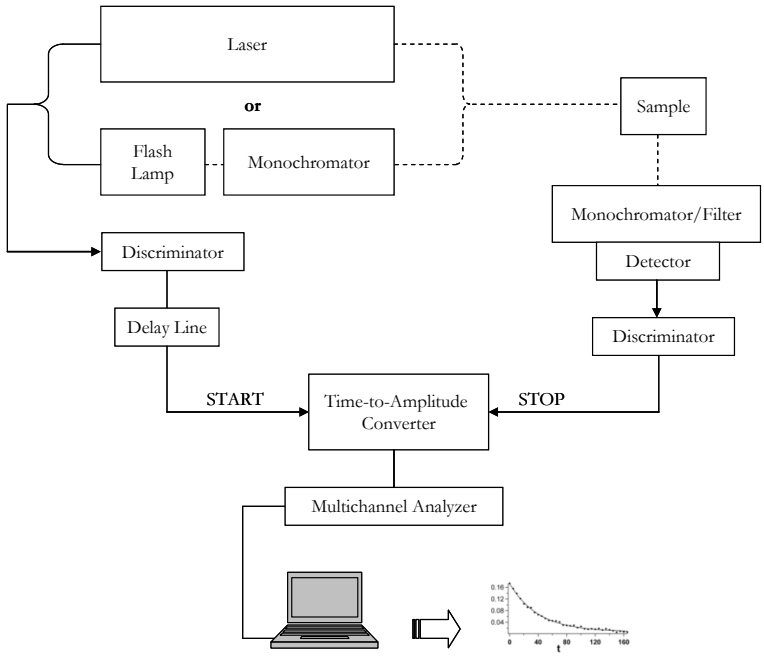

Figure 3.4 Single-photon counting (SPC) setup.

3.3 Absolute photoluminescence quantum yield

The integrating sphere method has been extensively used for measuring optical properties of surfaces, films and light sources. The light coming from the sample, placed at the center of the sphere, is reflected many times by the surface of the integrating sphere before hitting the detector, thus giving a good measure of the total emitted radiant power (figure 3.5).

The spherical geometry of the chamber makes this method completely insensitive to scattering and allows to use any geometry for the sample.[2] Recently, the integrating system technique has been applied to the measurement of quantum yield from films and solutions.

In this thesis, all the PLQYs on both solution and solid state samples, were collected by wavelength scanning with a Hamamatsu C11347-11 Quantaurus-QY Absolute PL quantum yield spectrophotometer, equipped with a L11562 xenon light source (150 W), monochromator, C7473 photonic multi-channel analyzer, spectralon integrating sphere, and employing the commercially available U6039-05 PLQY measurement software (Hamamatsu Photonics Ltd., Shizuoka, Japan).

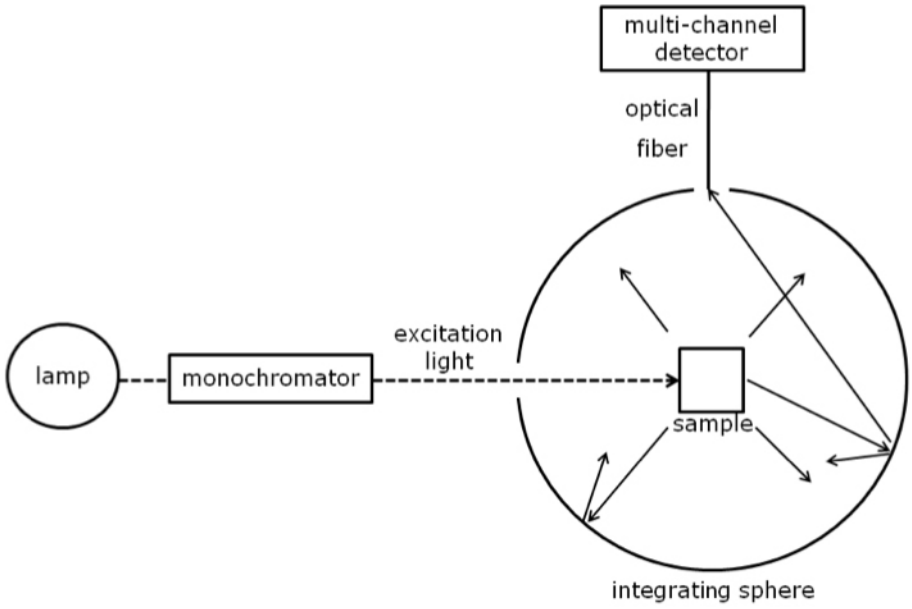

Figure 3.5 Schematic representation of an integrating sphere setup for photoluminescence quantum yield (PLQY) measurement.

3.4 Cyclic voltammetry

An increasing number of inorganic chemists use cyclic voltammetry (CV) to evaluate the effect of ligands on the oxidation/reduction potential of the central metal ion in complexes and multinuclear clusters. This type of information plays a major role in many approaches to optoelectronic applications. In CV (figure 3.6), the potential is applied between the working electrode and the reference electrode and it is scanned linearly from an initial value E_i to a predetermined limit, $E\lambda_1$, known as the switching potential where the direction of the scan is reversed; the instrument then cycles between $E\lambda_1$ and some other preselected value, $E\lambda_2$. The current is measured between the working electrode and the counter electrode and is plotted as a function of the applied potential.

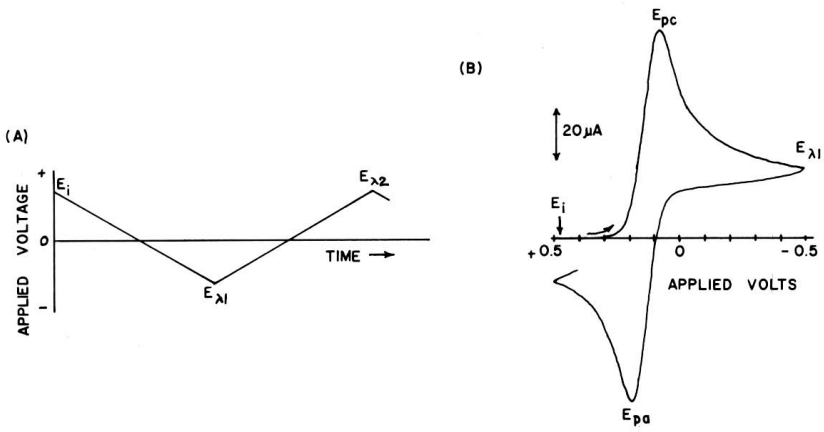

Figure 3.6 a) applied potential program, $E\lambda_1$ and $E\lambda_2$ are switching potentials b) typical cyclic voltammogram for a reversible process.

The current depends on two steps in the overall process, that is, the movement of electro-active material to the surface of the working electrode and the electron transfer reaction.

The electron transfer rate constant for a reduction process is a function of potential and can be described by equation 3.2:

$$k_f = k^0 e\left(\frac{-\alpha nF}{RT}\left(E - E^{0'}\right)\right) \qquad \text{(eq. 3.2)}$$

k^0 is the standard heterogeneous electron-transfer rate constant. The number of electrons transferred per molecule is *n*, *F* is the Faraday constant; *R* the universal gas constant; T is the Kelvin temperature; and $E^{0'}$ the formal reduction potential. The term α is known as the transfer coefficient. It arises from the fact that only a fraction of the energy that is put into the system lowers the activation energy barrier. Its value ranges from zero to unity (often ~ 0.5) depending on the shape of the free energy surfaces for the reactants and products.

An advantage of the cyclic voltammetry experiment is that a significant concentration of product has been generated near the electrode during the forward scan. When the scan direction is reversed, the analyte is brought back to the original starting material and the current for the reverse process is recorded. The electron transfer rate constant for the reverse process is similarly controlled by the applied potential:

$$k_f = k^0 e\left(\frac{(1-\alpha)nF}{RT}\left(E - E^{0'}\right)\right) \qquad \text{(eq. 3.3)}$$

It is common practice to report the average of the forward and return peak potentials as the formal potential for the redox couple. This is an approximation that is most accurate when the electron transfer process is reversible and the diffusion coefficients for the oxidized and reduced forms are the same. If the reaction is reversible, the separation in the peak potentials, ΔE_p will be close to 58/n mV.

This relationship can be used to evaluate n. Redox couples whose peaks shift further apart with increasing scan rate are categorized as irreversible systems. A subset of this class are those reactions that yield products that cannot be recycled electrochemically to give back the original reactants (for example, those involving extensive bond breaking and/or loss of substituents to solution). These are "chemically irreversible" reactions, and many yield no return peak at all. In these cases the separation in the peak potentials, ΔE_p is greater than 58/n mV and usually increases with the increase of the scan rate.

The cyclic voltammetry study of the complexes was performed at scan rates typically ranging 0.02 to 10 V s^{-1}, in HPLC-grade acetonitrile (CH_3CN, ACN) or dichloromethane (CH_2Cl_2, DCM) solutions at $2.5x10^{-4}$–$1x10^{-3}$ M concentration in each substrate, deaerated by N_2 bubbling, using tetrabutylammonium hexafluorophosphate $TBAPF_6$ (Aldrich) 0.1 M as supporting electrolyte, at 298 K. The ohmic drop was compensated by the positive feedback technique.[3] All measurements were carried out using an AUTOLAB PGSTAT potentiostat (EcoChemie, The Netherlands) run by GPES software. The working electrode was a glassy carbon (Metrohm, A = 0.031 mm^2) electrode cleaned by diamond powder (Alfa Aesar, ø < 1 μm) on a wet cloth (STRUERS DP-NAP); the counter electrode was a Pt wire; the reference electrode was a saturated calomel electrode (SCE), having in the working medium a potential of –0.385 V vs. the $Fc^+|Fc$ couple (the intersolvental redox potential reference currently recommended by IUPAC).[4-5]

3.5 Electrochemical impedance spectroscopy

Electrochemical impedance theory is a well-developed branch of alternate current (AC) theory describing the response of a circuit to an alternating current or voltage as a function of frequency. In recent years, electrochemical impedance spectroscopy (EIS) has found widespread applications in the characterization of materials. It is routinely used in the characterization of coatings, batteries, fuel cells, and corrosion phenomena, and it is now popular also in the investigation of diffusion of ions across membranes and in the study of semiconductor interfaces.[6]

In direct current (DC) theory (a special case of AC theory where the frequency equals 0 Hz) resistance is defined by Ohm's Law:

$$E = IR \qquad \text{(eq. 3.5)}$$

Using Ohm's law, one can apply a DC *potential* (E) to a circuit, measure the resulting current (I), and compute the *resistance (R)* - or determine any term of the equation if the other two are known. A *resistor* is the only element that impedes the flow of electrons in a DC circuit. In AC theory, where the frequency is non-zero, the analogous equation is:

$$E = IZ \qquad \text{(eq. 3.6)}$$

As in equation 3.5, E and I are here defined as *potential* and *current*, respectively, whereas Z is defined as *impedance*, the AC equivalent of resistance. In addition to resistors, *capacitors* and *inductors* impede the flow of electrons in AC circuits.

In an electrochemical cell, slow electrode kinetics, slow chemical reactions, and diffusion can all hamper electron flow, and can be considered analogous to the resistors, capacitors, and inductors that impede the flow of electrons in an AC circuit.

The fundamental approach of all impedance methods is to apply a small amplitude sinusoidal excitation signal to the system under investigation and measure the response (current or voltage or any other signal of interest). Figure 3.7 shows a typical plot of a voltage sinewave (E) applied across a given circuit and the resultant AC current waveform (I). Note that the two traces not only are different in amplitude, but are also shifted in time.

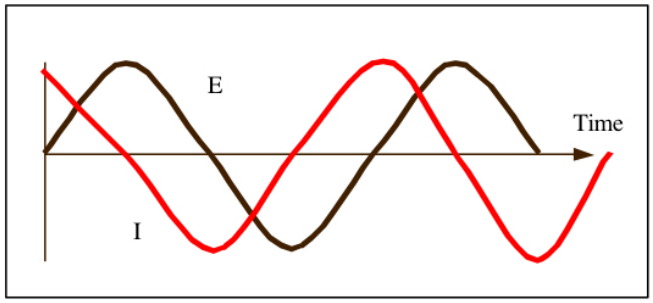

Figure 3.7 AC waveforms for an applied potential and a resulting current are shown.

A low amplitude sinewave $\Delta E\ sin(\omega t)$ of a particular frequency ω, is superimposed on the DC polarization voltage E_0. This results in a current response of a sinewave superimposed on the DC current $\Delta I\ sin(\omega t+\varphi)$. The current response is shifted with respect to the applied potential. The Taylor series expansion for the current is given by equation 3.7:

$$\Delta i = \left(\frac{di}{dE}\right)_{E_0,i_0} \Delta E + \frac{1}{2}\left(\frac{d^2i}{dE^2}\right)_{E_0,i_0} \Delta E^2 + \cdots \qquad \text{(eq. 3.7)}$$

If the magnitude of the perturbing signal ΔE is small, then the response can be considered linear in first approximation. The higher order terms in the Taylor series can be regarded as negligible. The impedance of the system can then be calculated using Ohm's law as:

$$Z(\omega) = \frac{E(\omega)}{I(\omega)} \qquad \text{(eq. 3.8)}$$

This ratio is called impedance of the system and is a complex quantity with a magnitude and a phase shift depending on the frequency of the signal. Therefore, by varying the frequency of the applied signal one can get the impedance of the system as a function of frequency. Given its nature of a complex quantity, impedance can be represented in Cartesian as well as polar coordinates. In polar coordinates the impedance of the data is represented by:

$$Z(\omega) = |Z(\omega)|e^{\varphi\omega} \qquad \text{(eq. 3.9)}$$

where $|Z(\omega)|$ is the magnitude of the impedance and φ is the phase shift. In Cartesian coordinates the impedance is given by:

$$Z(\omega) = Z'(\omega) - iZ''(\omega) \qquad \text{(eq. 3.10)}$$

where $Z'(\omega)$ is the real part of the impedance, $Z''(\omega)$ is the imaginary part, and $i = \sqrt{-1}$. The phase angle is defined by:

$$tan\theta = \frac{Z''(\omega)}{Z'(\omega)} \qquad \text{(eq. 3.11)}$$

To determine the best equivalent circuit for a given electrochemical system, measures are carried out over a range of frequencies, and the

system impedance is then calculated by analyzing the response signal at each frequency.

To describe completely the behavior of an electrochemical system, both the values of in-phase and out-of-phase impedance components at a number of frequencies across the range of interest are needed. One can calculate these values by applying equation 3.6 to the real and imaginary components of the excitation and response waveforms (equation 3.12):

$$Z_{total} = \frac{E' + E''i}{I' + I''i} \qquad \text{(eq. 3.12)}$$

The plot of the real part of impedance against the imaginary part gives a Nyquist plot, as shown in figure 3.8, useful for a quick overview of the data and allowing qualitative interpretations. It must be noted that the real axis must be equal to the imaginary axis not to distort the shape of the curve, of great importance in making qualitative interpretations of the data.

Although the Nyquist format emphasizes series circuit elements, if high and low impedance networks are in series, information about the low impedance circuit are hidden, since larger impedance controls plot scaling. The absolute value of impedance and the phase shifts are plotted as a function of frequency in two different plots, giving a Bode plot, also shown in figure 3.8.

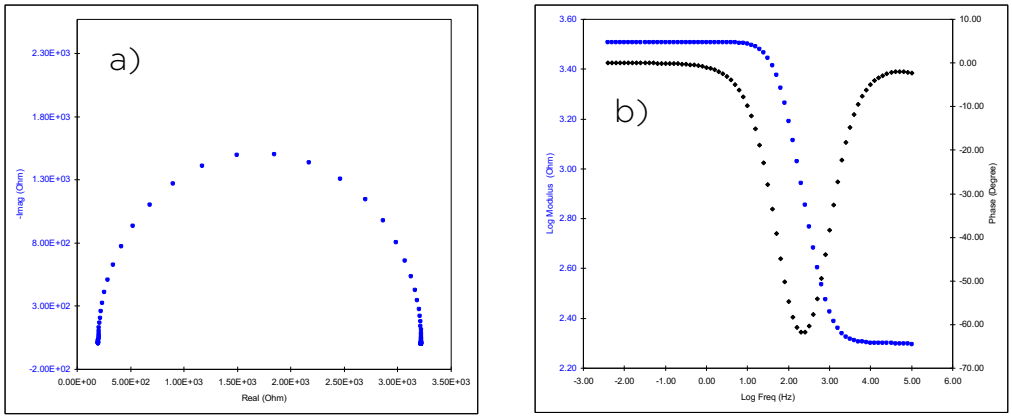

Figure 3.8 typical a) Nyquist (complex plane) plot and b) Bode magnitude and phase plot for impedance measurements.

In this thesis, electrochemical impedance spectroscopy (10 mV steps in the 10^{-1}-10^{-6}Hz range) has been carried out only on already assembled DSSC cells, using a BioLogic SP-300 potentiostat with Zview software, at open circuit, both in the dark and under illumination. Spectra were analyzed with Zview equivalent circuit modeling software, including the distributed element DX11 (transmission line model).[7] All the measurements were performed one day after cell preparation.

3.6 Device preparation and characterization

3.6.1 DSSC and SSD

In chapter 5, some rhenium complexes will be exploited as active layers in Dye-Sensitized Solar Cells (DSSCs). The first series of DSSC was prepared at the Center for Hybrid and Organic Solar Energy (CHOSE, Lazio, IT) while the second series was prepared at the Laboratory of Photomolecular Science (LSPM, EPFL, Lausanne, CH). The solution processed and the solid state devices were made using

respectively, 18 NR-T and 30 NR-D titanium oxide (TiO_2) paste obtained from Dyesol. HSE, a commercial iodine-based electrolyte was also provided by Dyesol, while lithium iodide (LiI), lithium bis(trifluoromethane)sulfonimide (LiTFSI), iodine, tert-butyl pyridine (TBP), and guanidinium thiocyanate (GuSCN) were purchased from Aldrich, and 2,2′,7,7′-tetrakis-(N,N-di-4-methoxyphenylamino)-9,9′-spirobifluorene (Spiro-OMeTAD) was obtained from Solaronix. $[Co(bpy)_3(B(CN)_4)_2]$ and $[Co(bpy)_3(B(CN)_4)_3]$ were synthesized at EPFL. The homemade substrates for liquid-containing cells have a size of approximately 1.4 cm x 1.6 cm, with an active area of 0.159 cm^2 and are depicted in figure 3.9. The device structure consists of a transparent fluorine doped tin oxide (FTO) layer as the bottom electrode, supported on a NSG TEC C10 glass substrate. After being cleaned and having undergone UV-O_3 treatment for 15 minutes, the FTO glass plates were immersed in a 40 mM aqueous $TiCl_4$ solution at 70 °C for 35 min and then washed with water and ethanol. Two screen-printed layer of nanocrystalline TiO_2 particles were used as the photoelectrode. The transparent mesoporous layer (tl), made of 18 nm sized TiO_2 particles (Dyesol DSL18NR-T) was printed on the FTO conducting glass, and the plates were then heated at 150 °C for 7 min. To render high PCE, a ~5-µm scattering layer (sl, 400 nm diameter, Catalysts & Chemicals Ind. Co. Ltd. (CCIC), HPW-400) was deposited on the transparent layer. A total film thickness of 7(tl) + 5(sl) µm was used. Sintering was carried out following a 4-step temperature ramp from 175 to 500 °C, with a residence time of 30 min. The sintered glass plates were immersed again in a 20 mM aqueous $TiCl_4$ solution at 70 °C for 35 min and washed with water and ethanol. The films were heated again at 500 °C for 30 min using a heat blower followed by cooling to 90 °C and dipping into a 0.3 mM toluene solution of the dyes overnight at room temperature.

To prepare the counter electrode, Pt catalyst was deposited on cleaned TEC 15 FTO glass by coating with a drop of H_2PtCl_6 solution (5 mM in 2-PrOH solution) with subsequent rapid thermal treatment at 400 °C for 15 min. Carbon counter electrodes followed the same procedure with a graphite/acetone solution.

For the assembly of DSSCs containing liquid electrolyte, the dye-containing TiO_2 electrode and the counter electrode were assembled into a sandwich-type cell and sealed with a hot-melt gasket of 25 μm thickness made of the ionomer Surlyn 1702 (Dupont). The redox electrolyte was driven into cells through two holes previously drilled in the counter electrode. The iodine-based type of electrolyte used for rhenium-based dyes, consists of 0.7 M LiI, 0.025 M I_2 and 0.2 M TBP in ACN. The cobalt-based type of electrolyte contained instead 1 M LiTFSI, 0.33 M $[Co(bpy)_3(B(CN)_4)_2]$, 0.06 M $[Co(bpy)_3(B(CN)_4)_3]$ and 0.2 M TBP in ACN. Finally, the hole was sealed using Surlyn and a cover glass (0.1 mm thickness).

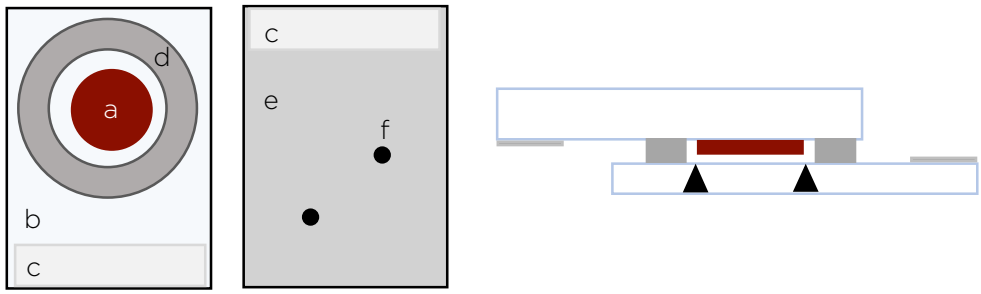

Figure 3.9 Scheme of a DSSC: a) active TiO_2/adsorbed dye layer b) NSG10 FTO glass c) electric contacts d) 25 mm spacer/sealer e) TEC 15 FTO glass f) holes for electrolyte injection.

Solid state devices (SSD) were prepared following a similar procedure. An FTO glass plate of 1.4 cm x 2.3 cm, depicted in figure 3.10, was laser etched to create non-conductive zone for separation of the contacts, then was cleaned and UV/O_3 treated before undergoing flame spray pyrolysis. A solution containing 0.6 mL of titanium isopropoxide acetylacetonate [$Ti(OiPr)_2(acac)_2$], 0.4 mL of acetylacetone and 9 mL of ethanol was then sprayed (gas carrier: O_2, 0.8 bar) on the glass plates at 450°C, creating a non-porous transparent TiO_2 layer.

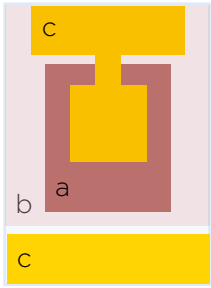

Figure 3.10 Scheme of an SSD: a) active TiO_2/adsorbed dye layer b) Spiro-OMeTAD layer c) gold electric contacts.

The transparent mesoporous layer, in this case made of 30 nm sized TiO_2 particles (Dyesol DSL30NR-D) was printed with a different mesh on the FTO conducting glass, followed by no scattering layer. Sintering was carried out as described above. The titania films were then dipped into a 0.3 mM toluene solution of the dyes overnight at room temperature, then dried, and transferred into a glove box. A solution of the hole transporting material (HTM), Spiro-OMeTAD, was spin coated onto the adsorbed dye. The final thickness of the whole cell resulted to be around 2 μm. The counter electrode, metallic gold, was deposed via physical vapor deposition, without sealing the cell before measurements.

3.6.2 Characterization of DSSC and SSD

All measurements were carried out in air directly after the fabrication of the cells. A black shadow mask with a fixed aperture was used on DSSCs and SSDs, so that the active area was set to 0.16 cm^2. Current-voltage characteristics were recorded by applying an external potential bias to the cell while recording the generated photocurrent with a digital source meter (Keithley model 2400) connected to a pc. The light source was a 450 W xenon lamp (Oriel) equipped with a Schott K113 Tempax sunlight filter (Präzisions Glas & Optik GmbH) to match the emission spectrum of the lamp with the AM 1.5 G standard. Before each measurement, the exact light intensity was determined using a calibrated Si reference diode equipped with an infrared cutoff filter (Schott KG-3). The incident photon to collected electron conversion efficiency (IPCE) measurement was plotted as function of wavelength by using the light from a 300-W xenon lamp (ILC Technology), which was focused through a Gemini-180 double monochromator (Jobin Yvon) onto the photovoltaic cell under test. A computer-controlled monochromator was incremented through the spectral range (300–800 nm) to generate a photocurrent action spectrum with a sampling interval of 10 nm and a current sampling time of 4 s to reduce scattered light from the edge of the glass electrodes of the dyed TiO_2 layer.

References

[1] B. Valeur, *Molecular Fluorescence: Principles and Applications*, Wiley-VCH Weinheim **2001**

[2] P. Elterman, Integrating Cavity Spectroscopy, *Applied Optics*, **1970**, 9, 2140

[3] A. J. Bard, L. R. Faulkner, in *Electrochemical Methods: Fundamentals and Applications*, Wiley, New York **2002**, 648

[4] G. Gritzner, J. Kuta, *Pure Appl. Chem.* **1984**, 56, 461

[5] G. Gritzner, *Pure Appl. Chem.* **1990**, 62, 183

[6] J. R. Macdonald, *Impedance Spectroscopy: Emphasizing Solid Materials and Systems;* John Wiley & Sons: New York, **1987**

[7] J. Bisquert, *J. Phys. Chem. B* **2002**, 106, 325

CHAPTER 4

Long-lived rhenium(I) complexes containing 4-phenylpyridazine ligands

Abstract

The preparation of a series of complexes containing functionalized 4-phenylpyridazines is presented along with their spectroscopic, electrochemical and photophysical properties, and rationalized on the basis of preliminary DFT calculations. Long-lived excited states with mixed ^{3}LC – ^{3}MLCT character have been identified in one of these species, suggesting a possible use as triplet photosensitizer for triplet-triplet annihilation (TTA) based upconversion. Some related preliminary results are here reported.

4.1 Introduction

As previously described in chapter 1, carbonyl complexes of rhenium(I) containing chelating diimine ligands have been extensively investigated over the last decades[1] because of their distinctive photochemical and photophysical properties. For such complexes, both wavelength and lifetime of the emission can be widely tuned by varying the ancillary ligands or the substituents on the diimine ligands,[1] and very high photoluminescence quantum yields (PLQY) have been obtained in the case of dinuclear complexes,[2-4] allowing widespread applications in electroluminescent devices[5] or as bio-imaging probes.[6] Those results, however, were all obtained by endowing the bridging 1,2-diazine with alkyl, electron donating substituents in its β position.

On these basis, we were prompted to investigate the modulation of the photophysical properties induced by an aryl, rather than an alkyl, substituent in the β position of the bridging 1,2-diazine. Five new complexes containing 4-phenylpyridazines bearing different substituents in the *para* position of the phenyl ring (see chart 4.1) have been prepared, their spectroscopic, electrochemical and photophysical properties have been investigated, and rationalized on the basis of preliminary computations at DFT level. Long lived excited states with mixed ^{3}LC - ^{3}MLCT character have been identified in one of these species, suggesting a possible use as triplet photosensitizer for triplet-triplet annihilation (TTA) based photon upconversion. Indeed, beside few recent papers, almost no Re(I) tricarbonyl complexes have been used as triplet photosensitizers in TTA upconversion to date.[7]

Photon upconversion is a process in which light of long wavelength is frequency converted to photons of higher energy. This is a two-quantum process involving triplet excited states which annihilate to produce a singlet state with energy doubled compared to the triplet states, leading to anti-Stokes delayed fluorescence. Therefore, the sensitized triplet–triplet annihilation mechanism involves the transfer of energy between a sensitizer (donor) molecule, usually a transition metal complex, and an acceptor/annihilator, based on a highly conjugated hydrocarbon chromophore.

Indeed, transition metal-based sensitizers present ^{3}MLCT excited states quasi-isoenergetic with the non-emissive $^{3}(\pi\text{-}\pi^{*})$ excited states of the acceptor. In this way, one state is thermally accessible from the other, even at room temperature, and the energy transfer process between these two triplets can occur.

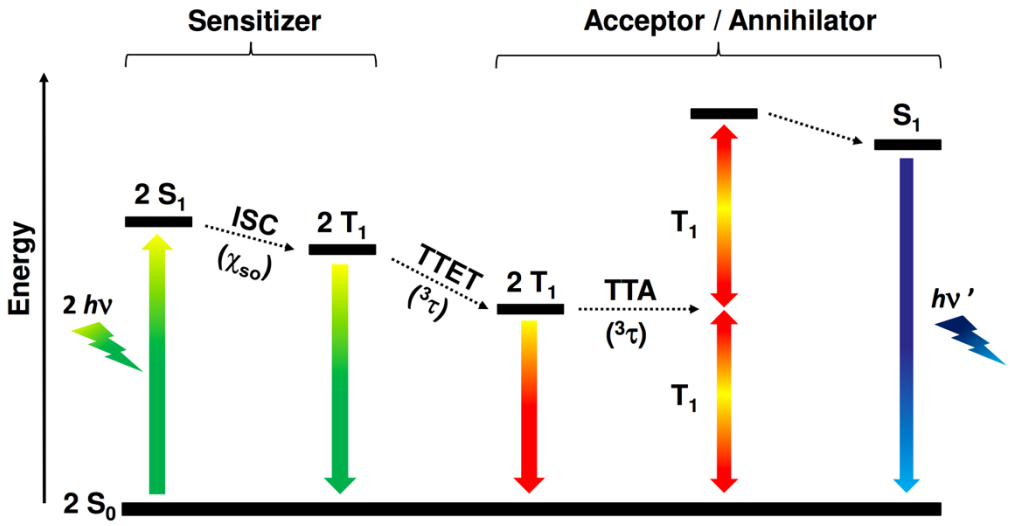

Figure 4.1 Jabłonski diagram for TTA photon upconversion depicting the main electronic transitions.

The Jabłonski diagram in figure 4.1 summarizes the processes involved in photon upconversion via sensitized triplet-triplet annihilation. Following selective excitation, via low energy radiation, the energy is transferred to the acceptor via triplet-triplet energy transfer (TTET), thus regenerating the ground state sensitizer. This process repeats and another long-lived excited triplet acceptor is formed, and then they annihilate to produce the emissive singlet state.

4.2 Results and discussion

4.2.1 Synthesis of the complexes

Five different derivatives have been prepared featuring differently substituted 4-phenylpyridazine ligands, complexes **1–5**, whose chemical structures are depicted in chart 4.1.

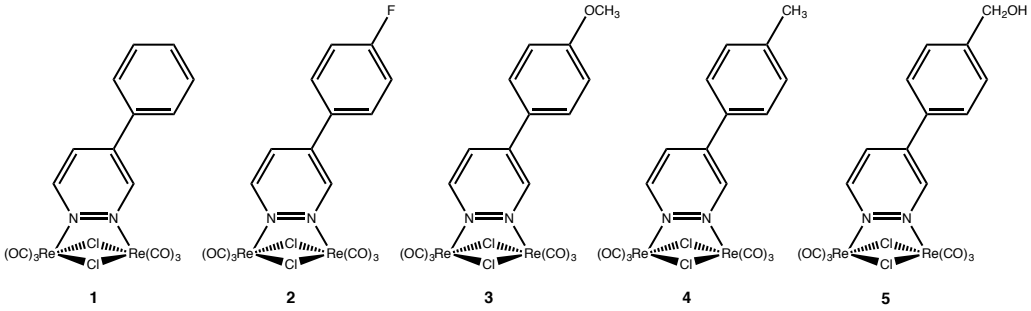

Chart 4.1 Molecular structures of the investigated complexes **1-5**.

The ligands were not commercially available and were synthesized by a literature procedure[8] involving an inverse-type [4+2] Diels-Alder cycloaddition reaction between the electron-poor 1,2,4,5-tetrazine and the proper functionalized alkyne (see scheme 4.1).

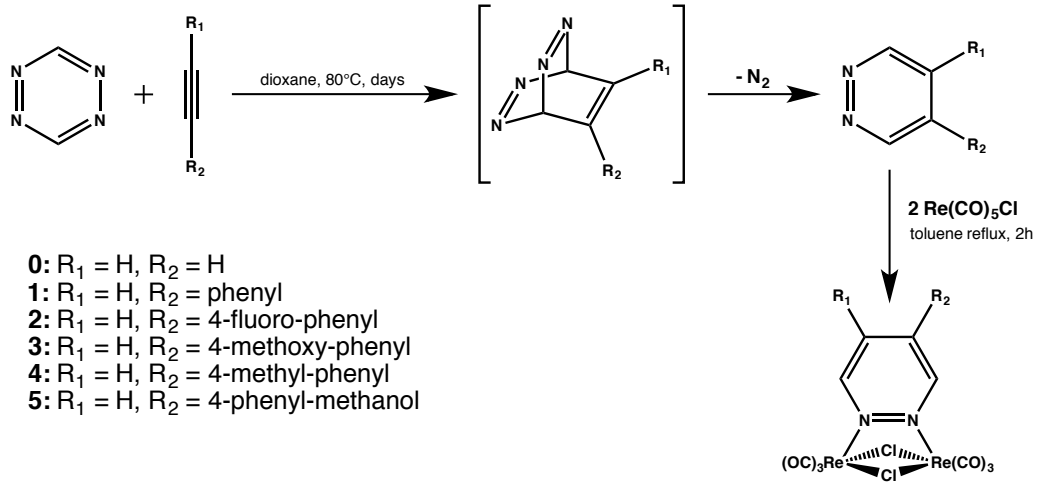

Scheme 4.1 Synthetic pathway to the diazine ligands and the corresponding dinuclear Re(I) complexes.

The so prepared diazine ligands were reacted with two equivalents of $[Re(CO)_5Cl]$ affording the corresponding complexes in good yields (60%-80%). The new complexes **1-5** have been characterized by elemental analysis and various spectroscopic techniques. The IR spectra in the ν(CO) region show the four band pattern typical of this class of $[Re_2(\mu\text{-}X)_2(CO)_6(\mu\text{-}1,2\text{-diazine})]$ complexes[9] at wavenumbers almost identical in the series, as shown in table 4.1, and similar to those of the parent complex, named **0,** bearing an unsubstituted pyridazine.[3] As expected, the ^{1}H NMR spectra show three resonances corresponding to the protons on the diazine ring, with the signals of the two *ortho* protons H3 and H6 slightly shifted towards opposite directions (H3 is de-shielded, while H6 is shielded, both by ca. 0.1 ppm), compared to the pyridazine derivative **0**, as also shown in table 4.1. The phenyl substituents are expected to be not coplanar with the diazine ring, due to steric hindrance between hydrogen atoms. However, the rotational barrier has been computed (see below) and found to be very low, thus accounting for the presence of only one

resonance for the two *ortho* and the two *meta* protons of the phenyl substituents, in line with the fast rotation that averages the different environments. The variation of the substituent in the *para* position of the phenyl ring in the **1-5** series appears to affect the *ortho* resonance only (table 4.1).

Table 4.1 Chemical shift for the hydrogens on the pyridazine ring and the phenyl ring in complexes 0-5 and **ν**(CO) IR bands.

Complex	H3	H5	H6	*ortho* Ph	*meta* Ph	IR **ν**(CO) [cm^{-1}]
0 (CD_2Cl_2)	9.85	8.08	9.85			2051, 2034, 1948, 1916
1 ($CDCl_3$)	9.98	8.16	9.77	7.84	7.73[a]	2049, 2033, 1946, 1917
2 (CD_2Cl_2)	9.95	8.13	9.76	7.87	7.44	2046, 2034, 1947, 1918
2 ($CDCl_3$)	9.91	8.06	9.74	7.82	7.42	2046, 2034, 1947, 1918
3 ($CDCl_3$)	9.93	8.07	9.64	7.84	7.21	2049 2033, 1947, 1915
4 ($CDCl_3$)	9.97	8.13	9.72	7.75	7.53	2049, 2033, 1946, 1917
5 ($CDCl_3$)	9.98	8.15	9.75	7.84	7.72	2049 2033, 1946, 1916

[[a] also *para* Ph]

Preliminary computed properties have been performed on complex **1**, containing the unsubstituted phenyl ring. Figure 4.1 depicts the dependence of the relative energy (E_r), the MLCT absorption maximum (λ_{abs}), and the HOMO–LUMO gap (ΔE) on the dihedral angle **ω** between the plane of the phenyl ring and that of the pyridazine ring. A stable conformation can be found for **ω** = 34°; however, the computed rotational barrier is quite low. Moving on from the coplanar conformation (**ω** = 0° , E_r = 6 kJ mol^{-1}) to the orthogonal one (**ω** = 90°, E_r = 14 kJ mol^{-1}) the delocalization of LUMO and LUMO+1 on the phenyl ring decreases down to zero.

As a consequence, the MLCT absorption maximum is blue shifted by 23 nm, and the HOMO–LUMO gap raised by 0.18 eV. This finding can be attributed to the limited conjugation between the phenyl moiety and the pyridazine ring, due to geometric constraints that hamper coplanarity and to the different relative energy of the π^* orbitals involved.

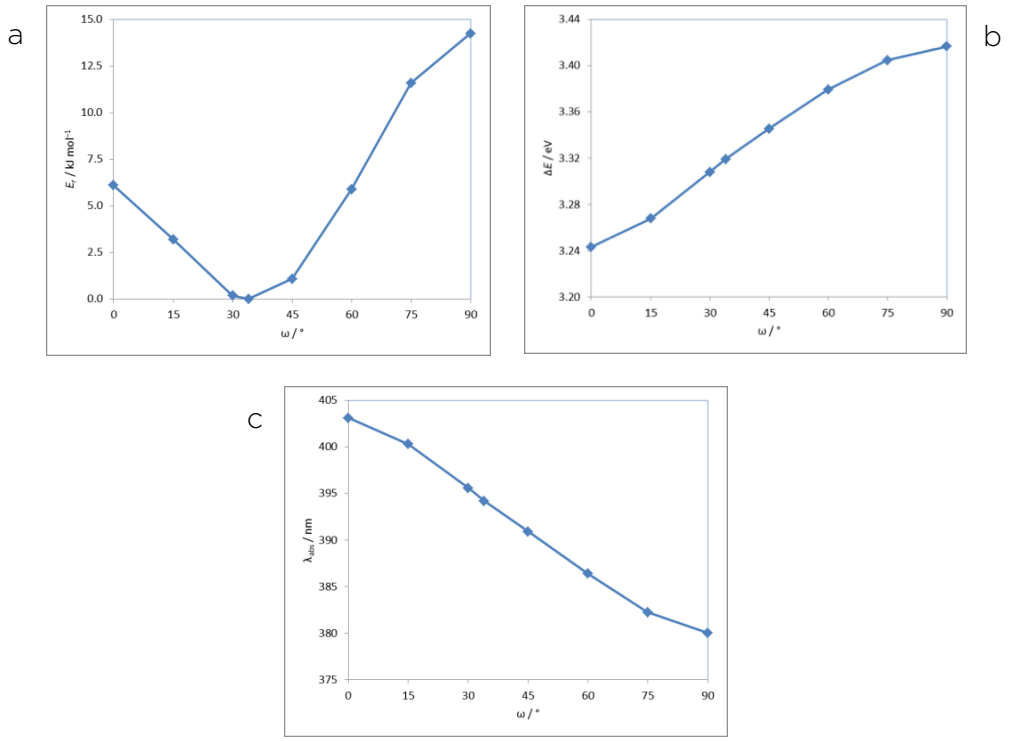

Figure 4.1 Dependence of a) the relative energy b) the HOMO-LUMO gap c) the absorption maximum on the dihedral angle ω between the phenyl and the pyridazine ring in complex **1**.

In agreement with the scarce conjugation between phenyl and pyridazine, it can be hypothesized that a modest variation of the HOMO–LUMO gap, and therefore of the absorption maximum, should be observed upon the introduction of different substituents at the *para* position of the phenyl ring.

4.2.2 Electrochemical characterization

Table 4.2 shows the results of the cyclic voltammetry (CV) analyses of complexes **1**–**5** in acetonitrile solution including for comparison previously published data concerning the parent complex **0**.[3] Cyclic voltammograms are reported in figure 4.2.

Table 4.2 Selected CV features for the complexes **0**-**5** recorded on GC electrode at 0.2 Vs^{-1} in dry acetonitrile + 0.1 M $TBAPF_6$ with ohmic drop compensation.

Complex	R	$E_{p,c}$ [V]	$E_{p,a}$ [V]	E_{LUMO} [eV]	E_{HOMO} [eV]	E_g [eV]
0	H	-1.345	1.315	-3.46	-6.12	2.66
1	Ph	-1.255	1.243	-3.37	-6.04	2.50
2	4-F-Ph	-1.253	1.237	-3.37	-6.04	2.49
3	4-OMe-Ph	-1.313	1.230	-3.43	-6.03	2.54
4	4-CH_3-Ph	-1.286	1.235	-3.40	-6.04	2.52
5	4-CH_2OH-Ph	-1.269	1.234	-3.53	-6.03	2.50

The first reduction peaks are quite similar for all the complexes, in terms of both shape and potential. Peaks are all monoelectronic and reversible, both from the chemical (symmetrical return peak and products stable in acetonitrile solution) and the electrochemical point of view (ca. 57 mV half-peak width, with facile transfer of a single electron). This indicates the very fast formation of a stable radical anion, in which the negative charge can be regarded as localized on the diazine ligand, in agreement with what previously reported for other related complexes.[3,9]

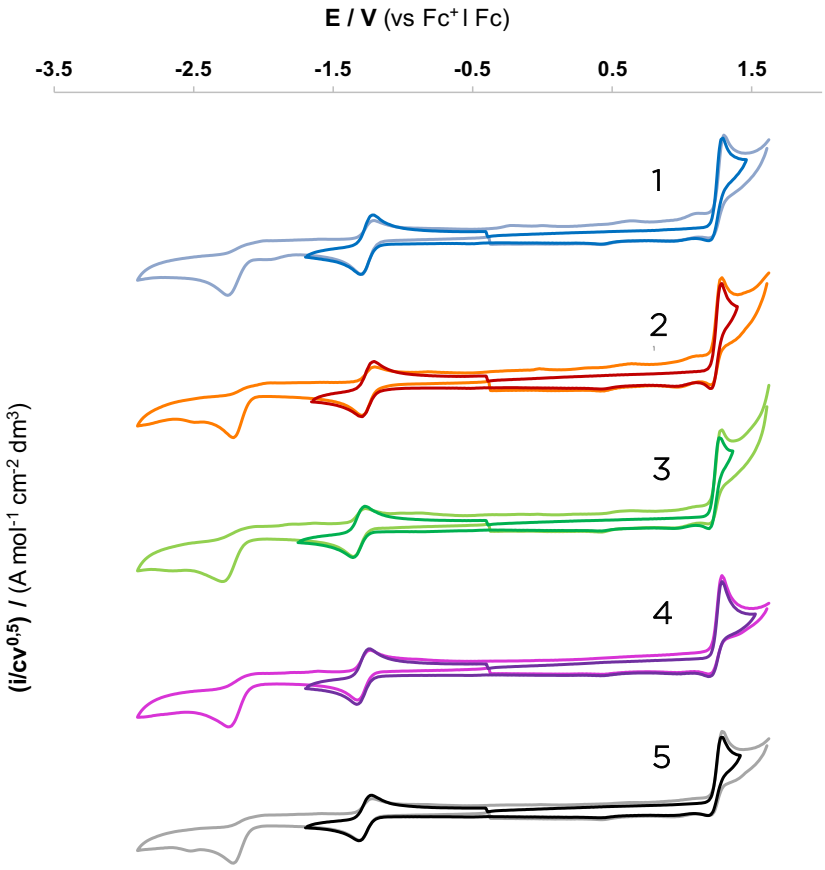

Figure 4.2 Normalized CV curves of the investigated complexes **1-5** recorded on a GC electrode at 0.2 V s^{-1} in dry acetonitrile + 0.1 M $TBAPF_6$ with ohmic drop compensation.

Previous work has also shown that the oxidation of $[Re_2(\mu\text{-}Cl)_2(CO)_6(\mu\text{-}1,2\text{-diazine})]$ complexes is a metal-centered Re(I)→Re(II) oxidation, and involves a simultaneous two-electron transfer, according to the i_L/c parameter, doubled if compared to the reduction peak. This is also the case for complexes **1**-**5**. The oxidation appears to be both chemically and electrochemically irreversible but, in the upper range of the explored scan rates, return peaks emerge (behavior of complex **2** depicted in figure 4.3) and, to a minor extent, for complex **3**.

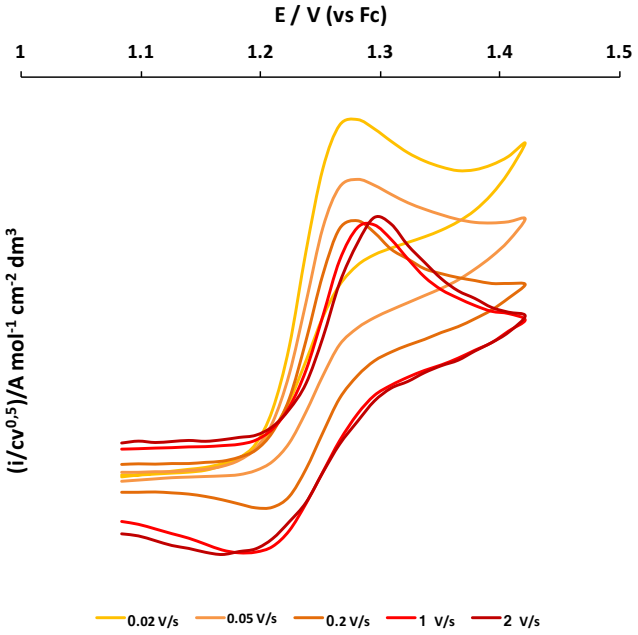

Figure 4.3 Anodic scan only for complex **2**. Scan rate 0.02 V s^{-1} to 2 V s^{-1}.

4.2.3 Photophysical characterization

The photophysical properties of complexes **0**-**5** in CH_2Cl_2 are reported in table 2.3. The lower energy broad absorption band can be assigned to a d(π)Re→π*(diazine) transition with metal-to-ligand charge transfer (^{1}MLCT) character.[3,9] The presence of the phenyl substituent on the pyridazine ring affords a small bathochromic shift and an increase of the molar absorption coefficient compared to complex **0** (ε = 0.79×10^4 M^{-1} cm^{-1} at λ_{abs} 375 nm), owing to the increasing probability of this transition, with the possibility to partially delocalize the charge. This assignment is also supported by the typical strong solvent dependence of the charge-transfer absorption band. Indeed, as already reported for the parent complex **0**,[3] a blue shift of more than 30 nm is observed upon increasing solvent polarity from toluene to acetonitrile. For instance, in complex **1** the absorption maximum shifts from 396 nm in toluene to 355 nm in ACN. The solvent effect for all the complexes is shown in table 4.4.

In agreement with the electrochemical analysis and the preliminary computational data, with the only exception of complex **3**, a negligible modulation effect has been observed on the absorption maximum upon changing the nature of the substituent in the *para* position of the phenyl ring. This finding can be attributed to geometric constraints which limit the conjugation between the phenyl moiety and the pyridazine ring. A different behavior is observed for complex **3**, which displays the highest bathochromic shift, about 20 nm, with a significant increase of the molar absorption coefficient (ε = 2.3×10^4 M^{-1} cm^{-1} at λ_{abs} 397 nm). Moreover, a lower modulation effect of the solvent polarity on the absorption maximum has been observed.

All these features are in agreement with the presence of a ligand centered (LC) π-conjugated state. Indeed, preliminary computations at DFT level have shown a significant delocalization of the three lowest lying t_{2g} orbitals on the phenyl ring of the methoxo derivative, which induces a higher degree of coplanarization between the diazine and the phenyl ring, lowering the LUMO levels.

Table 4.3 Photophysical data for complexes **1-5** in diluted CH_2Cl_2 solution ($1x10^{-5}$ M).

Complex	λ_{abs} (nm)	ε (10^4 M^{-1} cm^{-1})	λ_{em} (nm)	τ [a] (μs)	Φ [a]	τ [b] (μs)	Φ [b]	k_r (10^5 s^{-1})	k_{nr} (10^5 s^{-1})	λ_{em} [c] (nm)	τ [c] (μs)
0	375	0.79	613	0.35	0.036	0.43	0.044	0.93	22.2	512	25 (100%)
1	381	0.89	617	0.53	0.04	1.10	0.078	0.71	8.4	538	66 (58%) 170 (42%)
2	385	1.2	621	0.49	0.04	0.91	0.076	0.83	10.1	534	51.6 (45%) 125 (55%)
3	397	2.12	607	0.76	0.032	4.51	0.18	0.40	1.8	525, 560	185 (63%) 685 (37%)
4	384	1.81	610	0.69	0.05	1.89	0.12	0.63	4.6	535	111 (42%) 313 (58%)
5	382	1.32	619	0.55	0.027	1.14	0.077	0.67	8.2	537	90 (37%) 263 (63%)

[[a] air-equilibrated CH_2Cl_2, [b] deaerated CH_2Cl_2, [c] 2-MeTHF glassy matrix at 77K]

Upon optical excitation, all the samples show a rather intense, broad and featureless emission at room temperature that falls in the orange region of the visible spectrum. The absorption and photoluminescence spectra of all the complexes are reported in figure 4.4, and the corresponding data are collected in Table 4.3. The quenching of the emission and the corresponding reduction of the emission lifetime observed in air-equilibrated solution clearly indicate that the radiative transition arises from an excited state having a triplet character.

Table 4.4 Solvent effect for complexes 1-5 in diluted toluene, CH_2Cl_2, $CHCl_3$, ACN solution ($1x10^{-5}$ M).

COMPLEX	λ_{abs} (nm) TOL	λ_{em} (nm) TOL	λ_{abs} (nm) $CHCl_3$	λ_{em} (nm) $CHCl_3$	λ_{abs} (nm) CH_2Cl_2	λ_{em} (nm) CH_2Cl_2	λ_{abs} (nm) ACN	λ_{em} (nm) ACN
1	396	599	392	615	381	617	355	642
2	394	602	392	617	385	621	361	647
3	399	597	404	605	397	603	380	625
4	391	591	398	609	384	610	360	637
5	392	594	397	617	382	619	360	640

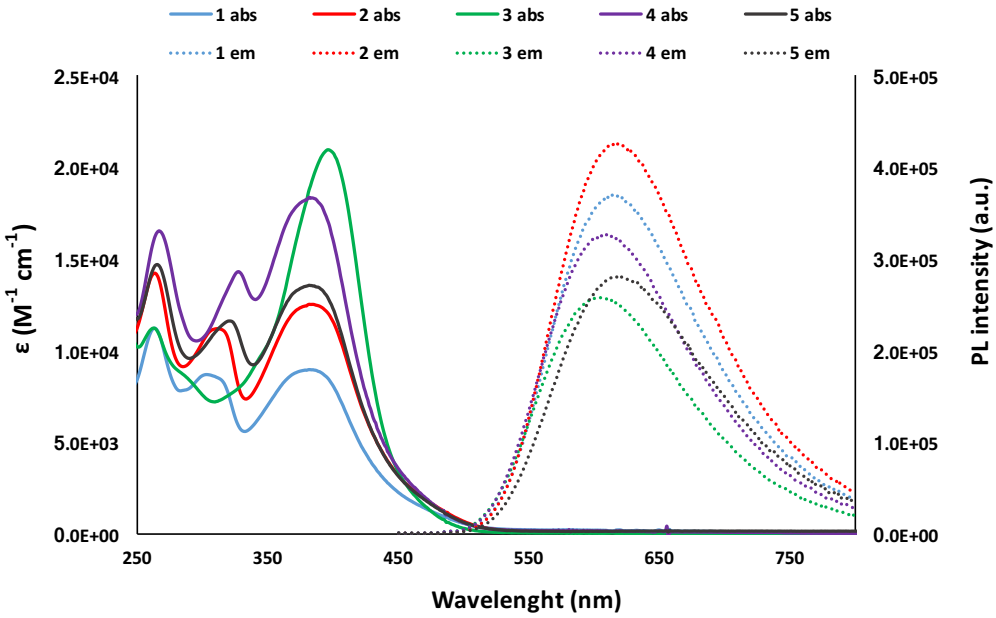

Figure 4.4 Absorption and emission spectra of complexes 1-5 in CH_2Cl_2 solution.

As already observed in the absorption spectra, with the only exception of complex 3, the position of the emission maximum is not affected by the nature of the *para* substituents and it results slightly red-shifted compared to the emission maximum of the parent complex 0.

All complexes display photoluminescence quantum yields higher than **0**, mainly due to the significant reduction of the non-radiative rate constant k_{nr} (see table 4.3). On the contrary, the values of $\phi_{em}/\tau_{em} = k_r \times \eta_{isc}$, where the latter term represents the efficiency of the intersystem crossing process, are in the range 0.63–0.83×10^5 s^{-1}, in line with the values measured for the other analogous dinuclear rhenium complexes.[3] Again, a different behavior is observed for complex **3**, whose emission maximum results slightly blue-shifted compared to complex **0**. Moreover, complex **3** displays a very long emission lifetime and increased photoluminescence quantum yield, which affords a drop of the $k_r \times \eta_{isc}$ value to 0.4×10^5 s^{-1}. All these features suggest the presence of an admixed ^{3}LC - ^{3}MLCT nature of the excited state. The small shift in emission energy observed upon variation of the solvent polarity observed for complex **3**, the structured emission spectrum acquired at low temperature in glassy matrix (see figure 4.5), observed for **3** only, and the long-lived excited-state lifetime, further support this assignment.

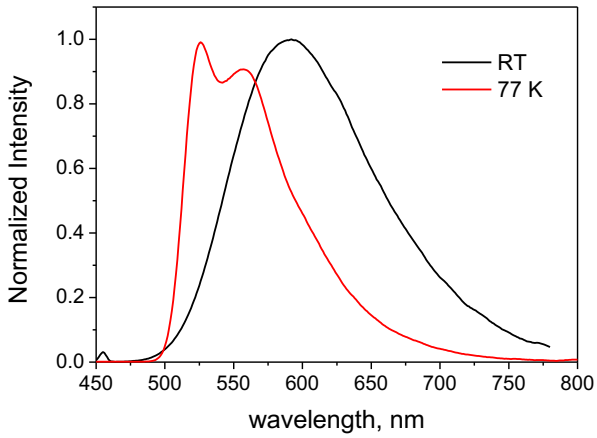

Figure 4.5 Emission spectra of complex **3** in toluene solution at room temperature (black line) and in 2-MeTHF glassy matrix at 77 K (red line).

4.2.4 Energy upconversion

The investigated Re(I) dinuclear complexes are good candidates to act as triplet sensitizers to populate the lower-lying triplet excited states of aromatic molecules because of the efficient intersystem crossing between the lowest ^{1}MLCT singlet and the long-lived phosphorescent ^{3}MLCT excited state of the complex, which is beneficial for the TTET, a crucial step for TTA upconversion (table 4.3). In particular, complex **3** displays the longest lifetime of the ^{3}MLCT state in deaerated conditions, thus standing out as the best option. This experiment has been carried out in collaboration with Prof. Paola Ceroni at the University of Bologna. 9,10-Diphenylanthracene (DPA) was chosen as acceptor since it was extensively used in the presence of $[Ru(bpy)_3]^{2+}$ complexes.[10] Upon excitation at 532 nm in deaerated dichloromethane solution (1.5×10^{-4} M) in presence of DPA (0.63×10^{-4} M), the phosphorescence of **3** was highly quenched (ca. 75%), and a delayed fluorescence of DPA peaking at 400 nm was observed with lifetime in the μs time-scale. This process is based on sensitized triplet-triplet annihilation of DPA chromophores, as described by the following equations:

$$\mathbf{3}(S_0) + h\nu \rightarrow {}^*\mathbf{3}(S_1) \quad (1)$$

$${}^*\mathbf{3}(S_1) \rightarrow {}^*\mathbf{3}(T_1) \quad (2)$$

$${}^*\mathbf{3}(T_1) + DPA(S_0) \rightarrow \mathbf{3}(S_0) + {}^*DPA(T_1) \quad (3)$$

$${}^*DPA(T_1) + {}^*DPA(T_1) \rightarrow {}^*DPA(S_1) + DPA(S_0) \quad (4)$$

$${}^*DPA(S_1) \rightarrow DPA(S_0) + h\nu' \quad (5)$$

This mechanism is consistent with the energy level diagram shown in figure 4.6. It takes advantage of the very high efficiency of process (2) for Re(I) complexes[9] and of the presence of DPA chromophores displaying staggered S_1 and T_1 excited states.

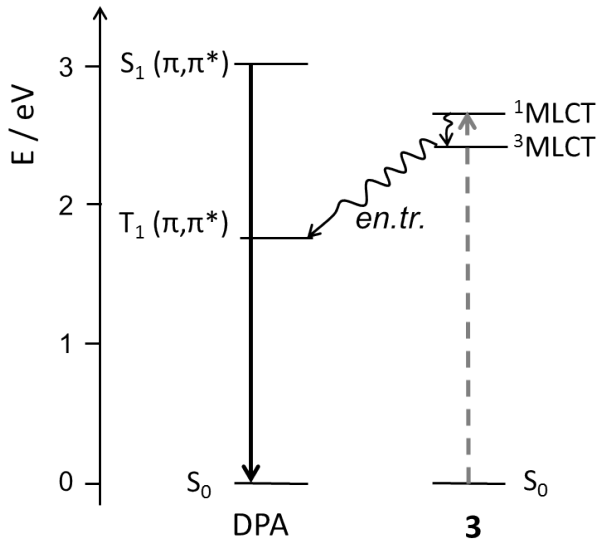

Figure 4.6 Schematic energy level diagram showing the absorption (dashed grey line), emission (solid black line), and non-radiative processes (wavy lines) occurring in a deaerated solution containing complex **3** and 9,10-diphenylanthracene (DPA) at room temperature.

Upon increasing the excitation laser power, the lifetime of the delayed DPA fluorescence decreases and the fluorescence intensity increases according to a quadratic law (see figure 4.7), as expected for a process involving triplet-triplet annihilation of DPA. The quantum yield of the upconversion process (ϕ_{UC}) is a function of the excitation source power and the DPA concentration and can be expressed by the following equation:

$$\Phi_{UC} = 2 \times \eta_{isc} \times \eta_{en.tr.} \times \eta_{TTA} \times \Phi_{fl} \qquad \text{(eq. 4.1)}$$

where η_{isc} is the efficiency of the intersystem crossing process for **3** (process 2), $\eta_{en.tr.}$ is the energy transfer efficiency (process 3), η_{TTA} is the triplet-triplet annihilation efficiency (process 4) and ϕ_{fl} is the fluorescence quantum yield of DPA (process 5).

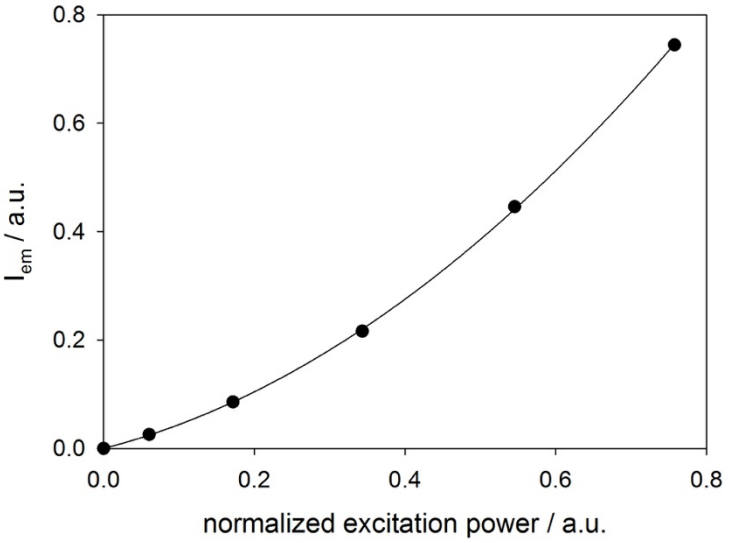

Figure 4.7 Fluorescence intensity of DPA at 430 nm as a function of the excitation power at 532 nm for a solution containing **3** (1.5×10^{-4} M) and DPA (0.63×10^{-4} M).

In order to quantify the efficiency of the TTET process, the quenching of the triplet excited state of complex **3** was evaluated: the bimolecular quenching constant k_q was estimated as 7×10^8 M^{-1} s^{-1}, close to the values reported for the mononuclear Re complexes (10^8 M^{-1} s^{-1}),[7] implying an efficient TTET. However, the overall efficiency of the upconversion process was 0.1%, much weaker than the values measured for the mononuclear complexes. This feature could be probably due to the weak absorption of complex **3** at the laser excitation wavelength and the shorter lifetime of the triplet excited state.

4.3 Conclusions

Five new complexes containing 4-phenylpyridazine ligands have been prepared and characterized. Along with the low degree of conjugation between the two aromatic rings, strong absorption in the visible region (ε = 2.3×10^4 M^{-1} cm^{-1} at 397 nm) and long-lived triplet excited states (4.5 μs) have been observed for complex **3**, containing a para-methoxo-4-phenylpyridazine ligand. These properties, in contrast with those usually reported for mononuclear rhenium complexes, and also with some other dinuclear complexes we previously reported, have been attributed to presence of an intra-ligand triplet excited state (^{3}IL), as proved also by the emission spectrum at 77 K. Although with low efficiency, partially due to the experimental setup, this is the first time a dinuclear rhenium complex is used as triplet sensitizer for triplet-triplet annihilation upconversion. These preliminary results prompt us to further investigate this application field by preparing other rhenium complexes containing diazine ligands with highly conjugated system showing strong absorption in the visible region.

4.4 Experimental

General methods

All the reagents were purchased from Aldrich and used as received. All the reactions were performed under inert N_2 atmosphere. All the solvents were deoxygenated and dried by standard methods prior to use: 1,4-dioxane was distilled on $Na_{(s)}$/benzophenone, toluene on $Na_{(s)}$, and CH_2Cl_2 on P_2O_5. Commercial deuterated solvents were used as received. Column chromatography was performed using Alfa Aesar silica gel 60 (0.032–0.063 mm). 1,2,4,5-tetrazine and the corresponding substituted diazines were synthesized according to literature procedures.[8] The completeness of the reaction was monitored by UV-Vis spectroscopy by observing the decrease of the characteristic tetrazine absorption band at 515 nm. The substituted diazines were not directly purified and used as obtained, once the non-reactivity of $[Re(CO)_5Cl]$ towards the excess of alkyne was verified. ^1H NMR spectra were recorded on a Bruker DRX-400 MHz instrument by using the residual signals δ = 7.28 ppm from $CDCl_3$ or δ = 5.32 ppm from CD_2Cl_2 as internal references. IR spectra in solution were acquired on a Bruker Vector 22 FT spectrophotometer.

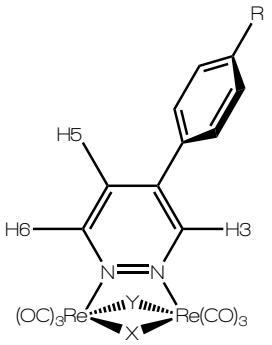

Electrochemical measurements

see chapter 3.

Spectroscopy

See chapter 3. Delayed fluorescence lifetimes were measured by a Hamamatsu R928 phototube connected to a Tektronix TDS380 (400 MHz) oscilloscope upon excitation with a Continuum Surelite I-10 Nd:YAG laser source (λ_{exc} = 532 nm). The intensity of the laser source was measured by a laser point power meter model Plus, equipped with a 10 UV-A detector head.

Synthesis of 4-phenylpyridazine. 83 µL (0.735 mmol) of phenylacetylene are dissolved in 2.5 mL of anhydrous 1,4-dioxane containing 0.613 mmol of 1,2,4,5-tetrazine. The reaction mixture is refluxed for 14 hours then left at RT in the dark for 3 weeks. The solution is then dried. The product obtained is not purified and directly used for the next synthesis, estimating a quantitative conversion of the tetrazine.

Synthesis of [$Re_2(\mu\text{-}Cl)_2(CO)_6(\mu$-4-phenylpyridazine)] (1). Half of the solid 4-phenylpyridazine from the previous reaction (0.306 mmol) is dissolved in 3.5 mL of freshly distilled toluene. 222 mg (0.614 mmol) of $Re(CO)_5Cl$ are added to the reaction mixture. The reaction is put under reflux for 3 hours, then cooled to RT. The so-formed precipitate is filtered through a sintered glass funnel. The crude product is dissolved in CH_2Cl_2 and re-precipitated with n-hexane. The supernatant solution is removed, the remaining powder washed with n-hexane (3 mL x 5) and dried under vacuum. The solid product is purified through column chromatography (CH_2Cl_2/n-hexane 7:3) affording 185 mg (0.22 mmol)

of the desired product (yield 72%). IR (CH_2Cl_2) ν(CO): 2049 (m), 2033 (s), 1946 (s), 1917 (s) cm^{-1}, ^1H NMR: ($CDCl_3$, 300K, 400 MHz) δ_H (ppm) 9.98 (dd, J = 2.5, 1.0 Hz, 1H, H_3); 9.77 (dd, J = 6.2, 1.0 Hz, 1H, H_6); 8.16 (dd, J = 6.1, 2.4 Hz, 1H, H_5); 7.84 (m, 2H, H_{ortho}); 7.73 (m, 3H, $H_{meta/para}$)

Synthesis of 4-(4-fluorophenyl)pyridazine. 63 µL (0.545 mmol) of 1-ethynyl-4-fluorobenzene are dissolved in 4 mL of anhydrous 1,4-dioxane containing 0.242 mmol of 1,2,4,5-tetrazine. The reaction mixture is put under reflux for 48 hours, then cooled to RT and dried under vacuum. The crude product is directly used for the next synthesis, estimating a quantitative conversion of the tetrazine.

Synthesis of $[Re_2(\mu\text{-}Cl)_2(CO)_6(\mu\text{-}4\text{-}(4\text{-fluorophenyl})pyridazine)]$ (2). The solid residue from the previous reaction (0.242 mmol) is dissolved in 5 mL of freshly distilled toluene. 175 mg (0.484 mmol) of $Re(CO)_5Cl$ are added to the reaction mixture. The mixture is put under reflux for 3 hours, then cooled to RT and evaporated to dryness. The crude product is purified through column chromatography (CH_2Cl_2/n-hexane 8:2) affording 140 mg (0.179 mmol) of the desired product (yield 74%). IR (CH_2Cl_2) ν(CO): 2046 (m), 2034 (s), 1947 (s), 1918 (s) cm^{-1}, ^1H NMR: (CD_2Cl_2, 300K, 400 MHz) δ_H (ppm) 9.95 (dd, J = 2.5, 1.0 Hz, 1H, H_3); 9.76 (dd, J = 6.1, 1.0 Hz, 1H, H_6); 8.13 (dd, J = 6.1, 2.5 Hz, 1H, H_5); 7.87 (m, 2H, H_{ortho}); 7.44 (m, 2H, H_{meta}), ^{19}F NMR: ($CDCl_3$, 300K, 400 MHz) δ_F (ppm) = -103.8 (m, 1F)

Synthesis of 4-(4-methoxyphenyl)pyridazine. 32 µL (0.24 mmol) of 4-ethynylanisole are dissolved in 2 mL of anhydrous 1,4-dioxane containing 0.20 mmol of 1,2,4,5-tetrazine. The reaction mixture is left refluxing for 24 hours. The crude product is directly used for the next synthesis, estimating a quantitative conversion of the tetrazine.

Synthesis of $[Re_2(\mu\text{-}Cl)_2(CO)_6(\mu\text{-}4\text{-}(4\text{-methoxyphenyl})pyridazine)]$ (3). 1 mL of the solution from the previous reaction (0.10 mmol) is evaporated to dryness and dissolved in 5 mL of freshly distilled toluene. 73 mg (0.2 mmol) of $Re(CO)_5Cl$ are added to the reaction mixture. The reaction is put under reflux for 3 hours, then cooled to RT and dried under vacuum. The crude product is purified through column chromatography (CH_2Cl_2/n-hexane 7:3) affording 59 mg (0.075 mmol) of the desired product (yield 75 %). IR (CH_2Cl_2) ν(CO): 2049 (m), 2033 (s), 1945 (s), 1917 (s) cm^{-1}, ^1H NMR: ($CDCl_3$, 300K, 400 MHz) δ_H (ppm) 9.93 (dd, J = 2.5, 1.0 Hz, 1H, H_3); 9.64 (dd, J = 6.2, 1.0 Hz, 1H, H_6); 8.07 (dd, J = 6.1, 2.4 Hz, 1H, H_5); 7.84 (m, 2H, H_{ortho}); 7.21 (m, 2H, H_{meta}); 3.97 (m, 3H, OMe)

Synthesis of 4-(*p*-tolyl)pyridazine. 70 µL (0.545 mmol) of 4-ethynyl-toluene are dissolved in 4 mL of anhydrous 1,4-dioxane containing 0.242 mmol of 1,2,4,5-tetrazine. The reaction mixture is put under reflux for 48 hours, then cooled to RT and dried under vacuum. The crude product is directly used for the next synthesis, estimating a quantitative conversion of the tetrazine.

Synthesis of $[Re_2(\mu\text{-}Cl)_2(CO)_6(\mu\text{-}4\text{-}(p\text{-tolyl})pyridazine)]$ (4). The solid residue from the previous reaction (0.242 mmol) is dissolved in 5 mL of freshly distilled toluene. 175 mg (0.484 mmol) of $Re(CO)_5Cl$ are added to the reaction mixture. The mixture is put under reflux for 3 hours, then cooled to RT and evaporated to dryness. The crude product is precipitated from CH_2Cl_2/n-hexane, collected and purified through column chromatography (CH_2Cl_2/n-hexane 8:2) affording 111 mg (0.142 mmol) of the desired product (yield 59%). IR (CH_2Cl_2) ν(CO): 2049 (m), 2033 (s), 1946 (s), 1917 (s) cm^{-1}, ^1H NMR: (CD_2Cl_2, 300K, 400

MHz) δ_H (ppm) 9.97 (dd, J = 2.5, 1.0 Hz, 1H, H_3); 9.72 (dd, J = 6.1, 1.0 Hz, 1H, H_6); 8.13 (dd, J = 6.1, 2.5 Hz, 1H, H_5); 7.75 (m, 2H, H_{ortho}); 7.53 (m, 2H, H_{meta}); 2.53 (s, 3H, CH_3)

Synthesis of (4-(pyridazinyl)phenyl)methanol. 70 µL (0.545 mmol) of 4-ethynyl-benzyl alcohol are dissolved in 4 mL of anhydrous 1,4-dioxane containing 0.242 mmol of 1,2,4,5-tetrazine. The reaction mixture is put under reflux for 48 hours, then cooled to RT and dried under vacuum. The crude product is directly used for the next synthesis, estimating a quantitative conversion of the tetrazine.

Synthesis of **$[Re_2(\mu\text{-}Cl)_2(CO)_6(\mu\text{-}4\text{-}(pyridazinyl)phenyl)methanol]$ (5).** The solid residue from the previous reaction (0.242 mmol) is dissolved in 5 mL of freshly distilled toluene. 175 mg (0.484 mmol) of $Re(CO)_5Cl$ are added to the reaction mixture. The mixture is put under reflux for 3 hours, then cooled to RT and evaporated to dryness. The crude product is precipitated from CH_2Cl_2/EtOAc, collected and purified through column chromatography (CH_2Cl_2/EtOAc 8:2) affording 100 mg (0.142 mmol) of the desired product (yield 52%). IR (CH_2Cl_2) ν(CO): 2049 (m), 2033 (s), 1946 (s), 1916 (s) cm^{-1}, ^1H NMR: (CD_2Cl_2, 300K, 400 MHz) δ_H (ppm) 9.98 (dd, J = 2.5, 1.0 Hz, 1H, H_3); 9.75 (dd, J = 6.2, 1.0 Hz, 1H, H_6); 8.16 (dd, J = 6.1, 2.4 Hz, 1H, H_5); 7.84 (m, 2H, H_{ortho}); 7.53 (m, 2H, H_{meta}); 4.88 (m, 2H, CH_2)

References

[1] (a) D. J. Stukfens, A. Vlček Jr., *Coord. Chem. Rev.* **1998**, 177, 127; (b) A. G. Crosby, *Coord. Chem. Rev.* **2001**, 211, 163; (c) A. J. Lees, *Coord. Chem. Rev.* **1998**, 177, 3; (d) M. Wrighton, D. L. Morse, *J. Am. Chem. Soc.* **1974**, *96*, 998

[2] Y.-H. Tseng, D. Bhattacharya, S.-H. Lin, P. Thanasekaran, J.-Y. Wu, L.-W. Lee, M. Sathiyendiran, M.-L. Ho, M.-W. Chung, K.-C. Hsu, P.-T. Chou, K.-L. Lu, *Inorg. Chem.* **2010**, *49*, 6805

[3] D. Donghi, G. D'Alfonso, M. Mauro, M. Panigati, P. Mercandelli, A. Sironi, P. Mussini, L. D'Alfonso, *Inorg. Chem.* **2008**, 47, 4243

[4] E. Quartapelle Procopio, M. Mauro, M. Panigati, D. Donghi, P. Mercandelli, A. Sironi, G. D'Alfonso, L. De Cola, *J. Am. Chem. Soc.* **2010**, *132*, 14397

[5] (a) M. Mauro, E. Quartapelle Procopio, Y. Sun, C. H. Chien, D. Donghi, M. Panigati, P. Mercandelli, P. Mussini, G. D'Alfonso, L. De Cola, *Adv. Funct. Mater.* **2009**, *19*, 2607–2614; (b) M. Mauro, C.-H. Yang, C.-Y. Shin, M. Panigati, C.-H. Chang, G. D'Alfonso, L. De Cola, *Adv. Mater.* **2012**, 24, 2054

[6] (a) E. Ferri, D. Donghi, M. Panigati, G. Prencipe, L. D'Alfonso, I. Zanoni, C. Baldoli, S. Maiorana, G. D'Alfonso, E. Licandro, *Chem. Commun.* **2010**, *46*, 6255; (b) C. Mari, M. Panigati, L. D'Alfonso, I. Zanoni, D. Donghi, L. Sironi, M. Collini, S. Maiorana, C. Baldoli, G. D'Alfonso, E. Licandro, *Organometallics* **2012**, 31 (16), 5918

[7] (a) X. Yi, J. Zhao, W. Wu, D. Huang, S. Ji, J. Sun, *Dalton Trans.* **2012**, 41, 8931; (b) X. Yi, J. Zhao, J. Sun, S. Guo, H. Zhang, *Dalton Trans.* **2013**, 42, 2062; (c) J. E. Yarnell, J. C. Deaton, C. E. McCusker, F. N. Castellano, *Inorg. Chem.* **2011**, 50, 7820

[8] J .Sauer, *Eur. J. Org. Chem.* **1998**, 2885

[9] M. Panigati, M. Mauro, D. Donghi, P. Mercandelli, P. Mussini, L. De Cola G. D'Alfonso, *Coord. Chem. Rev.* **2012**, 256, 1621

[10] (a) R. R. Islangulov, D. V. Kozlov, F. N. Castellano, *Chem. Commun.* **2005**, 3776; (b) G. Bergamini, P. Ceroni, P. Fabbrizi, S. Cicchi, *Chem. Commun.* **2011**, 47, 12780

CHAPTER 5

Hydrido-carbonyl rhenium(I) complexes as photosensitizers for DSSC

Abstract

We investigated the use of some dinuclear rhenium complexes as sensitizers for DSSC. An original synthetic strategy has been set up to prepare the most promising dyes indicated by TD-DFT computations, endowed with good light harvesting moieties. The best DSSC results have been obtained using an hydrido-carboxylate derivative containing an organic dye as carboxylate ligand, with an overall efficiency of 3.5%. Noteworthy, the presence of a hydrido ligand did not show any detrimental effect on the stability of the sensitizers under the operating conditions.

5.1 Introduction

Dye Sensitized Solar Cells (DSSC)[1] are hybrid nanostructured organic/inorganic cells that have attracted huge attention so far within both academy and industry, due to the use of abundant, cheap materials and simple, low cost fabrication processes, that can be applied to both rigid (glass) and flexible (plastics, metals) substrates[2] and easily scaled up.[3]

As already described in chapter 2, a DSSC, in its simplest assembly, is an electrochemical cell with two electrodes with an electrolyte filling in the space between them. The highest efficiency reported for small area DSSC based on ruthenium dye and iodide/triiodide electrolyte is 12.1%[4] with long-term stability,[5] while an efficiency as high as 13% was achieved using a molecularly engineered porphyrin dye in combination with a cobalt-based electrolyte.[6]

The most commonly used dyes in DSSC are complexes of ruthenium containing organic ligands functionalized with carboxylic substituents as anchoring groups to the TiO_2.[7] These poly-pyridine complexes are characterized by intense and broad absorptions due to metal-to-ligand charge transfer (MLCT) transitions, long excited state lifetimes, and long-term chemical stability.[8] Alternative dyes based on different metal complexes such as iron,[9] copper[10] and platinum[11] have been investigated to date, mainly containing bipyridine ligands.[12] On the other hand, the use of rhenium complexes has not been yet exploited in an operating DSSC, and only some preliminary studies concerning the electron transfer from Re-polypyridyl complexes to nanocrystalline TiO_2[13] are reported.

As discussed in chapter 1, a new series of dinuclear rhenium complexes, displaying spectroscopic and photophysical properties strongly dependent on the nature and the position of the diazine substituents, as well as the type of the ancillary ligands, has been recently developed.[14] Furthermore, we recently reported that the strongly emissive metal-to-ligand charge-transfer (^{3}MLCT) state can be efficiently quenched, in a molecular dyad containing {[Re_2(μ-Cl)$_2$(CO)$_6$(μ-pyridazine)]} moiety as the chromophore subunit, via oxidative electron transfer by a fullerene scaffold, covalently linked to the chromophore by a carbocyclic molecular bridge.[15] The charge-separated (CS) species Re^{2+} C_{60}^- is formed from the thermally-equilibrated ^{3}MLCT excited state of the dirhenium subunit by electron transfer to the fullerene acceptor unit, with a time constant of about 110 ps.

Encouraged by our recent results, we report here on the design and the preparation of five dinuclear rhenium complexes and we investigate their potential application as dyes in DSSC. The electrochemical, computational and spectroscopic characterization of all the complexes is also discussed in detail, in order to understand how changes in the molecular structure, in terms of nature of the ancillary ligands, can control the HOMO–LUMO gap, thus resulting in low-band-gap complexes, which are of interest for efficient light harvesting in solar cells. Computational studies showed that complexes containing one hydrido and one benzoate bridging ligands proved the more promising as dyes, with narrower gap and, subsequently, wider absorption in the visible range. Therefore, a new synthetic strategy has been set to obtain new hydrido-carboxylate derivatives, and their electrochemical and spectroscopical properties have been measured and compared with a previously reported

analogue containing two bridging chloride anions (**1**). Solar cells with each complex have been prepared and their performance evaluated, in relation to the molecular structure of the dyes and the nature of the ancillary ligands.

With reference to chart 5.1, together with the use of unfunctionalized benzoate anion (complex **2**) we also considered the 4-diphenylamino-benzoate anion (TPA-COO^- for complex **3**) and the carboxylate anion of **D35**, a commonly used organic dye (complexes **4** and **5**). During 2012 and 2013, the (E)-3-(5-(4-(bis(2′,4′-dibutoxy-[1,1′-biphenyl]-4-yl)amino)phenyl)thiophen-2-yl)-2-cyanoacrylic acid a.k.a. DN-F04 dye (from now on, **D35**, see chart 5.1), has been established worldwide as a reference organic dye for DSSCs; excellent device stability has been obtained both under light and after at least 1000 h storage in darkness at temperatures of 85°C.[16] The interest in organic molecules characterized by a D-π-A electronic structure as dyes in DSSCs has been growing fast over the past decade. It was initiated for reasons such as unlimited feedstock, improved prerequisites for scalability, recycling issues and economy on a large scale. The absorption spectrum of **D35** makes it interesting also for indoor applications due to a good match with fluorescent light and an attractive orange color.

In collaboration with the Laboratory of Photomolecular Science (LSPM) of the École Polytechnique Fédérale de Lausanne (EPFL) we have linked **D35** as bridging ligand to our dinuclear rhenium complexes to extend the light harvesting capacity and to allow their usage also with cobalt-based electrolytes. These new dyads have been characterized by means of spectroscopic and electrochemical techniques, and their solar cell performance was compared with either **D35** and other hydrido-carboxylate complexes.

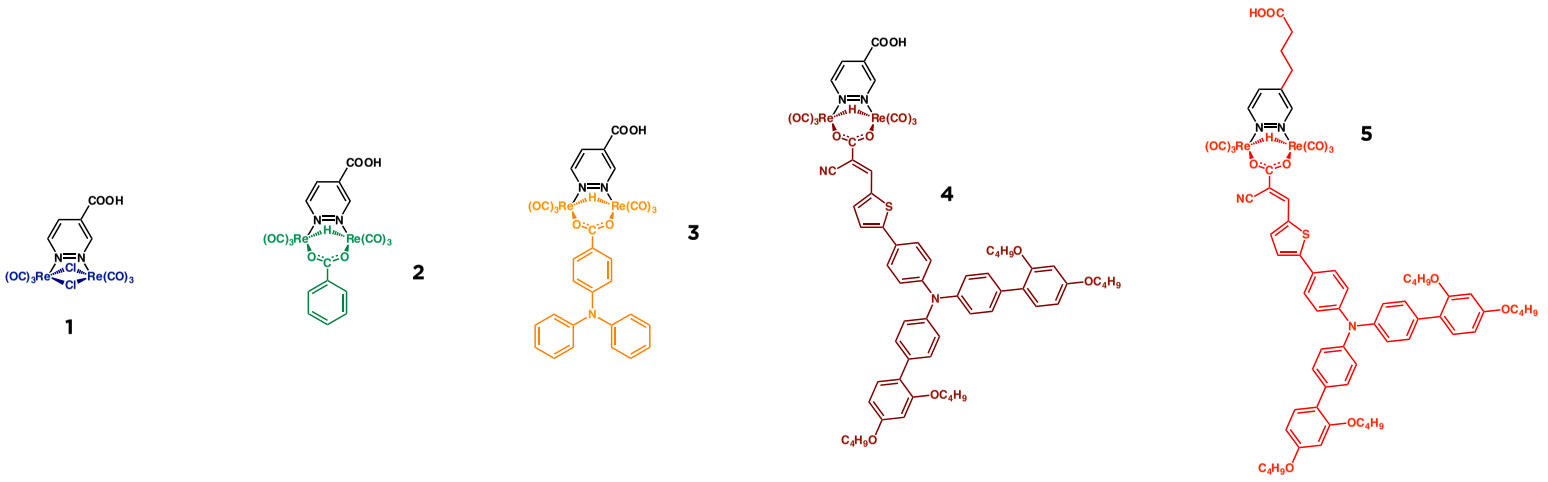

Chart 5.1 Molecular structure of the investigated sensitizers: the reference dichloride complex (**1**), the hydrido-benzoate complex (**2**), the TPA-based hydrido complex (**3**), the D35-based hydrido complexes (**4**-**5**).

5.2 Results and discussion

5.2.1 Computational study

DFT and TD-DFT computations have been previously used to investigate in detail the frontier orbitals and the electronic transitions of many [Re_2(μ-X)(μ-Y)$(CO)_6$(μ-diazine)] complexes.[14] However, none has ever included a carboxylic group on the bridging diazine ligand before. Therefore, the first aim of the present study was to understand the effect of a COOH substituent on the diazine ligand. The β position was chosen since, as previously reported,[17] the presence of substituents in the α position has detrimental effects on the stability of the complex due to the steric hindrance with the equatorial carbonyl ligands. To enlighten the effects of the COOH substituent on the molecular energy levels, we investigated and compared the [Re_2(μ-$Cl)_2(CO)_6$(μ-pydz-4-COOH)] complex (**1**) with the parent [Re_2(μ-$Cl)_2(CO)_6$(μ-pydz)] complex.[17]

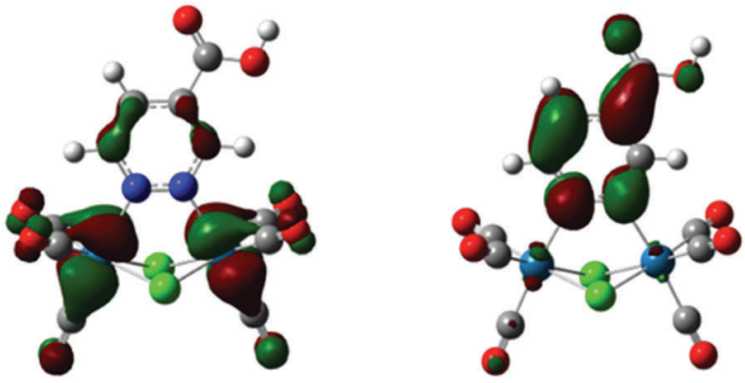

Figure 5.1 Surface plots of some relevant molecular orbitals of complex **1** [Re_2(μ-$Cl)_2(CO)_6$(μ-pydz-4-COOH)]: HOMO+3 (left) and LUMO (right).

In agreement with the results previously reported for analogous complexes,[14,17] DFT calculations on **1** showed that the six HOMOs correspond to the "t_{2g}" set of the two rhenium atoms in a pseudo-octahedral environment (three of them are combination of non-bonding d orbitals and the remaining three are Re-(μ-Cl) π* orbitals), whereas the two lowest unoccupied molecular orbitals are the lowest-lying π* orbitals of the diazine. These orbitals lie at much lower energy than in the parent compound containing unsubstituted pyridazine (0.47 eV), in accordance with the electron-withdrawing nature of the carboxylic group. In agreement with the nature of the frontier orbitals, the HOMO level is poorly affected (0.07 eV). The orbitals involved in the strongest MLCT electronic transition computed for **1** are represented in figure 5.1. This transition is red-shifted compared to the corresponding transition computed for the pyridazine derivative, due to the stabilization of the LUMO. In addition, figure 5.1 clearly shows that the LUMO in **1** is delocalized over the carboxylic substituent, used to anchor the sensitizer to the nanocrystalline TiO_2, possibly allowing a fast charge-injection process into the surface.

We have then investigated the possibility to further shift the absorption band to longer wavelengths, to increase the light harvesting capability of the dye. Taking into account the possibility to tune the energy gap for these species not only by modifying the substituents on the diazine (i.e. shifting the LUMOs) but also changing the nature of the ancillary ligands (i.e. shifting the HOMOs), we have systematically computed the energies of the frontier molecular orbitals and the electronic transition energies for two series of complexes containing different ancillary ligands and an unsubstituted pyridazine: $[Re_2(\mu\text{-}X)(CO)_6(\mu\text{-pydz})]$ and $[Re_2(\mu\text{-}H)(\mu\text{-}X)(CO)_6(\mu\text{-pydz})]$ (X = Cl, OPh, SPh, OOCPh).

Table 5.1 Computed orbital energies (E_{HOMO} and E_{LUMO}), energy gap (ΔE), most intense MLCT excitation energies (λ) and oscillator strengths (*f*, in parentheses) for the compounds **1**–**3** here presented and for a series of related rhenium complexes (each molecule is labeled with its symmetry group)

Compound	E_{HOMO} [eV]	E_{LUMO} [eV]	ΔE [eV]	λ [nm, eV] (f)	Transition[a]
C_s-[$Re_2Cl_2(CO)_6$(pydz-4-COOH)] (**1**)	−6.91	−3.99	2.92	428, 2.90 (0.178)	H−3 → L
C_1-[Re_2H(OOCPh)$(CO)_6$(pydz-4-COOH)] (**2**)	−6.53	−3.78	2.75	526, 2.36 (0.118)	H−1 → L
C_1-[Re_2H(OOC-TPA)$(CO)_6$(pydz-4-COOH)] (**3**)	−5.48	−3.71	1.77	530, 2.34 (0.079)	H−3 → L
				344, 3.60 (0.672)[b]	H → L+2
C_{2v}-[$Re_2Cl_2(CO)_6$(pydz)]	−6.84	−3.52	3.32	385, 3.22 (0.136)	H−3 → L
C_{2v}-[$Re_2(OPh)_2(CO)_6$(pydz)]	−6.31	−3.36	2.95	387, 3.20 (0.130)	H−9 → L
C_2-[$Re_2(SPh)_2(CO)_6$(pydz)]	−6.27	−3.22	3.05	415, 2.98 (0.059)	H−5 → L
C_2-[$Re_2(OOCPh)_2(CO)_6$(pydz)]	−6.50	−3.19	3.32	446, 2.78 (0.091)	H−2 → L
				411, 3.01 (0.090)	H−4 → L
C_s-[$Re_2HCl(CO)_6$(pydz)]	−6.69	−3.45	3.24	406, 3.06 (0.113)	H−3 → L
C_s-[$Re_2H(OPh)(CO)_6$(pydz)]	−6.39	−3.38	3.00	397, 3.12 (0.096)	H−6 → L
C_s-[$Re_2H(SPh)(CO)_6$(pydz)]	−6.27	−3.29	2.97	386, 3.21 (0.128)	H−1 → L+1
C_s-[Re_2H(OOCPh)$(CO)_6$(pydz)]	−6.44	−3.31	3.13	469, 2.64 (0.117)	H−1 → L
TPA-COOH	−5.48	−1.04	4.44	327, 3.79 (0.473)[b]	H → L

[a] A description of the electronic transition in terms of one-electron excitation between the pair of ground-state orbitals mainly involved (H = HOMO, L = LUMO). [b] π–π* transition.

It is important to compute both the energy gap and the strongest MLCT electronic transition energy because in these species the HOMO-LUMO transition is either symmetry forbidden or shows a very low oscillator strength. Therefore, no clear correlation between the energy gap (as measured for instance from electrochemical data) and the maximum of the absorption spectra can be found.[14] Moreover, the t_{2g} set of orbitals of the two rhenium atoms (involved in the MLCT transition) are not necessarily the six HOMOs for these species, since the presence of aromatic moieties in the ancillary ligands (OPh, SPh and OOCPh) determines the intercalation of some p orbitals between them. The data reported show that a more red-shifted absorption can be attained by using the hydrido derivative containing a μ-benzoate bridging ligand.

On account of these considerations, we focused our attention on complex **2**, in which the pyridazine-4-carboxylic acid ligand is combined with one hydrido and one benzoate ligand, and on the analogous derivative containing the 4-diphenylamino-benzoate anion (**3**) and the **D35** carboxylate anion (**4**-**5**), due to the recognized ability of the triarylamine moiety to promote charge separation after UV excitation.[18]

Figure 5.2 shows the electronic density difference maps for the two most intense electronic transitions computed for **3**. In the MLCT transition the electronic transfer from the "Re_2(μ-H)(μ-X)" moiety to the pyridazine ligand (and its carboxylic substituent) is clearly recognizable. Apparently, the diphenylamino substituent is not directly involved in this transition, but it drastically changes the energy of the HOMO (not a rhenium-centered orbital anymore). Its presence gives rise to an additional π–π* transition that can be ascribed to a charge

transfer from the diphenylamino moiety to the benzoate bridging ligand, very similar to the corresponding transition computed for the free ligand, although their energies are quite different as a consequence of their different charge distribution. The same feature is observed for complexes **4** and **5**.

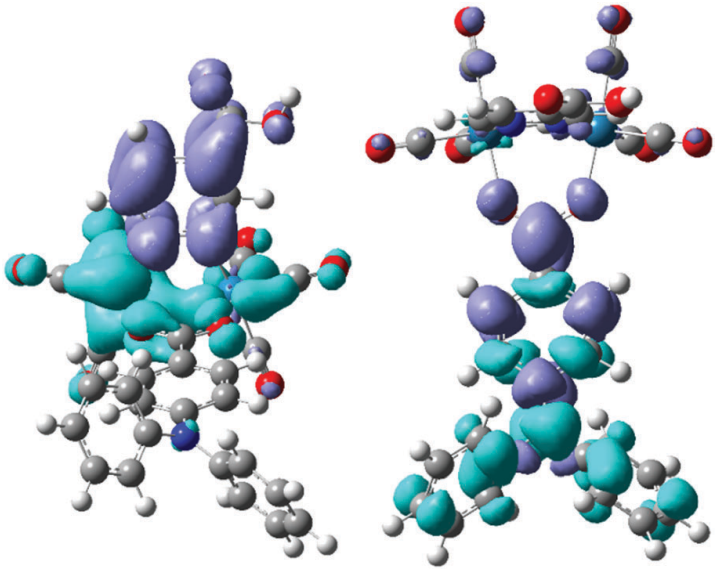

Figure 5.2 Electronic density difference maps for the two most intense electronic transitions computed for the rhenium complex [Re_2H(OOC-TPA)$(CO)_6$(pydz-4-COOH)] (**3**): the MLCT at 530 nm (left) and the π–π^* at 344 nm (right). Light blue indicates a decrease in electron density, blue indicates an increase.

5.2.2 Synthesis of the dyes

The dichloride complex **1** was prepared according to a literature procedure involving a high temperature reaction of $Re(CO)_5Cl$ with 0.5 equivalents of pyridazine-4-carboxylic acid.[19] In order to obtain the new hydrido-carboxylato derivatives a whole new synthetic strategy was designed and carried out successfully. This procedure involves three steps, (shown in scheme 5.1) and is based on the peculiar reactivity of the tetrahedral hydrido-carbonyl cluster $[Re_4(\mu_3\text{-}H)_4(CO)_{12}]$ with bridging donor ligands. Indeed this tetrahedral cluster possesses four electrons less than required by the effective atomic number rule (56 instead of 60 valence electrons, v.e.s),[20] and reacts very easily with any donor species L.[21]

By using pyridazine as donor ligand, the main reaction products are the tetrametallic derivatives $[Re_4(\mu\text{-}H)_4(CO)_{12}(\mu\text{-}pydz)_2]$, with a square geometry of the Re(μ-H)Re skeleton with two pyridazine molecules bridging on the opposite edges of the square, in E or Z position.[22] This reaction also produces the dinuclear unsaturated complex $[Re_2(\mu\text{-}H)_2(CO)_6(\mu\text{-}pydz)]$, which possesses 32 v.e.s, instead of the 34 v.e.s required by the effective atomic number rule.[22] Such dinuclear species is not formed in high yields in this reaction.

In contrast, dinuclear species of this type are the only reaction products using 3,6-disubstitued pyridazine ligands, thus indicating the occurrence of a *[2+2]* fragmentation pathway of the parent tetranuclear cluster without any spectroscopically recognizable intermediate. This is probably due to steric hindrance, which prevents the formation of the square-planar species by destabilizing some key intermediate of the addition reaction. [14]

Analogously, the selective formation of a dinuclear product is observed by reacting $[Re_4(\mu_3\text{-}H)_4(CO)_{12}]$ with 2,5-diphenyl-1,3,4-oxadiazole (ppd), a sterically hindered heterocycle containing two aromatic substituents in the α position of the oxadiazole ring.[23] The labile ppd ligand can be then easily replaced by a diazine molecule, thus providing a general route to $[Re_2(\mu\text{-}H)_2(CO)_6(\mu\text{-diazine})]$ complexes. Therefore, at first the complex $[Re_2(\mu\text{-}H)_2(CO)_6(\mu\text{-ppd})]$ was prepared in high yields by reacting $[Re_4(\mu_3\text{-}H)_4(CO)_{12}]$ with 2 equiv. of ppd at room temperature in CH_2Cl_2 solution.[23] Then the mixed hydrido-carboxylato complexes $[Re_2(\mu\text{-}H)(\mu\text{-}OOCR)(CO)_6(\mu\text{-ppd})]$ (scheme 5.1) were obtained by reaction 5.1, which exploits the reactivity of the hydride ligands towards the acidic protons of carboxylic acids. Through a simple reaction one of the two hydrides is removed as H_2 and the carboxylate anion take its place, bridging the two metal centers.[24] Three different carboxylic acids were used synthesize the complexes and, in particular, benzoic acid for complex **2**, the 4(diphenylamino)benzoic acid (TPA-COOH) for complex **3**, and the carboxylic acid of the **D35** dye for complexes **4** and **5**.

$$[Re_2(\mu - H)_2(CO)_6(ppd)] + RCOOH \rightarrow [Re_2(\mu - H)(\mu - OOCR)(CO)_6(ppd)] + H_2 \uparrow$$

(eq. 5.1)

Finally, substitution of the oxadiazole with functionalized diazine ligands, (namely the pyridazinyl-carboxylic acid for complexes **2**-**4** and the pyridazinyl-4-butanoic acid for complex **5**) afforded the desired products.

Noteworthy, the introduction of the diazine ligand must necessarily be the last step of the synthesis since both the precursors $[Re_4(\mu_3\text{-}H)_4(CO)_{12}]$ and $[Re_2(\mu\text{-}H)_2(CO)_6(\mu\text{-ppd})]$ could thoroughly react with the carboxylic substituent of the diazine ring, thus generating undesired by-products.

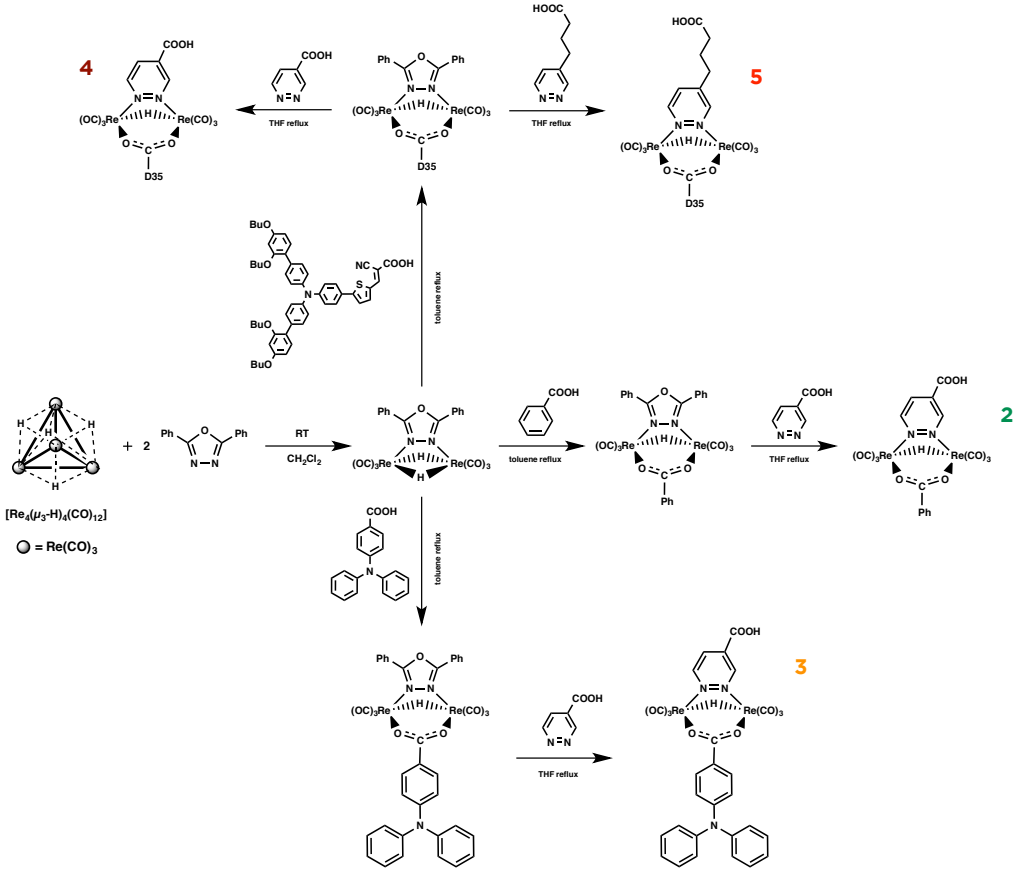

Scheme 5.1 Synthetic pathways to the preparation of rhenium hydrido carboxylate complexes 2, 3, 4 and 5.

5.2.3 Electrochemical characterization

Cyclic voltammetry analysis was performed on all the derivatives **1-COOMe**, **2-COOMe**, **3-COOMe**, **4-COOMe** and **5-COOMe**, containing the methyl ester of the corresponding diazine ligand in order to avoid the reduction of the acidic proton to gaseous H_2. The substitution of the carboxylic acid with the methyl ester derivative could afford a moderate shift of the reduction potentials of complexes **1-COOMe**-**4-COOMe** towards more negative values, due to the lower electron-withdrawing character of the methyl ester compared to the carboxylic group. In complex **5-COOMe**, due to the presence of the insulating aliphatic chain between the diazine ring and the carboxylic group, this shift is not observed and the obtained value of the reduction potential can be translated straight away to the non-methylated counterpart.

The cyclic voltammetry behavior in acetonitrile at 298 K is reported in figure 5.3. The peak potentials, together with the related HOMO and LUMO energy values, are collected in table 5.2. In the cathodic region complexes **1-4** show one monoelectronic reduction peak at about -0.9 V (vs. $Fc^+|Fc$), which is centered on the diazine ligand and whose chemical reversibility is confirmed by the presence of its anodic counterpart. Moreover, the position of this peak is unaffected by the scan rate, in agreement with the electrochemical reversibility of the reductive process. The peak potential is slightly modulated by the different nature of the ancillary ligand.

Comparing these data with analogous complexes of this family containing an unsubstituted pyridazine ligand,[14,17] a shift in the positive direction of the reduction potential can be observed (for instance, the reduction potential is -1.34 V for the parent complex $[Re_2(\mu\text{-}Cl)_2(CO)_6(\mu\text{-pyridazine})]$), consistent with the presence of the

electron-withdrawing substituent on the aromatic ring. On the contrary, the reduction peak for **5** is observed at -1.47 V, i.e. at the same reduction potential of complex $[Re_2(\mu\text{-}Cl)_2(CO)_6(\mu\text{-}4\text{-}n\text{-}hexylpydz)]$ (-1.46 V)[14] containing an electron-rich pyridazine ligand. Also in this case the reduction is chemically and electrochemically reversible.

All these features are in agreement with the localization of the reduction process on the diazine ring, as indicated also by the description of the LUMO provided by the DFT computations, which is stabilized and partially delocalized by the carboxylic group in β position.

In the anodic region significant differences have been observed for the five complexes. **1-COOMe** exhibits an oxidation potential at 1.34 V (vs. $Fc^+|Fc$), which corresponds to a metal-centered bi-electronic oxidation and appears to be irreversible.[14] However, it becomes partially reversible at higher scan rate, as demonstrated by the presence of the return peak.[14] This clearly points to an electrochemically quasi-reversible electron transfer step and a subsequent chemical step. The resulting electrochemical HOMO–LUMO gap was 2.25 eV and the HOMO and the LUMO energy levels of **1** are calculated to 6.14 eV and 3.88 eV, respectively. Interesting differences appear in the anodic behavior of complexes **2-COOMe** - **5-COOMe**. As already observed in the derivatives containing alcoholate or phenolate anions as ancillary ligands,[25] a close sequence of two monoelectronic oxidation peaks is observed, instead of a bi-electronic peak.

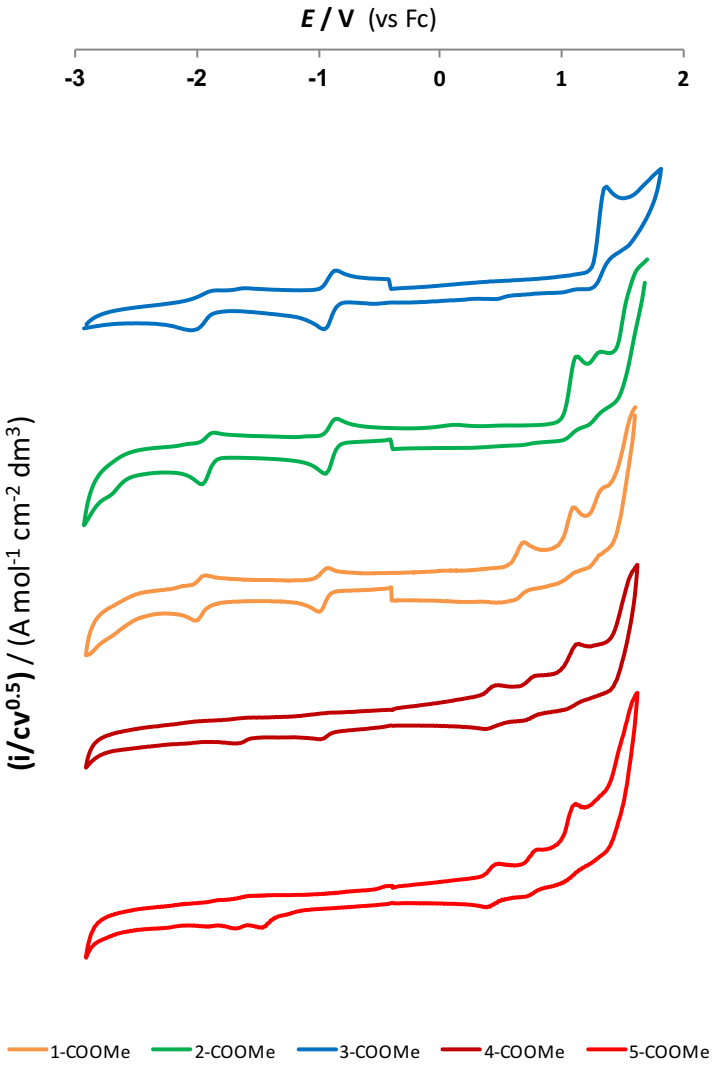

Figure 5.3 Normalized CV features of the methyl-ester derivatives of dyes **1-5** on GC electrodes, in ACN + 0.1 M $TBAPF_6$ solution, at 0.2 V s^{-1} with ohmic drop compensation.

These two oxidation processes are clearly localized on the metal core (as confirmed also by computational analysis)[25] and strongly indicate that the oxidation process is markedly different in the case of the oxygen-bridged derivatives with respect to the dichloride ones, also when only one oxygenated ancillary ligand is present.

This might be related to the closer "Re(μ-X)$_2$Re" scaffold and to the harder nature of the bridging ligands in the case of the derivatives containing oxygen donors. This feature could afford a less efficient stabilization of the cationic products compared to softer anions, such as halides.

The first oxidation peak for **2-COOMe** is observed at +1.11 V (vs. $Fc^+|Fc$), and it appears to be chemically irreversible. It is followed by a second peak at 1.32 V which is reversible in the whole scan rate range explored. This lower oxidation potential indicates a higher HOMO level, in agreement with the DFT calculations, and the resulting electrochemical energy gap is reduced to 2.00 eV.

On the other hand, for complexes **3-COOMe** - **5-COOMe**, beside the two oxidation peaks centered on the metal core (at 1.07 V and at 1.32 V), another chemically reversible oxidation peak at +0.66 V is detected. This peak is clearly attributed to the formation of a radical cation on the triarylamine (TPA) moiety, as indicated by the comparison with the electrochemical behavior of the free 4-diphenylamino-benzoic acid ($E_{p,a}$ = 0.70 V). This confirms the lack of communication between the pyridazine ring and the triarylamine moiety, which is verified also in the UV-Vis absorption data (the same behavior has been observed in the complex containing, as an ancillary ligand, the carboxylate derivative of cyclopentadithiophene).[24]

In spite of the lack of electronic communication, the presence of the TPA moiety affects (even if slightly) the position of the reduction of the pyridazine ring in **3-COOMe** and **4-COOMe** resulting in more negative potential values than **2-COOMe**. The slight destabilization of the LUMO level is also confirmed by computational data.

The introduction of the TPA moiety in **3-5** leads to a strong reduction of the electrochemical energy gap which, however, does not parallel the spectroscopic (absorption) gap. This is consistent with the fact that the electronic absorption arises from a ^{1}MLCT transition which in **3-5** does not involve the HOMO level, centered on the TPA moiety. In contrast, for dyes **1** and **2**, the electrochemical and spectroscopical energy gaps do parallel each other, although the spectroscopical gaps are always higher than the electrochemical, since the electronic transition responsible for the ^{1}MLCT absorption band is not a pure HOMO–LUMO transition.

Table 5.2 First reduction and oxidation peak potentials ($E_{p,c}$ and $E_{p,a}$) and electrochemical (ΔE_e) and spectroscopic (ΔE_S)[a] energy gaps of the complexes. Potentials are referred to the $Fc^+|Fc$ couple[b] in the operating medium (ACN, 0.1 M $TBAPF_6$). Scan rate 0.2 V s^{-1}.

COMPLEX	$E_{p,c}$ [V]	$E_{p,a}$ [V]	ΔE_e [eV]	ΔE_s [eV]	E_{LUMO} [eV]	E_{HOMO} [eV]
1-COOMe	-0.91	1.34	2.26	2.98	-3.88	-6.14
2-COOMe	-0.89	1.11, 1.32	2.01	2.56	-3.90	-5.91
3-COOMe	-0.97	0.66, 1.07, 1.32	1.64	2.56	-3.81	-5.45
4-COOMe	-0.94	0.41, 0.74, 1.10	1.36	2.52	-3.85	-5.21
5-COOMe	-1.42	0.42, 0.75, 1.10	1.84	2.55	-3.37	-5.21

[[a] The spectroscopic (ΔE_S) energy gap is the energy associated with the electronic transition determined from the maximum of the ^{1}MLCT absorption band, [b] $Fc^+|Fc$ potential is 0.385 V vs. SCE in ACN solution]

5.2.4 Photophysical characterization

UV-Vis absorption maxima and molar absorptivities are reported in table 5.3, both in solution and adsorbed on TiO_2. Figure 5.4 shows the spectra in toluene solution, where all the complexes exhibit a broad and featureless absorption band extending in a conspicuous part of the visible spectrum between 350 nm and 600 nm.

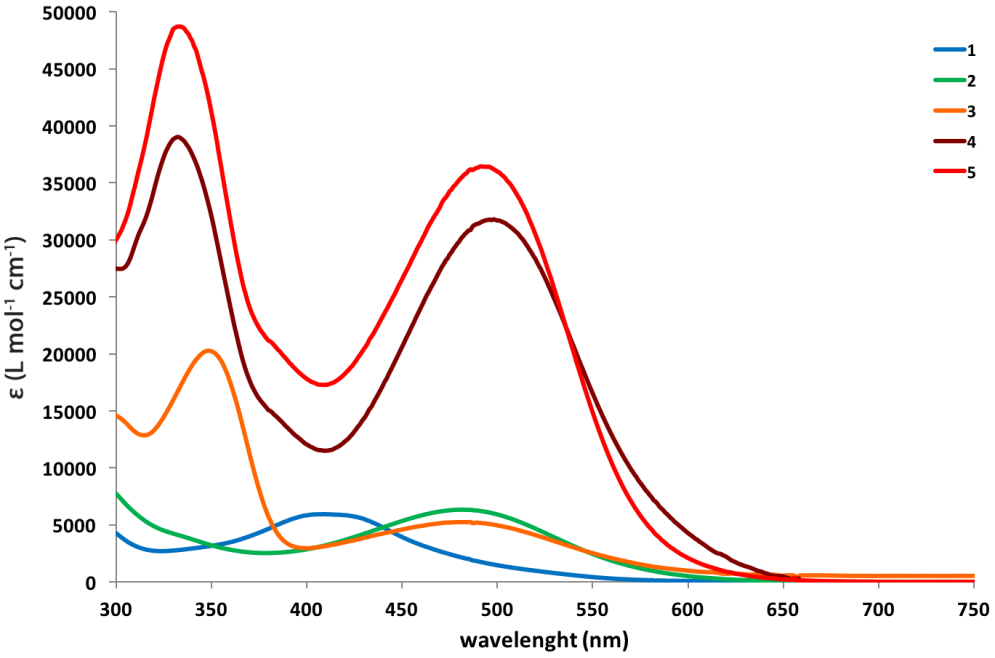

Figure 5.4 UV-Vis absorption spectra of complexes **1**-**5** in toluene solution.

The predicted red-shift of the absorption maximum (see computational study section 5.2.1) for all the hydrido-carboxylate complexes, compared to complex **1**, is observed. Furthermore, a very modest red-shift in the absorption maximum for the **D35**-based complexes **4** and **5**, compared to the bare TPA-based complex **3**, is detected.

This feature indicates that this band is ascribable to the metal-to-ligand $d\pi(Re) \rightarrow \pi^*$(diazine) charge transfer transition (^{1}MLCT), in agreement with DFT computations. This broad MLCT band arises from the convolution of multiple transitions, as testified by the more or less pronounced shoulders observed at longer wavelengths. This assignment is also supported by the weak intensity of these bands and by the observed solvatochromic behavior. Complexes **4** and **5** show an impressive tenfold increase of ε compared to **3**, thus greatly improving the light harvesting. This is due to a partial superposition between the MLCT band and the absorption band of the **D35** ligand, which displays an absorption band at 500 nm in CH_2Cl_2 solution with a high molar extinction coefficient (31,330 M^{-1} cm^{-1}).[26]

Table 5.3 UV-Vis MLCT absorption data of the dyes in solution and on TiO_2 film.

COMPLEX	$\lambda_{max}{}^a$ /nm	ε /M^{-1} cm^{-1}	$\lambda_{max}{}^b$ /nm	$\lambda_{max}{}^c$ /nm
1	416	6,5E+03	375	405
2	487	6,7E+03	430	440
3	483	5.2E+03	425	443
4	493	3.1E+04	486	493
5	486	3.5E+04	487	487

[^{a} toluene solution (2x10^{-5} M), ^{b} EtOH solution (2x10^{-5} M), ^{c} TiO_2 film]

All the complexes containing a triarylamine, namely **3**, **4** and **5**, also display another high energy absorption band at around 335-350 nm, whose position is totally independent from the polarity of the solvent. In agreement with the electrochemical and computational data, this band is attributed to the π-π^* transition involving the triarylamine moiety. Noticeably, in the **D35**–containing complexes **4** and **5** this band is moderately blue-shifted, as due to the presence of electron donor groups on the triarylamine moiety of **D35**.

5.2.5 Devices

Photovoltaic measurements have been carried out to evaluate the potential of the new rhenium complexes as dyes in DSSC devices. Unoptimized solar cells have been realized, in collaboration with the Center for Hybrid and Organic Solar Energy (CHOSE, Polo Solare Organico Regione Lazio, Rome)", to test the actual operating efficiency of complexes **1-3**. The main photovoltaic performance parameters of the solar cells under AM 1.5 G at 1 Sun (1000 W m^2) illumination are presented in table 5.4 and the current–voltage (J–V) curves are reported in figure 5.5.

Two different electrolytes were used, both based on the iodide/triiodide redox couple. The first (HSE, Dyesol) is commercially available, while the second (labeled El14) was developed in-house by reducing the concentration of iodine (and thus, of iodide), which strongly absorbs below 450 nm, and competes with the rhenium complexes absorption. Interestingly, an increase in the photogenerated currents was observed (see the aforementioned figures) for all the rhenium-based dyes when El14 was used instead of HSE. This was also confirmed by the incident photon-to-current conversion efficiency (IPCE) plots for the DSSCs sensitized by **1**, **2** and **3**, in presence of the two different electrolytes (figure 5.6).

The best performing cell, sensitized with complex **3**, gave an overall power conversion efficiency of 1% (with short-circuit photocurrent density J_{SC} = 2.9 mA cm^2, open-circuit photovoltage V_{OC} = 0.51 mV and fill factor FF = 0.70). These values are far from those obtained under similar conditions by cells assembled using the conventional ruthenium **N719** dye.

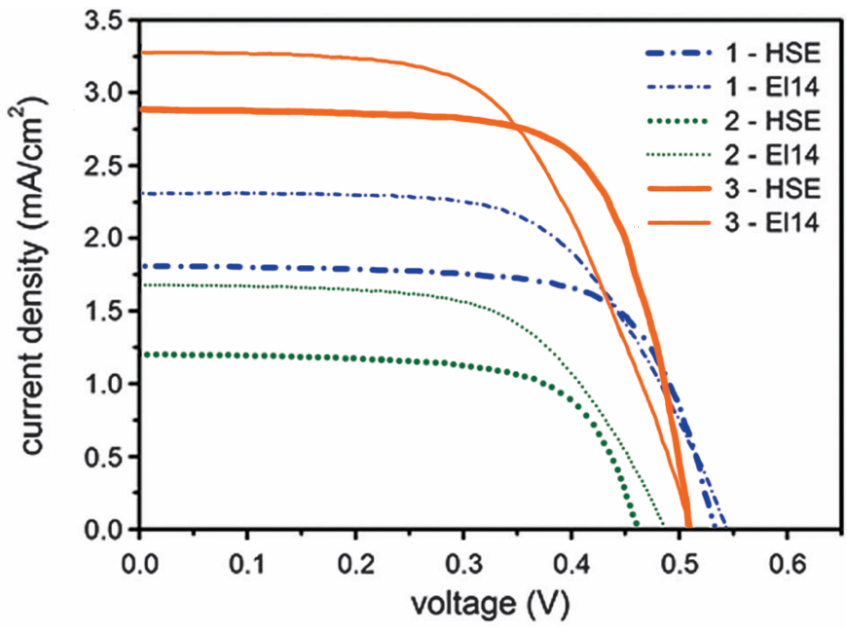

Figure 5.5 Current–voltage curves for unoptimized devices sensitized by rhenium-based dyes **1-3** under 1 Sun illumination, AM 1.5.

These dyes absorb in a very narrow spectral range compared to **N719** and, in addition, below 450 nm they compete with iodide/triiodide-based electrolytes in the absorption of light. However, the maximum of the absorption spectrum is not the only factor which determines the overall characteristics of the cell. In fact, despite the red-shift observed in the absorption spectrum, mainly due to the raise of the HOMO level, complex **2** displays the worst performances. This result is probably due to the particularly low LUMO level (see table 5.2) which, as in the case of complex **1**, hampers the electron injection into the TiO_2 conduction band (3.9 eV).

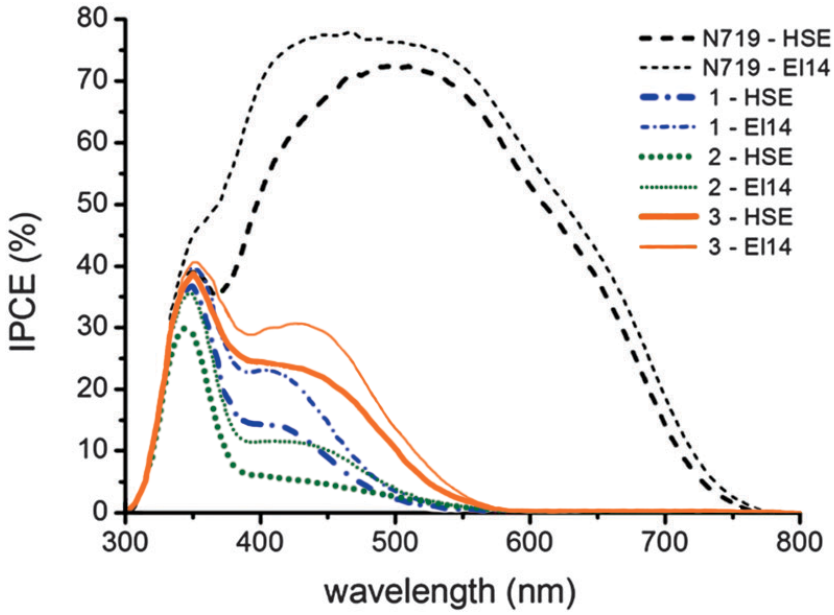

Figure 5.6 IPCE spectra for unoptimized devices sensitized by rhenium-based dyes **1-3** compared with those sensitized by **N719**.

Table 5.4 Photovoltaic parameters for **1-3** compared to **N719** using commercial HSE electrolyte (Dyesol) and homemade EI14 electrolyte.

CELL	J_{SC} (mA/cm^2)	V_{OC} (V)	FF	η (%)
N719 HSE	-13.6	0.735	63.2	6.3
N719 EL-14	-12.0	0.778	31.5	3.0
1 HSE	-1.8	0.534	69.9	0.67
1 EL-14	-2.3	0.545	62.1	0.77
2 HSE	-1.2	0.464	67.9	0.38
2 EL-14	-1.7	0.488	60.7	0.5
3 HSE	-2.9	0.510	70.5	1.0
3 EL-14	-3.3	0.512	57.9	0.97

The replacement of the simple benzoate anion with the carboxylate derivative of the triarylamine has a double role. First, the hole transport unit, now localized on the TPA moiety, is placed far away from TiO_2 and can better interact with the electrolyte. Moreover, the higher steric hindrance of the TPA unit, way bigger than the simple

benzoate anion, reduces the recombination of the electrons with the redox species on the surface of TiO_2. Such insulating effect is in agreement with the slightly higher V_{OC} value obtained for complex **3**. Finally, the LUMO level of the complex was slightly raised, thus allowing easier injection on the TiO_2.

Following these preliminary results, an extensive optimization of the cell components was carried out to obtain the best possible performance from the new rhenium complexes as dyes in DSSC devices, in collaboration with Prof. Anders Hagfeldt and the LSPM group at EPFL, Lausanne. Sets of cells were prepared and measured, changing one parameter at a time, in order to find the best operating conditions for each investigated parameter. Complex **3**, already tested in an unoptimized device, has been also re-tested after the engineering of optimized cells.

In particular, different semiconductor oxides (TiO_2, SnO_2) have been tried (in single or stacked-layer architectures), along with their relative thickness. The dyes have been adsorbed on the semiconductors in different media to find out the best solvent and adsorption time. At the same time, various counter electrode glasses with different sheet resistance have been tested with our complexes. The composition of the electrolytes has been also intensively investigated and the components of both iodine based and cobalt based electrolytes have been varied to obtain the best current-voltage compromise. It should be noted that **D35** works in different conditions compared to most organometallic dyes. For this reason, we have investigated the behavior of each **D35**-based dye, **4** and **5**, in two different types of electrolyte, one based on the iodide/triiodide redox shuttle, the other employing $Co^{2+/3+}$ metal complexes.

Each electrolyte was coupled with a suitable counter-electrode: platinum for iodine, carbon for cobalt. Both electrolytes have been developed in-house: the first (labeled IE) is devoid of any additive other than the redox couple, while the second (labeled CE) contains, in addition to the redox couple, LiTFSI and tert-butyl-pyridine (TBP). We used reference cells with pure **D35** as photosensitizer for this comparison. Unoptimized solid state devices (SSD) have been also prepared to investigate if these complexes may hold potential for this kind of devices, but the generally low efficiencies detected prevented us from further investigations. A careful engineering of the cells had afforded a new maximum performance of 1.8% for complex **3**, nearly doubling the previous value obtained for such dye.

Table 5.5 Photovoltaic parameters for optimized and solid state cells sensitized by **3-5** compared to **D35** using homemade iodine (IE) and cobalt (CE) based electrolytes.

CELL	J_{SC} (mA/cm^2)	V_{OC} (V)	FF	η (%)
3 IE/Platinum (non-optimized cell)	-2.9	0.51	70.5	1.00
3 IE/Platinum	-4.50	0.51	78	1.80
3 CE/Carbon	-1.41	0.47	72	0.47
3 SSD	-0.51	0.52	57	0.15
4 IE/Platinum	-7.88	0.52	51	2.04
4 CE/Carbon	-9.07	0.54	64	3.00
4 SSD	-0.41	0.46	53	0.34
5 IE/Platinum	-8.74	0.54	67	3.15
5 CE/Carbon	-7.56	0.65	71	3.50
5 SSD	-1.06	0.48	63	0.32
D35 CE/Carbon	-11	0.88	72	7

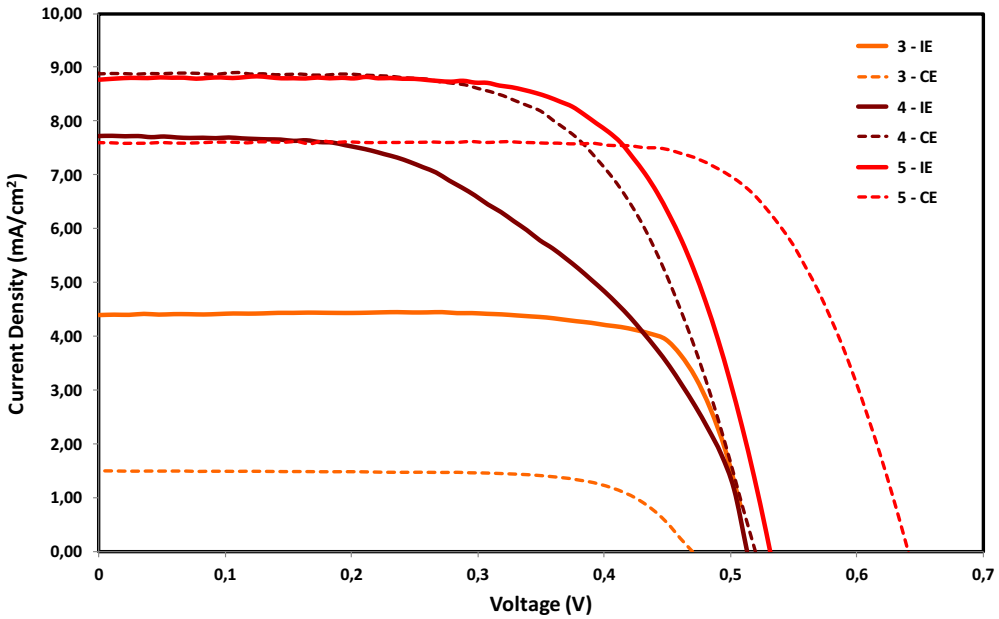

Figure 5.7 Current–voltage curves for optimized devices sensitized by rhenium-based dyes **3**-**5** under 1 Sun illumination, AM 1.5.

A substantial increase in the photogenerated currents can be observed (see table 5.5) for the rhenium-based dyes containing **D35** as light-absorbing moiety and it is confirmed by the incident photon-to-current conversion efficiency (IPCE) plots. The monochromatic IPCE spectra, reported in figure 5.8, show that the highest IPCE is obtained from the solar cell sensitized with **5** that, however, is not as red as **4**. The new complexes **4** and **5**, as expected, showed significant improvement in terms of photocurrent and efficiency (see figure 5.7). Due to the introduction of **D35**, the new dyes appear to work better in CE/C conditions, while complex **3**, with a simple triarylamine, remains more efficient in IE/Pt condition. The open current voltage (V_{OC}) was found similar for all the complexes, mainly ascribable to the presence of Li^+ in the electrolyte, but the current density (J_{SC}) was doubled for complexes **4** and **5**.

Complex **4** performed only slightly better than **3** in IE conditions affording 2% efficiency, despite being affected by the worst fill factor (FF) among all the cells (only 57%), while, under CE conditions a value of 3% in efficiency was recorded. The best performing cells were sensitized with complex **5**, giving an overall power conversion efficiency of 3.15% (IE) and 3.5% (CE). The less electron-withdrawing diazine afforded a gain both in J_{SC} and V_{OC}, leading to a 3.5% efficiency confirming how the replacement of the direct carboxylic moiety with the 4-butanoic acid derivative slightly raises the LUMO level of the complex allowing a better injection to the TiO_2. These values, however, remain well below those obtained under similar conditions by cells assembled using the conventional **D35** dye, reaching 7% (CE).

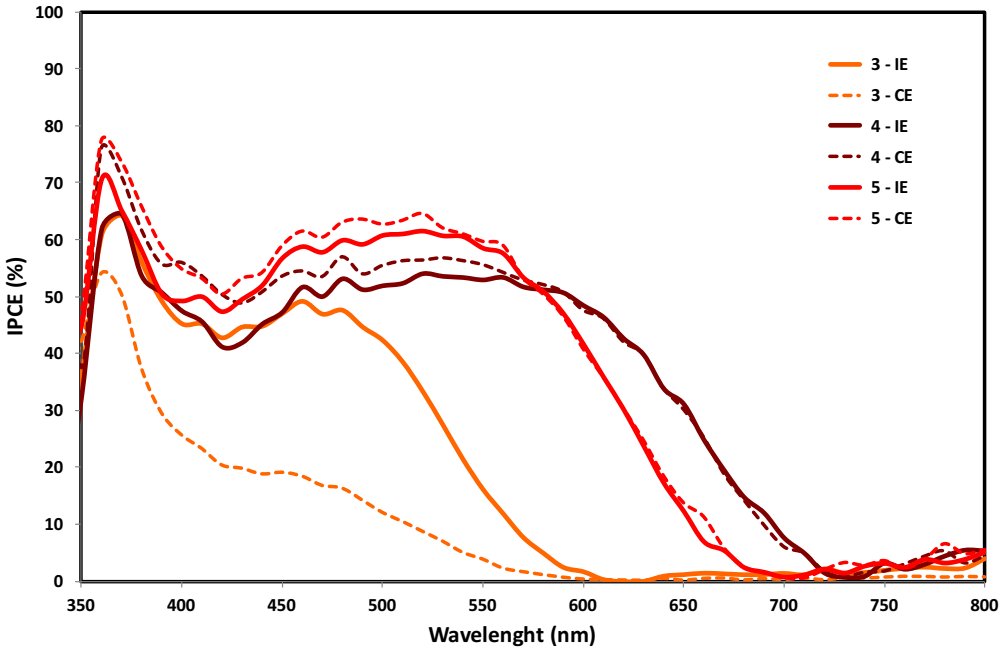

Figure 5.8 IPCE spectra for optimized devices sensitized by rhenium-based dyes **3**-**5**.

Even if these dyes absorb in a larger spectral range compared to **D35**, the maximum of the absorption spectrum is not the only factor which determines the overall characteristics of the cell. Electrochemical impedance spectroscopy (EIS) has been carried out on transparent layer-only version of the cells. From the plots in figure 5.9, reporting the data acquired in IE conditions, it can be seen that the charge transfer resistance, regarded as a measure of the charge collection efficiency, is highest for complex **4**. The expected voltage shift from the conduction band movement due to the massive presence of Li^+ in the electrolyte is significant, once again, only for complex **4**. The electron lifetimes, and the transport efficiency are also best for complex **4**, although the overall efficiency of the cell is lower than that observed for complex **5**. This suggests that the efficiency is also affected by regeneration efficiency and injection efficiency, for which fs/ps measurements are necessary.

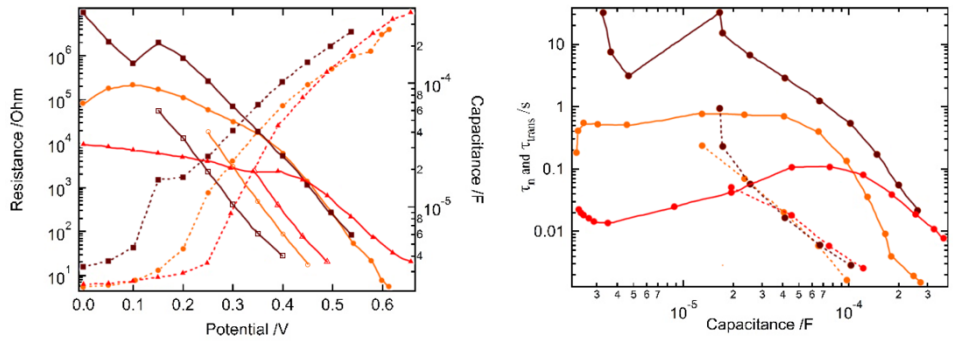

Figure 5.9 Resistance *vs* potential (left) and electron lifetimes *vs* capacitance (right) plots for devices sensitized by complexes **3**-**5** in IE/Pt conditions.

In the case of the cobalt based electrolyte, EIS shows a similar tendency (figure 5.10). The conduction band of **4** is once again the lowest among all the complexes, while **5** owns a slightly higher one compared to **3**, as expected after the introduction of a non-conjugated chain. The lifetimes are, in the case of the cobalt electrolytes, relatively similar between the three different dyes, but also in this case complex **4** shows the longest one.

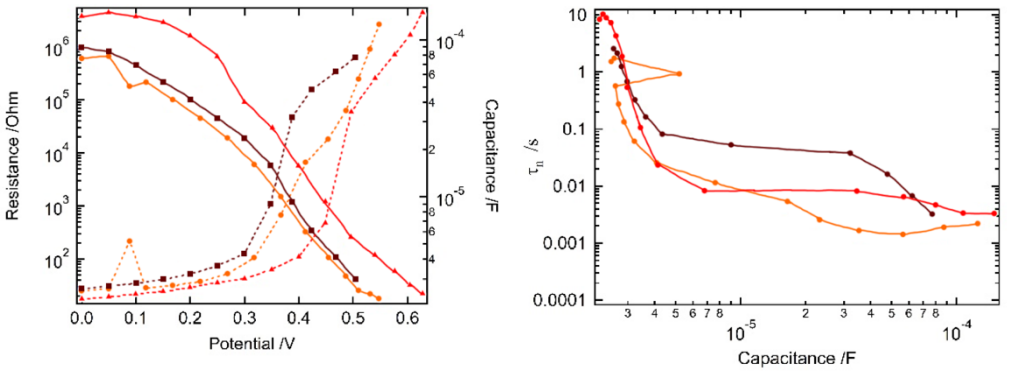

Figure 5.10 Resistance *vs* potential (left) and electron lifetimes *vs* capacitance (right) plots for devices sensitized by complexes **3**-**5** in CE/C conditions.

5.3 Conclusions

Dirhenium complexes designed as potential sensitizers in DSSCs have been prepared, characterized and tested in operating solar cells. Light-to-current conversion has been observed for all the investigated complexes, although with moderate efficiency. The best results have been obtained for the hydrido-carboxylato complex **5**, with maximum power conversion efficiency of about 3.5%. This feature results by combining molecular design with optimization of the cell. In particular, the introduction of the triarylamine-based **D35** as carboxylate ligand further suppresses the recombination of the injected electron with the oxidized state of the complex, thus improving the charge separation on TiO_2. This wider light harvesting and bulkier triarylamine moiety also reduces the back-reaction of the injected electron with the electrolyte. At the same time, the most serious problem concerning the electron injection into TiO_2, certainly represented by the excessive stabilization of the π^* orbitals of the diazine in complexes **1-4**, has been overcome by the use of a more electron-rich diazine ligand, contained in complex **5**, which provides a higher LUMO level. In addition to that, other metal oxide photoelectrodes than TiO_2, such as SnO_2, and different electrolytes, such as those based on cobalt complexes, have been tried in order to optimize the cell performances. This work further confirms the stability of hydrido complexes in the considered media and under the operating conditions of solar cells. Notably, the three-step synthetic procedure here developed has a wider scope than the preparation of the compounds here described and opens the way to a large number of dinuclear complexes of this family, tailored to specific applications.

5.4 Experimental

General methods

All the reactions were performed under a nitrogen atmosphere unless specified otherwise. The reagents were purchased from Aldrich, Fluka and Lancaster and used as received. D35 was purchased by Dyenamo and washed with H_2O then dried under vacuum before use. All the solvents were deoxygenated and dried by standard methods before use, toluene was distilled on Na(s) and CH_2Cl_2 on P_2O_5, both under N_2 atmosphere. Commercial deuterated solvents have been used as received. Column chromatography was performed using Alfa Aesar silica gel 60 (0.032–0.063 mm). $[Re_4(\mu_3\text{-}H)_4(CO)_{12}](C_6H_6)_2$,[27] $[Re_2(\mu\text{-}H)_2(CO)_6(\mu\text{-ppd})]$ (ppd = 2,5-diphenyl-1,3,4-oxadiazole)[23] and $[Re_2(\mu\text{-}Cl)_2(CO)_6(\mu\text{-pydz-4-COOH})]$ (**1**) (pydz-4-COOH = pyridazine-4-carboxylic acid)[19] were synthesized according to literature procedures. IR spectra in solution were acquired on a Bruker Vector 22 FT spectrophotometer. MS spectra were carried out on a Finnigant LCQt Advantage MAX ion trap instrument using methanol as the solvent (ESI-MS). FAB spectra were carried out on a mass spectrometer VG Autospec M246 using nitrobenzyl alcohol as the matrix.

Electrochemical measurements

see chapter 3.

Spectroscopy

see chapter 3.

Synthesis of $[Re_2(\mu\text{-}H)(\mu\text{-}OOCPh)(CO)_6(\mu\text{-}ppd)]$. A sample of benzoic acid (6.4 mg, 0.052 mmol) was added to a solution of $[Re_2(\mu\text{-}H)_2(CO)_6(\mu\text{-}ppd)]$ (40 mg, 0.052 mmol) previously dissolved in 15 mL of anhydrous toluene. The reaction mixture was stirred overnight, and the completeness of the reaction was monitored by IR spectroscopy. Then the solution was evaporated to dryness under vacuum, and the solid was dissolved in CH_2Cl_2. The addition of n-hexane caused the precipitation of the product, which was purified through column chromatography (eluent EtOAc/n-hexane 9:1), then dried under vacuum, yielding 30 mg (0.034 mmol) of white powder (isolated yield 65%). IR (CH_2Cl_2) ν(CO): 2041 (m), 2022 (vs), 1935 (vs), 1914 (s) cm^{-1}, ^1H NMR (CD_2Cl_2, 300K, 400 MHz) δ_H (ppm) 8.15 (d, J =7.3 Hz, 4H, $H_{ortho\ ppd}$), 8.03 (d, J = 7.1 Hz, 2H, $H_{ortho\ benz}$), 7.87 (t, J = 7.6 Hz, 2H, $H_{para\ ppd}$), 7.77 (t, J = 7.8 Hz, 4H, $H_{meta\ ppd}$), 7.51 (t, J = 7.3 Hz, 1H, $H_{para\ benz}$), 7.41 (t, J =7.6 Hz, 2H, $H_{meta\ benz}$), -7.08 (s, 1H, $_{hydride}$). Elemental anal. calcd. for $C_{27}H_{16}N_2O_9Re_2$: C 36.65, H 1.82, N 3.17. Found: C 36.70, H 1.96, N 3.14

Synthesis of $[Re_2(\mu\text{-}H)(\mu\text{-}OOCPh)(CO)_6(\mu\text{-}pydz\text{-}4\text{-}COOH)]$ (2). A sample of $[Re_2(\mu\text{-}H)(\mu\text{-}OOCPh)(CO)_6(\mu\text{-}ppd)]$ (5, 30 mg, 0.034 mmol) dissolved in freshly distilled THF solution (5 mL) was treated with 4-pyridazine-carboxylic acid (6.3 mg, 0.050 mmol). The temperature was set at 333 K for 2 h. The color of the solution became progressively deep red and the progress of the reaction was monitored by IR spectroscopy. Then the solution was evaporated to dryness under vacuum, the crude product dissolved in CH_2Cl_2, the addition of n-hexane affords the precipitation of a red powder. The solution was removed and the remaining powder was washed with n-hexane (5 x 3 mL), then dried under vacuum. The solid was dissolved again in CH_2Cl_2 and the complex was collected as microcrystalline powder after precipitation with n-hexane (13 mg, 0.165 mmol, isolated

yield 56%). IR (CH_2Cl_2) ν(CO): 2039 (m), 2018 (s), 1935 (s), 1918 (s) cm^{-1}, ^1H NMR (d_8-THF, 300K, 400 MHz) δ_H (ppm) 9.75 (m, 1H, $H_{3\ 4\text{-COOH-pydz}}$), 9.51 (d, J = 5.8 Hz, 1H, $H_{6\ 4\text{-COOH-pydz}}$), 8.34 (dd, J = 5.8, 1.9 Hz, 1H, $H_{5\ 4\text{-COOH-pydz}}$), 7.94 (d, J =7.3 Hz, 2H, $H_{ortho\ benz}$), 7.50 (t, J = 7.3 Hz, 1H, $H_{para\ benz}$), 7.38 (t, J =7.9 Hz, 2H, $H_{meta\ benz}$), -6.71 (s, 1H, $_{hydride}$). Elemental anal. calcd. for $C_{18}H_{10}N_2O_{10}Re_2$: C 27.48, H 1.28, N 3.56. Found: C 27.42, H 1.30, N 3.55

Synthesis of 4-(diphenylamino)benzoic acid (TPA-COOH). In a dried flask, a sample of 4-(diphenylamino)benzaldehyde (500 mg, 1.8 mmol) was dissolved in 60 mL of acetone. Separately, 40 mL of aqueous solution of $KMnO_4$ (0.157 M, 3.5 equiv.) was prepared, filtered, and then added dropwise to the solution containing the aldehyde. The reaction mixture was left at room temperature for 72 h, then filtered on a celite pad to remove MnO_2. The filtered solution was collected in an open vessel and left at room temperature until excess $KMnO_4$ decomposes and the solution becomes yellow and cloudy. Then it was filtered again on another celite pad. The yellow solution was treated with 2.5 mL of HCl/H_2O 1:1, a pale yellow precipitate appears, then stirred for 30 minutes in an ice bath, and filtered again. The resulting solution was dried under vacuum affording 270 mg (0.93 mmol) of pure microcrystalline product (isolated yield 50%). ^1H NMR (CD_2Cl_2, 300 K, 400 MHz) δ_H (ppm) 7.91 (d, J =8.9 Hz, 2H, $H_{ortho\ benz}$), 7.35 (t, J = 7.9 Hz, 4H, $H_{ortho\ phenyl}$), 7.17 (m, 6H, $H_{meta\ benz+phenyl}$), 7.01 (d, J = 8.8 Hz, 2H, $H_{para\ phenyl}$)

Synthesis of [Re_2(μ-H)(μ-4-OOC-TPA)$(CO)_6$(μ-ppd)]. A sample of [Re_2(μ-H)$_2(CO)_6$(μ-ppd)] (4.42 mg, 0.055 mmol) was dissolved in freshly distilled toluene (20 mL) and treated with a slight excess of 4-(diphenylamino)benzoic acid (19 mg, 0.066 mmol). The reaction

mixture was refluxed overnight, then the solution was evaporated to dryness under vacuum. The white residue was dissolved in CH_2Cl_2 and precipitated with n-hexane, affording a white powder that was further purified through column chromatography (eluent toluene/EtOAc 9:1), affording the desired product as white powder (32 mg, 0.034 mmol, isolated yield 55%). IR (CH_2Cl_2) ν(CO): 2041 (m), 2022 (vs), 1936 (vs), 1915 (s) cm^{-1}, ^1H NMR (CD_2Cl_2, 300 K, 400 MHz) δ_H (ppm) 8.16 (d, J = 7.4 Hz, 4H, $H_{ortho\ ppd}$), 7.89 (t, J = 7.6 Hz, 2H, $H_{para\ ppd}$), 7.84 (d, J = 8.8 Hz, 2H, $_{TPA}$), 7.77 (t, J = 7.8 Hz, 4H, $H_{meta\ ppd}$), 7.32 (t, J = 7.9 Hz, 4H, $_{TPA}$), 7.14 (m, 6H, $_{TPA}$), 6.95 (d, J = 8.8 Hz, 2H, $_{TPA}$), -7.09 (s, 1H, $_{hydride}$). Elemental anal. calcd. for $C_{39}H_{25}N_3O_9Re_2$: C 44.52, H 2.40, N 3.99. Found: C 44.93, H 2.45, N 3.96

Synthesis of $[Re_2(\mu\text{-}H)(\mu\text{-}4\text{-}OOC\text{-}TPA)(CO)_6(\mu\text{-}pydz\text{-}4\text{-}COOH)]$ (3). A sample of $[Re_2(\mu\text{-}H)(\mu\text{-}4\text{-}OOC\text{-}TPA)(CO)_6(\mu\text{-}ppd)]$ (12 mg, 0.011 mmol) dissolved in freshly distilled THF (5 mL) was treated at room temperature with 4-pyridazine-carboxylic acid (1.7 mg, 0.014 mmol). The solution was refluxed for 3 h. The solution was evaporated to dryness under vacuum and the crude product was dissolved in CH_2Cl_2 and precipitated with n-hexane. The supernatant solution was removed and the remaining powder was washed with n-hexane (5 x 3 mL), then dried under vacuum, affording the desired product (9 mg, 0.009 mmol, isolated yield 83%). IR (CH_2Cl_2) ν(CO): 2038 (m), 2018 (s), 1936 (s), 1917 (s) cm^{-1}, ^1H NMR (d_8-THF, 300 K, 400 MHz) δ_H (ppm) 9.70 (s, 1H, $H_{3\ 4\text{-}COOH\text{-}pydz}$), 9.45 (d, J = 5.8 Hz, 1H, $H_{6\ 4\text{-}COOH\text{-}pydz}$), 8.33 (dd, J = 5.8, 2.0 Hz, 1H, $H_{5\ 4\text{-}COOH\text{-}pydz}$), 7.74 (d, J = 8.8 Hz, 2H, $_{TPA}$), 7.31 (m, 4H, $_{TPA}$), 7.12 (m, 6H, $_{TPA}$), 6.91 (d, J = 8.9 Hz, 2H, $_{TPA}$), -6.70 (s, 1H, $_{hydride}$). FAB-MS: m/z 955, elemental anal. calcd. for $C_{30}H_{19}N_3O_{10}Re_2$: C 37.77, H 2.01, N 4.41. Found: C 37.56, H 2.01, N 4.37

Synthesis of methyl ester of pydz-4-COOH/pydz-4-BuCOOH and complexes (1-5)-COOMe. A sample of pyridazine-4-carboxylic acid (100 mg, 0.805 mmol) (for **1-4**) or pyridazine-4-butanoic acid (134 mg, 0.805 mmol) for **5**) was dissolved in MeOH (2 mL) and was treated with H_2SO_4 (40 mL, 96% w/w) at room temperature. The reaction mixture was heated at reflux temperature and was stirred overnight. Then, the solution was cooled at room temperature and the reaction was quenched by the addition of saturated solution of Na_2CO_3 until pH 8. The product was extracted with Et_2O and the organic fractions were collected, washed with brine, dried with Na_2SO_4 and evaporated to dryness to leave a pale yellow solid (isolated yield 30%). ^{1}H NMR (d_6-DMSO, 300 K, 400 MHz) $\delta_{H\ pydz\text{-}4\text{-}COOMe}$ (ppm) 9.58 (s, 1H, H_{ortho}), 9.51 (d, J = 5.2 Hz, 1H, H_{ortho}), 8.09 (dd, J = 5.2, 2.2 Hz, 1H, H_{meta}), 3.94 (s, 3H, CH_3); $\delta_{H\ pydz\text{-}4\text{-}COOMe}$ (ppm) 9.50 (d, J = 4.7 Hz, 1H, H_{ortho}), 9.41 (s, 1H, H_{ortho}), 8.21 (d, J = 3.8 Hz, 1H, H_{meta}), 3.74 (s, 3H, CH_3), 3.07 (m, 2H, CH_2), 2.49 (m, 4H, CH_2), 2.13 (m, 2H, CH_2). These pyridazines were used to synthesize the corresponding derivatives **1-COOMe**, **2-COOMe**, **3-COOMe**, **4-COOMe** and **5-COOMe** according to the previous procedures.

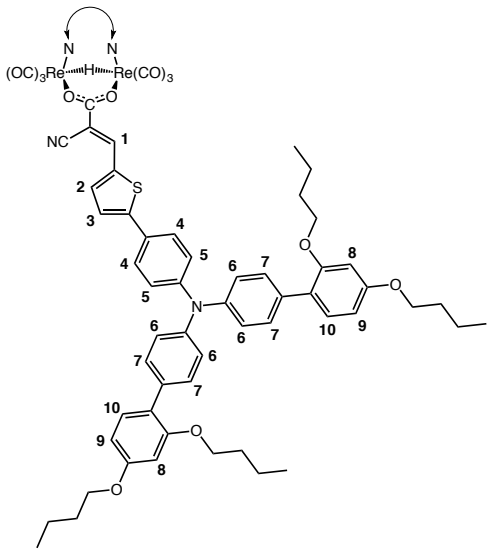

Synthesis of $[Re_2(\mu\text{-}H)(\mu\text{-}D35)(CO)_6(\mu\text{-}ppd)]$. 40 mg (0.046 mmol) of solid D35 are added to a solution of 32 mg (0.042 mmol) of $[Re_2(\mu\text{-}H)_2(CO)_6(\mu\text{-}ppd)]$ previously dissolved in 5 mL of anhydrous toluene. The reaction mixture is left stirring under reflux overnight, then the solution evaporated to dryness under vacuum. The solid obtained is purified through column chromatography (eluent CH_2Cl_2/n-hexane 75:25), then dried under vacuum, yielding 30 mg (0.018 mmol) of brick-red powder (yield 44%). IR (CH_2Cl_2) ν(CO): 2042 (s), 2024 (vs), 1937 (vs), 1917 (s) cm^{-1}, ^1H NMR: (CD_2Cl_2, 300K, 400 MHz) δ_H (ppm) 8.18 (d, J = 7.5 Hz, 4H, $H_{ortho\ ppd}$), 7.90 (m, 2H, $H_{para\ ppd}$), 7.79 (m, 4H, $H_{meta\ ppd}$), 8.16 (s, 1H, H_1), 7.75 (d, J =4.2 Hz, 1H, H_2), 7.60 (d, J = 8.88 Hz, 2H, H_5), 7.52 (d, J = 8.47 Hz, 4H, H_6), 7.37 (d, J = 4.2 Hz, 2H, H_3), 7.29 (d, J = 9.3 Hz, 2H, H_{10}), 7.21 (d, J = 8.47 Hz, 4H, H_7), 7.17 (d, J = 8.88 Hz, 2H, $_{H4}$), 6.59 (s, 2H, H_8), 6.58 (m, 2H, H_9), 4.02 (t, J = 6.98 Hz, 4H, CH_2), 4.01 (t, J = 6.98 Hz, 4H, CH_2), 1.79 (m, 8H, CH_2) 1.57 (m, 4H, CH_2), 1.50 (m, 4H, CH_2), 1.03 (m, 6H, CH_3), 0.97 (m, 6H, CH_3), -7.14 (s, 1H, $_{hydride}$)

Synthesis of $[Re_2(\mu\text{-}H)(\mu\text{-}D35)(CO)_6(\mu\text{-}pydz\text{-}4\text{-}COOH)]$ (4). 15 mg (0.009 mmol) of $[Re_2(\mu\text{-}H)(\mu\text{-}D35)(CO)_6(\mu\text{-}ppd)]$ are dissolved in 5 mL of freshly distilled and degassed THF, 1.5 mg (0.01 mmol) of 4-pyridazine-carboxylic acid are added to the reaction mixture. The reaction is set at 85°C for 2 hours. The solution is evaporated to dryness under vacuum, the crude product dissolved in CH_2Cl_2 and re-precipitated with n-hexane. The supernatant solution is removed and the remaining powder is washed with hexane (5 x 3 mL), then dried under vacuum affording 11 mg (0.072 mmol) of the desired product (yield 80%). IR (CH_2Cl_2) ν(CO): 2040 (m), 2020 (s), 1938 (s), 1920 (m) cm^{-1}, ^1H NMR: (CD_2Cl_2, 300K, 400 MHz) δ_H (ppm) 9.75 (s, 1H, $H_{3\ 4\text{-}COOH\text{-}pydz}$), 9.51 (d, J = 5.6 Hz, 1H, $H_{6\ 4\text{-}COOH\text{-}pydz}$), 8.39 (dd, J = 4.7, 2.9 Hz, 1H, H_5

$_{4\text{-COOH-pydz}}$), 8.13 (s, 1H, H_1), 7.73 (m, 1H, H_2), 7.62 (m, 2H, H_5), 7.51 (m, 4H, H_6), 7.36 (m, 2H, H_3), 7.27 (m, 2H, H_{10}), 7.22 (m, 4H, H_7), 7.18 (m, 2H, H_4), 6.59 (s, 2H, H_8), 6.57 (m, 2H, H_9), 4.02 (t, J = 6.98 Hz, 4H, CH_2), 4.01 (t, J = 6.98 Hz, 4H, CH_2), 1.79 (m, 8H, CH_2) 1.53 (m, 4H, CH_2), 1.49 (m, 4H, CH_2), 1.03 (t, J = 7.4 Hz, 6H, CH_3), 0.97 (t, J = 7.4 Hz, 6H, CH_3), -6.75 (s, 1H, $_{\text{hydride}}$)

Synthesis of [Re_2(μ-H)(μ-D35)(CO)$_6$(μ-4-pyridazinyl-butanoic acid)] (5). 15 mg (0.009 mmol) of [Re_2(μ-H)(μ-D35)(CO)$_6$(μ-ppd)] are dissolved in 5 mL of freshly distilled and degassed THF, 2 mg (0.012 mmol) of 4-pyridazinyl-butanoic acid are added to the reaction mixture. The reaction is put under reflux for 2 hours. The solution is evaporated to dryness under vacuum, the crude product dissolved in CH_2Cl_2, and re-precipitated with n-hexane. The supernatant solution is removed and the remaining powder is washed with hexane (5 x 3 mL) five times, then dried under vacuum affording 11 mg (0.007 mmol) of red powder (yield 78%). IR (CH_2Cl_2) ν(CO): 2042 (m), 2024 (s), 1943 (s), 1921 (m) cm^{-1}, ^{1}H NMR: (CD_2Cl_2, 300K, 400 MHz) δ_H (ppm) 9.22 (d, J = 5.9 Hz, 2H, $H_{6\ 4\text{-BuCOOH-pydz}}$), 9.21 (d, J = 5.9 Hz, 2H, $H_{3\ 4\text{-BuCOOH-pydz}}$), 8.12 (s, 1H, H_1), 7.78 (d, J = 2.0 Hz, 1H, $H_{5\ 4\text{-BuCOOH-pydz}}$), 7.74 (d, J =4.1 Hz, 1H, H_2), 7.60 (d, J = 8.88 Hz, 2H, H_5), 7.52 (d, J = 8.6 Hz, 4H, H_6), 7.36 (d, J = 4.1 Hz, 2H, H_3), 7.28 (m, 2H, H_{10}), 7.21 (d, J = 8.8 Hz, 4H, H_7), 7.17 (d, J = 7.4 Hz, 2H, H_4), 6.59 (s, 2H, H_8), 6.58 (d, J = 6.8 Hz, 2H, H_9), 4.02 (t, J = 6.98 Hz, 4H, CH_2), 4.01 (t, J = 6.98 Hz, 4H, CH_2), 1.79 (m, 8H, CH_2) 1.56 (m, 4H, CH_2), 1.47 (m, 4H, CH_2), 1.03 (m, 6H, CH_3), 0.97 (m, 6H, CH_3), -6.65 (s, 1H, $_{\text{hydride}}$)

Computational details

Ground state geometries were optimized by means of density functional calculations. The parameter-free hybrid functional PBE0[28-29] was employed along with the standard valence double-z polarized basis set 6-31G (d,p) for C, H, Cl, N, O and S. For Re, the Stuttgart–Dresden effective core potentials were employed along with the corresponding valence triple-z basis set. Preliminary calculations were done without imposing any symmetry. The nature of all the stationary points was checked by computing vibrational frequencies and all the geometries were found to be true minima. In order to simulate the absorption electronic spectrum down to 300 nm the lowest 20 singlet excitation energies were computed by means of time-dependent density functional calculations. Calculations were also done in the presence of solvent (toluene, used in the photophysical characterizations) described by the conductor-like polarizable continuum model (CPCM). All the calculations were done with Gaussian 09.[30]

DSSC and SSD preparation

see chapter 2.

DSSC and SSD characterization

see chapter 2.

References

[1] B. O'Regan, M. Grätzel, *Nature* **1991**, 353, 737

[2] T. M. Brown, *Jour. Mater. Chem. A*, **2014**, 28

[3] A. Fakharuddin, R. Jose, T. M. Brown, F. Fabregat-Santiago, J. Bisquert, *Energy & Environmental Science* **2014**, 7, 3952

[4] M. Nazeeruddin, F. De Angelis, S. Fantacci, A. Selloni, G. Viscardi, P. Liska, S. Ito, B. Takeru, M. Grätzel, *J. Am. Chem. Soc*. **2005** 127, 16835

[5] D. Kuang, S. Ito, B. Wenger, C. Klein, J. Moser, R. Humphry-Baker, S. Zakeeruddin, M. Grätzel, J. Am. Chem. Soc. **2006**, 128, 4146

[6] S. Mathew et al. *Nature chemistry* **2014**, 6.3, 242

[7] (a) M. Nazeeruddin, A. Kay, I. Rodicio, R. Humphry-Baker, E. Müller, P. Liska, N. Vlachopoulos, M. Grätzel, J. Am. Chem. Soc. **1993**, 115, 6382; (b) K. Kalyanasundaram, M. Grätzel, *Coord. Chem. Rev*. **1998**, *177*, 347

[8] S. Campagna, F. Puntoriero, F. Nastasi, G. Bergamini, V. Balzani, *Top Curr. Chem.* **2007**, 280, 117

[9] (a) S. Ferrere and B. A. Gregg, J. Am. Chem. Soc. **1998**, 120, 843-844; (b) P. Balraju, M. Kumar, M. S. Roy and G. D. Sharma, *Synth. Met*. **2009**, 159, 1325

[10] T. Bessho, E. C. Constable, M. Grätzel, A. H. Redondo, C. E. Housecroft, W. Kylberg, M. K. Nazeeruddin, M. Neuburger and S. Schaffner, *Chem. Commun.* **2008**, 3717; (b) C. L. Linfoot, P. Richardson, T. E. Hewat, O. Moudam, M. M. Forde, A. Collins, F. White and N. Robertson, *Dalton Trans*. **2010**, 39, 8945

[11] (a) W. Wu, X. Xu, H. Yang, J. Hua, X. Zhang, L. Zhang, Y. Longa, H. Tian *J. Mater. Chem.* **2011**, 21, 10666; (b) E. A. M. Geary, L. J. Yellowlees, L. A. Jack, I. D. H. Oswald, S. Parsons, N. Hirata, J. R. Durrant and N. Robertson, *Inorg. Chem*. **2005**, 44, 242

[12] B. Bozic-Weber, E. C. Constable, C. E. Housecroft, *Coord. Chem. Rev.* **2013**, 257, 3089

[13] (a) J. B. Asbury, E. Hao, Y. Wang, T. Lian, *J. Phys. Chem. B* **2000**, 104, 11957; (b) N. A. Anderson, X. Ai, D. Chen, D. L. Mohler, T. Lian, *J. Phys. Chem. B* **2003**, 107, 14231

[14] M. Panigati, M. Mauro, D. Donghi, P. Mercandelli, P. Mussini, L. De Cola, G. D'Alfonso, *Coord. Chem. Rev.* **2012**, 256, 1621

[15] F. Nastasi, F. Puntoriero, M. Natali, M. Mba, M. Maggini, P. Mussini, M. Panigati, S. Campagna, *Photochem. Photobiol. Sci.* **2015**, *14*, 909

[16] S. M. Feldt, E. A. Gibson, E. Gabrielsson, L. Sun, G. Boschloo, A. Hagfeldt, *J. Am. Chem. Soc.* **2010**, 132 (46), 16714

[17] D. Donghi, G. D'Alfonso, M. Mauro, M. Panigati, P. Mercandelli, A. Sironi, P. Mussini, L. D'Alfonso, *Inorg. Chem.* **2008**, *47*, 4243

[18] B.-G. Kim, K. Chung and J. Kim, *Chem. – Eur. J.* **2013**, 19, 5220

[19] E. Ferri, D. Donghi, M. Panigati, G. Prencipe, L. D'Alfonso, I. Zanoni, C. Baldoli, S. Maiorana, G. D'Alfonso and E. Licandro, *Chem. Commun.* **2010**, 46, 6255

[20] (a) R. Saillant, G. Barcelo and H. Kaesz, *J. Am. Chem. Soc.* **1970**, 92, 5739; (b) N. Masciocchi, G. D'Alfonso, W. Kockelmann, W. Schäfer and A. Sironi, *Chem. Commun.* **1997**, 1903

[21] (a) T. Beringhelli and G. D'Alfonso, *J. Chem. Soc., Chem. Commun.* **1994**, 2631; (b) T. Beringhelli, G. D'Alfonso and M. Zarini, *J. Chem. Soc., Dalton Trans.* **1995**, 2407; (c) T. Beringhelli, G. D'Alfonso and M. G. Garavaglia, *J. Chem. Soc., Dalton Trans.* **1996**, 1771

[22] M. Panigati, D. Donghi, G. D'Alfonso, P. Mercandelli, A. Sironi, L. D'Alfonso, *Inorg. Chem.* **2006**, *45*, 10909

[23] M. Mauro, M. Panigati, D. Donghi, P. Mercandelli, P. Mussini, A. Sironi, G. D'Alfonso, *Inorg. Chem.* **2008**, *47*, 11154

[24] E. Quartapelle Procopio, V. Bonometti, M. Panigati, P. Mercandelli, P. Mussini, T. Benincori, G. D'Alfonso and F. Sannicolò, *Inorg. Chem.* **2014**, 53, 11242

[25] A. Raimondi, M. Panigati, D. Maggioni, L. D'Alfonso, P. Mercandelli, P. Mussini, G. D'Alfonso, *Inorg. Chem.* **2012**, *51*, 2966

[26] X. Jiang, K. M. Karlsson, E. Gabrielsson, E. M. J. Johansson, M. Quintana, M. Karlsson, L. Sun, G. Boschloo, A. Hagfeldt, *Adv. Funct. Mater.* **2011**, 21, 2944

[27] (a) M. A. Andrews, S. W. Kirtley and H. D. Kaesz, *Inorg. Chem.*, **1977**, 16, 1556; (b) J. R. Johnson and H. D. Kaesz, *Inorg. Synth.* **1978**, 18, 60

[28] C. Adamo and V. Barone, *J. Chem. Phys.* **1999**, 110, 6158

[29] J. P. Perdew, K. Burke and M. Ernzerhof, *Phys. Rev. Lett.* **1997**, 78, 1396

[30] Gaussian 09 (revision D.01), Gaussian Inc., Wallingford, CT, **2013**

CHAPTER 6

Low-band gap rhenium(I) based metal-copolymers for organic photovoltaics

Abstract

Low-band gap copolymers containing bis-diimine aromatic ligands (1,2-diazine) as new electron-withdrawing monomers have been here designed and synthesized. The corresponding metal-copolymers, containing dinuclear rhenium complexes, have been also prepared. Spectroscopic and electrochemical characterization of the both monomers and the polymers have been performed along with NMR and MALDI-TOF characterization, that revealed different enchainment between comonomers in polymeric backbone depending on the nature of electron-withdrawing unit.

6.1 Introduction

As already discussed in chapter 2, organic photovoltaics hold the promise for a cost-effective, lightweight solar energy conversion platform benefiting from simple solution processing. Over recent years organic solar cells have been perfected at the laboratory level with a record PCE of 11.0%[1] for polymer solution processed devices and a large area module PCE of 5.5%[2] which may, in the near future, challenge amorphous Si PV technology.

In this framework, in collaboration with Dr. Silvia Destri at the CNR ISMAC research institute, we have developed donor low-band gap copolymers by combining carbazole with different electron-poor units. Our main effort inside this project was devoted towards the development of low-band gap metal-copolymers containing nitrogen aromatic ligands (1,2-diazine) to exploit metal coordination for lowering the LUMO level and increase absorption in the visible region (see chart 6.1). Metal coordination is also expected to enhance photo-induced charge separation, charge mobility and thermal stability. Characterization of the materials from a molecular point of view (NMR, SEC, MALDI-TOF) has been performed, together with optical characterization (UV-Vis, photoluminescence) both in solution and as spin coated films. Cyclic voltammetric analysis of the monomers has been also performed. The fabrication of simple OPV devices for a preliminary optoelectronic characterization (J-V curves) of the synthesized materials is currently in progress in collaboration with Prof. Thomas Brown at the Center for Hybrid and Organic Solar Energy (CHOSE) in Rome.

6.2 Results and discussion

6.2.1 Synthesis of the monomeric units

Three electron-poor monomers have been chosen as co-monomers, in the polymerization reaction,[3] all constituted by electron-deficient dibromoheteroarenes. The molecular structures are depicted in chart 6.1 and, besides **M1** which is commercially available, **M2** and **M3** were synthesized via pericyclic reaction of a brominated precursor of dibenzyliden-hydrazine or of 1,2-bis(thiophen-3-ylmethylene)hydrazine respectively (see schemes 6.1 and 6.2).

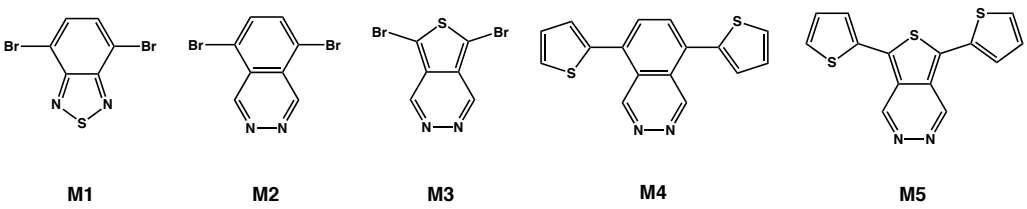

Chart 6.1 Structures of the electron-poor monomeric units employed.

Since the overall isolated yield of the pericyclic reaction for the synthesis of the 5,7-dibromothieno[3,4-d]pyridazine (**M3**) is quite low, different synthetic pathways, involving the bromination reaction of the thieno[3,4-d]pyridazine, have been investigated. However, unfortunately, treatment of the thieno[3,4-d]pyridazine with either Br_2 or NBS, to yield direct bromination was unsuccessful. Due to the low selectivity of this reaction, the main products results showed functionalization at different positions on both the thiophene and the diazine ring (see scheme 6.3).

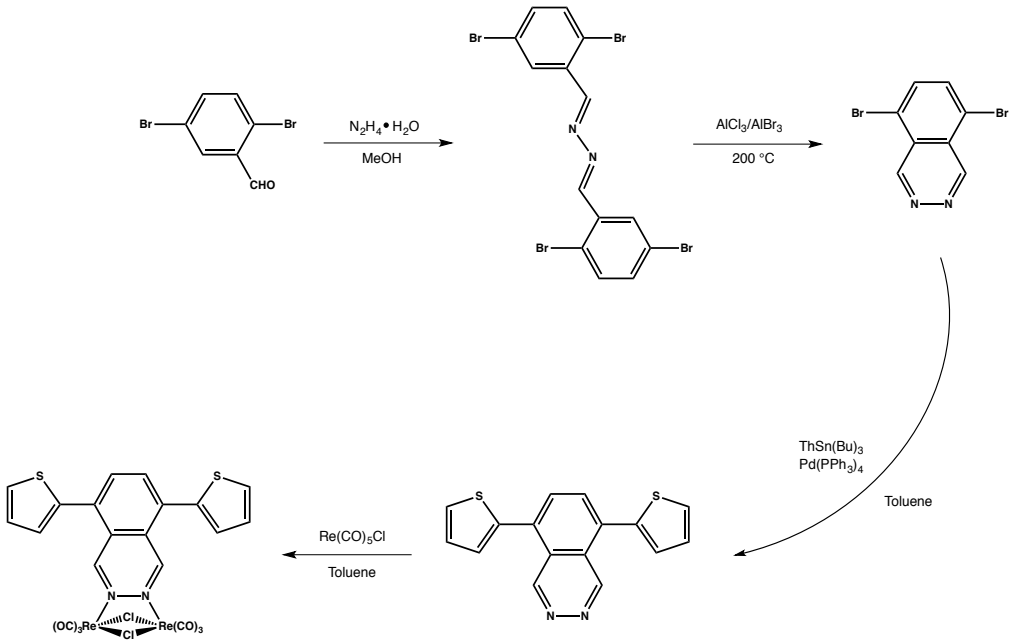

Scheme 6.1 Synthetic pathway to monomeric units M2, M4 and complex C4.

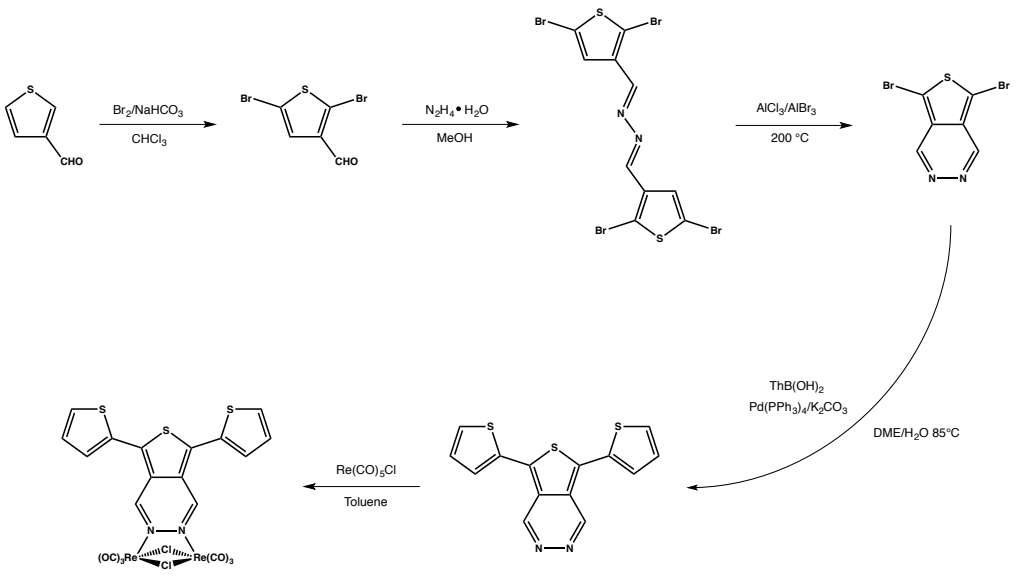

Scheme 6.2 Synthetic pathway to monomeric units M3, M5 and complex C5.

The bromination reaction was also performed on the corresponding dinuclear rhenium complex. It was expected that the increased steric hindrance around the *ortho* position of the diazine ring provided by the carbonyl ligands could prevent the formation of the side products. However, also in this case the desired brominated complex was not obtained, resulting in the complete decomposition of the compound.

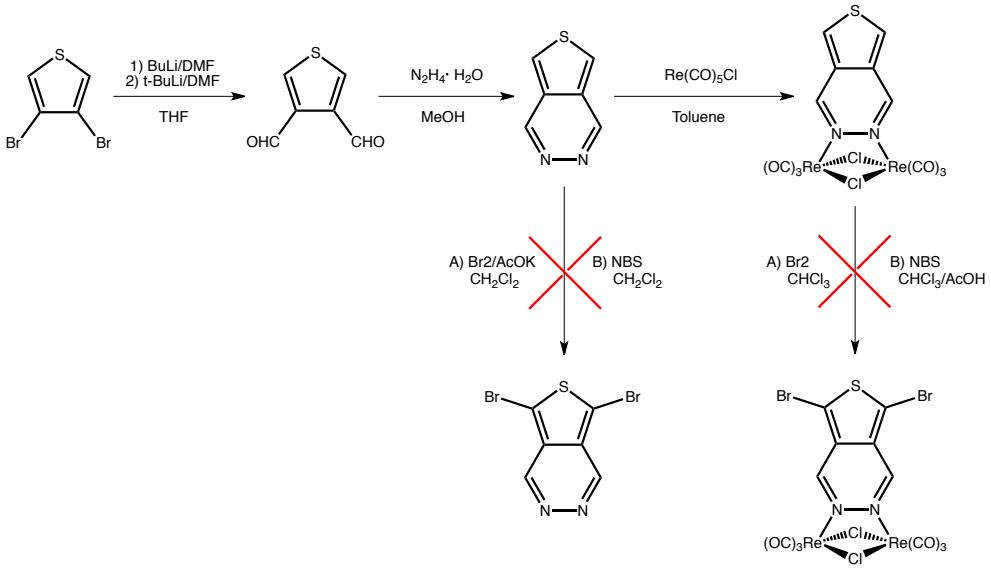

Scheme 6.3 Bromination trials on thieno[3,4-d]pyridazine and corresponding dinuclear rhenium complex.

Starting from the dibromo derivatives M2 and M3, the corresponding thiophene functionalized diazine ligands M4 and M5, were prepared following the Stille coupling reaction in the presence of two equivalents of 2-tributyl-stannyl thiophene in toluene solution. Attempts to obtain the dibromo derivatives, treating M4 and M5 with *n*-bromosuccinimide (NBS) in CH_2Cl_2 at room temperature, according to the previously mentioned methodology, were not successful. Indeed the bromine atoms resulted mainly bound at the *ortho* position of the diazine ring, beside the α positions of the two lateral thiophene ring.

Therefore, **M4** and **M5** were not suitable for polymerization reaction via Stille or Suzuki coupling, but direct arylation could be exploited. Anyway, they were used for the synthesis of the corresponding dinuclear rhenium complexes, namely **C4** and **C5** (see schemes 6.1 and 6.2), obtained by reaction of these functionalized diazine ligand with two equivalents of $[Re(CO)_5Cl]$ in toluene at reflux.

6.2.2 Polymer synthesis

The three new polymers **P1-P3** were synthesized according to scheme 6.4, the overall polymerization conditions being reported in table 6.1. A typical Suzuki polycondensation (SPC) of 2,7-bis(4',4',5',5'-tetramethyl-1',3',2'-dioxaborolan-2'-yl)-N-9''-heptadecanylcarbazole[4] (Cbz) and the desired dibrominated co-monomers **M1-M3** was performed in toluene at high temperature over 70 hours, the final addition of 5-methylthiophene-2-boronic acid pinacol ester quenching the growth of the polymeric chains. The carbazole unit was functionalized with two octyl chains in order to increase the solubility in organic halogenated solvents and the filmability of the resulting polymers. The reaction products were filtrated through a celite pad, in order to remove metal catalyst traces that could affect the spectroscopic features of the polymers. The crude product was recovered with $CHCl_3$ and subsequently precipitated in a $MeOH/H_2O$ 5:1 mixture, then sequentially extracted in Soxhlet with MeOH, acetone and $CHCl_3$, to minimize the molar mass dispersity. Each fraction was characterized with size exclusion chromatography (SEC) to define the Molecular Mass Distribution (MMD) using a relative calibration built up with commercially available narrow MMD polystyrene (PS) standards, using $CHCl_3$ as mobile phase for **P1** and THF for **P2** and **P3**.

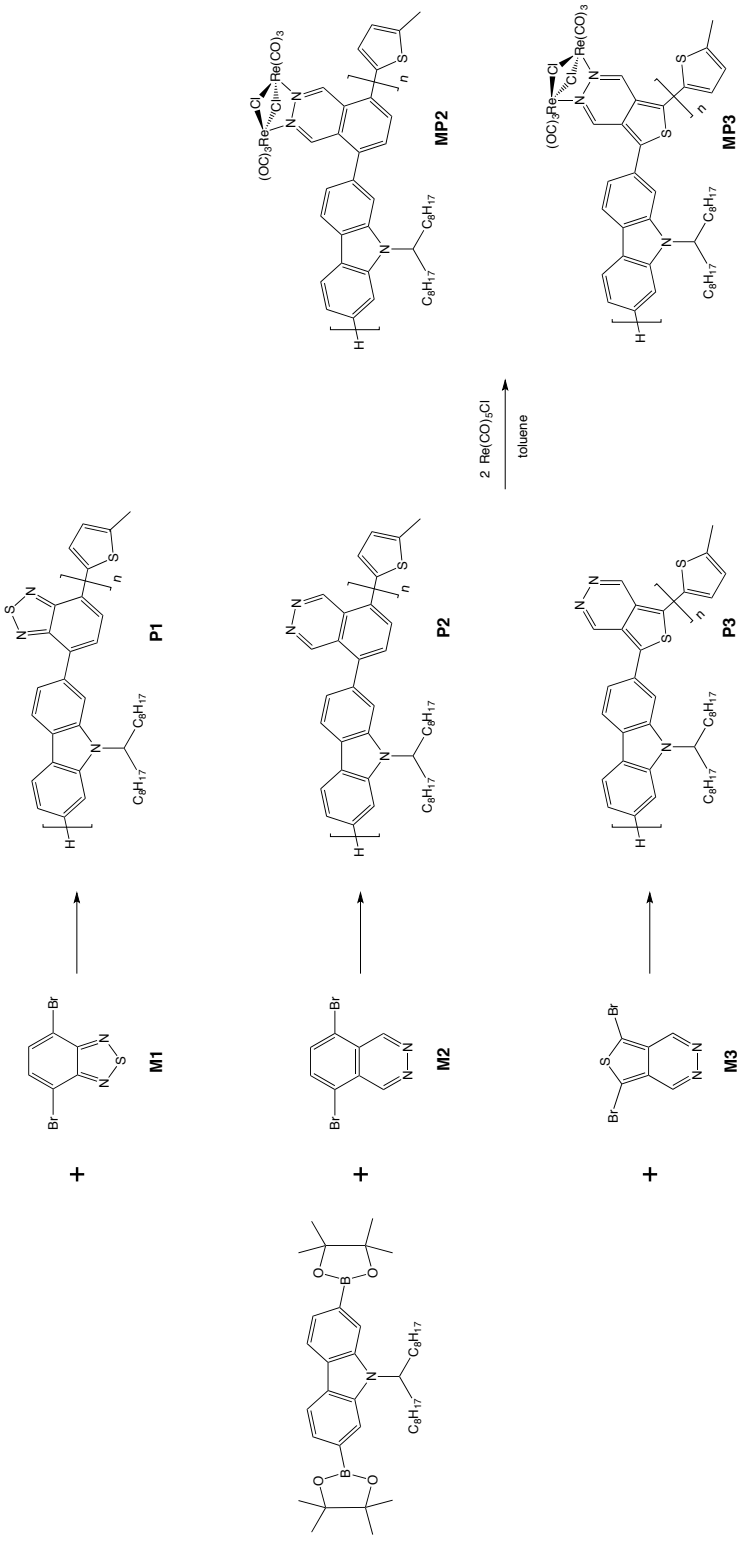

Scheme 6.4 Suzuki polycondensation reaction (SPC) for the synthesis of the copolymers **P1**, **P2** and **P3** and subsequent coordination affording metal-copolymers **MP2** and **MP3**.

Three catalysts, $[Pd_2(dba)_3]$, $[P(o\text{-}tol)_3]$ and $[Pd(PPh_3)_4]$, were selected according to their air stability and activity, as reported in the literature. Using $[Pd_2(dba)_3]$/$[P(o\text{-}tol)_3]$, **P1** and **P2** resulted in enormously higher molecular weights than **P3**, even if each monomer showed similar purity and was polymerized under the same conditions.

Table 6.1 Experimental conditions of the Suzuki polycondensation carried out with **M1**-**M3**.

SAMPLE	Catalyst	K_2CO_3 (eq)	T (°C)	Yield (%)
P1	$Pd_2(dba)_3$ 1% P(*p*-tol)$_3$ 4%	2	90	68
P2-BATCH 1	$Pd_2(dba)_3$ 1% P(*p*-tol)$_3$ 4%	2	90	12
P2-BATCH2	$Pd_2(dba)_3$ 1% P(*o*-tol)$_3$ 4%	10	90	51
P2-BATCH3	$Pd_2(dba)_3$ 1% P(*o*-tol)$_3$ 4%	10	100	69
P2-BATCH4	$Pd_2(dba)_3$ 1% P(*o*-tol)$_3$ 4%	10	110	75
P3-BATCH1	$Pd_2(dba)_3$ 1% P(*o*-tol)$_3$ 4%	10	90	39
P3-BATCH2	$Pd(PPh_3)_4$ 1%	4	90	24
P3-BATCH3	$Pd(PPh_3)_4$ 1%	4	100	49
P3-BATCH4	$Pd(PPh_3)_4$ 1%	4	110	68

Homocoupling reactions in Suzuki polycondensation, which involves oligomeric chains having boronic ester end groups, are well known in the literature.[5] If occurring, they afford the incorporation of structural defects in the main chain of the polymer that cannot be further removed. This deviation from the perfect alternating enchainment can modify the optoelectronic properties of the resulting material and,

hence, their photovoltaic performances. For this reason, it is important to control all the polycondensation conditions in order to reduce or, better, to fully eliminate these side-reactions, thus obtaining homocoupling-free materials.[6]

^{1}H NMR analysis allowed the amount of Cbz homocoupling to be assessed under different SPC conditions, showing that in the synthesis of **P1** with $[Pd_2(dba)_3]/[P(o\text{-}tol)_3]$, only 1% of homocoupling occurred, increasing to more than 60% in the case of **P3**. No homocoupling reaction is observed in the synthesis of **P2**. To further decrease the Cbz-Cbz homocoupling in **P3** the polymerization should be carried out at 110°C, as proved by ^{1}H NMR spectra. The higher temperature increases also the yields of both pyridazine-based polymers. We attributed the Cbz-Cbz coupling to the presence of two growing chains on the same catalytic site in $[Pd_2(dba)_3]/[P(o\text{-}tol)_3]$, while a possible complexation of the diazine nitrogen atoms to the Pd catalyst could slow down the polymerization rate allowing side reactions to take place. Therefore, other Suzuki coupling polymerization conditions were tried for **P3**, in order to improve the molecular weight and to reduce the presence of the homocoupling reaction. In particular, this amount was partially reduced to about 40% if the SPC reaction was performed using the mononuclear $[Pd(PPh_3)_4]$ as catalyst. Matrix-assisted Laser Desorption/Ionization (MALDI) was performed on selected samples to confirm these data. MALDI characterization confirmed the presence of Cbz-Cbz enchainment defects in **P3** sample obtained at 100°C, their reduction at 110°C and the total lack in **P2** sample. Moreover, this technique allowed to determine the nature of the ending groups of the different chains contained in the mixture (see figure 6.2).

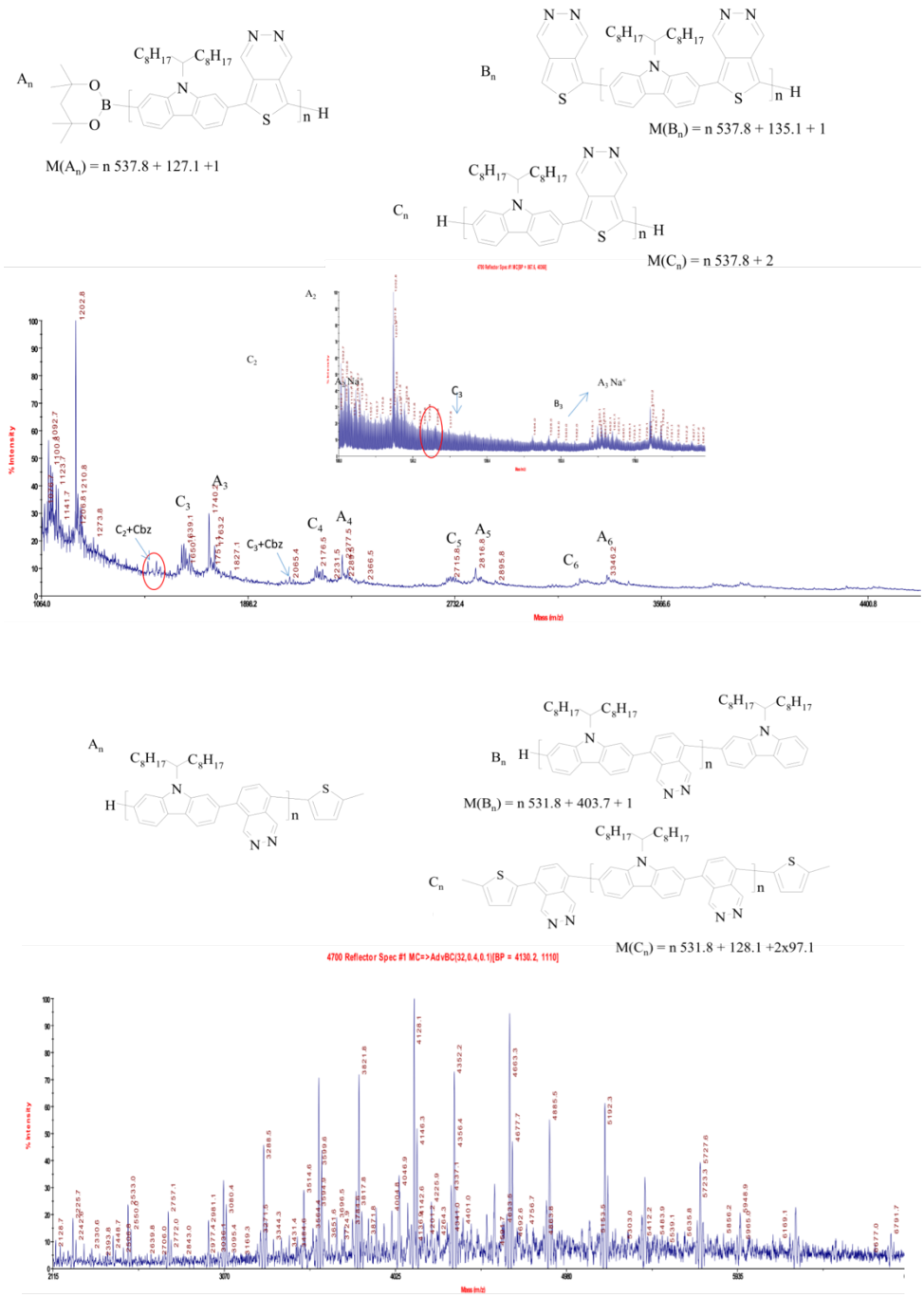

Figure 6.2 MALDI spectra of copolymers P3 (top) and P2 (bottom) together with the structures of the polymer chains having different end groups. Cbz-Cbz linkages are highlighted by a red circle.

Except **P1**, not containing the diazine ligand, **P2** and **P3** were further converted into the corresponding metallo-polymers **MP2** and **MP3**, by refluxing in the presence of an excess of $[Re(CO)_5Cl]$. The resulting metallo-polymers **MP2** and **MP3** were isolated in high yields (about 70%) by precipitation with *n*-hexane from the saturated dichloromethane solution.

6.2.3 Spectroscopic characterization

The UV-Vis absorption properties of the polymers **P1-P3** and of the corresponding metallo-polymers **MP2-MP3**, in CH_2Cl_2 solution are summarized in table 6.2.

Table 6.2 Summary of optical data including the maximum absorption peaks for the different transition bands in the three polymers and in the two metal-polymers in CH_2Cl_2 solution at room temperature.

POLYMER	$\lambda_{\pi-\pi^*}$ [nm] (ε x 10^4)	λ_{CT} [nm] (ε x 10^4)	λ_{MLCT} [nm] (ε x 10^4)
P1	340 (2.43)	460 (2.38)	-
P2	366, 370 (1.16)	-	-
P3	332 (1.02)	461 (1.05)	-
MP2	385 (2.44)	-	424 (2.35)
MP3	360 (1.59)	554 (0.80)	388 (1.18)

For polymers **P1** and **P3**, two main absorption bands are observed. A low energy band, centered at about 460 nm, mainly described as a HOMO–LUMO transition featuring a CT like character (i.e. from π-delocalized system to π^*-localized orbitals on the benzothiadiazole or on the thienopyridazine unit). The electron-poor moieties are indeed at the origin of the partial charge transfer character in the dominant transitions of the polymers, and they are responsible for the typical "camel back" shape of the polymer's absorption spectra.

It is interesting to note that for polymer **P2** this "camel back" shape is not observed (see figure 6.1). A high energy band, centered at about 340 nm and assigned to π–π^* transitions delocalized all over the oligomer backbone, is also observed for **P1** and **P3**.

On the contrary, the spectrum of **P2** shows only one absorption band, which is red-shifted compared to the high energy absorption band of **P1** and **P3**. Since both the ^{1}H NMR spectrum and MALDI analysis of **P2** indicate the presence of the diazine moiety in the backbone and the lack of Cbz-Cbz homocoupling, this band can be considered as the superposition of two absorption bands, one ascribed to the π–π^* transition delocalized all over the oligomer backbone, and the other one arising from the n-π^* transition involving the phtalazine moiety.

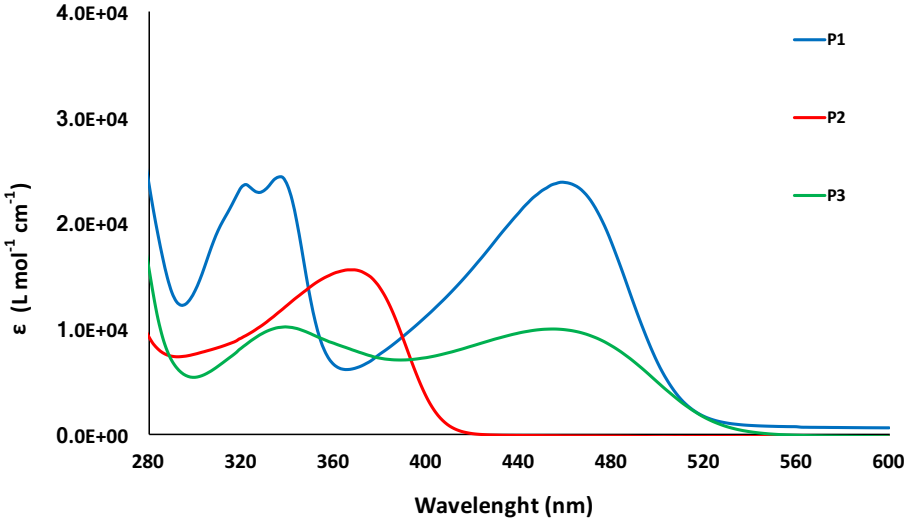

Figure 6.1 UV-Vis absorption spectra of **P1-P3** in CH_2Cl_2 solution at room temperature.

The spectra of both **P2** and **P3** are significantly perturbed upon metal coordination, although in different ways. In **MP3** a significant bathochromic shift of the CT band (from 460 in **P3** to 554 nm, see figure 6.2) is observed, due to the stabilization of the LUMO level upon coordination to metal centers.

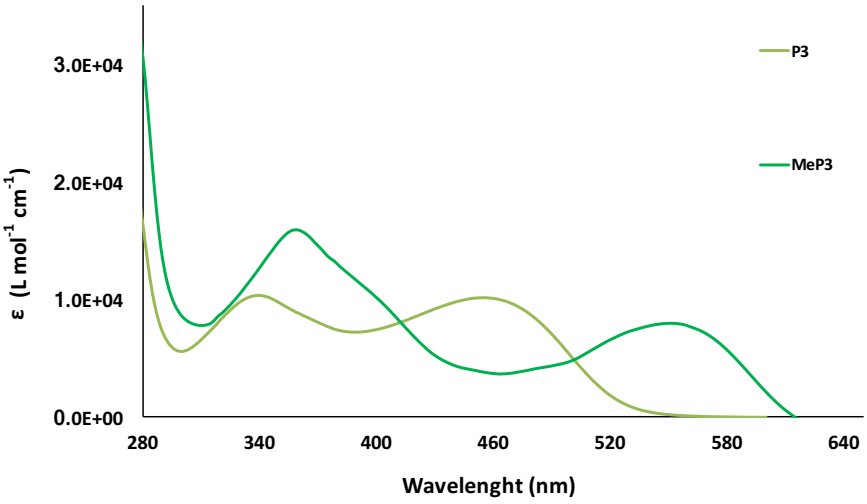

Figure 6.2 UV-Vis absorption spectra of **P3** and **MP3** in CH_2Cl_2 solution at room temperature.

Moreover, the presence of the "Re(μ-Cl)$_2$Re" moiety introduces a further electronic transition, namely the ^{1}MLCT transition from the d_π(Re) orbitals of the metal centers to the π* orbital of the thieno[3,4-d]pyridazine. However, the corresponding absorption band is not observed in **MP3**, overlapped by the leading edge of the π-π* transition of the conjugated polymer backbone, which is slightly red-shifted compared to the metal-free polymer.

On the contrary, in MP2 due to the lack of the CT band the MLCT band is well observed as a broad shoulder of the π-π^* transition of the conjugated backbone (see figure 6.3), which results slightly red-shifted due to the coordination to the metal, as in the case of MP3.

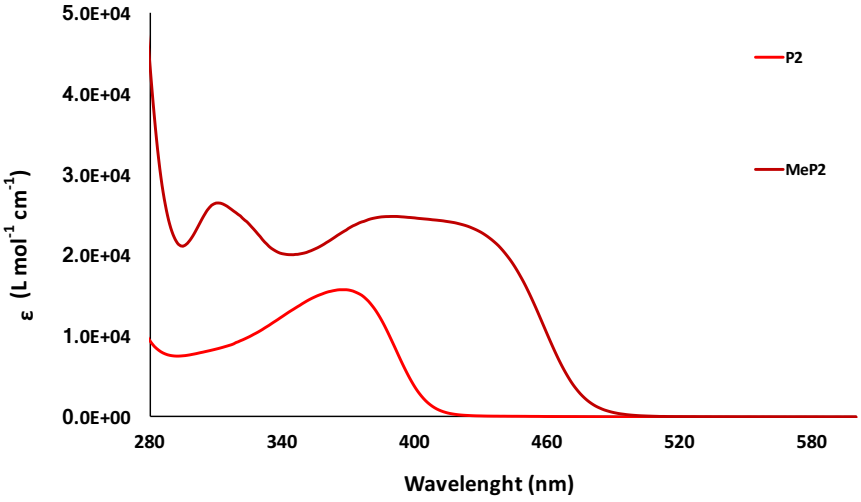

Figure 6.3 UV-Vis absorption spectra of P2 and MP2 in CH_2Cl_2 solution at room temperature.

The same features are observed also in the UV-Vis absorption spectra of the model monomers M4 and M5 and the related complexes C4 and C5, as shown in figure 6.4 and included in table 6.3.

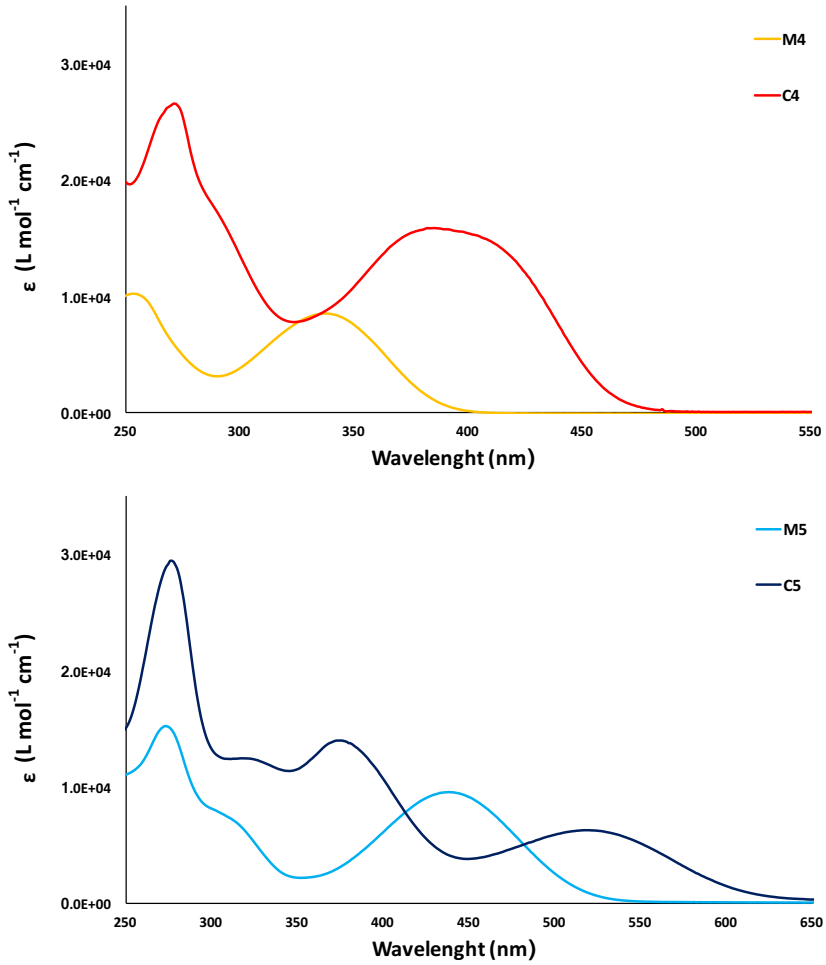

Figure 6.4 UV-Vis absorption spectra of M4 and C4 (top) and of M5 and C5 (bottom) in CH_2Cl_2 solution at room temperature.

Table 6.3 Summary of optical data including the maximum absorption peaks for the different transition bands in the two model diazine ligands and in the corresponding rhenium complexes in CH_2Cl_2 solution at room temperature.

MODEL	$\lambda_{\pi-\pi^*}$ [nm] (ε x 10^4)	λ_{CT} [nm] (ε x 10^4)	λ_{MLCT} [nm] (ε x 10^4)
M4	336 (0.86)	-	-
M5	314 (0.69)	437 (0.95)	-
C4	383 (1.59)	-	406 (1.49)
C5	323 (1.24)	521 (0.63)	375 (1.40)

Remarkably, in the spectrum of **M4** only one absorption band at 336 nm is observed, resulting from the superposition of the two π-π* e n-π* transitions, involving the thiophene subunit and the phtalazine moiety, respectively. On the contrary, **M5** shows the typical "camel back" shape with the well recognizable charge-transfer band at 437 nm. Upon coordination to the metal, in the UV spectra of both **C4** and **C5**, the MLCT band is clearly observable at 406 and 375 nm, respectively, here lacking the leading absorption edge of the polymer backbone. Moreover, for **C5** the CT band results red-shifted of about 90 nm, while a slight red shift is observed for the π-π* transition band (now observed at 323 nm). On the other hand, for complex **C4** the π-π* transition band results significantly red-shifted (of about 50 nm), and only a widened band appears due to the close presence of the MLCT absorption band.

From these results, we can conclude that the band gap of the metal-free conjugated polymer **P3**, having CT character, can be significantly reduced by introducing the rhenium(I) moieties into the polymer backbone, making this metal-copolymer a promising photosensitizer for photovoltaic cells.

Upon optical excitation all the polymers **P1-P3**, the corresponding metallo-polymers **MP2** and **MP3**, and the monomers **M4**, **M5** and **C5**, are luminescent in the visible range of the electromagnetic spectrum. The photophysical data are reported in tables 6.4 and 6.5, respectively. It is interesting to note that emission of **P2** is strongly blue-shifted with respect to the emission of **P1** and **P3**, in agreement with the absence of the CT excited state. The same feature is observed for **M4**, whose emission maximum is almost 50 nm blue-shifted compared to the emission maximum of **M5**.

The coordination to the metal center strongly quenched the emission intensity, and caused a bathochromic shift of the emission maximum of more than 100 nm, both in the polymers and in the corresponding model **C5**. This emission could be attributed to the radiative decay of the ^{3}MLCT excited state, in comparison with closely related complexes. Indeed **MP2** displayed the lowest emission quantum yield and the corresponding model **C4** is not emissive at all, as the analogous complex $[Re_2(\mu\text{-}Cl)_2(CO)_6(\mu\text{-phtz})]$ containing the phtalazine ligand.[7] This feature is in agreement with the reduction of the HOMO-LUMO gap afforded by the coordination of the metal.

Table 6.4 Photophysical properties obtained for polymers **P1-P3** and the corresponding metallo-polymers **MP2** and **MP3**, in air-equilibrated CH_2Cl_2 solution ($1x10^{-5}$ M) at room temperature.

POLYMER	λ_{EM} [nm]	PLQY
P1	568	34.2
P2	450	11.0
P3	572	10.1
MP2	614	3.0
MP3	670	5.8

Table 6.5 Photophysical properties obtained for molecular models **M4** and **M5** and the corresponding complexes **C4** and **C5**, in air-equilibrated diluted samples at room temperature.

MODEL	λ_{EM} [nm]	τ [ns]	PLQY[a]	PLQY[b]
M4	505	0.95, 6.15	0.8	8.8
C4	-	-	-	-
M5	560	2.42, 7.71	20.0	29.6
C5	664	1.49	4.7	5.2

[[a] air-equilibrated diluted CH_2Cl_2 solution ($1x10^{-5}$ M), [b] solid state film]

6.2.4 Electrochemical characterization

Energy levels are crucial for the selection of appropriate materials acting as acceptors in BHJ solar cells. The HOMO and LUMO energy levels of the molecular models and their corresponding complexes were evaluated by cyclic voltammetry (CV) carried out in solution on glassy carbon electrode at a scan rate of 0.2 Vs^{-1}, with a platinum wire counter electrode and a SCE reference electrode in a 0.1 M solution of $TBAPF_6$ in nitrogen-saturated acetonitrile. The corresponding peak potentials (calibrated against the $Fc^+|Fc$ couple) and the HOMO and LUMO energy values (in eV) were calculated by using equations (1) and (2), respectively and are reported in table 6.6.

$$E_{HOMO} = -e\,(E_{ox} + 4.4) \qquad (1)$$

$$E_{LUMO} = -e\,(E_{red} + 4.4) \qquad (2)$$

where E_{ox} and E_{red} are the oxidation and reduction potentials, respectively, versus SCE.[8] The electrochemical characterizations of the polymers and the metallo-polymers are still ongoing.

As shown in figure 6.5, the model ligands **M4** and **M5**, and the complexes **C4** and **C5** exhibit a reversible monoelectronic reduction wave, which is located on the pyridazine ligand, as indicated by the modulation of the peak potential by the nature of the fused ring. In particular, **M4** displays a lower reduction potential than the bare phtalazine ligand (-2.46 V vs -2.06 V),[7] in agreement with the aromatic delocalization between the benzene ring and the two lateral thiophene rings.

Table 6.6 First reduction and oxidation peak potentials ($E_{p,c}$ and $E_{p,a}$), the HOMO e LUMO levels and electrochemical (ΔE_e) and spectroscopic (ΔE_s) energy gaps of the ligands and the complexes. Potentials are referred to the $Fc^+|Fc$ couple in the operating medium (MeCN + 0.1 M $TBAPF_6$). Scan rate 0.2 V s^{-1}.

MODEL	E_{red} [V]	E_{ox} [V]	λ_{abs} [nm]	E_{LUMO} [eV]	E_{HOMO} [eV]	ΔE_e [eV]	ΔE_o [eV]
M4	-2.06	1.15	336	-2.74	-5.95	3.21	3.69
C4	-1.35	1.35	406	-3.45	-6.15	2.70	2.84
M5	-1.65	0.76	437	-3.15	-5.56	2.41	2.84
C5	-1.03	1.09	521	-3.77	-5.89	2.12	2.38

As expected, this delocalization is more extended in **M5** which is endowed by a terthiophene moiety, thus lowering the reduction potential at -1.65 V. The coordination to the metal centers affords a further shift of the reduction potential to more positive values, as already observed in analogous complexes.[9] Therefore **C4** and **C5** display a reversible reduction peak at -1.35 V and -1.03 V respectively. In the anodic part of the CV scan, two irreversible oxidation peaks are observed for **M4** and **M5**. The first is monoelectronic and it is tentatively attributed to the oxidation of the α position of the thiophene rings. The modulation of the peak potential upon changing the size of the central aromatic ring supports this hypothesis. Actually, the more conjugated terthiophene moiety in **M5** displays a lower oxidation potential than that observed for the thiophene rings in **M4**. Moreover, this oxidation is affected by the presence of the electron-poor condensed diazinic ring, which hampers the oxidation reaction. Indeed, the first oxidation peak of **M5** is at +0.77 V, instead of +0.5 V as in the bare terthiophene.

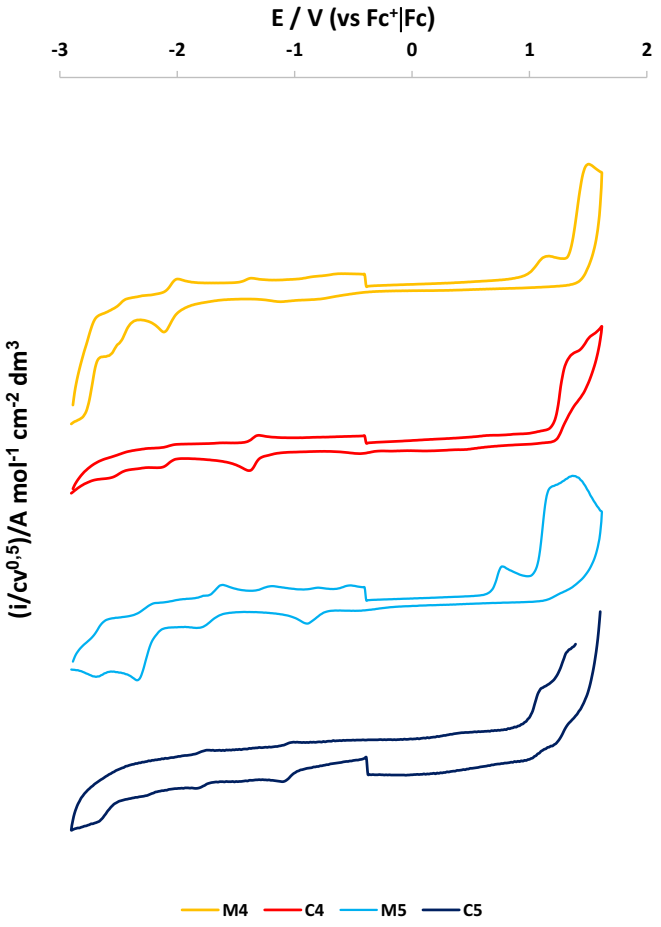

Figure 6.5 Normalized CV curves of the model ligands M4 and M5 and of the corresponding complexes C4 and C5 on GC electrodes, in ACN + 0.1 M $TBAPF_6$ solution, at 0.2 V s^{-1} with ohmic drop compensation.

The coordination to the metal centers further shifts the oxidation potential at higher values and, in C4 and C5, it is no more visible since it lays upon the other oxidation peaks. Moreover, the presence of the positive charge shifts at higher potentials also the oxidation of the metal centers, observed at +1.53 and +1.32 V for C4 and C5, respectively.

6.3 Conclusions

In strict collaboration with the ISMAC-CNR research institute, focus has been put on synthesizing new condensed diazine ligands, designed with the aid of TD-DFT calculations, also containing conjugated thiophene systems. Three D-A metal-copolymers based on carbazole and dinuclear rhenium(I) complexes, bearing diazine rings condensed to delocalized π systems, have been synthesized, as well as some mock-up molecular complexes with extended thiophene system. The new diazines **M2** (5,8-dibromophtalazine) and **M3** (5,7-dibromothienopyridazine) were both synthesized via pericyclic rearrangement of a precursor dibenzyliden- or dithiophenylmethylen-hydrazine, respectively. Alternatively, the introduction of two lateral thiophenes via Stille coupling afforded the π-extended diazines **M4** and **M5**. Their synthesis was followed by Suzuki polycondensation with carbazole to generate the desired D-A copolymers **P2** and **P3**. Both NMR and MALDI analyses revealed that the extent of the Cbz-Cbz homocoupling is strictly correlated to the nature of the catalytic system used (monometallic instead of bimetallic catalyst). The reaction with $[Re(CO)_5Cl]$ has been carried out as last step, generating the metal-copolymers **MP2** and **MP3** and the mock-up complexes **C4** and **C5**. A complete investigation of the structural, thermal, photophysical and electrochemical properties was carried out. The synthesized copolymers and metal-copolymers (together with a non-diazinic carbazole-thiadiazole copolymer named **P1**) are currently under investigation as light harvesters and donors in D:$PC_{61}BM$ (D=**P1**, **P2**, **P3**, **MP2**, **MP3**) active layers in direct architecture OPV devices.

6.4 Experimental

General methods

All the reagents were purchased from Aldrich and Alfa Aesar and used as received. All the reactions were performed under an inert N_2 atmosphere. All the solvents have been deoxygenated and dried by standard methods before use, toluene was distilled on $Na_{(s)}$, CH_2Cl_2 on P_2O_5, both under N_2 atmosphere. Commercial deuterated solvents were used as received. Column chromatography was performed using Alfa Aesar silica gel 60 (0.032–0.063 mm). ^1H NMR spectra were recorded on a Bruker DRX-400 MHz instrument by using the residual signals δ = 7.28 ppm from $CDCl_3$ or δ = 5.32 ppm from CD_2Cl_2 as internal references. IR spectra in solution were acquired on a Bruker Vector 22 FT spectrophotometer. Size Exclusion Chromatography (SEC) measurements were carried out by using an integrated GPCV2000 SEC system from Waters equipped with the two on-line detectors: 1) a differential viscometer (DV); 2) a differential refractometer (DRI) as concentration detector. The columns were two Polymer Laboratories (2PLGel Mixed C + 100Å) while $CHCl_3$ was used as eluent at 0.6 mL min^{-1}, universal calibration of the SEC-DV chromatographic system was constructed using some polystyrene (PS) standards with narrow MMD. Matrix assisted laser desorption/ionization time of flight mass spectrometry (MALDI-TOF MS) was used in reflectron mode to record spectra by means of a 4800 Proteomic Analyzer (Applied Biosystems) MALDI-TOF/TOF instrument equipped with a Nd:YAG laser at a wavelength of 355 nm with <500 ps pulse and 200 Hz firing rate.

The accelerating voltage was 15 kV. External calibration was performed using an Applied Biosystems calibration mixture consisting of polypeptides with different molecular weight values. The irradiance was maintained slightly above the threshold, to obtain a mass resolution of about 6000-8000 fwhm. Mass accuracy was about 50 ppm. All measurements were performed by using trans-2-[3-(4-tert-butylphenyl)-2-methyl-2-propenylidene]malononitrile (DCTB) as the matrix.

Electrochemical measurements

see chapter 3.

Spectroscopy

see chapter 3.

Synthesis of 1,2-bis(-2,5-dibromobenzylidene)hydrazine. 2.00 g of dibromobenzaldehyde (7.35 mmol) were dissolved in 40 mL of MeOH, and 180 µL of hydrazine monohydrate (3.67 mmol) were added to the solution. The reaction mixture was refluxed for 2 hours, leading to the formation of a suspension. The product was filtered and dried, yielding 1.75 g (3.34 mmol) of whitish powder (isolated yield 91%). ^{1}H NMR (CD_2Cl_2, 300K, 400 MHz) δ_H (ppm) 8.96 (s, 2H, CH), 8.39 (s, 2H, $H_{6\ phenyl}$), 7.57 (d, J = 8.5 Hz, 2H, $H_{3\ phenyl}$), 7.51 (d, J = 8.5 Hz, 2H, $H_{4\ phenyl}$)

Synthesis of 5,8-dibromophtalazine (M2). 1.75 g (3.34 mmol) of 1,2-bis(-2,5-dibromobenzylidene)hydrazine, 6.7 g (50 mmol) of $AlCl_3$ and 6.7 g (25 mmol) of $AlBr_3$ were mixed together and heated up to 195°C for 3 hours. Then, the reaction was quenched with H_2O and left stirring for 1 hour. The colorless solution was filtered, and the grey solid

residue washed again with HCl 6M several times. The acidic solutions were gathered and made basic with KOH. The product was extracted from the aqueous solution with copious amounts of ethyl acetate (EtOAc), the organic layer made anhydrous with $MgSO_4$ and the solvent evaporated. The crude product was purified through chromatography (eluent EtOAc), then dried under vacuum, yielding 215 mg (0.77 mmol) of solid product (isolated yield 23%). ^{1}H NMR (CD_2Cl_2, 300K, 400 MHz) δ_H (ppm) 9.82 (s, 2H, $H_{1,4\ phtal}$), 8.05 (s, 2H, $H_{6,7\ phtal}$)

Synthesis of 5,8-dithiophenylphtalazine (M4). 100 mg (0.347 mmol) of 5,8-dibromophtalazine, and 10 mg (0.0087 mmol) of $Pd(PPh_3)_4$ were dissolved in 10 mL of toluene, N_2 was bubbled in the solution for 15 min. 240 µL (0.764 mmol) of tributyl-stannylthiophene were added dropwise to the reaction mixture. The solution was refluxed overnight at 110°C. After being quenched with H_2O the organic layer was separated, made anhydrous with $MgSO_4$ and filtered through celite pad. The crude product was purified through chromatography (eluent CH_2Cl_2/hexane/MeOH 8:2:1), then dried under vacuum, yielding 85 mg (0.284 mmol) of solid product (isolated yield 82%). ^{1}H NMR (CD_2Cl_2, 300K, 400 MHz) δ_H (ppm) 9.92 (s, 2H, $H_{1,4\ phtal}$), 8.02 (s, 2H, $H_{6,7\ phtal}$), 7.63 (d, J =5.2 Hz, 2H, $H_{2\ thioph}$) 7.43 (d, J = 3.6 Hz, 2H, $H_{4\ thioph}$), 7.32 (dd, J= 5.1, 3.6 Hz, 2H, $H_{3\ thioph}$)

Synthesis of $[Re_2(\mu\text{-}Cl)_2(CO)_6(\mu\text{-}5,8\text{-dithiophenylpthalazine})]$ (C4). One eq. of 5,8-dithiophenylpthalazine (30 mg, 0.102 mmol) was dissolved in freshly distilled toluene (8 mL) and treated with two eq. of $Re(CO)_5Cl$ (74 mg, 0.204 mmol). The reaction mixture was refluxed for 3 hours, then the solution was evaporated to dryness under vacuum. The solid

residue was purified through column chromatography (eluent CH_2Cl_2/hexane 8:2), affording the desired product (68 mg, 0.076 mmol, isolated yield 75%). IR (CH_2Cl_2) ν(CO): 2047 (m), 2033 (vs), 1942 (s), 1915 (s) cm^{-1}, ^1H NMR (CD_2Cl_2, 300K, 400 MHz) δ_H (ppm) 10.51 (s, 2H, $H_{1,4\ phtal}$), 8.39 (s, 2H, $H_{6,7\ phtal}$), 7.80 (dd, J = 5.2, 1.2 Hz, 2H, $H_{2\ thioph}$) 7.54 (dd, J = 3.7, 1.2 Hz, 2H, $H_{4\ thioph}$), 7.42 (dd, J = 5.1, 3.6 Hz, 2H, $H_{3\ thioph}$)

Synthesis of 1,2-bis((2,5-dibromothiophen-3-yl)methylene)hydrazine. A sample of di 2,5-dibromo-3-thiophenecarboxaldehyde (3.58 g, 13.2 mmol) was dissolved in 50 mL of MeOH. Hydrazine monohydrate (300 μL, 6.6 mmol) was added to the solution. The reaction mixture was refluxed for 2 hours, leading to the formation of a yellow suspension. The product was filtered and dried, yielding 3.2 g (5.8 mmol) of yellow powder (isolated yield 88%). ^1H NMR (CD_2Cl_2, 300K, 400 MHz) δ_H (ppm) 8.55 (s, 2H, CH), 7.56 (s, 2H, $H_{3\ thioph}$)

Synthesis of 5,7-dibromothieno-3,4-pyridazine (M3). 1.7 g (3 mmol) of 1,2-bis((2,5-dibromothiophen-3-yl)methylene)hydrazine, 5.5 g (42 mmol) of $AlCl_3$ and 5.6 g (21 mmol) of $AlBr_3$ were mixed together and heated up to 195°C for 3 hours. After 3 hours the reaction was quenched with H_2O and left stirring for 1 hour. The yellow solution was filtered, and the black solid residue washed again with HCl 6M several times. The acidic solutions were gathered and made basic with KOH, turning colorless. The product was extracted from the aqueous solution with copious amounts of ethyl acetate (EtOAc), the organic layer made anhydrous with $MgSO_4$ and the solvent evaporated. The crude product was purified through chromatography (eluent EtOAc), then dried under vacuum, yielding 170 mg (0.60 mmol) of yellow

powder (isolated yield 20%). ^{1}H NMR (CD_2Cl_2, 300K, 400 MHz) δ_H (ppm) 9.12 (s, 2H, $H_{1,4\ pydz}$)

Synthesis of 5,7-dithiophenylthieno-3,4-pyridazine (M5). 100 mg (0.34 mmol) of 5,7-dibromothieno-3,4-pyridazine, 97 mg (0.75 mmol) of thiophenyl-boronic acid, 10 mg (0.0087 mmol) of $Pd(PPh_3)_4$ were dissolved in 6 mL of dimethoxyethane and the solution was degassed by bubbling N_2 for 15 min. A sample of K_2CO_3 (282 mg, 2.04 mmol) was simultaneously dissolved in H_2O and also bubbled with N_2. The aqueous solution was then added to the organic solution and the resulting reaction mixture was refluxed overnight at 85°C. The reaction was quenched with H_2O and the organic product extracted with CH_2Cl_2, then made anhydrous with $MgSO_4$ and filtered through celite pad. The crude product was purified through chromatography (eluent EtOAc/MeOH 9:1), then dried under vacuum, yielding 84 mg (0.28 mmol) of orange powder (isolated yield 83%). ^{1}H NMR (CD_2Cl_2, 300K, 400 MHz) δ_H (ppm) 9.55 (s, 2H, $H_{1,4\ thienopydz}$), 7.59 (dd, J = 5.2, 1.1 Hz, 2H, $H_{2\ thioph}$) 7.52 (dd, J = 3.7, 1.1 Hz, 2H, $H_{4\ thioph}$), 7.26 (dd, J =5.2, 3.7 Hz, 2H, $H_{3\ thioph}$)

Synthesis of [$Re_2(\mu\text{-}Cl)_2(CO)_6$(μ-5,7-dithiophenylthieno-3,4-pyridazine)] (C5). A sample of $Re(CO)_5Cl$ (42 mg, 0.116 mmol) was dissolved in freshly distilled toluene (7 mL) and treated with 5,7-dithiophenylthieno-3,4-pyridazine (18 mg, 0.058 mmol). The reaction mixture was refluxed for 4 hours, then the solution was evaporated to dryness under vacuum. The solid residue was purified through column chromatography (eluent CH_2Cl_2/hexane 8:2), affording the desired product as red powder (38 mg, 0.042 mmol, isolated yield 72%). IR (CH_2Cl_2) ν(CO): 2046 (m), 2032 (vs), 1941 (s), 1915 (s) cm^{-1}, ^{1}H NMR

(CD_2Cl_2, 300K, 400 MHz) δ_H (ppm) 10.02 (s, 2H, $H_{1,4\ thienopydz}$), 7.79 (d, J = 5.2 Hz, 2H, $H_{2\ thioph}$), 7.64 (d, J = 3.8 Hz, 2H, $H_{4\ thioph}$), 7.37 (dd, J = 5.1, 3.6 Hz, 2H, $H_{3\ thioph}$)

Suzuki polycondensation (Synthesis of P1, P2 and P3). The two monomers (1 eq each) and K_2CO_3 were introduced into a Schlenk tube and deaerated with three vacuum/N_2 cycles. The correct ratio of freshly distilled toluene and of degassed MilliQ water was then added to the reaction mixture. A drop of Aliquat336 phase transfer catalyst was added to ease the mixing of the two phases. Separately, the catalyst was degassed, dissolved into anhydrous toluene, and then added to the reaction mixture. The reaction mixture was heated at 90°C for 70 h. The addition of 10 equivalents of 5-methylthiophene-2-boronic acid-pinacol ester as end-capper quenched the polycondensation, and the mixture was kept stirring overnight. Finally, the reaction mixture was cooled to RT and filtered through a pad of celite to completely remove any trace of catalyst. The crude was poured into MeOH and recovered through filtration on PTFE filter (0.4 µm). A Soxhlet extraction (MeOH, acetone, and CH_2Cl_2) finally yielded the desired polymers.

SAMPLE	M_p [g mol^{-1}]	M_n [g mol^{-1}]	M_w [g mol^{-1}]	M_w/M_n	Rpt. units
P1[a]	47,929	8,498	49,294	5.8	89
P1[b]	40,091	16,704	81,497	4.9	74
P2[b]	7,053	5,084	88,113	17.3	13
P3[b]	5,452	2,710	42,544	15.7	10

[[a] SEC eluent: $CHCl_3$ only, [b] SEC eluent: $CHCl_3$ + 0.5% CH_3COOH. Acetic acid was used to reduce the interaction between the diazine N atoms in **P2** and **P3** and the column's stationary phase]

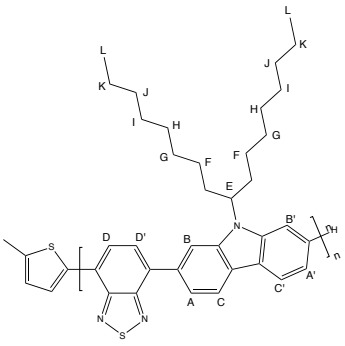

P1. ^{1}H NMR ($CDCl_3$, 300K, 400 MHz) δ_H (ppm) 8.42 (s, 1H, H_D), 8.35 (m, 2H, $H_{C,C'}$), 8.20 (s, 1H, $H_{D'}$), 8.03 (s, 2H, $H_{B,B'}$), 7.91 (s, 2H, $H_{A,A'}$), 4.81 (s, 1H, H_E), 2.51 (m, 2H, H_F), 2.07 (m, 2H, H_F), 1.19 (m, 24H, H_{G-K}), 0.80 (m, 6H, H_L) according to ACS Macro Lett. **2015**, 4, 21

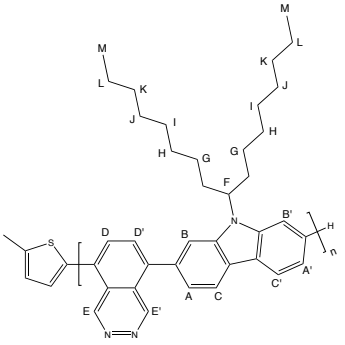

P2. ^{1}H NMR ($CDCl_3$, 300K, 400 MHz) δ_H (ppm) 9.88 (s, 2H, $H_{E,E'}$), 8.43 (m, 2H, $H_{D,D'}$), 8.21 (s, 2H, $H_{C,C'}$), 7.83 (s, 1H, H_B), 7.67 (s, 1H, H_B), 7.53 (m, 2H, $H_{A,A'}$), 4.70 (s, 1H, H_F), 2.36 (m, 2H, H_G), 2.01 (m, 2H, H_G), 1.18 (m, 24H, H_{H-L}), 0.80 (m, 6H, H_M)

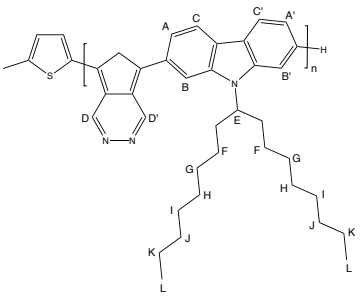

P3. ^{1}H NMR ($CDCl_3$, 300K, 400 MHz) δ_H (ppm) 9.63 (m, 2H, $H_{D,D'}$), 8.35 (m, 2H, $H_{C,C'}$), 7.98 (m, 1H, H_B), 7.80 (m, 1H, H_B), 7.69 (m, 2H, $H_{A,A'}$), 4.76 (s, 1H, H_E), 2.43 (m, 2H, H_F), 2.10 (m, 2H, H_F), 1.14 (m, 24H, H_{G-L}), 0.79 (m, 6H, H_M)

Synthesis of MP2. 40 mg (0.071 mmol) of **P2** and 60 mg (0.16 mmol) of $Re(CO)_5Cl$ were dissolved in 8 mL of freshly distilled toluene. The reaction mixture was put under reflux for 3 hours at 120 °C, a dark yellow precipitate slowly forming. The solution was evaporated to dryness. The crude material was dissolved in CH_2Cl_2, the addition of n-hexane caused the precipitation of the product, that was subsequently washed with n-hexane (3 x 5 mL), affording the desired

metallopolymer as ochre powder. IR (CH_2Cl_2) ν(CO): 2046 (m), 2032 (vs), 1941 (s), 1915 (s) cm^{-1}, ^1H NMR (CD_2Cl_2, 300K, 400 MHz) δ_H (ppm) 10.43 (d, J = 23.4 Hz, 2H, H_E), 8.54 (m, 4H, $H_{C,D}$), 8.03 (s, 1H, H_B), 7.86 (s, 1H, H_B), 7.61 (m, 2H, H_A), 4.83 (s, 1H, H_F), 2.43 (m, 2H, CH_2), 2.16 (m, 2H, CH_2), 1.21 (m, 24H, CH_2), 0.85 (m, 6H, CH_3)

Synthesis of MP3. 42 mg (0.077 mmol) of P3 and 60 mg (0.16 mmol) of $Re(CO)_5Cl$ were dissolved in 7 mL of freshly distilled toluene. The reaction mixture was put under reflux for 3 hours at 120 °C, the solution slowly turning deep purple. The solvent was evaporated to dryness, then the crude material was dissolved in CH_2Cl_2, the addition of n-hexane causing the precipitation of the product. The so obtained solid was subsequently washed with n-hexane (3 X 5 mL), affording the desired metallopolymer as dark purple powder. IR (CH_2Cl_2) ν(CO): 2047 (m), 2032 (vs), 1943 (s), 1912 (s) cm^{-1}. ^1H NMR (CD_2Cl_2, 300K, 400 MHz) δ_H (ppm) 10.12 (d, J = 24.4 Hz, 2H, H_D), 8.56 (m, 2H, H_C), 8.10 (s, 1H, H_B), 7.95 (s, 1H, H_B), 7.77 (m, 2H, H_A), 4.83 (s, 1H, H_E), 2.45 (m, 2H, H_Z), 2.16 (m, 2H, H_Z), 1.17 (m, 24H, H_Z), 0.81 (m, 6H, H_Z)

References

[1] M. A. Green, K. Emery, Y. Hishikawa, W. Warta, E. D. Dunlop, *Prog. Photovoltaics* **2015**, 23, 805

[2] IMEC and Solvay, **2012**

[3] N. Blouin, A. Michaud, D. Gendron, S. Wakim, E. Blair, R. Neagu-Plesu, M. Belletete, G. Durocher, Y. Tao, M. Leclerc, *J. Am. Chem. Soc.* **2008**, 130, 732

[4] N. Blouin, A. Michaud, M. Leclerc, *AdV. Mater.* **2007**, 19, 2295

[5] C. Adamo, C. Amatore, I. Ciofini, A. Jutand, H. Lakmini, *J. Am. Chem. Soc.* **2006**, *128*, 6829

[6] F. Lombeck, H. Komber, D. Fazzi, D. Nava, J. Kuhlmann, D. Stegerer, K. Strassel, J. Brandt, A. Diaz de Zerio Mendaza, C. Müller, W. Thiel, M. Caironi, R. Friend, M. Sommer, *Adv. Energy Mater.* **2016**, *6*, 1601232

[7] D. Donghi, G. D'Alfonso, M. Mauro, M. Panigati, P. Mercandelli, A. Sironi, P. Mussini, L. D'Alfonso, Inorg. Chem. **2008**, 47, 4243

[8] C. M. Cardona, W. Li, A. E. Kaifer, D. Stockdale, G. C. Bazan, *Adv. Mater.* **2011**, 23, 2367

[9] M. Panigati, M. Mauro, D. Donghi, P. Mercandelli, P. Mussini, L. De Cola and G. D'Alfonso, *Coord. Chem. Rev.* **2012**, 256, 1621

CHAPTER 7

Organochalcogen-bridged rhenium(I) complexes: structure to property correlation

Abstract

The synthesis of a series of neutral dinuclear rhenium complexes of general formula $[Re_2(\mu\text{-}XR)_2(CO)_6(\mu\text{-pydz})]$ (X = O, S, Se and Te; R = Me, Ph) has been performed via new, either one-pot or two-step, synthetic routes. Combined NMR studies allowed the assessment of both the structures and behavior in solution. Preliminary DFT and TD-DFT studies of the geometry and electronic structure of the complexes, coupled with extensive photophysical and electrochemical characterization, led to a complete structure to property correlation.

7.1 Introduction

The conversion of solar energy into electrical energy and the storage of solar energy into chemical bonds are a very attractive strategy to produce and store environmentally-friendly energy. From the molecular point of view, for transducing solar energy into chemical potentials, the photocatalyst (for fuel production) or the photosensitizer (for the conversion into current) should be a multi-functional system able to perform several distinct acts in series.[1] First of all, this molecule must be coloured. This is the case of several metal complexes used as photosensitizes in solar cells, which are characterized by intense MLCT or LMCT absorption bands.[2] Such excited states have triplet character and usually survive for several ns, thus avoiding possible charge recombination.[3]

Recently we have reported on some dinuclear rhenium complexes as sensitizers for Dye Sensitized Solar Cells (DSSCs), having general formula $[Re_2(\mu\text{-}X)(\mu\text{-}Y)(CO)_6(\mu\text{-pydz-4-COOH})]$, (with X = halide or hydride and Y = halide or carboxylate).[4] Light-to-current conversion has been indeed recorded, although with moderate efficiency (see chapter 5).

Both computational studies at TD-DFT level and experimental data showed that complexes containing one hydrido and one carboxylato ancillary ligands, or two thiophenolate ligands display the narrowest HOMO-LUMO gap and thus the widest absorption in the visible range, making these complexes promising as photosensitizers.

These features prompted us to investigate the optical properties of complexes containing other chalcogenide anions as ancillary ligands. Only a few examples of chalcogen-bridged rhenium complexes are available in the literature. Hupp and co-workers reported the synthesis of the sulfide bridged dinuclear rhenium complex $[Re_2(\mu\text{-}SPh)_2(CO)_8]$ from thiols and $[Re(CO)_5(OTf)]$.[5] In the same report they also mentioned the stepwise synthesis of selenium bridged rhenium dimers $[Re_2(\mu\text{-}SeR)_2(CO)_8]$ from selenol and $[Re(CO)_5(OTf)]$. Alternatively, the dinuclear complex $[Re_2(\mu\text{-}SR)_2(CO)_8]$ was obtained by reacting a diaryl disulfide with $[Re_2(CO)_{10}]$ under photolytic conditions[6] and, in much lower yields, under thermolytic conditions. When a similar reaction was carried out in the presence of pyridyl ligands it resulted in the facile oxidative addition of the diaryl disulfide to the Re-Re bond, affording the dinuclear neutral metallacycles $[Re_2(\mu\text{-}SR)_2(CO)_6(L)_2]$ (L = pyridine ligand).[7]

The same one-pot synthesis, involving the oxidative addition of the Se-Se bond of a Se_2R_2 diselenide to rhenium carbonyl and affording the analogous selenium bridged neutral metallacycles $[Re_2(\mu\text{-}SeR)_2(CO)_6(L)_2]$, was recently reported.[8] The replacement of monodentate pyridyl ligands with rigid bidentate bi-pyridine ligands generated the novel tetranuclear selenium bridged metallacyclophanes $[Re_2(\mu\text{-}SeR)_2(CO)_6(\mu\text{-}L)_2]$.[9]

Some dinuclear pyridazine complexes of rhenium containing thiophenolate ligands were previously obtained in our group, but the synthetic route was unsatisfactory in many respects, as detailed in paragraph 7.2.1.[10] Therefore, we have investigated the possibility to exploit the previously reported results to establish a simple and

effective general route to dinuclear $[Re_2(\mu\text{-}XR)_2(CO)_6(\mu\text{-pydz})]$ complexes containing XR anions as ancillary ligands (X = S, Se, Te; R = phenyl, methyl, see chart 7.1). In this regard, the oxidative addition reaction of disulfide, diselenide, ditelluride derivatives on $[Re_2(CO)_{10}]$ in presence of the bridging 1,2-diazine ligand has been investigated and here reported.

Since dimethylperoxide is not commercially available and diphenylperoxide is quite unstable under the current reaction conditions, the corresponding phenolato and methanolato derivatives were prepared following the already reported synthetic procedures.[10]

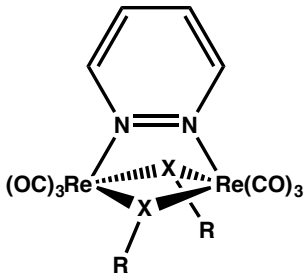

1a: X = O, R = Ph
1b: X = O, R = Me
2a: X = S, R = Ph
2b: X = S, R = Me
3a: X = Se, R = Ph
3b: X = Se, R = Me
4a: X = Te, R = Ph

Chart 7.1 Structure of the chalcogenide complexes investigated.

In addition to the one-pot synthesis, a general two-step reaction, involving the chalcogen-bridged rhenium cubane-like $[Re(\mu_3\text{-}X)(CO)_3]_4$ complexes as starting materials has been also investigated. The synthesis of the cubane derivatives was already reported, involving the oxidative addition of X-X bonds to $[Re_2(CO)_{10}]$.[11] The cubane complexes are able to react with the bridging diazine to give the corresponding dinuclear derivatives.

All the complexes have been fully characterized, by means of preliminary DFT computations and exhaustive electrochemical and spectroscopic measurements. The spectroscopic properties of the dyes have been correlated to their molecular structure and, in particular, to the nature of the ancillary ligands, which can modulate the HOMO and LUMO levels and the efficiency of light harvesting.

7.2 Results and discussion

7.2.1 Synthesis of the complexes

The synthesis of the dinuclear rhenium complexes $[Re_2(\mu\text{-}XR)_2(CO)_6(\mu\text{-pydz})]$, (X = O or S) was previously reported,[10] using several synthetic routes. However, they were more demanding than those used for the related dihalide $[Re_2(\mu\text{-}X)_2(CO)_6(\mu\text{-1,2-diazine})]$ complexes,[12] because of the unavailability of the $[Re(CO)_5XR]$ starting materials. In particular the dinuclear rhenium complex containing thiophenolate ligands $[Re_2(\mu\text{-}SPh)_2(CO)_6(\mu\text{-diazine})]$ was obtained by treating $[Re(CO)_5(OTf)]$, containing the labile triflate $CF_3SO_3^-$ anion ($^-$OTf), with one equivalent of thiophenol in presence of a base, such as bis(dimethylamino)naphthalene (DMAN) or Na_2CO_3.[10]

As mentioned in the previous paragraph, here we have investigated the possibility to find a general synthetic procedure to the synthesis of the dinuclear complexes containing either $^-$SR, $^-$SeR or $^-$TeR anions as ancillary ligands. The method involved the spontaneous formation of the dinuclear complexes $[Re_2(\mu\text{-}XR)_2(CO)_6(\mu\text{-diazine})]$ (X = S, Se, Te and R = methyl, phenyl) by self-assembly of five components via the so-called *orthogonal-bonding* approach.

This synthetic procedure was previously reported by Manimaran and Lu for the synthesis of rhenium-based metallacycles and molecular rectangles. [7-8, 13-14]

In this case, the formation of the dinuclear complexes is accomplished by the oxidative addition of the dichalcogenide ligand (disulfide, diselenide or ditelluride) to rhenium pentacarbonyl, through replacement of one CO ligand in each metal center, followed by the further substitution of the two axial CO groups (orthogonal to the initially replaced carbonyls) by the bridging N-donor pyridazine ligand, in mesitylene solution at high temperature. This reaction yielded the corresponding dinuclear complex $[Re_2(\mu\text{-}XR)_2(CO)_6(\mu\text{-pydz})]$ (X = S, Se, Te; R = phenyl, methyl, see scheme 7.1) in high yields (ca. 85%).

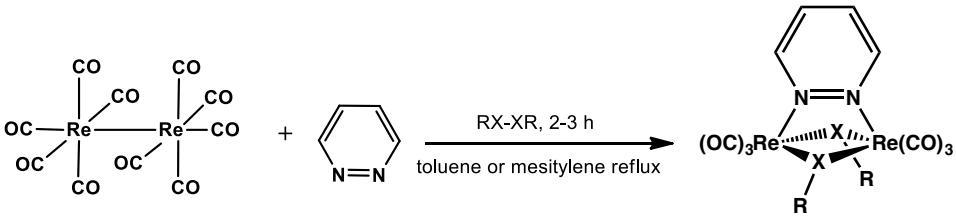

2a: X = S, R = Ph
2b: X = S, R = Me
3a: X = Se, R = Ph
3b: X = Se, R = Me
4a: X = Te, R = Ph

Scheme 7.1 One-pot synthetic pathway employed for complexes 2-4a.

This simultaneous approach can be carried out only when the ancillary ligands are stable at high temperature and do not react in a parallel way with the N-donor ligand under the same conditions. For this reason, it cannot be used for the synthesis of the analogous derivatives containing chloride or bromide as ancillary ligands.

Indeed, the oxidative addition of Cl_2 or Br_2 to $[Re_2(CO)_{10}]$ occurs at room temperature, and affords quantitatively $[Re(CO)_5Cl]$, which can react with the N-donor ligand in a subsequent step at high temperature, according to equation 7.1, representing the common synthetic route to the dihalide complexes.[12]

$$2\,[Re(CO)_5Cl] + pydz \rightarrow\ [Re_2(\mu-Cl)_2(CO)_6(pydz)] +\ 4\,CO\uparrow$$

(eq. 7.1)

In addition to the one-pot synthesis, a two-step reaction involving the formation of the heterocubane structure $[Re_4(\mu_3\text{-}XR)_4(CO)_{12}]$ was investigated in the case of the telluride derivative. Actually, the cubane-like $[Re_4(\mu_3\text{-}OH)_4(CO)_{12}]$ complex, containing four bridging hydroxo ligands, was already used as starting material for the synthesis of the dinuclear complex $[Re_2(\mu\text{-}OH)_2(CO)_6(\mu\text{-}pydz)]$,[10] in the presence of 2 equivalents of pydz, according to equation 7.2.

$$[Re_4(\mu_3-OH)_4(CO)_{12}] + 2\,pydz \rightarrow\ 2\,[Re_2(\mu-OH)_2(CO)_6(pydz)]$$

(eq. 7.2)

This reaction resembles the previously reported fragmentation of the unsaturated tetranuclear cluster $[Re_4(\mu_3\text{-}H)_4(CO)_{12}]$ with 2 equiv. of pydz,[15] but in this case only the *[2+2]* fragmentation pathway was observed, quantitatively affording $[Re_2(\mu\text{-}OH)_2(CO)_6(\mu\text{-}pydz)]$.[10]

The tellurium-bridged molecular cubane $[Re_4(\mu_3\text{-}TePh)_4(CO)_{12}]$ (**4**) has been obtained following the synthetic procedure reported for the synthesis of the analogous sulfur derivative (**2**)[11] by a one-pot reaction via oxidative addition of the diaryl ditelluride to $[Re_2(CO)_{10}]$ in mesitylene solution.

Differently from what observed for the disulfide, this reaction proceeds also without the catalytic amount of dimethylformamide, which facilitates the removal of terminal carbonyl groups, even if complex **4** was obtained in low yields (about 32%). The reaction of complexes **2** and **4** with 2 equivalents of pyridazine in refluxing toluene quantitatively afforded complexes **2a** and **4a**, respectively.

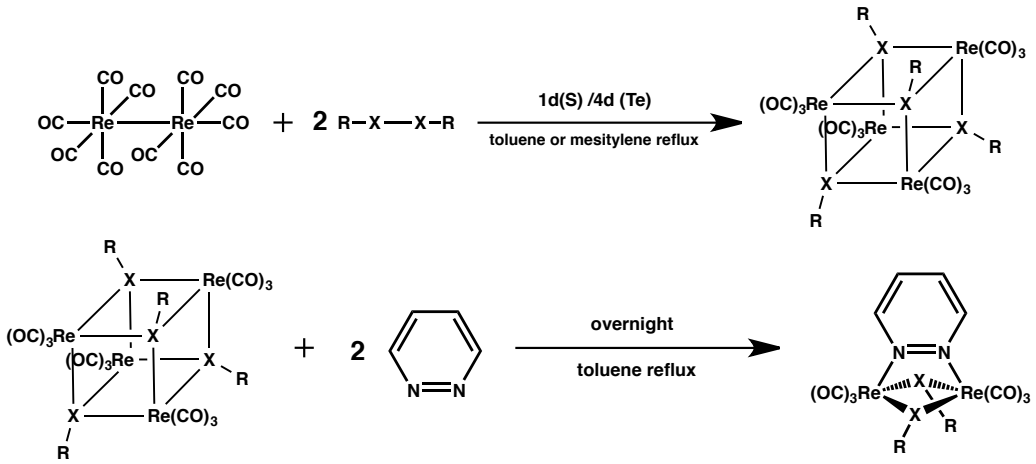

Scheme 7.2 Two-step synthetic procedure for the μ-XR complexes (X = S, Te) via heterocubane intermediate.

The nature of the new complexes was unambiguously established by spectroscopical characterization. All the dinuclear complexes displayed, in the ν(CO) regions of the IR spectra the four-band pattern typical of this class of compounds (see table 7.1).[16]

Accordingly, the position of the stretching bands of the carbonyl ligands is affected by the d_π electron density on the metal centre, as a result of the π-back donation. For the aryl derivatives **1a**-**4a**, the position of the highest-frequency A_1 mode shifts on varying the ancillary ligands, as to the trend 2036 (O-Ph) > 2035 (S-Ph) > 2032 (Se-Ph) > 2027 (Te-Ph) cm^{-1}.

This is in agreement with the Re atoms becoming progressively more electron rich as the electronegativity of the X ligands decreases.

Table 7.1 IR carbonyl stretching bands (in CH_2Cl_2, 298 K) of the complexes investigated.

COMPLEX	IR **ν** (CO) [cm^{-1}]
$[Re_2(\mu\text{-}OPh)_2(CO)_6(\mu\text{-}pydz)]$ **(1a)**	2036 (m) 2021 (s) 1927 (s) 1903 (s)
$[Re_2(\mu\text{-}OMe)_2(CO)_6(\mu\text{-}pydz)]$ (**1b**)	2027 (m) 2010 (s) 1915 (s) 1892 (s)
$[Re_2(\mu\text{-}SPh)_2(CO)_6(\mu\text{-}pydz)]$ **(2a)**	2035 (m) 2018 (s) 1936 (s) 1911 (s)
$[Re_2(\mu\text{-}SMe)_2(CO)_6(\mu\text{-}pydz)]$ (**2b**)	2029 (m) 2011 (s) 1928 (s) 1914 (s)
$[Re_2(\mu\text{-}SePh)_2(CO)_6(\mu\text{-}pydz)]$ **(3a)**	2032 (m) 2016 (s) 1938 (s) 1910 (s)
$[Re_2(\mu\text{-}SeMe)_2(CO)_6(\mu\text{-}pydz)]$ (**3b**)	2027 (m) 2009 (s) 1930 (s) 1902 (s)
$[Re_2(\mu\text{-}TePh)_2(CO)_6(\mu\text{-}pydz)]$ **(4a)**	2027 (m) 2011 (s) 1933 (s) 1912 (s)

The ν(CO) stretching modes of all the X-Me derivatives **1b**-**3b** shifted to lower wavenumbers than the analogous X-Ph derivatives, **1a**-**3a**, in agreement with the stronger donating character of the corresponding anions. The ^{1}H NMR data support the expected structures. In particular, the two resonances of the bridging pyridazine are downfield shifted by ca. 0.5-0.6 ppm compared to the free ligand, as observed in related complexes.[16]

7.2.2 Dynamic processes in solution by ^{1}H NMR

The ^{1}H NMR spectra of the three aryl derivatives **2a**, **3a** and **4a** at variable temperature present some substantial differences with each other. The spectra of the aryl-telluride derivative **4a** at all the investigated temperatures clearly show, in the aromatic region, two sets of sharp signals, with intensity ratio 1:0.14 (see the traces in figure 7.2). The two set of signals can be attributed to the two isomers depicted in figure 7.1, whose *up/up* and *up/down* structures correspond to the structures previously determined by X-ray analysis for the OC_6F_5 and the SC_6H_5 derivatives, respectively.[10] In particular, the set of signals with the greater intensities (in the order, from higher to lower chemical shifts: H_{ortho} (pydz), H_{meta} (pydz), H_{para} (Ph), H_{ortho} (Ph), H_{meta} (Ph), relative ratio 1:1:1:2:2) are consistent with a C_2 symmetry isomer, in which free rotation around the Te-C_{hypso} bonds equalizes the *ortho* and *meta* positions within each phenyl ring.

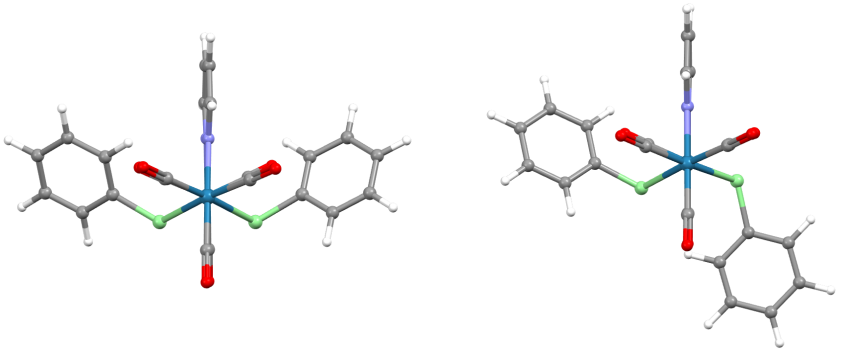

Figure 7.1 Major (C_2 symmetry - *up/up*) and minor (C_1 symmetry - *up/down*) isomers for aryl-chalcogenide complexes **2a**, **3a** and **4a**.

A 2D ^{1}H NOESY experiment at 243 K (figure 7.2) returned, for the major isomer (87.7%), the development of a NOE cross-peak between the signal of the *ortho* protons of the pyridazine ring and the signal of the *ortho* protons on the aryl rings (see figure 7.1), which confirmed

unambiguously the attribution of this set of signals to the *up/up* C_2 isomer.

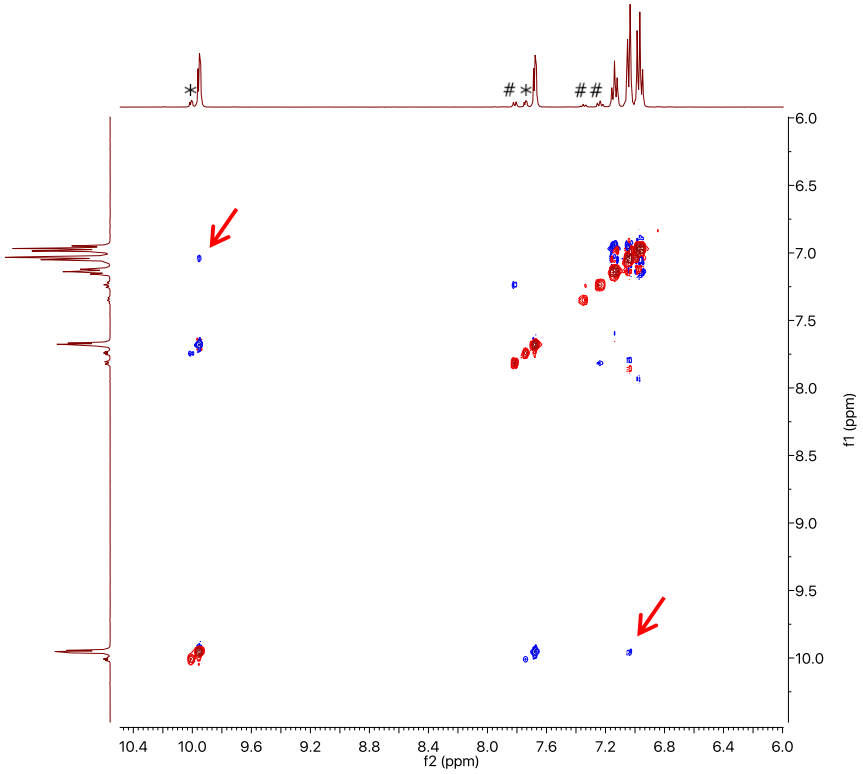

Figure 7.2 ^{1}H NOESY at 243 K for ditelluride complex **4a**. The asterisks mark the pydz signals, and the hash symbols mark the downward phenyl ring of the minor up/down isomer. The arrows indicate the cross peak discussed in the text.

The other signals with lower integrated intensities are consistent with the minor *up/down* isomer (12.3%). It also shows two pydz signals only (marked with an asterisk in figure 7.2), owing to the apparent C_s symmetry arising from the free rotation (or simple flipping) around the Te-C_{hypso} bonds. A 2D ^{1}H EXSY experiment showed that a slow interconversion between the two isomers is active on the NMR time scale only at temperatures higher than 300 K.

Contrary to **4a**, the room temperature spectra of **3a** and **2a** showed reduced number of signals. Most of the peaks of **3a** were broad, suggesting the occurrence of dynamic processes interconverting the isomers. Consequently, the appearance of the spectra was significantly temperature-dependent, although a different trend was observed for **3a** compared to **2a**.

In the case of the diselenide derivative **3a**, a limit spectrum including sharp multiplets for each isomer could be observed only at temperatures lower than 233 K, showing a larger amount (20.1%, integration ratio 1:0.26) of the minor isomer than in the case of the tellurium derivative **4a**. At higher temperatures the pyridazine resonances of the two isomers broadened and coalesced (at 273 K), generating two sharp averaged signals at room temperature.

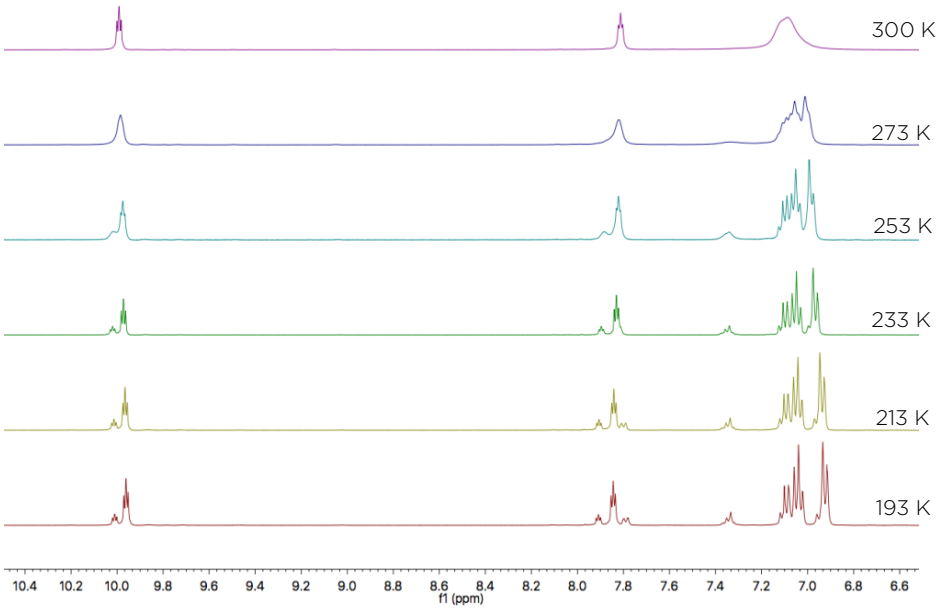

Figure 7.3 ^{1}H NMR at variable temperature for the diselenide derivative **3a**.

Within the same temperature range the aryl signals broadened and coalesced in one averaged signal, which remained very broad even at 300 K, in line with the larger chemical shift difference between the three couples of aryl signals, requiring higher exchange rate for their averaging. For the aryl-sulfide complex **2a** (see figure 7.4), the two isomers identified in the case of the homologues **3a** and **4a** were not clearly detectable. Indeed, the minor isomer was hardly detected only at a temperature as low as 168 K (see inset above the first trace of the stacked plot, which enhances 10x the intensity of the portion of spectrum in the range 7.0-7.9 ppm). The separation in two sharp sets of signals, observed for **4a** and **3a** (at least at low temperature for the latter), was not detected for **2a**, while only a slight broadening of the two pydz signals, together with a relevant broadening and separation of the aryl signals, were observed below 193 K. This variable temperature evolution of the spectra is attributable to the very fast interconversion of the two isomers *up/up* – *up/down*, occurring at an exchange rate regime still too high on the NMR time scale. The amount of the minor isomer (ca. 40%), although affected by a very large uncertainty, resulted in line with the increasing trend observed moving from Te to Se derivatives.

By comparing the data for the three chalcogenide derivatives, we can conclude that the *up/up* – *up/down* interconversion process is favoured when moving from Te to S, being in a very slow regime on the NMR time scale also at 300 K for the Te derivative, and being in an intermediate situation for Se derivative (showing already mediated signals at room temperature which separate in two distinct set of signals on lowering the temperature), and reaching the faster process exchange in the S derivative. In all cases, the aryl rings freely rotate around the S-C_q bond at any temperature. The trend is explained by

taking into account the different sp character of the orbital hybridization of the chalcogenide, which passes from pure sp^2 character in the O derivative[10] to a growing sp^3 character when moving from S to Se and Te, thus constraining the Re-X-Ph angles (X = chalcogenide) along the series and increasing the steric crowding with the CO ligands.

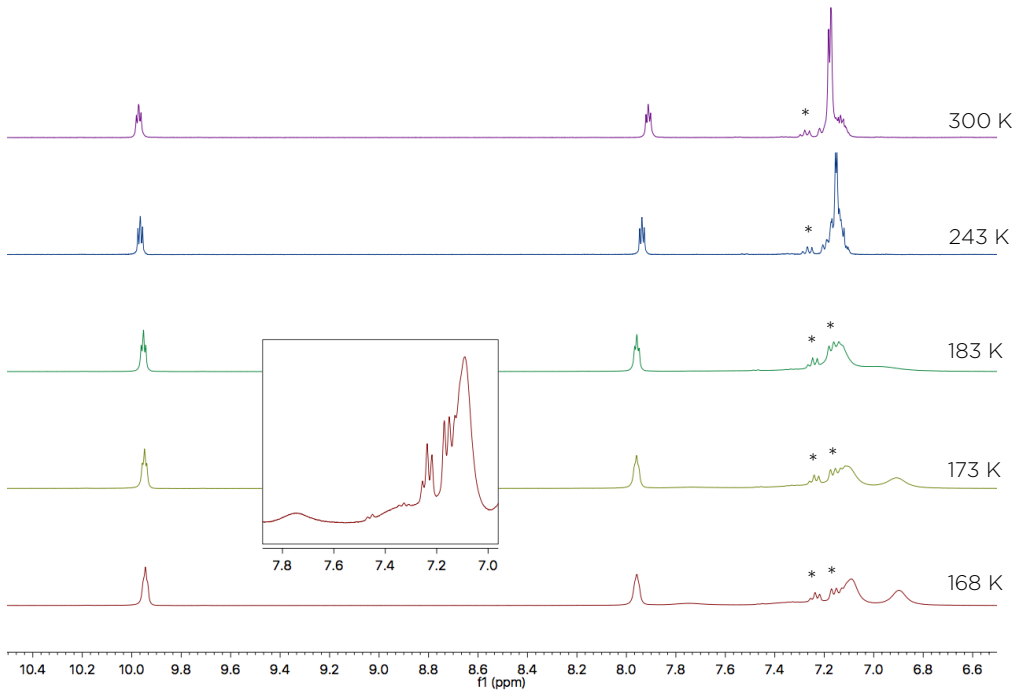

Figure 7.4 ^{1}H NMR at variable temperature for disulfide derivative **2a** (sharp signals overlapping the phenyl signals marked with an asterisk indicate an impurity). Inset: 10x enhancement of 168 K trace, range 7.0-7.9 ppm.

Preliminary DFT calculations supported and confirmed this interpretation. In fact, the energy difference between the two isomers *up/up* and *up/down* increases from S to Se and Te (1.5, 5.9 and 8.0 kJ, respectively), and the activation barrier showed the same trend (calculated $\Delta H^{\#}$ = 37.7, 63.8, 87.9 kJ/mol for S, Se and Te, respectively).

7.2.3 Electrochemical characterization

Figure 7.5 shows the results of cyclic voltammetry (CV) analyses of the complexes in acetonitrile solution, while the most significant CV features are reported in table 7.2.

The first reduction peaks are localized for all complexes on their common pyridazine ligand, as already observed for related complexes,[10,16] and therefore are quite similar both in shape and potential value. The reduction is monoelectronic and reversible, both from the chemical (symmetrical return peaks, stable products) and the electrochemical one (facile transfer of a single electron, which is taken into account by the ~57 mV half-peak widths together with the almost-zero E_p versus log ν slopes) point of view, thus indicating very fast formation of a stable radical anion.

In our former study,[16] the first oxidation site was found to be localized on the metal core and, therefore, it was strongly affected by the nature of the ancillary ligands, as confirmed also by the DFT computations.[16] However, a very different behaviour in the oxidation process has been observed between the dinuclear complexes containing $^-$OR anions and those containing the other chalcogenide counterparts.

As previously reported, in the OR derivatives a close sequence of two monoelectronic peaks is observed. In the case of the alkyl derivative **1b**, the first oxidation peak tends to be chemically irreversible at low scan rates, while the phenolato complex **1a** shows a combination of an irreversible first peak followed by a reversible second peak over the whole scan rate range explored.[10]

On the contrary, in the chalcogenide series **2-4** only one oxidative peak, chemically and electrochemically reversible, is observed, as in the halide derivatives.[12]

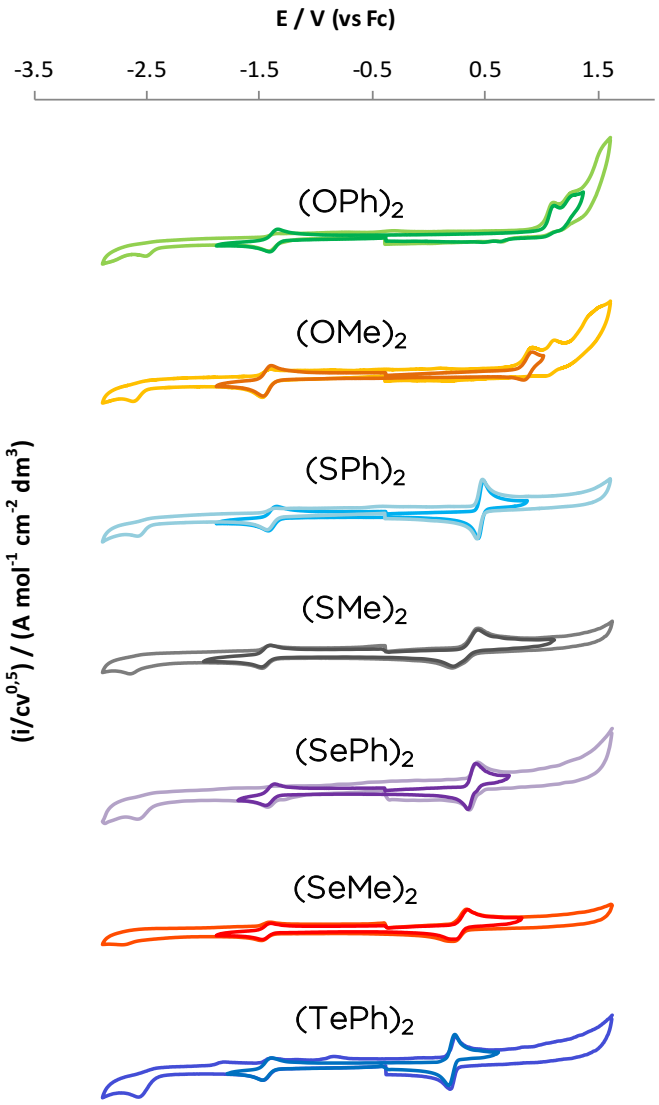

Figure 7.5 Full scan (thin line) and HOMO-LUMO (bold line) CV curves for **1-4a** complexes.

Table 7.2 First reduction and oxidation[a] peak potentials ($E_{p,c}$ and $E_{p,a}$), electrochemical (ΔE_e) and spectroscopic (ΔE_s)[b] energy gaps of the complexes **1-4a**. Potentials are referred to the $Fc^+|Fc$ couple[c] in the operating medium (ACN, 0.1 M $TBAPF_6$). Scan rate 0.2 V s^{-1}.

Complex	X	$E_{p,c}$ [V]	$E_{p,a}$ [V]	E_{LUMO} [eV]	E_{HOMO} [eV]	ΔE_e [eV]	ΔE_s [eV]
1a	OPh	-1.416	1.100	-3.38	-5.90	2.52	3.38
1b	OMe	-1.475	0.911	-3.33	-5.71	2.39	3.36
2a	SPh	-1.431	0.473	-3.37	-5.27	1.90	3.07
2b	SMe	-1.440	0.332	-3.36	-5.13	1.77	3.12
3a	SePh	-1.403	0.385	-3.40	-5.18	1.78	2.95
3b	SeMe	-1.446	0.250	-3.35	-5.05	1.70	3.05
4a	TePh	-1.429	0.212	-3.37	5.01	1.64	2.87

[[a] First oxidation peak potential not located on the metal core, [b] The spectroscopic (ΔE_s) energy gaps is the energy associated to the electronic transition determined from the maximum of the MLCT absorption band, [c] $Fc^+|Fc$ potential is 0.385 V vs. SCE in acetonitrile solution]

The neat ~30 mV peak width indicates that this process corresponds to a bielectronic oxidation in which a simultaneous two-electron transfer occurs, rather than two monoelectronic processes. In agreement with the stronger donating power of the X-Me anions (X = O, S, Se), the oxidation potential of the alkyl derivatives **1b-3b** are lower than the corresponding aryl complexes **1a-3a**.

An interesting correlation is observed by plotting the peak potential values *vs.* the wavenumbers of the **ν**(CO) stretching at the highest frequency, which are reliable indicators of the electron density on the metal atoms (see figure 7.6). The chalcogenide derivatives follow the same trend of the halides, whereas the OR derivatives lie on a different line. This behaviour could be related to the hard-soft nature of the bridging ancillary ligands.

In fact, the softer $^{-}$SR, $^{-}$SeR and $^{-}$TeR anions can better stabilize the cationic products, favouring the simultaneous loss of two electrons instead of two mono-electronic oxidations, as observed in the case of the harder $^{-}$OR donors.

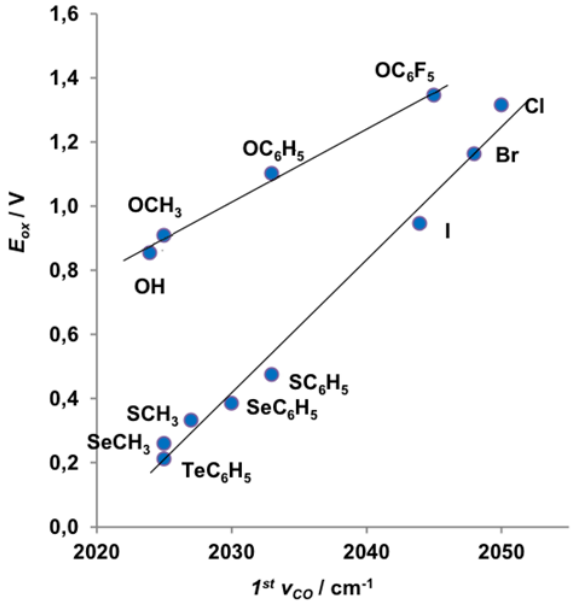

Figure 7.6 Plot of the first oxidation peak (in ACN) versus the wavenumbers of the highest energy ν(CO) band (in ACN).

The last columns of table 7.2 show the electrochemical and the spectroscopic HOMO-LUMO gaps. It is interesting to note that while the electrochemical gap parallels the trend of the first oxidation potential, the same behaviour is not observed for the spectroscopic parameter, suggesting that the electronic transition associated to the absorption maximum is not strictly a HOMO-LUMO transition. Anyway, the energy gap for the TePh derivative **4a** is the smallest in the series.

7.2.4 Photophysical characterization

The UV-Vis absorption spectra of the three dyes in diluted CH_2Cl_2 solution are reported in table 7.3, while figure 7.7 shows the corresponding spectra. At room temperature all the complexes exhibit an intense absorption band at high energy (about 270 nm), whose position is independent of the polarity of the solvent. In addition, a less intense broad and featureless absorption band is observed for all the complexes, covering a large part of the visible spectrum between 350 nm and 550-600 nm.

This band can be attributed to metal-ligand-to-ligand charge transfer (MLLCT) transitions, and the significant contribution of the ancillary ligands to the metal-centered HOMO set (indicated by the DFT computations in the related OR and SR derivatives)[10] is supported by the strong red-shift of the absorption maximum on moving from the OR to the TeR derivatives. This broad band arises from the convolution of multiple transitions, as confirmed by the more or less pronounced shoulders observed at longer wavelengths.

It is interesting to note that, in contrast with the electrochemical data, for the alkyl derivatives **1b-3b** the absorption maximum is blue-shifted in comparison with the corresponding aryl derivatives **1a-3a**. This feature strongly underlines that, as already observed for other analogous complexes,[16] the electronic transitions responsible for the MLCT absorption band are not HOMO-LUMO but would rather involve as starting orbitals the metal-centred HOMO–n set and, as final orbitals, the two low-lying π^* orbitals of the diazine, LUMO and LUMO+1.

Table 7.3 The low energy absorption band for complexes **1-4a**.

Complex	*X*	$\lambda_{max}{}^{a}$ [nm]	ε [10^4 M^{-1} cm^{-1}]	$\lambda_{max}{}^{b}$ [nm]
1a	OPh	367	0.69	
1b	OMe	369	0.87	
2a	SPh	403	0.57	382
2b	SMe	397	1.1	
3a	SePh	421	0.69	391
3b	SeMe	406	0.85	382
4a	TePh	433	0.71	396

[^{a} CH_2Cl_2 solution (1×10^{-5} M), ^{b} CH_3CN solution (1×10^{-5} M)]

The charge transfer character of the low energy band is also supported by the observed solvatochromic behavior. Indeed, a significant blue-shift of the absorption maximum has been observed in a more polar solvent, such as acetonitrile (see table 7.3).

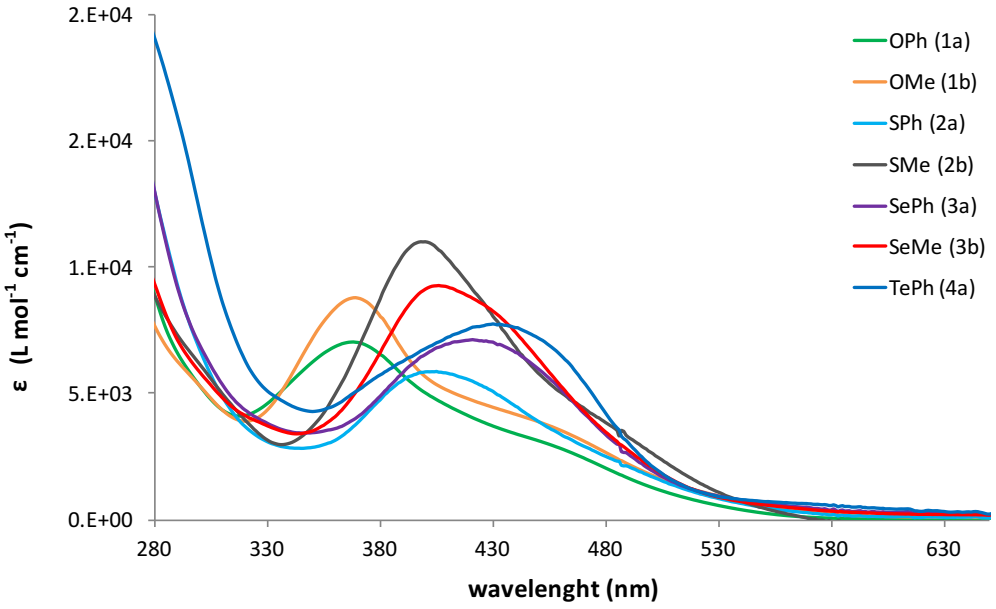

Figure 7.7 UV-Vis absorption spectra of **1-4a** complexes in CH_2Cl_2 solution.

Upon optical excitation at 450 nm at room temperature in CH_2Cl_2, only the complexes with OR ancillary ligands (**1a** and **1b**) showed broad and featureless emission band in the range 608-708 nm.[10] The emission for the other complexes **2-4a** is instead completely negligible.

7.3 Conclusions

We have demonstrated the spontaneous association of six components into a dinuclear complex containing pyridazine ligands, via the tandem addition of a RX-XR bond (X = S, Se, Te and R = Me, Ph) across the Re-Re bond. The reaction of $[Re_2(CO)_{10}]$ with dialkyl- or diaryl-dichalcogenides, in presence of one equivalent of pyridazine ligand, affords the corresponding dinuclear complexes $[Re_2(\mu\text{-}XR)_2(CO)_6(\mu\text{-diazine})]$ containing XR anions as ancillary ligands in high yields (ca. 85%). In addition to the one-pot synthesis, we managed to define a general two-step reaction involving the synthesis of the heterocubane $[Re_4(\mu_3\text{-}XR)_4(CO)_{12}]$ intermediate, containing the XR anions bridging on three metal centers, generated by the reaction of $[Re_2(CO)_{10}]$ and the dichalcogenide only. In the literature very few reports are available for the spontaneous formation of molecular cubanes and we have demonstrated that the same synthetic route reported for the sulfur-bridged cubanes can be extended to all the other chalcogenide anions. This heterocubane can be further reacted with any bridging diazine to give the corresponding dinuclear complex, following a *[2+2]* fragmentation pathway without any spectroscopically recognizable intermediate. The starting idea that the use of potentially bridging ligands might favor the symmetric *[2+2]* fragmentation, already observed for the hydride $[H_4Re_4(CO)_{12}]$[15] and the μ-hydroxo $[Re_4(\mu\text{-}OH)_4(CO)_{12}]$[10] clusters, has been further

confirmed also for these tetranuclear clusters. The molecular structure of the complexes has been elucidated by single crystal XRD analysis, and a combination of TD-DFT calculations and low temperature NMR studies clarified the presence of different structural isomers with different abundance in solution for each chalcogen, as well as the fluxional processes between them. A complete electrochemical and photophysical investigation showed the progressive narrowing of the HOMO-LUMO gap going from O to Te, arising from an increase of the HOMO level with a consequent important red-shift of the absorption maximum. This is in line with the decreasing electron-withdrawing strength of the chalcogenide bridging ligand. From the electrochemical point of view S, Se and Te complexes display a bi-electronic reversible oxidation peak, while O derivatives show two mono-electronic irreversible oxidation peaks. No photoluminescence is observed upon optical excitation with the only exception of the OPh derivative, displaying a moderate luminescence at 608 nm with Φ = 0.6%.

7.4 Experimental

General methods

All the reagents were purchased from Aldrich and used as received. All the reactions were performed under an inert N_2 atmosphere. All the solvents have been deoxygenated and dried by standard methods before use, toluene and mesitylene were distilled on $Na_{(s)}$, CH_2Cl_2 on P_2O_5. Commercial deuterated solvents were used as received. Column chromatography was performed using Alfa Aesar silica gel 60 (0.032–0.063 mm). ^{1}H NMR spectra were recorded on a Bruker DRX-400 MHz instrument by using the residual signals δ = 7.28 ppm from $CDCl_3$ or δ = 5.32 ppm from CD_2Cl_2 as internal references. Where isomers are present, the signals here reported belong to the major isomer for each complex. IR spectra in solution were acquired on a Bruker Vector 22 FT spectrophotometer.

Electrochemical measurements

see chapter 3.

Spectroscopy

see chapter 3.

Synthesis of $[Re_2(\mu\text{-}SPh)_2(CO)_6(\mu\text{-}pydz)]$ (2a). 130 mg (0.20 mmol) of Re_2CO_{10} and 43.5 mg (0.20 mmol) of diphenyldisulfide are dissolved in 8 mL of anhydrous toluene. 15 µL (0.2 mmol) of pyridazine are added to the reaction mixture, which is left stirring under reflux for 10 days, slowly turning black. The solution is evaporated to dryness under

vacuum. The orange solid remains are dissolved in CH_2Cl_2 and precipitated with n-hexane. The precipitate is washed with n-hexane (3 x 5 mL), yielding 150 mg (0.178 mmol) of orange powder (yield 89%). IR (CH_2Cl_2) ν(CO): 2034 (m), 2018 (vs), 1937 (s), 1911 (s) cm^{-1}, ^1H NMR: ($CDCl_3$, 300K, 400 MHz) δ_H (ppm) 9.94 (m, 2H, $H_{ortho\ pydz}$), 7.86 (m, 2H, $H_{meta\ pydz}$), 7.06-7.24 (m, 12H, $_{phenyl}$)

One-pot synthesis of $[Re_2(\mu\text{-}SMe)_2(CO)_6(\mu\text{-}pydz)]$ (2b). 100 mg (0.153 mmol) of Re_2CO_{10} are dissolved in 8 mL of anhydrous toluene. 14 μL (0.153 mmol) of dimethyldisulfide and 11 μL (0.153 mmol) of pyridazine are added to the reaction mixture, which is left stirring under reflux for 15 days. The solution is evaporated to dryness under vacuum. The solid remains are dissolved in CH_2Cl_2 and precipitated with n-hexane. The precipitate is washed with n-hexane (3 x 5 mL) and then purified through column chromatography (toluene/EtOAc 9:1) yielding 57 mg (0.08 mmol) of product (yield 52%). IR (CH_2Cl_2) ν(CO): 2029 (m), 2011 (vs), 1928 (s), 1904 (s) cm^{-1}, ^1H NMR: ($CDCl_3$, 300K, 400 MHz) δ_H (ppm) 10.01 (m, 2H, $H_{ortho\ pydz}$), 7.86 (m, 2H, $H_{meta\ pydz}$), 2.23 (s, 6H, CH_3)

Synthesis of $[Re_4(\mu_3\text{-}SMe)_4(CO)_{12}]$ (2). 75 mg (0.115 mmol) of Re_2CO_{10}, 10.2 μL (0.115 mmol) of dimethyldisulfide are dissolved in 6 mL of anhydrous toluene. 50 μL of dimethylformamide are then added to the reaction mixture, which is left stirring under reflux overnight. The solution is evaporated to dryness under vacuum. The dark brown solid remains are purified through column chromatography (CH_2Cl_2/n-hexane 8:2) yielding 17 mg (0.014 mmol) of product (yield 23%). IR (CH_2Cl_2) ν(CO): 2029 (s), 1942 (s) cm^{-1}, ^1H NMR: (CD_2Cl_2, 300K, 400 MHz) δ_H (ppm) 2.08 (m, 12H, CH_3)

Synthesis of $[Re_2(\mu\text{-}SMe)_2(CO)_6(\mu\text{-}pydz)]$ from $[Re_4(\mu_3\text{-}SMe)_4(CO)_{12}]$ (2b). 5 mg (0.014 mmol) of $[Re_4(\mu_3\text{-}SMe)_4(CO)_{12}]$ are dissolved in 5 mL of anhydrous toluene. 2 µL (0.027 mmol) of pyridazine is added to the reaction mixture, which is left stirring under reflux for ten days, slowly turning red. The solution is evaporated to dryness under vacuum. The dark orange solid remains are purified through column chromatography (CH_2Cl_2/n-hexane 8:2) yielding 13 mg (0.018 mmol) of microcrystalline powder (yield 77%). IR (CH_2Cl_2) ν(CO): 2028 (m), 2011 (vs), 1929 (s), 1903 (s) cm^{-1}, ^1H NMR: (CD_2Cl_2, 300K, 400 MHz) δ_H (ppm) 10.03 (m, 2H, $H_{ortho\ pydz}$), 7.89 (m, 2H, $H_{meta\ pydz}$), 7.14 (m, 6H, $_{phenyl}$), 2.21 (s, 6H, CH_3)

Synthesis of $[Re_2(\mu\text{-}SePh)_2(CO)_6(\mu\text{-}pydz)]$ (3a). 100 mg (0.153 mmol) of Re_2CO_{10} and 48 mg (0.153 mmol) of diphenyldiselenide are dissolved in 7 mL of anhydrous mesitylene. 11 µL (0.153 mmol) of pyridazine are added to the reaction mixture, which is left stirring under reflux for 2 days, slowly turning dark brown. The solution is evaporated to dryness under vacuum. The dark orange solid remains are dissolved in CH_2Cl_2 and precipitated with n-hexane. The precipitate is washed with n-hexane (3 x 5 mL), yielding 116 mg (0.125 mmol) of microcrystalline powder (yield 82%). IR (CH_2Cl_2) ν(CO): 2032 (m), 2016 (vs), 1938 (s), 1910 (s) cm^{-1}, ^1H NMR: ($CDCl_3$, 300K, 400 MHz) δ_H (ppm) 9.95 (m, 2H, $H_{ortho\ pydz}$), 7.75 (m, 2H, $H_{meta\ pydz}$), 6.91-7.16 (m, 12H, $_{phenyl}$)

Synthesis of $[Re_2(\mu\text{-}SeMe)_2(CO)_6(\mu\text{-}pydz)]$ (3b). 100 mg (0.153 mmol) of Re_2CO_{10} are dissolved in 7 mL of anhydrous mesitylene. 15 µL (0.153 mmol) of dimethyldiselenide and 11 µL (0.153 mmol) of pyridazine are added to the reaction mixture, which is left stirring under reflux for 2 days. The solution is evaporated to dryness under vacuum. The solid remains are dissolved in CH_2Cl_2 and precipitated with n-hexane. The

precipitate is washed with n-hexane (3 x 5 mL). The resulting powder is slowly recrystallized from CH_2Cl_2/n-hexane yielding 45 mg (0.055 mmol) of product (yield 36%). IR (CH_2Cl_2) ν(CO): 2027 (m), 2009 (vs), 1930 (s), 1902 (s) cm^{-1}, ^1H NMR: ($CDCl_3$, 300K, 400 MHz) δ_H (ppm) 10.07 (m, 2H, $H_{ortho\ pydz}$), 7.80 (m, 2H, $H_{meta\ pydz}$), 1.74 ppm (s, 6H, CH_3)

One-pot synthesis of [$Re_2(\mu$-TePh)$_2(CO)_6(\mu$-pydz)] (4a). 100 mg (0.153 mmol) of Re_2CO_{10} and 63 mg (0.153 mmol) of diphenylditelluride are dissolved in 8 mL of anhydrous mesitylene. 11 μL (0.153 mmol) of pyridazine are added to the reaction mixture, which is left stirring under reflux for 1 day, slowly turning black. The solution is evaporated to dryness under vacuum. The dark red solid remains are dissolved in CH_2Cl_2 and precipitated with n-hexane. The precipitate is washed with n-hexane (3 x 5 mL) and then purified through column chromatography (CH_2Cl_2/n-hexane 8:2) yielding 113 mg (0.11 mmol) of microcrystalline powder (yield 72%). IR (CH_2Cl_2) ν(CO): 2027 (m), 2011 (vs), 1933 (s), 1912 (s) cm^{-1}, ^1H NMR: (CD_2Cl_2, 300K, 400 MHz) δ_H (ppm) 9.95 (m, 2H, $H_{ortho\ pydz}$), 7.65 (m, 2H, $H_{meta\ pydz}$), 7.16 (m, 6H, $_{phenyl}$), 6.97 (m, 4H, $_{phenyl}$)

Synthesis of [$Re_4(\mu_3$-TePh)$_4(CO)_{12}$] (4). 125 mg (0.19 mmol) of Re_2CO_{10} and 78 mg (0.153 mmol) of diphenylditelluride are dissolved in 8 mL of anhydrous mesitylene. The reaction mixture is left stirring under reflux for 6 days. The solution is evaporated to dryness under vacuum. The dark brown solid remains are dissolved in CH_2Cl_2 and precipitated with n-hexane. The precipitate is washed with n-hexane (3 x 5 mL), yielding 60 mg (0.03 mmol) of product (yield 32%). IR (CH_2Cl_2) ν(CO): 2025 (s), 1936 (m) cm^{-1}, ^1H NMR: (CD_2Cl_2, 300K, 400 MHz) δ_H (ppm) 7.50 (m, 24H, $_{phenyl}$)

Synthesis of $[Re_2(\mu\text{-}TePh)_2(CO)_6(\mu\text{-}pydz)]$ from $[Re_4(\mu_3\text{-}TePh)_4(CO)_{12}]$ (4a). 15 mg (0.008 mmol) of $[Re_4(\mu_3\text{-}TePh)_4(CO)_{12}]$ are dissolved in 6 mL of anhydrous toluene. 1 µL (0.008 mmol) of pyridazine is added to the reaction mixture, which is left stirring under reflux overnight, slowly turning dark red. The solution is evaporated to dryness under vacuum. The dark orange solid remains are dissolved in CH_2Cl_2 and precipitated with n-hexane. The precipitate is washed with n-hexane (3 x 5 mL), yielding 13 mg (0.006 mmol) of microcrystalline powder (yield 77%). IR (CH_2Cl_2) ν(CO): 2026 (m), 2010 (vs), 1932 (s), 1913 (s) cm^{-1}, ^1H NMR: (CD_2Cl_2, 300K, 400 MHz) δ_H (ppm) 9.96 (m, 2H, $H_{ortho\ pydz}$), 7.67 (m, 2H, $H_{meta\ pydz}$), 7.14 (m, 6H, $_{phenyl}$), 6.97 (m, 4H, $_{phenyl}$)

References

[1] Y. Pellegrin, F. Odobel, *Coord. Chem. Rev.* **2011**, 255, 2578

[2] (a) B. Bozic-Weber, E. C. Constable, C. E. Housecroft, *Coord. Chem. Rev.* **2013**, 257, 3089; (b) M. Nazeeruddin, A. Kay, I. Rodicio, R. Humphry-Baker, E. Müller, P. Liska, N. Vlachopoulos, M. Grätzel, *J. Am. Chem. Soc.* **1993**, *115*, 6382–6390; (c) K. Kalyanasundaram, M. Grätzel, *Coord. Chem. Rev.* **1998**, *177*, 347

[3] (a) L. M. Kiefer, J.T. King, K. J. Kubarych, *Acc. Chem. Res.* **2015**, 48, 1123–1130; (b) S. Campagna, F. Puntoriero, F. Nastasi, G. Bergamini, V. Balzani, *Top Curr. Chem.* **2007**, *280*, 117

[4] L. Veronese, E. Quartapelle Procopio, F. De Rossi, T. M. Brown, P. Mercandelli, P. Mussini, G. D'Alfonso, M. Panigati, *New. J. Chem.* **2016**, 40, 2910

[5] K.D. Benkstein, J.T. Hupp, C.L. Stern, *Inorg. Chem.* **1998**, 37, 5404

[6] F. Calderazzo, R. Poli, P.F. Zanazzi, *Inorg. Chem.* **1991**, 30, 3942

[7] Vanitha, A.; Sathiya, P., Sangilipandi, S., Mobin, S. M., Manimaran, B. *J. Organomet. Chem.* **2010**, 695, 1458

[8] Vanitha, A., Mobin, S. M., Manimaran, B. *J. Organomet. Chem.* **2011**, 696, 1609

[9] B. Manimaran, A. Vanitha, M. Karthikeyan, B. Ramakrishna, S. M. Mobin, *Organometallics* **2014**, 33, 465

[10] A. Raimondi, M. Panigati, D. Maggioni, L. D'Alfonso, P. Mercandelli, P. Mussini and G. D'Alfonso, *Inorg. Chem.* **2012**, 51, 2966

[11] M. Karthikeyan, B. Manimaran, *J. Organomet. Chem.* **2014**, *769*, 130

[12] (a) M. Mauro, M. Panigati, D. Donghi, P. Mercandelli, P. Mussini, A. Sironi and G. D'Alfonso, *Inorg. Chem.* **2008**, 47, 11154; (b) M. Mauro, E. Quartapelle Procopio, Y. Sun, C.-H. Chien, D. Donghi, M. Panigati, P. Mercandelli, P. Mussini, G. D'Alfonso, L. De Cola, *Adv. Funct. Mater.* **2009**, 19, 2607; (c) M. Mauro, C.-H. Yang, C.-Y. Shin, M. Panigati, C.-H. Chang, G. D'Alfonso, L. De Cola, *Adv. Mater.* **2012**, 24, 2054

[13] Sathiyendiran, M., Liao, R. T., Thanasekaran, P., Luo, T. T., Venkataramanan, N. S., Lee, G. H., Peng, S. M., Lu, K. L. *Inorg. Chem.* **2006**, 45, 10052

[14] Liao, R. T.; Yang, W. C.; Thanasekaran, P.; Tsai, C. C.; Sathiyendiran, M.; Liu, Y. H.; Rajendran, T.; Lin, H. M.; Tseng, T. W.; Lu, K. L. *Chem. Commun.* **2008**, 3175

[15] M. Panigati, D. Donghi, G. D'Alfonso, P. Mercandelli, A. Sironi, L. D'Alfonso, *Inorg.Chem.* **2006**, *45*, 10909

[16] M. Panigati, M. Mauro, D. Donghi, P. Mercandelli, P. Mussini, L. De Cola and G. D'Alfonso, *Coord. Chem. Rev.* **2012**, *256*, 1621

CHAPTER 8

Neutral Mn(I) complexes: synthesis, electrochemical and spectroscopic characterization

Abstract

Ten new neutral dinuclear manganese complexes of general formula [$Mn_2(\mu\text{-}X)_2(CO)_6(\mu\text{-pydz})$] have been synthesized, where X = halides, $^-$OMe, $^-$SMe, $^-$SPh and $^-$TePh and pydz = 1,2 diazine and 4,5-bipentylpyridazine. The novel compounds have been characterized by means of spectroscopic techniques (^{1}H NMR, FTIR, and UV-Vis) and their photophysical and electrochemical properties discussed in comparison with the analogous dinuclear rhenium counterparts.

8.1 Introduction

Manganese, as the 3rd most abundant transition metal in the earth's crust, is an appealing alternative to rhenium.[1] Although the chemistry of rhenium complexes and their use in different application fields, has been extensively investigated, the comparable manganese chemistry is still at the beginning. In particular, manganese carbonyl compounds have been recently studied for a number of applications, such as electrocatalysts for CO_2 reduction[2] and photo-CO releasing molecules.[3]

In the framework of polynuclear systems, even if *fac*-$Mn(CO)_3$-core based supramolecular rectangles have been recently reported and used as sensor for various organic compounds,[4] to the best of our knowledge no other polynuclear carbonyl manganese complexes have been reported to date. Therefore, in this research work we investigate the synthesis of novel dinuclear manganese complexes, analogous to the dinuclear rhenium counterparts, having general formula $[Mn_2(\mu\text{-}X)_2(CO)_6(\mu\text{-pydz})]$, where X are halides or chalcogenides anions and pydz is a 1,2-diazine containing alkyl substituents in the β positions. We also compare their electrochemical and spectroscopic properties with those already known for the analogous Re(I) complexes and preliminary tests on the electrocatalytic production of H_2 have been performed.

8.2 Results and discussion

8.2.1 Synthesis of the complexes

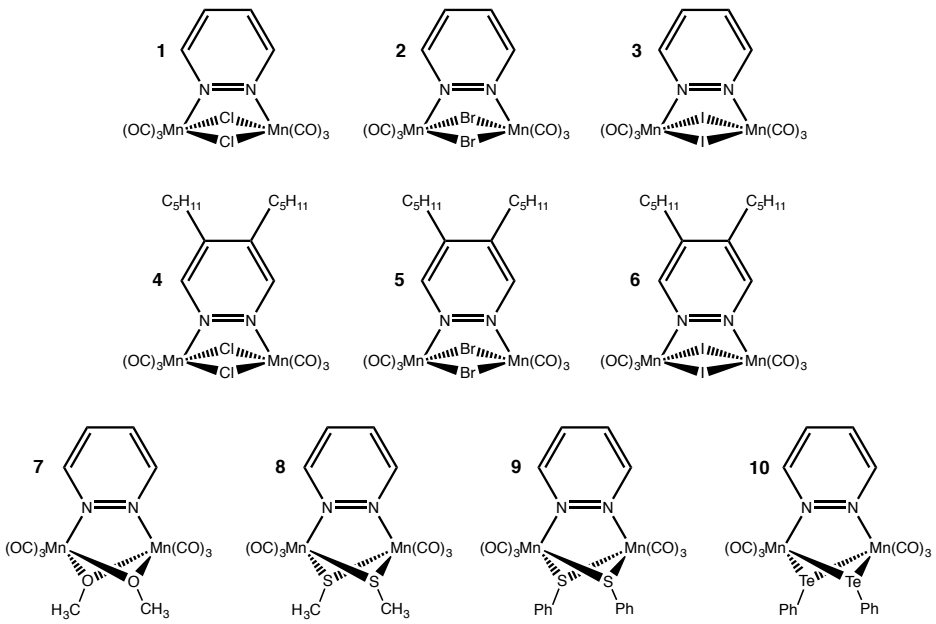

Chart 8.1 Structures of the investigated Mn(I) dinuclear complexes.

The structures of the ten new manganese complexes are depicted in chart 8.1. Two series of complexes, namely **1-3** and **4-6** are characterized by the presence of halide ancillary ligands. Complexes **1-3** contain a bare pyridazine ring, while complexes **4-6** are endowed with the electron-rich 4,5-bipentylpyridazine, already employed in the Re(I) complexes found to be active towards CO_2 electroreduction.[5] The last series, namely **7-10**, resembles instead the class of complexes investigated in chapter 7, bearing two chalcogenide anions as ancillary bridging ligands and an unsubstituted pyridazine.

The synthetic approaches used for the synthesis of the manganese complexes here investigated are depicted in schemes 8.1 and 8.2. Manganese is more reactive than rhenium; therefore, milder synthetic conditions have been adopted compared with the analogous rhenium complexes. Moreover, all the reactions and subsequent purification processes have been carried out in the dark, due to the high photosensitivity of manganese complexes.

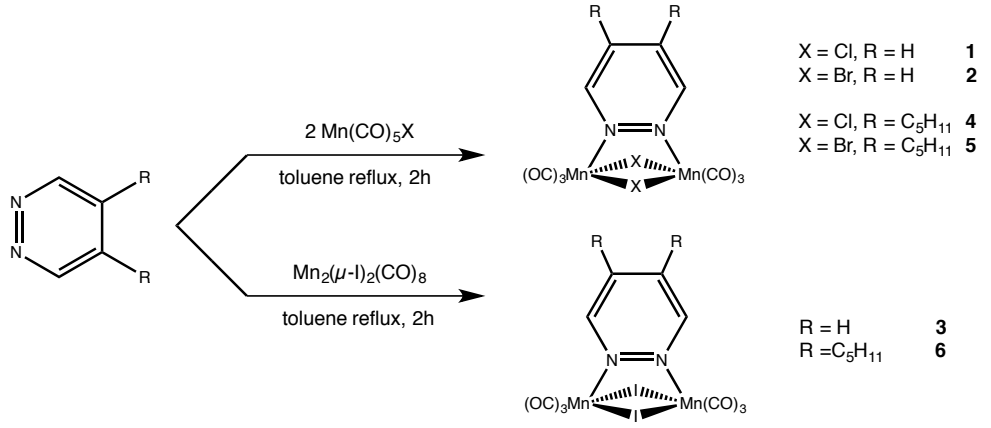

Scheme 8.1 Procedure for the synthesis of halide derivatives 1-6.

The $[Mn_2(\mu\text{-}X)_2(CO)_6(\mu\text{-pydz})]$ (X = Cl, Br) complexes were obtained by reacting equimolar amounts of pyridazine (1-2) or 4,5-bipentylpyridazine (4-5) and $Mn(CO)_5X$ in toluene solution at different temperature (room temperature in the case of chloride derivatives 1 and 4, and at 60 to 80 °C in the case of the bromide complexes, 2 and 5). Iodine derivatives 3 and 6, were instead prepared starting from the dinuclear precursor $[Mn_2(\mu\text{-}I)_2(CO)_8]$, that was synthesized by reacting $[Mn_2CO_{10}]$ with I_2 in a flask sealed under vacuum and kept at 120°C for 24 hours. This dinuclear precursor, in the presence of one equiv. of each pyridazine ligand, gave rise to the corresponding diazinic derivatives after 2 hours of reflux in toluene.

The chalcogenide-bridged series **7-10** was instead obtained through the one-pot synthesis via "orthogonal bonding approach" previously discussed for the rhenium dinuclear analogues (see chapter 7). Hence, two ligands were coordinate simultaneously and orthogonally (one axial and one equatorial) to the manganese dinuclear skeleton, given by Mn_2CO_{10} (see scheme 8.2).

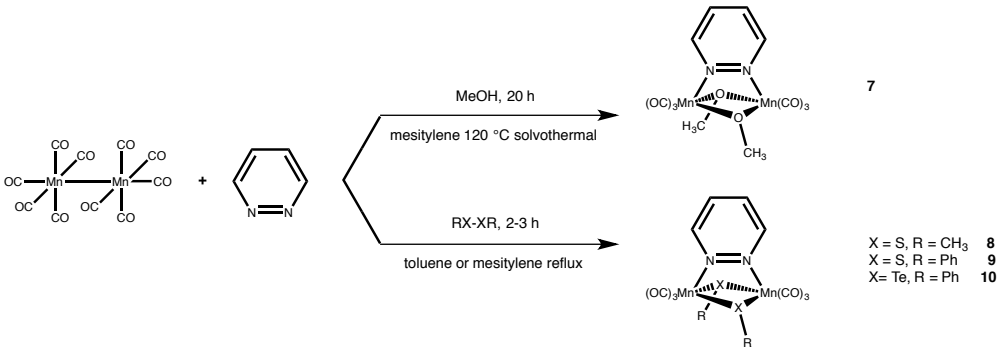

Scheme 8.2 Procedure for the synthesis of the chalcogenide derivatives **7-10**.

As for the dirhenium methoxo complex, methanol was used as source of ˉOMe anions to get complex **7**. To avoid evaporation of the reagent the reaction was carried out in a sealed solvothermal bomb at 120°C in toluene solution. Disulfide complexes **8** and **9** and the ditelluride derivative **10** have been obtained following the synthetic procedures already reported for the rhenium complexes. Notably, even for the heaviest chalcogenide the higher reactivity of manganese allowed to work at lower temperature using therefore toluene as solvent instead of mesitylene. The number and the intensity of the IR bands in the ν(CO) region are consistent with the idealized C_{2V} symmetry of these complexes, as in the case of the dirhenium complexes. Five stretching bands are expected according to group theory, but the overlapping of one B_2 mode with one A_1 gives rise to a four-band pattern, with s, vs, s, s respective intensity.

Table 8.1 IR ν (CO) stretching bands for the investigated complexes **1-10** in CH_2Cl_2.

COMPLEX	IR **ν**(CO) [cm^{-1}]
$[Mn_2(\mu\text{-}Cl)_2(CO)_6(\mu\text{-}pydz)]$ (**1**)	2054 (s) 2036 (vs) 1966 (s) 1935 (s)
$[Mn_2(\mu\text{-}Br)_2(CO)_6(\mu\text{-}pydz)]$ (**2**)	2050 (s) 2033 (vs) 1964 (s) 1935 (s)
$[Mn_2(\mu\text{-}I)_2(CO)_6(\mu\text{-}pydz)]$ (**3**)	2041 (s) 2025 (vs) 1959 (s) 1933 (s)
$[Mn_2(\mu\text{-}Cl)_2(CO)_6(\mu\text{-}4,5\text{-}(C_5H_{11})\text{-}pydz)]$ (**4**)	2052 (s) 2035 (vs)1962 (s) 1932 (s)
$[Mn_2(\mu\text{-}Br)_2(CO)_6(\mu\text{-}4,5\text{-}(C_5H_{11})\text{-}pydz)]$ (**5**)	2048 (s) 2032 (vs) 1960 (s) 1932 (s)
$[Mn_2(\mu\text{-}I)_2(CO)_6(\mu\text{-}4,5\text{-}(C_5H_{11})\text{-}pydz)]$ (**6**)	2039 (s) 2024 (vs) 1955 (s) 1930 (s)
$[Mn_2(\mu\text{-}OMe)_2(CO)_6(\mu\text{-}pydz)]$ (**7**)	2033 (s) 2014 (vs) 1934 (s) 1906 (s)
$[Mn_2(\mu\text{-}SMe)_2(CO)_6(\mu\text{-}pydz)]$ (**8**)	2026 (s) 2005 (vs) 1940 (s) 1914 (s)
$[Mn_2(\mu\text{-}SPh)_2(CO)_6(\mu\text{-}pydz)]$ (**9**)	2031 (s) 2012 (vs) 1948 (s) 1923 (s)
$[Mn_2(\mu\text{-}TePh)_2(CO)_6(\mu\text{-}pydz)]$ (**10**)	2014 (s) 1996 (vs) 1934 (s) 1919 (s)

As already observed for the rhenium complexes, also in these Mn analogues the CO stretching bands act as indicators of the electron density on the metals, since the position of the bands is affected by the strength of the π-back donation. Accordingly, significant shifts are observed on varying the ancillary ligands X within the different series. For instance, the position of the highest frequency A_1 mode in the series of pydz complexes **1-3** varies according to the trends 2054 (Cl) > 2050 (Br) > 2041 (I) and 2033 (OMe) > 2014 (TePh) cm^{-1} in the series **7-10**, in agreement with the Mn atoms becoming progressively more electron-rich as the donor power of the ancillary ligand increases. Interestingly, variation of the substituents on the diazine ligand did not cause significant variation of the position of the ν(CO) bands in the halide series.

In the ^{1}H NMR spectra, the resonances of the protons on the diazine ligands are downfield shifted when coordinated to the metal, compared to the free ligands, as it also happens in the case of the rhenium dinuclear complexes and in agreement with a reduced electron density on the heterocyclic ring. In addition, the position of the resonances is affected by the nature of the substituents on the diazine ring and, to a lower extent, of the ancillary ligands. As in the case of rhenium complexes, a consistent upfield shift is observed when introducing the electron rich 4,5-bipentylpyridazine ligand compared to the unsubstituted pyridazine (see table 8.2).

Table 8.2 ^{1}H NMR resonances (300K, CD_2Cl_2) for protons on the diazine ring upon modulation of the substituents and the ancillary ligands.

COMPLEX	$^1H_{diazine}$ ∂ (ppm)
$[Mn_2(\mu\text{-}Cl)_2(CO)_6(\mu\text{-pydz})]$ (**1**)	α 10.01, β 7.94
$[Mn_2(\mu\text{-}Br)_2(CO)_6(\mu\text{-pydz})]$ (**2**)	α 10.06, β 7.90
$[Mn_2(\mu\text{-}I)_2(CO)_6(\mu\text{-pydz})]$ (**3**)	α 10.02, β 7.78
$[Mn_2(\mu\text{-}Cl)_2(CO)_6(\mu\text{-4,5-}(C_5H_{11})\text{-pydz})]$ (**4**)	α 9.64
$[Mn_2(\mu\text{-}Br)_2(CO)_6(\mu\text{-4,5-}(C_5H_{11})\text{-pydz})]$ (**5**)	α 9.68
$[Mn_2(\mu\text{-}I)_2(CO)_6(\mu\text{-4,5-}(C_5H_{11})\text{-pydz})]$ (6)	α 9.63
$[Mn_2(\mu\text{-OMe})_2(CO)_6(\mu\text{-pydz})]$ (**7**)	α 10.15, β 8.32
$[Mn_2(\mu\text{-SMe})_2(CO)_6(\mu\text{-pydz})]$ (**8**)	α 10.04, β 7.68
$[Mn_2(\mu\text{-SPh})_2(CO)_6(\mu\text{-pydz})]$ (**9**)	α 10.05, β 7.77
$[Mn_2(\mu\text{-TePh})_2(CO)_6(\mu\text{-pydz})]$ (**10**)	α 9.85, β 7.45

8.2.2 Spectroscopic characterization

The UV-Visible absorption spectra of the investigated manganese complexes, depicted in figure 8.1, exhibit two main absorption features, as already reported for the rhenium complexes. The low energy band, with maxima in the range 395-475 nm and tails up to 550 nm (ε ranging from 5.7 to 8.8x10^3) is attributed to the metal-to-ligand-charge-transfer (^{1}MLCT) transitions, also according to the shift of the maxima depending on the solvent polarity. As expected for a MLCT transition, the position of the maximum is highly dependent on the nature of the ancillary ligands, as well as on the nature and position of the substituents on the diazine rings.

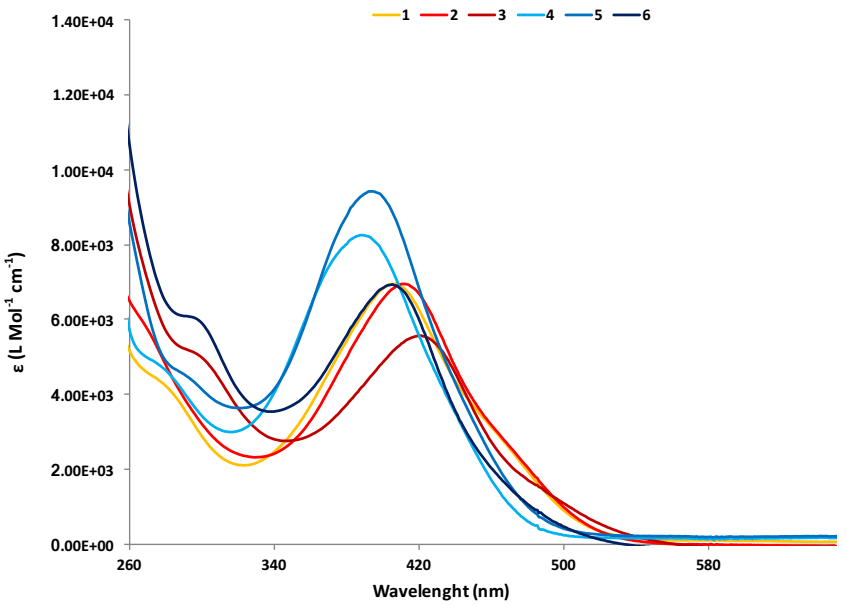

Figure 8.1 UV-Vis absorption spectra in CH_2Cl_2 solution of the **1-6** halide derivatives.

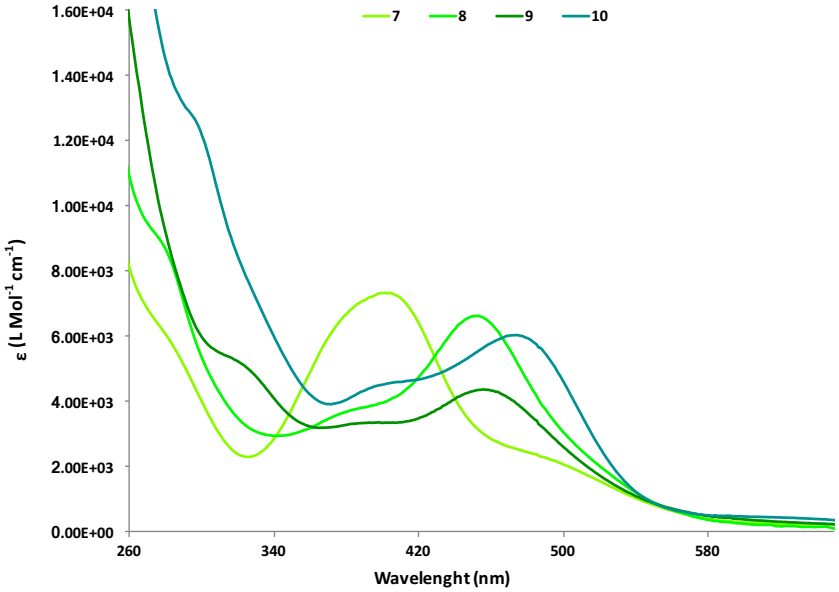

Figure 8.2 UV-Vis absorption spectra in CH_2Cl_2 solution of the **7-10** chalcogenide derivatives.

In resemblance to the dirhenium analogues, a red-shift is observed moving from chloride (**1**) to iodide (**3**) derivatives, in agreement with the decrease of the electronegativity of the halide ancillary ligand. We can state that upon modulation of the ancillary ligands the HOMO energy level is changed. The same intra-series red-shift is observed, to a much greater extent, also in the series **7-10** when moving from oxygen to tellurium. The least electronegative ligand telluride induces a high electron density on the metal sites, therefore resulting in a marked red-shifted absorption maximum. On the contrary, a blue shift in the absorption maximum is observed upon changing the substituents on the diazine ring. Actually, the LUMO levels of the **4-6** complexes, containing the electron rich 4,5-bipentylpyridazine ligand, are slight destabilized with respect to complexes **1-3**, containing the unsubstituted pyridazine.

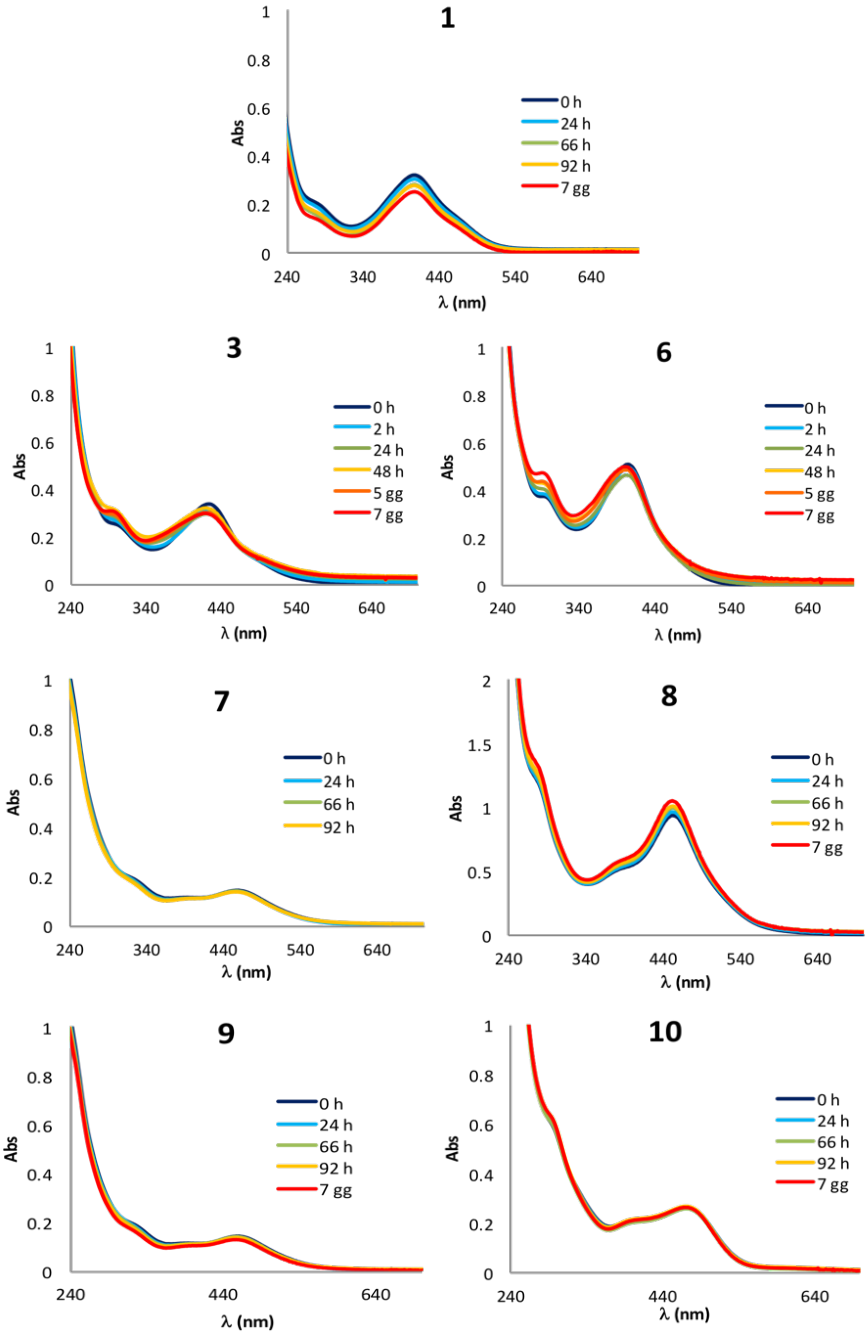

Figure 8.3 Stability in CH_2Cl_2 solution (dark) for halides 1, 3 and 6 and chalcogenides 7-10.

The higher energy bands (λ = 295-320 nm), less sensitive to the polarity of the solvent are instead tentatively attributed to singlet π-π* excitations of the pyridazine ligands, in a very similar way to what happens on rhenium complexes.

The stability of the manganese complexes was investigated in both solid state and solution. As shown in the series of plots in figure 8.3, when kept in the dark the dissolved complexes remain stable for several days and their absorption spectra show no sign of degradation. In the same way, no degradation is observed for the complexes in the solid state, whether in the dark or exposed to sunlight.

A completely different behavior is observed upon direct illumination of the complexes in solution in various solvents (CH_2Cl_2, acetone, THF, acetonitrile). Photostability tests were carried out by positioning a LED lamp (3 W cm^{-2}) at a fixed distance of 6 cm and measuring the absorption spectrum at regular time intervals. All the investigated complexes **1-10** proved highly photosensitive and degraded completely after a few minutes of irradiation. However, upon exposure to indirect sunlight, the disulfide and ditelluride derivatives **8-10** exhibited a moderate photostability in the considered solvents, whereas the halide complexes **1-6** and the methoxo complex **7** proved completely unstable.

8.2.3 Electrochemical Characterization

The intrinsic low stability of the here investigated manganese complexes in acetonitrile solution allowed to perform a reliable electrochemical characterization only on the sulfide and telluride derivatives **8-10**.

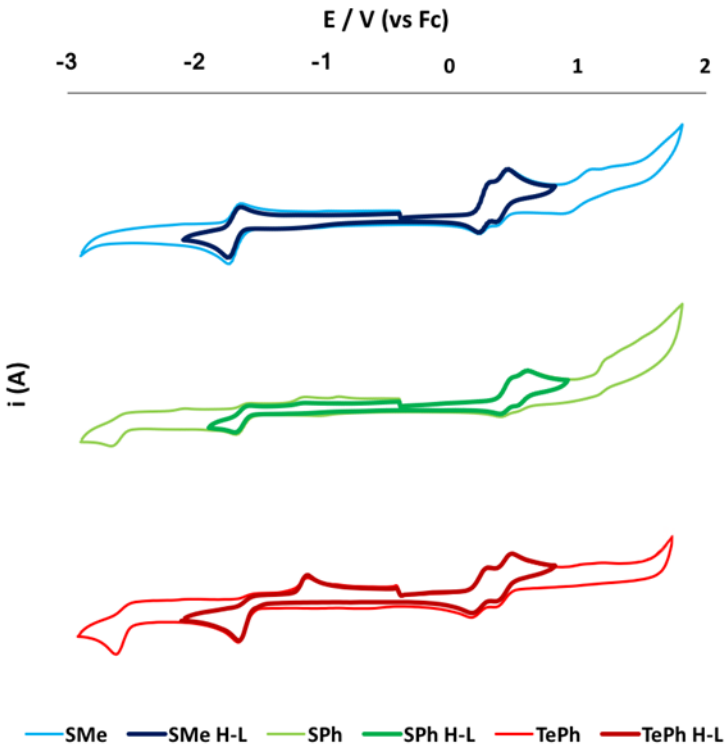

Figure 8.4 Cyclic voltammetry of dichalcogenide complexes **8-10** in dry ACN, $TBAPF_6$ 0.1 M, using a GC electrode of 1 mm in diameter. Scan rate 0.2 Vs^{-1}.

The cyclic voltammograms are shown in figure 8.4. A first monoelectronic reduction peak, located on the diazine ring, is found at ca -1.7 V (vs $Fc^+|Fc$). Differently from the dirhenium analogues, in which this peak is always completely reversible, here the reversibility depends on the nature of the ancillary ligand.

In fact, only the methylsulfide derivative **8** shows a completely reversible reduction peak, whereas for the phenylsulfide **9** and the phenyltelluride **10** this reduction is partially reversible and gives rise to a stable reduced species which can be re-oxidized at lower potential (ca. -1.0 V).

Also the oxidation behavior of these manganese complexes is quite different from that observed for the analogous rhenium complexes. First of all, two partially reversible monoelectronic oxidation peaks, instead of a bielectronic oxidation (see chapter 7), are here detected. The modulation of the peak potential with the nature of the chalcogenide atom strongly indicates that the oxidation is located on the metal centers and it is affected by the nature of the ancillary ligands.

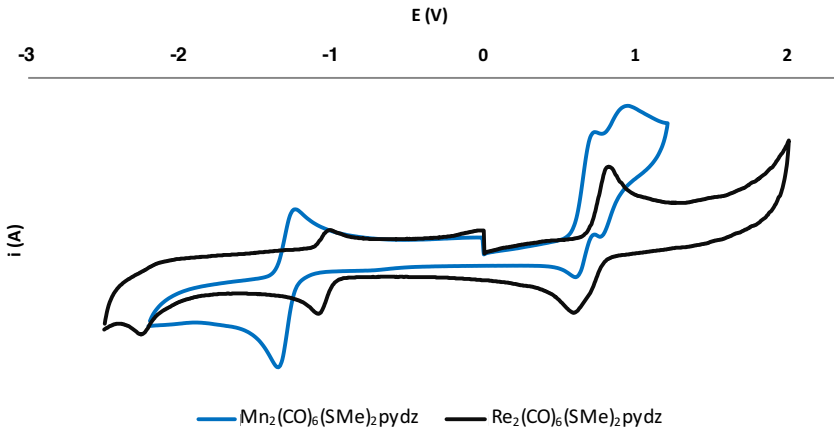

Figure 8.5 Comparison between the cyclic voltammetry of Mn (blue line) and Re (black line) analogous complexes.

The inductive effect of the metal center on the cyclic voltammetric behavior is pointed out by the comparison between Mn(I) and a Re(I) derivatives, as depicted in figure 8.5.

Intriguingly, for the manganese complex both the reduction and the oxidation potentials are lower than the analogous rhenium derivatives. This feature is in agreement with what already reported for the analogous mononuclear complexes[6] and related to the higher electronegativity of Re(I) compared to Mn(I), accounting for the higher stability of the metal complexes of the third transition, in low oxidation states, compared to the analogous metal complexes of the first as manganese. This inductive effect does not modify the HOMO-LUMO gap which remains similar, as also confirmed by the same MLCT absorption maxima observed for the two families.

8.3 Conclusions

A new family of dinuclear manganese complexes has been synthesized using 1,2-diazine as bridging ligand and various anions as ancillary ligands. The new complexes were prepared exploiting the same synthetic procedures already developed for the syntheses of the analogous rhenium complexes. However, taking into account the higher reactivity of manganese derivatives, milder synthetic conditions and more precautions in the storage of the products have been adopted. These complexes have been characterized by means of spectroscopic techniques such as IR, NMR and UV-Vis, observing the same features of the rhenium-based counterparts. Noteworthy differences have been observed in the electrochemical behavior, in particular in the oxidation process, where two monoelectronic oxidation peaks, instead of a bi-electronic one, have always been recorded. Further work is currently in progress in our laboratory to explore the applications of these dinuclear manganese complexes, especially as catalysts for CO_2 electro-reduction and H_2 production.

8.4 Experimental

General methods

All the reactions and the purification procedures were performed in the dark to avoid photo-oxidation and degradation of the considered complexes. All the reagents were purchased from Aldrich and used as received. All the reactions were performed under an inert N_2 atmosphere. All the solvents have been deoxygenated and dried by standard methods before use, toluene and mesitylene were distilled on $Na_{(s)}$, CH_2Cl_2 on P_2O_5. Commercial deuterated solvents were used as received. Column chromatography was performed using Alfa Aesar silica gel 60 (0.032–0.063 mm). $[Mn(CO)_5Cl]$, $[Mn(CO)_5Br]$ and $[Mn(\mu\text{-}I)_2(CO)_8]$ were synthesized according to literature procedures.[7] ^1H NMR spectra were recorded on a Bruker DRX-400 MHz instrument by using the residual signals δ = 7.28 ppm from $CDCl_3$ or δ = 5.32 ppm from CD_2Cl_2 as internal references. Due to the formation of paramagnetic species while preparing the NMR tube (also under inert atmosphere) and during the measurement (photochemical degradation), the peaks are usually very broad, and the resolution is very low, therefore we could not attribute any J value. IR spectra in solution were acquired on a Bruker Vector 22 FT spectrophotometer.

Electrochemical measurements

see chapter 3.

Spectroscopy

see chapter 3.

Synthesis of $[Mn_2(\mu\text{-}Cl)_2(CO)_6(\mu\text{-}pydz)]$ (1). 60 mg (0.26 mmol) of $Mn(CO)_5Cl$ are dissolved in 25 mL of anhydrous acetone, previously bubbled for 10 mins with N_2. 9.6 µL (0.13 mmol) of pyridazine are then added to the reaction mixture, which is left stirring at room temperature for 5 hours in the dark. The solution is then evaporated to dryness under vacuum. The yellow-orange solid remains are purified trough column chromatography (eluent CH_2Cl_2/n-hexane 1:1) and collected as amber powder, yielding 40 mg (0.09 mmol) of powder (yield 70%). IR (CH_2Cl_2) ν(CO): 2054 (m), 2036 (vs), 1966 (s), 1935 (s) cm^{-1}, ^1H NMR: (CD_2Cl_2, 300K, 400 MHz) δ_H (ppm) 10.01 (broad, 2H, $H_{ortho\ pydz}$), 7.94 (broad, 2H, $H_{meta\ pydz}$)

Synthesis of $[Mn_2(\mu\text{-}Br)_2(CO)_6(\mu\text{-}pydz)]$ (2). 75 mg (0.185 mmol) of $Mn(CO)_5Br$ are dissolved in 10 mL of anhydrous acetone, previously bubbled for 10 mins with N_2. 6.7 µL (0.092 mmol) of pyridazine are then added to the reaction mixture, which is left stirring at room temperature for 3 hours, then heating up to 60°C for 1 hour, always keeping the reaction vessel in the dark. The solution is then evaporated to dryness under vacuum. The obtained orange crude is purified trough column chromatography (eluent CH_2Cl_2/n-hexane 1:1) and collected as light orange powder, yielding 40 mg (0.09 mmol) of powder (yield 70%). IR (CH_2Cl_2) ν(CO): 2050 (m), 2033 (vs), 1964 (s), 1935 (s) cm^{-1}, ^1H NMR: (CD_2Cl_2, 300K, 400 MHz) δ_H (ppm) 10.06 (broad, 2H, $H_{ortho\ pydz}$), 7.90 (broad, 2H, $H_{meta\ pydz}$)

Synthesis of $[Mn_2(\mu\text{-}I)_2(CO)_6(\mu\text{-}pydz)]$ (3). 60 mg (0.102 mmol) of $Mn_2(CO)_8I$ are dissolved in 4 mL of anhydrous toluene, previously bubbled for 10 mins with N_2. 7.4 µL (0.102 mmol) of pyridazine are then added to the reaction mixture, which is left stirring under reflux for 6 hours in the dark. The solution is then evaporated to dryness under

vacuum. The obtained dark orange remains are purified trough column chromatography (eluent CH_2Cl_2/n-hexane 1:1) and collected as brick red powder, yielding 40 mg (0.09 mmol) of powder (yield 70%). IR (CH_2Cl_2) ν(CO): 2041 (m), 2025 (vs), 1959 (s), 1933 (s) cm^{-1}, ^1H NMR: (CD_2Cl_2, 300K, 400 MHz) δ_H (ppm) 10.02 (broad, 2H, $H_{ortho\ pydz}$), 7.78 (broad, 2H, $H_{meta\ pydz}$)

Synthesis of $[Mn_2(\mu\text{-}Cl)_2(CO)_6(\mu\text{-}4,5\text{-}(C_5H_{11})_2\text{-}pydz)]$ (4). 35 mg (0.123 mmol) of $Mn(CO)_5Cl$ are dissolved in 4 mL of anhydrous toluene, previously bubbled for 10 mins with N_2. 260 µL of a toluene solution containing 0.061 mmol of 4,5-bipentylpyridazine are then added to the reaction mixture, which is left stirring at room temperature for 4 hours in the dark. The solution is then evaporated to dryness under vacuum. The obtained dark orange remains are purified trough column chromatography (eluent CH_2Cl_2/n-hexane 1:1) and collected as bright yellow powder, yielding 15 mg (0.026 mmol) of powder (yield 43%). IR (CH_2Cl_2) ν(CO): 2052 (m), 2035 (vs), 1962 (s), 1932 (s) cm^{-1}, ^1H NMR: (CD_2Cl_2, 300K, 400 MHz) δ_H (ppm) 9.64 (broad, 2H, $H_{ortho\ pydz}$), 2.87 (m, 4H, CH_2), 1.77 (m, 4H, CH_2), 1.48 (m, 8H, CH_2), 0.98 (m, 6H, CH_3)

Synthesis of $[Mn_2(\mu\text{-}Br)_2(CO)_6(\mu\text{-}4,5\text{-}(C_5H_{11})_2\text{-}pydz)]$ (5). 82.5 mg (0.254 mmol) of $Mn(CO)_5Br$ are dissolved in 6 mL of anhydrous toluene, previously bubbled for 10 mins with N_2. 520 µL of a toluene solution containing 0.112 mmol of 4,5-bipentylpyridazine are then added to the reaction mixture, which is left stirring at 80°C for 6 hours in the dark. The solution is then evaporated to dryness under vacuum. The obtained dark orange remains are purified trough column chromatography (eluent CH_2Cl_2/n-hexane 1:1) and collected as amber-orange powder, yielding 43 mg (0.065 mmol) of powder (yield 53%). IR (CH_2Cl_2) ν(CO): 2048 (m), 2032 (vs), 1960 (s), 1932 (s) cm^{-1}, ^1H NMR:

(CD_2Cl_2, 300K, 400 MHz) δ_H (ppm) 9.68 (broad, 2H, $H_{ortho\ pydz}$), 2.86 (m, 4H, CH_2), 1.77 (m, 4H, CH_2), 1.48 (m, 8H, CH_2), 0.98 (m, 6H, CH_3)

Synthesis of $[Mn_2(\mu\text{-}I)_2(CO)_6(\mu\text{-}4,5\text{-}(C_5H_{11})_2\text{-}pydz)]$ (6). 60 mg (0.102 mmol) of $Mn_2(CO)_8I$ are dissolved in 6 mL of anhydrous toluene, previously bubbled for 10 mins with N_2. 475 µL of a toluene solution containing 0.102 mmol of 4,5-bipentylpyridazine are then added to the reaction mixture, which is left stirring at room temperature for 4 hours in the dark. The solution is then evaporated to dryness under vacuum. The obtained dark orange remains are purified trough column chromatography (eluent CH_2Cl_2/n-hexane 1:1) and collected as dark orange powder, yielding 44 mg (0.059 mmol) of powder (yield 58%). IR (CH_2Cl_2) ν(CO): 2039 (m), 2024 (vs), 1955 (s), 1930 (s) cm^{-1}, ^1H NMR: (CD_2Cl_2, 300K, 400 MHz) δ_H (ppm) 9.63 (broad, 2H, $H_{ortho\ pydz}$), 2.86 (m, 4H, CH_2), 1.77 (m, 4H, CH_2), 1.48 (m, 8H, CH_2), 0.98 (m, 6H, CH_3)

Synthesis of $[Mn_2(\mu\text{-}OMe)_2(CO)_6(\mu\text{-}pydz)]$ (7). In a solvothermal bomb 100 mg (0.256 mmol) of $Mn_2(CO)_{10}$ and 18.5 µL (0.256 mmol) of pyridazine are added to 7 mL of anhydrous toluene and 3 mL of anhydrous MeOH. The bomb is sealed and heated up to 120°C. After 20 hours the bomb is opened and the solution transferred to a Schlenk flask where the solvent is evaporated to dryness under vacuum. The reddish solid remains are purified trough column chromatography (eluent CH_2Cl_2/EtOAc 8:2) and collected as red powder, yielding 18 mg (0.09 mmol) of powder (yield 70%). IR (CH_2Cl_2) ν(CO): 2033 (m), 2014 (vs), 1934 (s), 1906 (s) cm^{-1}, ^1H NMR: (acetone-d_6, 300K, 400 MHz) δ_H (ppm) 10.15 (m, 2H, $H_{ortho\ pydz}$), 8.32 (m, 2H, $H_{meta\ pydz}$), 3.81 (m, 6H, CH_3)

Synthesis of $[Re_2(\mu\text{-}SMe)_2(CO)_6(\mu\text{-}pydz)]$ (8). 100 mg (0.256 mmol) of Mn_2CO_{10} are dissolved in 8 mL of anhydrous toluene. 23 µL (0.256 mmol) of dimethyldisulfide and 19 µL (0.256 mmol) of pyridazine are added to the reaction mixture, which is left stirring under reflux in the dark overnight. The solution is evaporated to dryness under vacuum. The solid remains are purified through column chromatography (CH_2Cl_2) yielding 63 mg (0.139 mmol) of the desired product as brownish powder (yield 54%). IR (CH_2Cl_2) ν(CO): 2026 (m), 2005 (vs), 1940 (s), 1914 (s) cm^{-1}, ^1H NMR: (CD_2Cl_2, 300K, 400 MHz) δ_H (ppm) 10.04 (broad, 2H, $H_{ortho\ pydz}$), 7.68 (broad, 2H, $H_{meta\ pydz}$), 1.58 (broad, 6H, CH_3)

Synthesis of $[Mn_2(\mu\text{-}SPh)_2(CO)_6(\mu\text{-}pydz)]$ (9). 50 mg (0.128 mmol) of Mn_2CO_{10} and 28 mg (0.128 mmol) of diphenyldisulphide are dissolved in 5 mL of anhydrous toluene. 9 µL (0.128 mmol) of pyridazine are added to the reaction mixture, which is left stirring under reflux overnight in the dark. The solution is evaporated to dryness under vacuum. The dark brown solid remains are purified through column chromatography (CH_2Cl_2) yielding 20 mg (0.035 mmol) of brown powder (yield 27%). IR (CH_2Cl_2) ν(CO): 2031 (m), 2012 (vs), 1948 (s), 1923 (s) cm^{-1}, ^1H NMR: (CD_2Cl_2, 300K, 400 MHz) δ_H (ppm) 10.05 (broad, 2H, $H_{ortho\ pydz}$), 7.77 (broad, 2H, $H_{meta\ pydz}$), 7.20-7.05 (broad, 12H, $_{phenyl}$)

Synthesis of $[Mn_2(\mu\text{-}TePh)_2(CO)_6(\mu\text{-}pydz)]$ (10). 50 mg (0.128 mmol) of Mn_2CO_{10} and 52.5 mg (0.128 mmol) of diphenylditelluride are dissolved in 4 mL of anhydrous toluene. 9.3 µL (0.128 mmol) of pyridazine are added to the reaction mixture, which is left stirring under reflux for 15 hours in the dark. The solution is evaporated to dryness under vacuum. The dark solid remains are purified through column chromatography (CH_2Cl_2) yielding 40 mg (0.052 mmol) of dark brown powder (yield

41%). IR (CH_2Cl_2) ν(CO): 2014 (m), 1996 (vs), 1934 (s), 1919 (s) cm^{-1}, ^1H NMR: (CD_2Cl_2, 300K, 400 MHz) δ_H (ppm) 9.85 (m, 2H, $H_{ortho\ pydz}$), 7.45 (m, 2H, $H_{meta\ pydz}$), 7.07-6.95 (m, 12H, $_{phenyl}$)

References

[1] J. Elmsley, The Elements, Oxford University Press, Oxford, **1989**, 218

[2] (a) M. Bourrez, F. Molton, S. Chardon-Noblat, A. Deronzier, *Angew. Chem., Int. Ed.* **2011**, 50, 9903; (b) J.M. Smieja, M.D. Sampson, K.A. Grice, E.E. Benson, J.D. Froehlich, C.P. Kubiak, *Inorg. Chem.* **2013**, 52, 2484; (c) J. Agarwal, T.W. Shaw, C.J. Stanton, G.F. Majetich, A.B. Bocarsly, H.F. Schaefer, *Angew. Chem., Int. Ed.* **2014**, 53, 5152; (d) M. Bourrez, M. Orio, F. Molton, H. Vezin, C. Duboc, A. Deronzier, S. Chardon-Noblat, *Angew. Chem., Int. Ed.* **2014**, 53, 240; (e) D.C. Grills, J.A. Farrington, B.H. Layne, S.V. Lymar, B.A. Mello, J.M. Preses, J.F. Wishart, *J. Am. Chem. Soc.* **2014**, 136, 5563; (f) M.D. Sampson, A.D. Nguyen, K.A. Grice, C.E. Moore, A.L. Rheingold, C.P. Kubiak, *J. Am. Chem. Soc.* **2014**, 136, 5460; (g) H. Takeda, H. Koizumi, K. Okamoto, O. Ishitani, *Chem. Commun*. **2014**, 50, 1491

[3] (a) M.A. Gonzalez, S.J. Carrington, N.L. Fry, J.L. Martinez, P.K. Mascharak, *Inorg. Chem.* **2012**, 51, 11930; (b) H. Berends, P. Kurz, *Inorg. Chim. Acta* **2012**, 380, 141; (c) P. Rudolf, F. Kanal, J. Knorr, C. Nagel, J. Niesel, T. Brixner, U. Schatzschneider, P. Nuernberger, *J. Phys. Chem. Lett*. **2013**, 4, 596; (d) P. Govender, S. Pai, U. Schatzschneider, G.S. Smith, Inorg. Chem. **2014**, 52, 5470

[4] (a) C. A. Kumar, R. Nagarajaprakash, B. Ramakrishna, B. Manimaran, *Inorg. Chem*. **2015**, 54 (17), 8406; (b) S. Karthikeyan, R. Nagarajaprakash, G. Satheesh, C. A. Kumar, B. Manimaran, *Dalton Trans*. **2015**, 44, 17389; (c) K. D. Benkstein, J. T. Hupp, C. L. Stern, *Angew. Chem. Int. Ed*. **2000**, 39, 2891

[5] G. Valenti, M. Panigati, A. Boni, G. D'Alfonso, F. Paolucci L. Prodi, *Inorg. Chim. Acta* **2014**, *417*, 270

[6] A. M. Bond, R. Colton, P. Panagiotidou, *Organomet*. **1988**, *7*, 1767

[7] (a) E. O. Brimm, M. A. Lynch Jr., W. J. Sesny, *J. Am. Chem. Soc.* **1954**, 76, 3831; (b) E. W. Abel, G. Wilkinson, *J. Chem. Soc.* **1959**, 1501